



University  
of Stavanger

**FREDERIK THORBJØRN HULD**  
FACULTY OF SCIENCE AND TECHNOLOGY

---

# **Exploring the behaviour of Silicon by empirical analysis of galvanostatic charge-discharge curves.**

---

PhD Thesis - - January 2024

University of Stavanger  
NO-4036 Stavanger  
NORWAY  
[www.uis.no](http://www.uis.no)

©2024 Frederik Thorbjørn Huld

ISBN: 978-82-8439-218-9  
ISSN: 1890-1387.  
PhD: Thesis UiS No. 746

*“Truth ... is much too complicated to allow anything but approximation.”*

– John von Neumann



# Abstract

The capability of battery materials to deliver not only high lithium (Li) storage capacity, but also the ability to operate at high charge/discharge rates is an essential property for development of new batteries. First, the influence on the charge/discharge rate behaviour of substoichiometric concentrations of phosphorus (P) in silicon (Si) nanoparticles was studied. The results revealed an increase in rate capability as a function of the P concentration between 0 and 5.2 at%, particularly during delithiation. The stoichiometry of the nanoparticles was found to strongly affect the formation of the  $\text{Li}_{3.5}\text{Si}$  phase during lithiation. Cyclic stability experiments demonstrated an initial increase in capacity for the  $\text{SiP}_x$  materials. Galvanostatic intermittent titration technique (GITT) and electrochemical impedance spectroscopy (EIS) demonstrated the increased Li diffusivity with inclusion of P. Density functional theory and *ab initio* molecular dynamics were deployed to provide a rationale for the electrochemical behaviour of  $\text{SiP}_x$ .

This study revealed the need for further studies into the behaviour of pure Si, given that the galvanostatic charge-discharge (GCD) behaviour of Si is known to depend strongly on morphology, cycling conditions and electrochemical environment. One common method for analysing GCD curves is through differential capacity, but the data processing required necessarily degrades the results. We therefore present a method of extracting empirical information from the delithiation step in GCD data for Si at C-rates above equilibrium conditions. We find that the function is able to quickly and accurately determine the best fit to historical half-cell data on amorphous Si nanowires and thin films, and analysis of the results reveals that the function is capable of distinguishing the capacity contributions from the  $\text{Li}_{3.5}\text{Si}$  and  $\text{Li}_2\text{Si}$  phases to the total capacity. The method is can also pick up small differences in the phase behaviour of the different samples, making it a powerful technique for further analysis of Si data from literature. The

method was also used for predicting the size of the reservoir effect (the apparent amount of Li remaining in the electrode), making it a useful technique for quickly determining voltage slippage and related phenomena. This work is presented as a starting point for more in-depth empirical analysis of Si GCD data.

However, half cells commonly used for Si studies are limited by polarization of the Li counter electrode, especially at high Si loading. To study the interplay between Si and Li electrodes, a set of EIS spectra are generated using cycled Si half cells at four different potentials in the charge-discharge profile, and then repeated using symmetric Si/Si and Li/Li cells assembled from half cells cycled to equivalent stages in the cycle. Distribution of relaxation times (DRT) analysis is used to design equivalent circuits (ECs) for both Si/Si and Li/Li symmetric cells incorporating both electrolyte and electrode-related diffusion, and these are applied to the half cells. The results demonstrate that the behaviour of half cells is dominated by the solid electrolyte interphase (SEI) impedances at the Li counter electrode at the low and high potentials where the  $\text{Li}^+$  mobility signal in Si is limited, while the Si electrode is dominant at intermediate potentials where the signal from mobile  $\text{Li}^+$  is strong. EIS studies of Si half cells should therefore be performed at intermediate potentials, or as symmetric cells.

Finally, we applied the empirical fitting function presented earlier to aid in the analysis of GCD data of commercial Si half-cells with high loading. We find that the fitting procedure is capable of detecting dynamic changes in the cell, such as reversible capacity fade of the Si electrode. This fading is found to be due to the highly lithiated  $\text{Li}_2\text{Si} \rightleftharpoons \text{Li}_{3.5}\text{Si}$  phase and that the behaviour is strongly dependent on the potential of this phase. EIS reveals that the Si electrode is responsible for the reversible behaviour due to progressive loss of  $\text{Li}^+$  leading to increasing resistance. To complete the characterization SEM/EDX and XPS are also employed to determine the origin of the irreversible resistance growth on the Si electrodes.

# Acknowledgements

The number of people who have helped me in one way or another would span multiple pages, and so I am forced to mention only a few. Firstly I would like to thank my wife Charlotte for her unending support. I would like to thank my supervisors doctor Fengliu Lou and professor Zhixin Yu for their guidance and patience throughout this project; my fellow PhD students Obinna Eleri and Yang Zhang for many fruitful discussions; as well as professor Alexey Kuposov for his thorough and honest criticisms. I would also like to thank my co-workers at Beyonder for their help, not least Ana Trindade and doctor Rasim Batmaz, whose boundless positivity kept me motivated. Finally I would like to thank the management at Beyonder, especially Bjarte Magnussen, doctor Hanho Lee and Svein Kvernstuen, whose belief in the project were critical the success of this PhD.





# List of publications

- i. Enabling Increased Delithiation Rates in Silicon-Based Anodes through Alloying with Phosphorus  
**Frederik T. Huld**, Samson Y. Lai, Wakshum M. Tucho, Rasim Batmaz, Ingvild T. Jensen, Song Lu, Obinna E. Eleri, Alexey Y. Kopusov, Zhixin Yu, Fengliu Lou  
*ChemistrySelect*, **2022**, doi:10.1002/slct.202202857
- ii. Revealing Silicon's Delithiation Behaviour through Empirical Analysis of Galvanostatic Charge–Discharge Curves  
**Frederik T. Huld**, Jan Petter Mæhlen, Caroline Keller, Samson Y. Lai, Obinna E. Eleri, Alexey Y. Kopusov, Zhixin Yu, and Fengliu Lou  
*Batteries*, **2023**, doi:10.3390/batteries9050251
- iii. Unravelling the electrochemical impedance spectroscopy of silicon half cells with commercial loading  
**Frederik T Huld**, Zhixin Yu, and Fengliu Lou  
*Energy Advances*, **2023**, doi:10.1039/D3YA00181D
- iv. New insights into the behaviour of commercial silicon electrode materials *via* empirical fitting of galvanostatic charge-discharge curves  
**Frederik T Huld**, Obinna E Eleri, Fengliu Lou, and Zhixin Yu  
*Submitted*



# Additional publications

- v. Challenges, mitigation strategies and perspectives in development of Li metal anode  
Zaisheng Wang, Jiawen Yu, Mumin Rao, Xiaojin Jin, **Frederik Huld**, Zhenming Xu, Yong Li, Fengliu Lou, Daiqi Ye, Yongcai Qiu  
*Nano Select*, **2020**, doi:10.1002/nano.202000123
- vi. Revisiting Polytetrafluoroethylene Binder for Solvent-Free Lithium-Ion Battery Anode Fabrication  
Yang Zhang, **Frederik Huld**, Song Lu, Camilla Jektvik, Fengliu Lou, and Zhixin Yu  
*Batteries*, **2022**, doi:10.3390/batteries8060057
- vii. Enhanced activated carbon lithium-ion capacitor electrochemical stability through electrolyte dielectric optimisation  
Obinna Egwu Eleri, Julie Pires, **Frederik Huld**, Song Lu, Philipp Schweigart, Ann Mari Svensson, Fengliu Lou, and Zhixin Yu  
*Sustainable Energy Fuels*, **2023**, doi:10.1039/D3SE00122A
- viii. Revealing mechanisms of activated carbon capacity fade in lithium-ion capacitors  
Obinna Egwu Eleri, **Frederik Huld**, Julie Pires, Wakshum Mekonnen Ticho, Philipp Schweigart, Ann Mari Svensson, Fengliu Lou, Zhixin Yu  
*Electrochimica Acta*, **2023**, doi:10.1016/j.electacta.2023.142359
- ix. Deciphering electrolyte dielectric extended electrochemical stability in lithium-ion capacitors

Obinna Egwu Eleri, **Frederik Huld**, Fengliu Lou, Zhixin Yu

*Electrochimica Acta*, **2023**, doi:<https://doi.org/10.1016/j.electacta.2023.142960>

# Software

- Neware\_reader

A Python Package was developed to help researchers to extract data from Neware battery analyzers.

[https://github.com/FTHuld/neware\\_reader](https://github.com/FTHuld/neware_reader)



# Conference presentations

- **Frederik T. Huld**, Samson Y. Lai, Wakshum M. Tucho, Rasim Batmaz, Ingvild T. Jensen, Song Lu, Obinna E. Eleri, Alexey Y. Kuposov, Zhixin Yu, Fengliu Lou

Diffusivity and rate enhancement of low-concentration Silicon-Phosphorus alloy nanoparticles

Poster presentation at the International Meeting on Lithium Batteries (IMLB).  
Sydney (Australia), *July 2022*

This poster received a “Certificate for highly recommended poster” at the IMLB.





# Contribution statement

I, Frederik Huld, declare that this thesis titled, “Exploring the behaviour of Silicon by empirical analysis of galvanostatic charge-discharge curves” and the work presented in it are my own. I confirm that:

1. This work was done wholly or mainly while in candidature for a PhD degree at the University of Stavanger.
2. Where I have consulted the published work of others, this is always clearly attributed.
3. Where I have quoted from the work of others, the source is always given. With the exception of such quotations, this thesis is entirely my own work.

Sources of help and work performed by others regarding the various works are acknowledged below for each paper. All other work was performed by me:

1. Enabling Increased Delithiation Rates in Silicon-Based Anodes through Alloying with Phosphorus  
P-containing nanoparticles were produced and supplied by S. Y. Lai and A. Y. Kuposov at IFE. The experimental section relating to the synthesis of nanoparticles was written together with/based on information obtained from them. *ab initio* calculations and analysis were performed by S. Lu at UiS, and XPS analysis was performed by I. T. Jensen at SINTEF. ICP-OES experiments were contracted to an external company (SINTEF, Norway). The experimental section relating to computational methods was written together with/based on information obtained from Song Lu.
2. Revealing Silicon’s Delithiation Behaviour through Empirical Analysis of Galvanostatic Charge–Discharge Curves

Thin film data was supplied by J. P. Mæhlen. Thin films were made by A. Y. Kuposov, and thin film cells were made and tested by S. Y. Lai. Nanowire data was supplied by C. Keller from previously published work. The experimental sections relating to the synthesis, electrode manufacturing, cells assembly and testing of these cells was written based on information provided by them.

3. New insights into the behaviour of commercial silicon electrode materials *via* empirical fitting of galvanostatic charge-discharge curves

SEM/EDX and XPS experiments were contracted to an external company (Shiyanjia, China). XPS fitting and analysis was performed by O. E. Eleri.

# Contents

<b>Abstract</b>	<b>iii</b>
<b>Acknowledgements</b>	<b>v</b>
<b>List of publications</b>	<b>vii</b>
<b>Additional publications</b>	<b>ix</b>
<b>Software</b>	<b>xi</b>
<b>Conference presentations</b>	<b>xiii</b>
<b>Contribution statement</b>	<b>xv</b>
<b>List of figures</b>	<b>xxi</b>
<b>List of tables</b>	<b>xxvii</b>
<b>1 Introduction</b>	<b>1</b>
1.1 Si nanostructuring . . . . .	2
1.2 Coatings, heteroatoms and conversion materials . . . . .	2
1.3 Understanding Si during charging and discharging . . . . .	3
<b>2 Literature review</b>	<b>5</b>
2.1 Si and Si materials . . . . .	5
2.2 Lithiation and delithiation of Si . . . . .	7
2.2.1 A note on nomenclature . . . . .	8
2.3 Studying Si materials . . . . .	8

2.4	Interpreting GCD data . . . . .	13
2.4.1	Distinction between fitting and modelling . . . . .	15
2.5	Towards commercialization . . . . .	16
<b>3</b>	<b>Objectives and scope of this project</b>	<b>17</b>
<b>4</b>	<b>Experimental</b>	<b>19</b>
4.1	Material preparation . . . . .	19
4.2	Electrode preparation . . . . .	19
4.2.1	Electrode preparation for chapter 5 . . . . .	20
4.2.2	Electrode preparation for chapter 6 . . . . .	20
4.2.3	Electrode preparation for chapters 7 & 8 . . . . .	21
4.3	Cell assembly and disassembly . . . . .	22
4.4	Electrochemical testing . . . . .	23
4.4.1	Formation and cycling . . . . .	23
4.4.2	EIS and DRT analysis . . . . .	24
4.4.3	GITT . . . . .	24
4.5	Material and electrode characterization . . . . .	24
4.6	Computational methods . . . . .	25
4.6.1	Modelling . . . . .	25
4.6.2	Fitting of EIS data and DRT analysis . . . . .	26
4.6.3	Fitting of GCD data . . . . .	26
<b>5</b>	<b>Delithiation rates of silicon-phosphorus based alloys</b>	<b>27</b>
5.1	Materials characterisation of SiP <sub>x</sub> and Si NPs . . . . .	27
5.2	Stability and rate capability of SiP <sub>x</sub> NPs . . . . .	29
5.3	DFT and AIMD on SiP <sub>x</sub> and Si . . . . .	37
5.4	GITT and EIS of SiP <sub>x</sub> and Si . . . . .	38
<b>6</b>	<b>Empirical analysis of silicon GCD curves</b>	<b>41</b>
6.1	Physical considerations of the fitting function . . . . .	41
6.2	Parameter setup and goodness of fit . . . . .	42
6.3	Comparison of thin films and nanowires . . . . .	45
6.3.1	Phases of Si delithiation . . . . .	49
6.4	Voltage slippage and excess Li effects . . . . .	51

<b>7</b>	<b>Electrochemical impedance spectroscopy of silicon half cells</b>	<b>55</b>
7.1	EIS of half and symmetric cells . . . . .	55
7.2	DRT of half and symmetric cells . . . . .	57
<b>8</b>	<b>Empirical GCD analysis of commercial silicon materials</b>	<b>63</b>
8.1	GCD fitting of commercial Si . . . . .	63
8.2	EIS and DRT of commercial Si . . . . .	67
<b>9</b>	<b>Concluding remarks</b>	<b>75</b>
<b>A</b>	<b>Appendix</b>	<b>79</b>
<b>B</b>	<b>Papers</b>	<b>99</b>
	Paper I and supporting information . . . . .	100
	Paper II and supporting information . . . . .	124
	Paper III and supporting information . . . . .	140
	Paper IV and supporting information . . . . .	149
	<b>References</b>	<b>159</b>



# List of Figures

2.1	Schematic illustration showing present work on $\text{SiP}_x$ anode materials displayed as a function of the atomic % of P in Si, as well as the main effect attributed to the P in the given concentration range. The contribution to the literature of this thesis is shown as off-set red circles. . . . .	7
2.2	Schematic showing the phases of Si as a plot of the $dQ/dV$ as a function of the potential ( <i>vs</i> $\text{Li}/\text{Li}^+$ ). Displayed in this way phase I (green filled curves) always appear at lower potentials than phase II (red filled curves) . . . . .	9
5.1	(a) TEM image showing a micron-sized aggregate of $\text{P}_{5.2}$ ; (b) HAADF image of a single particle of the $\text{P}_{5.2}$ material; (c) HAADF-EDS mapping of P in a particle of $\text{P}_{5.2}$ material. . . . .	28
5.2	Cyclic stability and rate capability behaviour using asymmetric GCD. (a) Cyclic stability with delithiation set to 0.3 C and lithiation set to 0.1 C. (b) Cyclic stability with lithiation set to 0.3 C and delithiation set to 0.1 C. Error bars were calculated from the average of three cells. (c) Normalized delithiation rates with slow lithiation at 0.1 C. (d) Normalized lithiation rates with slow delithiation at 0.1 C. A diagnostic cycle at 0.05 C was included after every tenth cycle for the tests shown in the panels a and b. The star at cycle four in panels c and d is the normalization point, the first point after formation. . . . .	32
5.3	$dQ/dV$ of rate capability experiments with lithiation rate fixed at 0.1 C and varying delithiation rates. (a, b) increasing C-rate; (c, d) decreasing C-rate. (a, c) sample P0; (b, d) sample P1.5. . . . .	34

5.4	dQ/dV of rate capability experiments with delithiation rate fixed at 0.1 C and varying lithiation rates. (a, b) increasing C-rate; (c, d) decreasing C-rate. (a, c) sample PO; (b, d) sample P1.5. . . . .	35
5.5	Diffusivity as a function of potential for Si and SiPx. (a) Diffusivity calculated from GITT data using Equation 5.1. (b) Diffusivity calculated from the Warburg constants from EIS data using Equation 5.2. The diffusivities are calculated at the electrode level. . . . .	38
6.1	An example of the goodness of fit of cycle number 5 from a 40 nm SiTF cell. <b>(a)</b> The raw output of the fitting model, showing the input data as blue points overlaid with the best-fit determined by the program (orange line). The dotted lines are the curves of the individual phases which together make up the full fitting function. <b>(b)</b> Residuals of the fit, displayed as a percentage difference from the measured points. <b>(c)</b> The data from (a), displayed as a dQ/dV plot. The top offset shows the data as blue points overlaid with the best fit (orange line). The middle offset shows the contribution to the fit of phase I (green) and phase II (red). The bottom offset shows how the phases are composed of skew-Gaussian and Lorentzian curves.	44
6.2	Output of fitting equation 2.8 to the data, displayed as dQ/dV and showing the evolution of the curves with cycling for <b>(a)</b> 40 nm TFs, and <b>(b)</b> 9 nm NWs. Each curve is an average of x cycles, where x is $1/10^{th}$ of the total number of cycles. The locations of the dots and diamonds correspond to $c_I$ and $c_{II}$ , respectively. The dotted vertical lines denote c for the first cycles. . . . .	46
6.3	Comparison of the capacities of phases I (blue) and II (orange), for an example of thin films (dots) and nanowires (crosses). The data is normalized to the total capacity of each point as determined by the fitting. The horizontal dotted lines denote the initial guess of full conversion between the two phases. . . . .	50



6.4	<p><b>(a)</b> An example of the capacity vs cycle life of a thin film sample (blue points), including the capacity contributions of each phase (green and red points) to the total capacity from the model (orange points). <b>(b)</b> Plot showing the capacity of the cell as the voltage is extended beyond the cutoff potential. The blue dots denote the raw data, while the orange line denotes the best fit. The black vertical line at <math>\sim 0.85</math> V denotes the end of the measured data (i.e. the cut-off potential). The orange shaded area is the reservoir. <b>(c)</b> The reservoir of the different materials as calculated from equation 6.1. The data is displayed as a percentage of the <math>Q_{measured}</math> for each material. . . . .</p>	53
7.1	<p>EIS spectra collected for comparison between half cells and symmetric cells at <b>(a)</b> 0.2 V in the lithiation step; <b>(b)</b> 0.07 V in the lithiation step; <b>(c)</b> 0.3 V in the delithiation step; <b>(d)</b> 0.48 V in the delithiation step. . . . .</p>	56
7.2	<p>DRT spectra generated for comparison between half cells and symmetric cells at <b>(a)</b> 0.2 V in the lithiation step; <b>(b)</b> 0.07 V in the lithiation step; <b>(c)</b> 0.3 V in the delithiation step; <b>(d)</b> 0.48 V in the delithiation step. The coloured regions above and below the curves denote the confidence interval of the analysis, while the greyed out area denotes the extrapolated curves beyond the edges of the available data. . . . .</p>	57
7.3	<p>ECs of symmetric and half-cells determined by fitting to EIS data</p>	60
7.4	<p>Schematic describing the behaviour of Si half cells at different points in the charge-discharge curve. The dominant diffusion behaviour is denoted on the right hand side. . . . .</p>	61
8.1	<p><b>(a)</b> Capacity (blue) and Coulombic efficiency (grey) as a function of cycle life. The crosses denote the slow cycles used for generating EIS spectra, while the points denote the faster cycles used for GCD fitting. <b>(b)</b> EIS spectra generated at 4 potentials in the GCD curve. <b>(c)</b> An example of the fitting function applied to the GCD curves along with the shapes of the individual phases. . . . .</p>	64

8.2	Results of fitting equation 2.8 to the GCD data. <b>(a)</b> Total $dQ/dV$ of the first ten cycles at $C/3$ (grey lines) and the component phases (green and red for phases I and II, respectively). Darker lines correspond to later cycles. The points and diamonds denote the location of the apparent equilibrium potentials $c_I$ and $c_{II}$ , respectively. <b>(b)</b> Comparison between the $iR$ drop immediately after the start of delithiation and the apparent equilibrium potentials $c_I$ and $c_{II}$ , as a function of the cycle number. <b>(c)</b> Total capacity of the cells along with the capacities of the individual phases, as a function of cycle number. . . . .	66
8.3	Results of performing EIS on Si half cells. <b>(a)</b> The capacity as a function of time for the slow cycle used for EIS. The circles at 40 h denote the point in time at which the EIS spectra displayed in <b>(b)</b> were collected. <b>(b)</b> EIS spectra taken at the end of the 0.07 V step. <b>(c)</b> DRT of the EIS spectra shown in <b>(b)</b> . The shape of the curves in the greyed out area are artefacts of the analysis. . . . .	68
8.4	SEM images of Si electrodes <b>(a)</b> before and <b>(b)</b> after cycling. . . .	71
8.5	<b>(a)</b> Spot EDX of Si anodes before and after cycling. <b>(b)</b> XPS C1s spectrum of the Si anode before cycling. <b>(c)</b> XPS C1s spectrum of the Si anode after cycling. . . . .	72
8.6	Schematic showing the process of irreversible and reversible resistance growth, and its relationship to the fast capacity fade seen in Si half cells. . . . .	74
A.1	TEM images of the four silicon samples, showing the micron-sized aggregates of SiNPs typical of silane decomposition. The four images are for a) P0, b) P1.5, c) P3.2. P5.2 is shown in Figure 1 in the main text . . . . .	80
A.2	Particle size distributions (counts) for SiP <sub>x</sub> NPs from TEM. a) P0, b) P1.5, c) P3.2, and d) P5.2. . . . .	81
A.3	EDS spectra for the 4 samples as determined from TEM. a) P0, b) P1.5, c) P3.2, and d) P5.2. . . . .	81
A.4	XRD spectra for the 4 samples . . . . .	82
A.5	Galvanostatic cycling of SiP <sub>x</sub> alloy. (a) Voltage profiles of the 1 <sup>st</sup> cycle; (b) $dQ/dV$ profiles for the 1 <sup>st</sup> cycle. . . . .	82

A.6	An example of $\text{SiP}_x$ /Active Carbon full cell. The $\text{SiP}_x$ material used consists of 5 atomic % P in Si, equivalent to P5.2 in the text. The anode consists of 60% $\text{SiP}_x$ , with the remaining 40% being made up of carbon black, conductive graphite, and sodium carboxymethylcellulose. . . . .	83
A.7	dQ/dV for cycles 6-14 of the cyclic stability data presented in Fig. 5.1c. The arrows show the behaviour of the $\text{Li}_{3.5}\text{Si}$ peak. (a) P0, (b) P1.5, (c) P3.2, (d) P5.2. . . . .	83
A.8	dQ/dV for cycles 6-14 of the cyclic stability data presented in Fig. 5.1d. The arrows show the behaviour of the $\text{Li}_{3.5}\text{Si}$ peak. (a) P0, (b) P1.5, (c) P3.2, (d) P5.2. . . . .	84
A.9	XPS spectra for Electrodes before and after cycling, showing the P2p peak at 130eV. The middle (green) and bottom (red) spectra correspond to the P5.2 material before and after formation cycles, respectively. The top red line is the spectrum for the uncycled pure Si electrodes. . . . .	85
A.10	Configuration of $\text{Si}_{63}\text{PLi}_4$ (1.6% P concentration), where medium-blue, limegreen and mistyrose denote the Si, Li and P atoms, respectively . . . . .	86
A.11	Total energy variations of $\text{Si}_{64}\text{Li}$ , $\text{Si}_{63}\text{P}_1\text{Li}_4$ , $\text{Si}_{62}\text{P}_2\text{Li}_4$ and $\text{Si}_{61}\text{P}_3\text{Li}_4$ as a function of time for the AIMD simulation. The respective initial and final structures are shown as insets . . . . .	86
A.12	(a) Typical GITT curve, in this case for P3.2. (b) Diffusivity of lithiation process for the four samples. (c) Equivalent circuit used for EIS fitting. (d) Example of EIS curve with fit. The EIS spectra were fitted to the equivalent circuit shown in (d) using modulus weighting, which gave low error values (1-5%) for the Si-related charge transfer loop and the Warburg diffusion . . . . .	87
A.13	The skew parameter $\alpha$ for phases I and II for (a) NWs and (b) TFs, as a function of the cycle life. . . . .	88
A.14	The equilibrium potential $c$ for phases I and II for (a) NWs and (b) TFs, plotted as a function of the cycle life. . . . .	88
A.15	The scale parameter $s$ of the Gaussian component for phases I and II for (a) NWs and (b) TFs, plotted as a function of the cycle life. . . . .	88

A.16	The scale parameter $\gamma$ of the Lorentzian component for phase I for (a) NWs and (b) TFs, plotted as a function of the cycle life. . . . .	89
A.17	The weighting parameter $w$ for phases I and II for (a) NWs and (b) TFs, as a function of the cycle life. . . . .	89
A.18	An example of the cycle used for preparing the electrode for EIS, showing how the CCCV procedure is set to each “stop” potential. EIS was taken at the end of each CCCV step, as shown by the orange circles. . . . .	91
A.19	An example of the formation cycles performed on Si half-cells used in this study. The first cycle was performed at 1/20 C, while the second and third cycles were performed at 1/10 C . . . . .	92
A.20	EIS spectra of half cell (blue points) and the half-sum of the equivalent symmetric cells (red points) (a) 0.2 V in the lithiation step; (b) 0.07 V in the lithiation step; (c) 0.3 V in the delithiation step; (d) 0.48 V in the delithiation step. . . . .	93
A.21	Example EIS spectrum of a half-cell taken at 0.2 V, showing how the ECs given in 7.3 fit the data. The reduced $\chi^2$ is given in the legend for each EC, with “ $W_o$ ” corresponding to the EC containing a finite space Warburg, and “ $W_s$ ” corresponding to the EC containing a finite length Warburg. . . . .	94
A.22	Galvanostatic charge curves of the commercial Si material used in this work, and showing the progressive loss of graphitic character of the electrodes with repeated cycling. Cycle 4 is made up of two constant-current-constant-voltage steps and has therefore been omitted. . . . .	95
A.23	Fit and residual of applying equation 2.8 to the delithiation step of Si. The purple line is the capacitance, which was used as a baseline for the fitting procedure. . . . .	96
A.24	An example of the GCD curves of the first batch of 10 cycles after formation and the EIS cycle. The dQ/dV curves shown in Fig. 8.2 are derived by fitting equation 2.8 to the delithiation (charge) curves shown here. . . . .	97

# List of Tables

4.1	Physical properties of the Si materials used in this work. . . . .	21
4.2	The procedure used for charging and discharging the cells to the desired potential for EIS experiments. . . . .	24
5.1	Chemical and initial electrochemical parameters for the four Si-based materials prepared for the present study. . . . .	29
A.1	Results from DFT simulation of $\text{SiP}_x$ . . . . .	80



# Chapter 1

## Introduction

Lithium-ion batteries (LIBs) are one of the most used energy storage devices due to their relatively high energy storage capacity, an ability to operate under high charge/discharge rates, and possibility for small size and portability.[1] As requirements for LIBs continue to grow, design and research into new active materials for LIBs have become necessary to enable the delivery of high power and improvement of energy storage capacity. Much of the recent work has been focussed on optimizing the properties of silicon (Si) as an anode material, due to its ten-fold greater Li-ion storage capacity compared to conventionally used graphite (3579 vs 372 mAh/g).[2, 3, 4, 5, 6] However, the volume change of Si during lithiation/delithiation is also much greater than for graphite (300% vs 10%), which leads to fracturing of Si particles, delamination of the active materials from the current collector, and unstable solid electrolyte interphase (SEI) formation. All of these factors lead to rapid degradation of Si-based electrodes during electrochemical cycling.[7, 8, 9] In addition, the diffusivity of Lithium (Li) ions in Si is also lower than that in graphite ( $10^{-10}$  vs  $10^{-7}$  cm<sup>2</sup>/s).[10, 11] Low diffusivity of Li<sup>+</sup> inside Si, as well as high charge-transfer resistance at the surface contribute to the low rate capability, which impedes the use of Si in high power applications.[4, 5, 6]

Researchers have explored many different strategies to mitigate the swelling of Si, protect the electrode from excess SEI formation (and *vice versa*), and improve the rate capability and cycling stability of Si.

## 1.1 Si nanostructuring

The physical dimensions of Si within an electrode has a large effect on the properties. Si structures above a certain critical size (roughly 150 nm) will fracture during charging, leading to disintegration of the electrode within a few cycles.[12, 13] Si particles below a certain critical size will not crack during charging, which helps to extend the lifetime of LIBs incorporating Si. Changing the morphology of Si also alters its behaviour, as considerations of thickness and surface area change how the Si is able to accept and conduct both  $\text{Li}^+$  ions and electrons.[14, 15] The morphology of Si also affects the SEI formation on the anode during charging. Some SEI is formed at each cycle (especially for uncoated Si), which decreases the cycle life of the cell by depleting the electrolyte. Given that swelling during charging is an intrinsic property of Si, high surface area materials will generally degrade faster than low-surface area electrodes. Crack formation and SEI formation make up the main mechanisms for failure of cells containing Si. Several strategies have been explored to mitigate and limit these failure mechanisms by modifying both the surface of Si and the material itself.

## 1.2 Coatings, heteroatoms and conversion materials

To hinder SEI formation on Si materials, coatings have been employed to prevent contact between the Si and the electrolyte. By covering the Si in a hard shell such as carbon the swelling is minimised, and the cycle life can be extended.[16] While this can help to mitigate some negatives surrounding the use of Si in LIBs, this does little to affect the intrinsic cycling behaviour of Si. The inclusion of heteroatoms in Silicon can help to improve both the stability and performance of Si. Small amounts of heteroatoms may improve the rate capability, while large concentrations form conversion materials which envelop cyclable Si nanoparticles and protect it from degradation in a similar manner to a coating.[17, 18, 19, 20] While significant progress has been made by using these strategies the problem of stability of Si electrodes has still not been adequately solved. An overarching understanding of Si electrochemistry is still needed to help solve these issues.



### **1.3 Understanding Si during charging and discharging**

As the charging and discharging behaviour of Silicon is strongly affected by the material and its surrounding environment, it is important to understand what fundamental behaviour exists and how these physical changes affect them. Using a variety of physical characterisation techniques combined with novel data analysis can elucidate these differences and help to gain a more complete picture of the behaviour of Si electrochemistry.



## Chapter 2

# Literature review

### 2.1 Si and Si materials

More than a decade of work has been dedicated to mitigating the effects of the volume change in Si and other materials through alloying mechanisms, the use of coatings, materials engineering, and/or by nanostructuring of Si.[15, 14, 16, 21] Alternatively, Si-based alloys and substoichiometric compounds have been proposed to change the cycling behaviour of Si,[22, 23, 24, 25] thereby improving the intrinsic properties in combination with extrinsic methods such as nanostructuring and/or coatings. In the search for improvement of the Si-based materials and synergistic effects between Si and heteroatoms, alternative strategies have been deployed including physical mixing of Si nanoparticles and layered black phosphorus.[26] Recently, materials such as  $\text{SiO}_x$ ,  $\text{SiN}_x$  or  $\text{SiP}_x$  have shown great promise due to their incredible cycling stability originating from conversion/alloying mechanisms.[27, 20, 28, 29, 18, 30] Work by Ulvestad *et al*, Pan *et al* and others has shown that for  $\text{SiO}_x$ ,  $\text{SiN}_x$  and  $\text{SiP}_x$  with  $x < 1$  the added element participates in the formation of an inactive matrix during initial lithiation, leaving domains of pure Si as the main source of reversible capacity.[4, 27, 31] The advantage of these materials is the high  $\text{Li}^+$  diffusivity through the inactive matrix and the substantial decrease in swelling compared to Si, which leads to an increase in both rate capability and stability during cycling. For instance, lithium phosphidosilicates (possible products of  $\text{SiP}_x$  conversion), which consist of Li, Si and P in various ratios, have been shown to have high  $\text{Li}^+$  ion mobility, which can increase the  $\text{Li}^+$  diffusivity of Si-based anodes.[32, 33] However, the major disadvantage

of relatively high concentrations of added element (i.e., high  $x$ ) is a decreased initial Coulombic efficiency (ICE) due to the irreversible in situ conversion reaction, as shown by Ulvestad *et al* in 2018.[4, 27] In addition, the electrochemistry of Si-based alloys is not straightforward, as some of the elements used for alloying can react with  $\text{Li}^+$  to form Li-Si-containing compounds, complicating the data analysis and further improvement of these otherwise promising materials.[27, 34] At the present moment the results for Si nanoparticles (SiNPs),[35, 36]  $\text{SiO}_x$ ,[37, 38, 39]  $\text{SiP}_x$ [24, 20, 29, 18, 40, 19, 41] and  $\text{SiN}_x$ [31] materials systems are still quite scattered in terms of methods of preparation, chemical compositions, particle morphologies and sizes (these are differences only at the material level) due to relative novelty of the approach. All of those discrepancies makes a direct comparison of these promising materials extremely difficult and more studies yet to be performed to develop a full understanding of these Si-based compounds. Alternatively, the intrinsic properties of Si battery active materials can also be modified by doping. The aim of such doping is to provide a stabilization effect similar to the conversion/alloying mechanism observed at high  $x$ , but without decreasing ICE.[24, 27, 40, 19, 41] For instance, boron-doped Si nanoparticles were reported by Ge *et al* (2013), but this doping was found not to improve the rate capability of the Si because boron (B) is a p-type dopant.[25] Conversely, n-type dopants, such as P and arsenic (As) showed promising results for improvement of anode materials.[23, 37, 19, 41, 17] Furthermore, Huang *et al* (2017) showed that P-doped Si/graphite composites demonstrated good rate capabilities due to lower charge transfer resistance and improved  $\text{Li}^+$  transport in the material compared to pure Si.[19] P is a promising choice as an n-type dopant due to its lower toxicity compared to other candidates such as As. Depending on P concentration in Si (at doping or substoichiometric levels),  $\text{SiP}_x$  is expected to maintain some of the advantages of doped Si, namely the increased conductivity relative to pure Si, but also possibly the advantages of conversion materials such as increased  $\text{Li}^+$  diffusivity and high cycling stability. Previous work by Long *et al* (2020) on substoichiometric  $\text{SiP}_x$  materials has shown the increase in both the conductivity and  $\text{Li}^+$  diffusivity of  $\text{SiP}_x$  at low P%.[40] However, the mechanism by which the addition of P affects the electrochemical behaviour is difficult to determine, as effects due to surface oxides and material nanostructuring play a significant role in the electrochemical behaviour. Fig. 2.1 shows some  $\text{SiP}_x$  materials recently reported in the literature. This survey is displayed on a scale of the atomic % of P in the Si

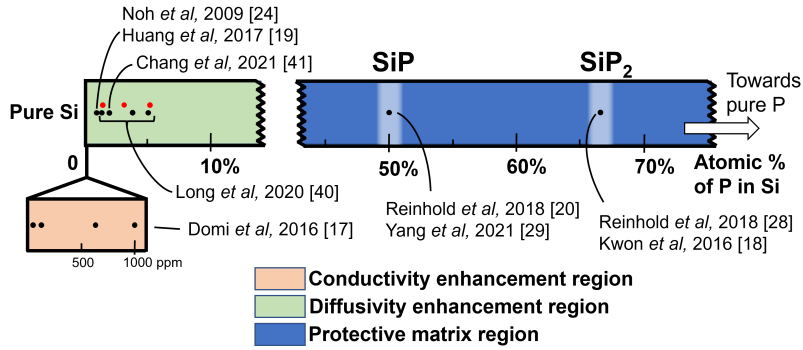
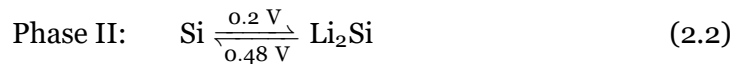
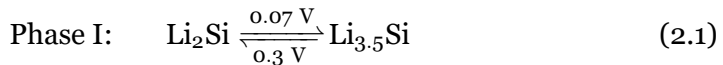


Figure 2.1: Schematic illustration showing present work on  $\text{SiP}_x$  anode materials displayed as a function of the atomic % of P in Si, as well as the main effect attributed to the P in the given concentration range. The contribution to the literature of this thesis is shown as off-set red circles.

material used, which is divided into regions depending on the major mechanism attributed to material enhancements at that P%. The contribution of this thesis is shown as offset red circles.

## 2.2 Lithiation and delithiation of Si

Ogata *et al* (2014) used *in-situ* NMR during cycling, and showed that the lithiation/delithiation phases of amorphous Si materials can be generalized by:[42, 43, 44]



Phase I (equation 2.1) exists at low potentials *vs*  $\text{Li}/\text{Li}^+$ , forming  $\text{Li}_{3.5}\text{Si}$  at 0.07 V during lithiation and  $\text{Li}_2\text{Si}$  at around 0.3 V during delithiation. Phase II (equation 2.2) exists at higher potentials (again *vs*  $\text{Li}/\text{Li}^+$ ), forming  $\text{Li}_2\text{Si}$  at 0.2 V, and delithiating to Si at around 0.48 V. Note that these values are approximations, calculated from the maxima of the  $dQ/dV$ , and vary depending on the electrochemical and physical environment of the cell (intrinsic and extrinsic resistances,

material morphologies, electrode setup, current density, state of health, etc.).[45, 46, 47] Si materials incorporating heteroatoms have also been shown to follow the same mechanism, with the heteroatoms reacting irreversibly with Li and forming ionically conductive matrices surrounding nanometre-sized Si particles.[20, 48, 49] The behaviour of these two phases has been shown to vary depending on factors such as morphology and C-rate.[47] Further, the use of lithium (Li) metal as counter electrode (CE) for studying Si has been shown to have significant effect on the results.[50, 51]

### 2.2.1 A note on nomenclature

A large portion of this thesis relies on an understanding of the “phases” of Si. The formation of these phases is sequential and reversible, which leads to a labelling problem: the first phase to form during lithiation is the last phase to form during delithiation, and so we must choose whether to start counting phases starting from the fully delithiated high-potential state (and subsequently lithiating), or *vice versa*, starting from the fully lithiated low-potential state, and subsequently delithiating. In this work the choice has been the latter, and this is because the work is mainly focussed on studying the delithiation of Si. However, the problem of nomenclature can be displayed rather more elegantly by showing the phases as they appear along the potential (in our case *vs* Li/Li<sup>+</sup>) using the dQ/dV. This is shown schematically in Fig. 2.2. Here phase I (green filled curves) is the first to appear on the dQ/dV *vs* potential plot while phase II (red filled curves) appears last, regardless of whether one is looking at the lithiation or the delithiation portion of the charge-discharge curve.

## 2.3 Studying Si materials

The study of Si electrochemistry has often proceeded by comparing physical and chemical analysis as measured by e.g. nuclear magnetic resonance (NMR), energy dispersive spectrometers (EDS) or X-ray photoelectron spectroscopy (XPS); and imaging such as transmission electron microscopy (TEM) and scanning electron microscopy (SEM). Together with galvanostatic charge-discharge (GCD) behaviour this has been used to determine the relationship between the electrochemistry of Si and its physical changes.[42, 44, 52, 53, 13] However, since it

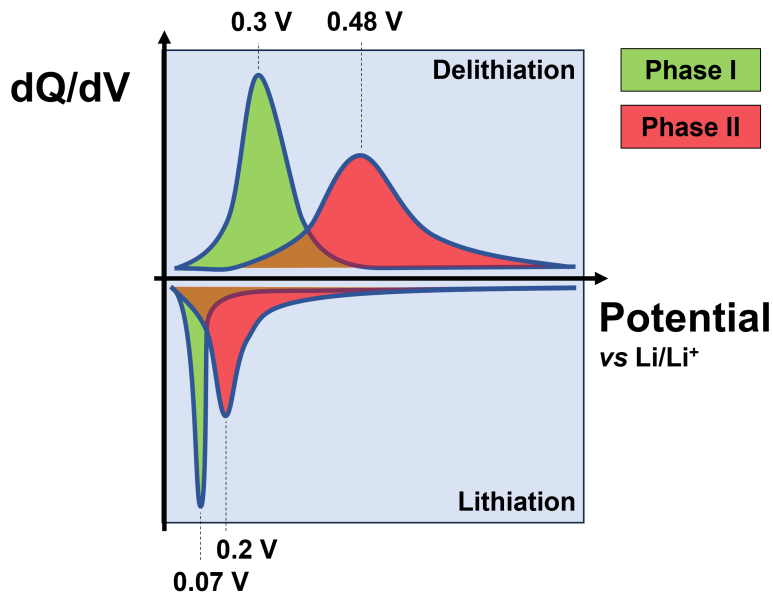


Figure 2.2: Schematic showing the phases of Si as a plot of the  $dQ/dV$  as a function of the potential (*vs*  $\text{Li/Li}^+$ ). Displayed in this way phase I (green filled curves) always appear at lower potentials than phase II (red filled curves)

is often difficult to see features in GCD curves, this relationship has often been displayed using the differential capacity ( $dQ/dV$ ) plotted versus the voltage. The  $dQ/dV$  produces peaks at the voltages where the faradaic reactions occur most strongly, and is therefore a simple way to visualise the changes in electrochemical behaviour of a cell during charging or discharging.[54] The position, size, and shape of a given peak gives information about the electrochemical processes and changes in the cell.[55, 56, 57, 58] Unfortunately, the often heavy data processing required to generate  $dQ/dV$  curves from raw GCD data complicates the extraction of quantitative information. Digital data output from cell cyclers is discontinuous and the resolution is limited. This means generating  $dQ/dV$  curves requires smoothing, interpolation, and/or binning in order to produce feasible fits.[46, 59, 60] The choice of method and the degree of smoothing performed affects the final shape of the  $dQ/dV$  curve, which in turn can affect the interpretation. A highly smoothed  $dQ/dV$  curve may produce a more visually appealing plot than a less smoothed one but the amount of information displayed is also decreased

as sharp peaks are de-emphasised or removed completely. As a result dQ/dV plots are used for qualitative rather than quantitative assessment. Nevertheless, the understanding that more quantitative information is available in dQ/dV plots has lead some researchers to propose data analysis techniques such as fitting of normal distributions to analyse dQ/dV plots.[61, 62] Good quality dQ/dV plots with minimal smoothing can give a good fit to the data, but GCD data produced by less precise cyclers or data generated without the express purpose of applying fitting functions do not contain the necessary resolution to allow for this type of analysis.

Another established and sensitive method for studying the electrochemistry of Si is electrochemical impedance spectroscopy (EIS).[63] EIS is the study of the varying resistance of an electrochemical system as a function of frequency  $f$ . Impedance is often denotes using the symbol  $Z$ .

The fundamental relationship between a resistance  $R$ , current  $I$ , and voltage  $V$  is given by Ohm's law:

$$R \equiv \frac{V}{I} \quad (2.3)$$

According to equation 2.3, any change in  $V$  will immediately cause a change in  $I$  (and *vice versa*), and  $R$  will remain constant. However, if there is a delay (a phase difference) in the change in  $I$  when  $V$  changes,  $R$  is no longer constant, and cannot be described by equation 2.3. The magnitude of this phase difference is dependent on the rate of change of the independent variable, which means that for a constant rate of change (i.e. frequency of oscillation), the phase difference is constant and the impedance can be calculated. Because the phase difference is a response to a perturbation of the system, accurate measurements can only be made if the system in question is at equilibrium. In practice, this means only using very small oscillation amplitudes in order not to change the equilibrium of the system during measurement.

Consider an oscillating voltage:

$$V_t = V_0 \sin(\omega t) \quad (2.4)$$

where  $V_t$  is the potential at time  $t$ ,  $V_0$  is the amplitude of the oscillating voltage and  $\omega = 2\pi f$  is the radial frequency of the oscillation.

The current response to equation 2.4 is therefore:



$$I_t = I_0 \sin(\omega t + \phi) \quad (2.5)$$

where  $I_t$  is the current at time  $t$ .  $I_0$  is the amplitude of the oscillating current, and  $\phi$  is the phase difference between the applied and response oscillations.

Substituting equations 2.4 and 2.5 into equation 2.3 gives:

$$\begin{aligned} Z(\omega) &= \frac{V_t}{I_t} \\ &= \frac{V_0 \sin(\omega t)}{I_0 \sin(\omega t + \phi)} \\ &= Z_0 \frac{\sin(\omega t)}{\sin(\omega t + \phi)} \end{aligned} \quad (2.6)$$

where  $Z_0$  is the magnitude of the impedance.

Equation 2.6 can also be expressed using Eulers relationship, to give:

$$\begin{aligned} Z(\omega) &= Z_0(\cos\phi + j\sin\phi) \\ &= Z' - jZ'' \end{aligned} \quad (2.7)$$

where  $j = \sqrt{-1}$ , and  $Z'$  and  $Z''$  are the real and imaginary parts of the impedance, respectively.  $Z'$  and  $Z''$  represent the *resistive* and *reactive* parts of the impedance, respectively.

Unfortunately, this sensitivity means that distinguishing between features and noise is very difficult, and the design of the cell and the experiment surroundings is very important. For instance, performing EIS directly on half cells will result in the generated spectrum containing information from both the working and counter electrodes (WE and CE, respectively), as well as the electrolyte and separator located in between them. This can be avoided by introducing a reference electrode (RE) into the cell in proximity with the WE, but this increases the construction complexity and cost, and requires consideration of the RE electrode chemistry.[51] The use of symmetric cells (where both the WE and CE are identical) is also an option, but these cells cannot be cycled, and can therefore not

easily be used for cycling studies. Therefore, in much of the high loading Si literature EIS is used as a complementary technique in full-cell or half-cell (*vs* Li/Li<sup>+</sup>) setup to show e.g. the increase in resistance of a cell before and after cycling.[64, 65] Equivalent circuits (ECs) have been designed to describe the behaviour of Si electrodes at low loading by researchers such as Pan *et al* (2020), Lozhkina *et al* (2020), and Paloukis *et al* (2016).[50, 66, 67] These ECs vary considerably due to differences in electrochemical conditions, but work by Levi *et al* (2001) and Pan *et al* (2020) has shown that the inclusion of a finite-length Warburg diffusion element ( $W_o$ ) is useful for describing the diffusion behaviour of Li<sup>+</sup> ions within the Si material.[50, 68] A similar diffusion element, the finite-space Warburg ( $W_s$ ) has also been shown to be useful for describing Li<sup>+</sup> diffusion through thin films such as SEI layers formed on the Li CE.[68] Recently, the use of distribution of relaxation times (DRT) analysis has also been employed to deconvolve the data generated by impedance experiments.[50, 69, 70] This technique relies on the assumption that the response to a perturbation will decay exponentially, in a manner akin to the decay of a nucleus in a magnetic resonance machine. Indeed, Boukamp (2015) used a Fourier transform to show differences between the finite length Warburg (FLW) element and the Gerischer element.[71]

The result of deconvoluting the frequency response gives information on the number of processes occurring in the data, and is a useful technique for designing ECs. A peak in the DRT spectrum corresponds to a polarization process and the position (in Hz), size (in  $\Omega \cdot \text{cm}^2$ ), and shape gives information on the electrochemistry of the process.[50, 69, 70, 72]

Si has very different behaviour during charging and discharging, and EIS offers the possibility of helping to understand these differences.[50] Amorphous Si cycled in the region 0.05 to 1.5 V *vs* Li/Li<sup>+</sup> displays two electrochemical phases. During lithiation, Li reacts with Si to form Li<sub>2</sub>Si at around 0.25 V. As the potential is decreased to about 0.07 V Li<sub>2</sub>Si reacts to form Li<sub>3.5</sub>Si. Delithiation reverses this reaction, with Li<sub>3.5</sub>Si forming Li<sub>2</sub>Si at about 0.28 V, and the resulting Li<sub>2</sub>Si forming pure Si at about 0.48 V and higher.[42, 43, 48] The ECs of Si half cells at these potentials are not necessarily all the same, especially when considering the effect of the Li CE.

## 2.4 Interpreting GCD data

Beyond  $dQ/dV$ , GCD curves can also be interpreted as integrals (i.e., cumulative distribution functions, or CDFs) of  $dQ/dV$  peaks. The Yan group at KTH (Sweden) has developed empirical methods for fitting LIB cycling data based on such CDFs.[45, 46, 73] Fitting functions used in previous research include Lorentzian, Gaussian, and pseudo-Voigt distributions where the number of components corresponds to the number of phases in the GCD curve. This solves the issues that arise from data smoothing when fitting  $dQ/dV$  curves and allows for fitting of lower-resolution data, but the main focus has been on estimating the state-of-health (SOH) of full cells. These methods have been shown to give excellent fit to cells containing lithium iron phosphate (LFP), nickel manganese cobalt oxide (NMC), and graphite, especially at low charge-discharge rates.[45, 46, 73, 74, 75] For half-cells where Li foil is used as a counter electrode, this approach can be used to extract information about material behaviour from cycling data without the need for relying on  $dQ/dV$  curves.

Before setting up empirical fitting experiments it is necessary to consider the advantages and limitations of the techniques and methods in use. The main advantage is to apply relatively simple equations that describe the data as it is, rather than how it ought to be, without the express need for specialized experiments. This allows for the use of data which was not initially designed for this purpose. The obvious disadvantage of empirical fitting is that the meaning of the variables is not clear, they are “black boxes” whose meaning is dependent on as-yet unknown physical phenomena. Nevertheless, applying an empirical fitting function to data and extracting empirical parameters can give important groundwork for later analyses, and can elucidate trends in data that may prove to be important even if the interpretation of the results is not straightforward.

In the context of Si, empirical fitting could be used to determine changes in electrochemical behaviour of various Si-based materials or under different cycling conditions. To do this, the chosen fitting function must account for the behaviour of Si during cycling. For example, diffusivity is lower for Si than for the graphite/NMC or graphite/LFP cells used in previous research.[45, 76, 46, 73, 77] The shape of the  $dQ/dV$  curves is affected by these factors, with curves being skewed away from normal as conditions deviate from equilibrium.[55] Further to this, fitting these empirical equations is usually done using data generated at or

near equilibrium conditions, C-rates which are too low for long cycle life experiments, and which are therefore not often reported in the literature beyond use as either formation or diagnostic cycles. For data which is cycled at rates far above equilibrium, the assumption of normality which is shown to be a good approximation for other systems may not be true for Si. Hence, the Gaussian portion of the pseudo-Voigt function used in previous literature has been replaced with a skew-normal distribution function to describe the Si phases.[46] The empirical CDF for the capacity  $Q_k$  of a silicon material as a function of the potential  $E$  with  $n$  delithiation phases is therefore defined as:

$$f(E) = \sum_{k=1}^n Q_k [w_k G_k(E) + (1 - w_k) L_k(E)] \quad (2.8)$$

where  $w_k$  is a weighting factor and  $G_k(E)$  and  $L_k(E)$  are the skew-Gaussian and Lorentzian components of phase  $k$ , respectively.  $G_k(E)$  and  $L_k(E)$  are given by:

$$G_k(E) = \frac{1}{2} \left( 1 + \Phi_k \left( \frac{E - c_k}{\sqrt{2}s_k} \right) \right) - 2T_k \left( \frac{E - c_k}{\sqrt{2}s_k}, \alpha_k \right) \quad (2.9)$$

and

$$L_k(E) = \frac{1}{\pi} \arctan \left( \frac{E - c_k}{\gamma} \right) + \frac{1}{2} \quad (2.10)$$

where  $c_k$  is the position (*i.e.* apparent equilibrium potential) of the phase,  $s_k$  is the width of the Skew-Gaussian, and  $\alpha_k$  is the skewness factor describing the deviation from equilibrium.[47, 55] In equation 2.10,  $\gamma_k$  is the width of the Lorentzian. There are advantages to using an empirical equation such as this one over a theoretical model, and there are many examples of empirical equations, such as the Stefan-Boltzmann equation for thermal radiation of a blackbody, or rate equations used in chemical rate kinetics.[78, 79] Firstly, the equations can be relatively simple, allowing for fast determination of important features. Secondly, they can be applied to a broad variety of datasets generated from experiments or cells which were not designed with this particular application in mind. For example, cumulative CDFs have been used on commercial cells, as well as on Si half cell data from published works.[45, 47] However, the empirical nature of these equations means that the exact behaviour of the parameters involved must be determined experimentally.

This is also why the position of the phase c is deemed an “apparent” equilibrium potential.[47] Note that due to the presence of the skewness factor  $\alpha$  in equation 2.9, the position of the phase c is not the same as the maximum point of the peak in a plot of  $dQ/dV$  vs  $V$ .

### 2.4.1 Distinction between fitting and modelling

The equation presented above is empirical, and therefore requires experimental data. A philosophically distinct method for studying Si materials is through modelling, whereby physical equations are employed to build a model of a system.[80, 81, 82, 83, 84, 85] The advantage of this approach is that the model is a completely explained system. The downside is that the model eventually needs to be evaluated experimentally to prove its correctness, which can prove challenging if the model requires very precise instrumentation or highly engineered materials. Despite these drawbacks the existence of theoretical models are invaluable to the understanding of materials such as Si because they can predict behaviour before an experiment takes place. As such, they provide an excellent litmus test for experimental results, even if the experimental setup is not in perfect accordance with those of the model. For example, Chevrier & Dahn (2009) provided a first-principles model using density functional theory (DFT) for the lithiation of amorphous Si, and comparing their model experiments on sputtered amorphous Si gave reasonably good (but not exact) agreement.[80] Similarly, Dhillon *et al* (2021) used a concentrated solution theory to predict the capacity fade of Si-graphite half cells, again with reasonably good agreement with experiment.[85] As seen from the above examples, the power of these models is that they are *predictive*, and that they can give insights into what may be the reason for a certain result. In contrast the fitting function presented in this work is *descriptive*, and analyses the results as they are, rather than how we hope they should appear. By coupling the insights provided by theoretical models with the results of fitting empirical equations, it may be possible to eventually bridge the gap and provide a more complete picture of the behaviour of Si.

## 2.5 Towards commercialization

Commercially available Si materials for use in LIBs are a convenient way for battery manufacturers to improve their own products without the need for extremely costly and time-consuming in-house material development. Several such Si materials are already available, ranging from pure Si with capacities close to theoretical values, to heavily coated, modified or blended materials. This poses a challenge, as comparing across materials from different suppliers is not straightforward. To fairly evaluate a given Si material therefore requires taking the intrinsic behaviour into account and analysing this to determine if it is suitable for the desired system. In order to achieve good performance Si electrodes in the literature often contain very low loading.[86] This makes it difficult to assess the suitability of these materials for commercial applications where the loading requirements are much higher. Higher loading of Si in the electrode exacerbate the issues of swelling and poor conductivity. As a result testing of these materials at high loading is a relatively unexplored area of research.[64, 65, 86] A further issue affecting high loading Si electrodes is the almost ubiquitous use of Li counter electrodes (CE). As shown by LaMantia *et al* (2013) Li is highly polarizable and forms dendrites above  $1 \text{ mA/cm}^2$ , which makes it difficult to produce reliable data.[51, 87] Despite these disadvantages the use of Si/Li half cells in the literature is unlikely to cease, and it is therefore important to understand the interplay of the electrodes in these systems.

## Chapter 3

# Objectives and scope of this project

The scope of this thesis is to increase our understanding of Si during delithiation. To do this, we first set out to study the effect of adding small concentrations of heteroatoms to SiNPs. The results of this are detailed in paper **i**, where a silane pyrolysis process is used to disambiguate the effect of low concentrations of P in Si nanoparticles by synthesizing particles of very similar morphology and with low surface oxide levels. We describe the synthesis of amorphous SiP<sub>x</sub> nanoparticles with the atomic % of phosphorus in the particles ranging from 1.5 to 5.2 at% and compare their electrochemical performance to pristine Si nanoparticles of the same size.

The results of paper **i** highlighted the need for more in-depth analytical techniques for studying the GCD behaviour of Si. Paper **ii** presents the results of fitting the empirical fitting function 2.8 to Si half-cell data and analyses the resulting fit parameters. We correlate the fit parameters to the expected physical behaviour of the cell, and ascribe general physical behaviour to the components of each phase. In order to showcase the analytical method presented here, Si GCD data was obtained with the permission of the authors from previous work involving Si. The datasets were chosen based on the simple, well-defined morphologies of the Si without addition of coatings or dopants. Two datasets consisting of GCD data from nanowires (NWs) and thin films (TFs) were chosen. This gave two avenues for exploration, namely a morphology with controlled 2D diffusion radius and large surface area (the NWs), and a morphology with controlled 1D diffusion

length and small surface area (the TFs). The suitability of the fitting method will be validated and the meaning of the parameters will be discussed to reveal the differences and similarities in behaviour of Si in different morphologies. As a result, this methodology allows analysing the electrochemical data in greater details and exploring the contributions of multiple electrochemical processes.

While the ability of the fitting function was shown to work well for very well-defined Si materials at low electrode loading, the behaviour at high loading remains a challenge. Further, the interaction between Si and the Li counter electrode needs to be further elucidated. In paper **iii**, we construct and test a commercially available Si material in electrodes with high loading in both half-cell and symmetric configuration to investigate the changes to the EIS spectrum at different potentials. This comparison will be used to differentiate between effects occurring due to the Si WE and those due to the Li CE in half cells. The EIS spectra will be collected at the potentials at which each phase is at equilibrium using a constant-current constant-voltage (CCCV) step to ensure that the phase is allowed to run to completion and the electrode consists mainly of the product of the desired phase. The symmetric cells will be assembled from half cells which have been cycled to each of these points in the cycle. DRT analysis will be used to inform the design of the ECs used in this work, and these will be used to elucidate the behaviour of the high loading Si electrodes in half cells.

With knowledge of the interaction between high loading Si electrodes and the Li CE, it is then possible to apply the equation developed in paper **ii** to commercial Si materials such as that studied in paper **iii**. Paper **iv** applies the empirical GCD analysis developed previously to GCD cycling data from a commercial Si material at high loading. EIS is performed at various potentials corresponding to the maxima of the  $dQ/dV$  during both the lithiation and delithiation. SEM with energy-dispersive X-ray spectroscopy (EDX) and XPS will be used to validate the results of the GCD analysis. The aim of this work is therefore both to gain a deeper understanding of the behaviour of a Si material at high loading when in half-cell configuration.



## Chapter 4

# Experimental

### 4.1 Material preparation

Amorphous nanoparticles (NPs) of Si and SiP<sub>x</sub> were synthesized by S. Y. Lai and A.y Koposov at IFE through monosilane (SiH<sub>4</sub>) pyrolysis as described in previous reports.[37] For the synthesis of SiP<sub>x</sub> NPs, alloying was performed in situ by introducing phosphine gas (PH<sub>3</sub>) into the free space reactor (FSR) along with SiH<sub>4</sub>. Proper safety protocols are required: SiH<sub>4</sub> and PH<sub>3</sub> gases are both hazardous gases due to being pyrophoric, while PH<sub>3</sub> gas is toxic at concentrations as low as 50 ppm. The resultant Si and SiP<sub>x</sub> NPs were isolated through filtration of the gas stream. Si and SiP<sub>x</sub> NP alloys were synthesized with P levels of 0, 1.5, 3.2, and 5.2 at% are referred to as P0, P1.5, P3.2, and P5.2 respectively throughout the study.

The Si materials used for chapters 7 & 8 were purchased directly from the manufacturer and used without further purification.

### 4.2 Electrode preparation

The electrode preparation methods used for this thesis were not constant throughout the work. Due to the small amount of SiP<sub>x</sub> materials available for chapter 5 (< 1 g), regular slurry methods such as dispermat could not be used. In this case a ball mill was chosen to mimic the action of a planetary mixer. The data used for chapter 6 was obtained from previously published work and from experiments intended for a separate publication (i.e. data produced where the intended use was for a separate publication and not the current work), and so the electrodes

(and by extension the cells) were produced externally. The details of the slurry preparation are given below. Since chapters 7 & 8 use commercially obtained materials, the quantity was sufficient to make electrode slurries in larger quantities, and so the ball mill was abandoned in favour of the dispermat.

#### **4.2.1 Electrode preparation for chapter 5**

An aqueous anode slurry (20 wt% solids content) was prepared using KOH/citric acid buffer (pH 3, <5 wt%) with the solid fraction, carboxymethylcellulose (CMC, 15 wt%, 10000 Mw, Walcofel), SiP<sub>x</sub> (60 wt%), conductive graphite (10 wt%, SFG-6L, Imerys), and carbon black (15 wt%, C65, Imerys). The slurry was mixed in a planetary ball mill (MSK-SFM-1, MTI Corp.) at 400 rpm. To avoid contamination of the materials, an agate cup and zirconia balls were used for ball milling. The balls weighed 10 g each, and a ball:slurry mass ratio of 10:1 was used. The mixing procedure was as follows: water and buffer solution were mixed in the agate cup before addition of CMC, which was then dissolved by mixing for 15 minutes. The graphite, carbon black, and SiP<sub>x</sub> NPs were added sequentially, mixing for 15 minutes between addition of each ingredient. After the addition of SiP<sub>x</sub> NPs, the mixing continued for 2 hours to produce a smooth dark brown slurry. The slurry was then deposited on 19 μm thick dendritic copper foil (SE-Cu58, Schlenk) by doctor blade height set to 80 μm. After drying at room temperature, the electrodes were calendered (MSK-HRP-4, MTI) at 120 °C and cut into 15 mm diameter discs. The final mass of active material per electrode was 1.8 ± 0.2 mg cm<sup>-2</sup>. The calendaring reduced the electrode thickness to 7 ± 1 μm (together with Cu current collector - from 29 ± 2 μm to 26 ± 1 μm).

#### **4.2.2 Electrode preparation for chapter 6**

Electrode manufacturing and cell testing for chapter 6 was performed by S. Y. Lai, A. Y. Kopusov, and C. Keller. The amorphous TF electrodes were produced by sputtering Si directly onto the copper current collector as described elsewhere.[88] The NW electrodes consisted of 50 wt.% Si, 25 wt.% carboxymethylcellulose (CMC) and 25 wt.% carbon black by weight, and loading ranged from 0.25 to 0.41 mg/cm<sup>2</sup>. CR2032 half cells were constructed using Celgard separator and the electrolyte consisted of 1/1 v/v ethylene carbonate/diethylene carbonate (EC/DEC), with

1M LiPF<sub>6</sub>, 10 wt% fluoroethylene carbonate (FEC), and 2 wt% vinylene carbonate (VC). Further details can be found in the original manuscript.[89] The thin film electrodes were prepared by plasma enhanced chemical vapor deposition (PECVD, Oxford Instruments Plasmalab System133) using silane (SiH<sub>4</sub>) as a precursor. The films were deposited on flat copper substrates, which were washed with ethanol prior to deposition. The thickness of the film was controlled by the deposition time.[49]

A summary of the Si materials along with the source is given in table 4.1.

Table 4.1: Physical properties of the Si materials used in this work.

<b>Si morphology</b>	<b>Thickness/ diameter (nm)</b>	<b>Surface area (m<sup>2</sup>/g)</b>	<b>Electrode density (g/cm<sup>3</sup>)</b>	<b>Current density at 1 C (mA/g)</b>	<b>Reference</b>
Nanowire	9	194	0.42	0.52	[89]
	42	108	0.33	0.73	
	55	85	0.29	0.85	
Thin Film	40	10.7		0.033	This work
	60	7.15	2.329	0.045	
	80	5.36		0.067	

### 4.2.3 Electrode preparation for chapters 7 & 8

Si electrode slurries were prepared in an overhead stirrer (Dispermat LC30). The slurry consisted of 5% carboxymethylcellulose (CMC, Walcofel 10000), 2% KOH/citric acid buffer (pH 3), 0.5% carbon nanotubes (CNT, Lanxi Zhide), 9.5% carbon black (C65, Imerys), 80% Si powder, and 3% SBR (BM-451B, Zeon). For chapter 7, the Si powder used was SCC55 (Group 14), while for chapter 8 the Si powder used was SL650-SOC (Iopsilion). The slurry was made by sequential addition of powders and stirring at 2500 rpm for 15 minutes, followed by a stirring step of 2 h at 2500 rpm. The final addition consisted of SBR, which was mixed slowly at 700 rpm for 15 minutes. Electrodes containing higher concentrations of Si material were found to be too brittle after cycling to be disassembled and reassembled. The chosen concentration of carbon black was found to increase the stability of

the electrode while having a negligible effect on the electrochemistry. The slurry was coated onto 10  $\mu\text{m}$  copper foil using a doctor blade with a blade height of 130  $\mu\text{m}$  and dried at room temperature overnight. 15 mm diameter electrodes were cut from the electrode sheet for coin cell assembly. For electrodes made with SCC55, this resulted in an electrode loading of 3.38  $\text{mg}/\text{cm}^2$  and a thickness of 59.6  $\mu\text{m}$ . The electrolyte uptake and porosity were 89 % and 35.6 %, respectively. Details of these experiments may be found in the Appendix (A.2 on page 90).[90] The reversible gravimetric capacity of the SCC55 Si material in the 0.05-1 V range was 1,290  $\text{mAh}/\text{g}$  at a current density of 0.179  $\text{mA}/\text{cm}^2$ , yielding an area capacity of 3.49  $\text{mAh}/\text{cm}^2$  for these electrodes. Electrodes made using SL650-SOC and the same coating parameters yielded electrodes with a loading of 3.27  $\text{mg}/\text{cm}^2$  and a thickness of 48  $\mu\text{m}$ . The reversible capacity of these electrodes was  $520 \pm 10$   $\text{mAh}/\text{g}$  at 83  $\mu\text{A}/\text{cm}^2$ , resulting in an area capacity of 1.65  $\text{mAh}/\text{cm}^2$ .

### 4.3 Cell assembly and disassembly

All assembly, disassembly and reassembly was performed in an Argon-filled glove box. CR3023 coin cells (stainless steel, MTI) were assembled by placing the Si electrode (15 mm dia.) in the cap (the o-ring and the cap are glued together in MTI's coin cell parts), followed by electrolyte (25  $\mu\text{l}$ , TC-E8593, TINCI) to wet the electrode surface. This was then covered with two layers of paper separator (19 mm dia., Tf4030), followed by a further 25  $\mu\text{l}$  of electrolyte. Next, the Li electrode (16 mm dia, 750  $\mu\text{m}$  thick, Sigma Aldrich) was placed on top of the separator followed by the spacer (0.5 mm), the spring, and finally the base. Three-electrode cells were assembled using PAT-cells (EL-Cell) with Li as the reference and counter electrodes, which were used for the EIS experiments in chapter 5.

Disassembly was performed using a decrimping machine (Hohsen), taking care not to short-circuit or damage the electrodes.

Reassembly was performed in almost the same manner as for half-cells, using fresh coin cell parts, separator, and electrolyte. For Si/Si symmetric cells the 0.5 mm spacer was replaced with a 1 mm spacer to account for the thickness of the Si electrodes.

## 4.4 Electrochemical testing

### 4.4.1 Formation and cycling

For chapter 5 GCD tests were performed in triplicate, and all cells were subjected to formation cycling prior to testing (BTS4000, Neware). The formation cycles consisted of one cycle at 0.05 C, followed by three cycles at 0.1 C. The formation current was initially calculated assuming an active material capacity of 3,579 mAh g<sup>-1</sup>, but later adjusted to reflect the experimentally determined initial (1st lithiation) capacities of the materials. A 4-hour rest was used to equilibrate the cells between each step. The lower and upper potential limits for all the experiments was set to 0.05 and 1.5 V, respectively. Asymmetric rate testing was performed by lithiating at a fixed 0.1 C and varying the delithiation rate, and vice versa. Due to the short cycle life of Si electrodes with high Si content only three cycles were performed at each C-rate. Asymmetric stability tests were performed by lithiating at a fixed 0.1 C and delithiating at 0.3 C.

Given the differences in purpose of the original work used for chapter 6, the data generated from the materials in table 4.1 were not produced under identical conditions. After formation at 0.05 C (22.5 to 36  $\mu\text{A}/\text{cm}^2$  depending on the electrode loading), the SiNWs were cycled at 0.2 C (90 to 144  $\mu\text{A}/\text{cm}^2$ ) in the range of 0.01-1 V with a constant voltage hold at the end of each lithiation step. The capacity of the carbon black (20 mAh/g) contributed less than 0.3% to the total capacity of the cells, and was therefore ignored. Cycling was performed on an Biologic VMP3 multichannel potentiostat (Biologic, Seyssinet-Pariset, France).[89] After a formation stage consisting of three cycles at 0.05 C (1.7 to 3.4  $\mu\text{A}/\text{cm}^2$  depending on the film thickness), the SiTFs were cycled using a constant current of 0.5 C (16.8 to 33.5  $\mu\text{A}/\text{cm}^2$ ) in the range of 0.05-1 V with regular diagnostic cycles after every 50 cycles. The diagnostic cycles consisted of one cycle at 0.05 C, two cycles at 0.2 (6.7 to 13.4  $\mu\text{A}/\text{cm}^2$ ), C, and two cycles at 0.5 C. Cycling experiments were conducted at 25 °C in temperature-controlled cabinets (VWR INCU-Line) using an Arbin LBT battery tester.

For chapter 8 the slow EIS cycle was followed by a batch of 10 “fast” cycles at C/3 (0.55 mA/cm<sup>2</sup>) were performed. This procedure of one slow EIS cycle and 10 fast cycles was repeated until the cells failed.

### 4.4.2 EIS and DRT analysis

EIS was performed on a Metrohm Autolab and Nova 2.1 software. EIS experiments were prepared by titrating at 0.05 C for 1 h, followed by a 24 h rest. The EIS was performed between 105 and 0.01 Hz, with an amplitude VRMS of 5 mV. The EIS cycling procedure was started immediately at the end of the formation, and is given in table 4.2. The C-rate for each step in table 4.2 was 1/10 C.

For chapters 7 & 8 EIS experiments were performed at the end of each CCCV step. A plot of this procedure can be seen in Fig. A.18 on page 91 in the Appendix.

Table 4.2: The procedure used for charging and discharging the cells to the desired potential for EIS experiments.

Step type	Stop potential (V)	Step time (h)
CCCV	0.2	20
CCCV	0.07	20
CC	0.05	-
Rest	-	0.3
CCCV	0.3	20
CCCV	0.48	20
CC	1.5	-

DRT analysis was performed in Python using the Gaussian Process (GP) GP-DRT method described by Liu and Ciucci (2019).[69] This models the DRT based on the assumption that the peaks in the DRT spectrum are normal distributions.

### 4.4.3 GITT

GITT was performed by titrating at 0.04 C for 900 s followed by a 2 h rest. This yielded roughly 100 points per curve.

## 4.5 Material and electrode characterization

Energy-dispersive X-ray spectroscopy (EDS) equipped on transmission electron microscope (TEM, JEOL JEM-2100) was used to determine the presence of P in the particles, and P concentrations were determined using inductively coupled plasma-optical emission spectroscopy (ICP-OES). X-ray diffraction (XRD,

Bruker, D8 Advance) was performed on powder samples that had been dispersed in ethanol and dropped onto a silicon low background sample holder. Samples for TEM/EDS analysis were prepared by sonicating 1 mg of NPs in 10 mL of ethanol for 30 minutes, before dropping onto the grid (holey carbon films on 200 mesh Cu grids, Micro to Nano) and allowing them to dry at room temperature. High-angle annular dark-field (HAADF) and HAADF-EDS were performed by S.Y. Lai on an FEI Titan G2 60-300 scanning transmission electron microscope (STEM). Uncycled electrodes for XPS were used as-is. Cycled electrodes for X-ray photoelectron spectroscopy (XPS) were disassembled, rinsed in DMC to remove excess electrolyte, and dried. Ablation was performed by Ar<sup>+</sup> sputtering prior to measurement. XPS was performed on a Thetaprobe (Thermo Scientific). XPS experiments were performed by I. T. Jensen.

## 4.6 Computational methods

### 4.6.1 Modelling

Modelling of Si-P structures was performed by S. Lu. A  $2 \times 2 \times 2$  Si supercell with different number of Li and P atoms ( $\text{Si}_{64-x}\text{P}_x\text{Li}_4$ ) (see Fig. A.10) was used for the calculation of insertion energy at diverse situations. In our calculation, the concentration of Li atom was fixed to 12.5%, which is consistent with previous studies.[17] The first principle calculation was performed in the Vienna ab initio simulation package (VASP).[91] The ion-electron interactions were described by projector augmented wave (PAW) method,[92] and the generalized gradient approximation (GGA) of Perdew-Burke-Ernzerhof (PBE-sol) was chosen to describe electron exchange and correlation energy.[93] A kinetic cutoff energy was set to 500 eV. The Brillouin zone was sampled by a  $\Gamma$ -centered Monkhorst-Pack. A  $2 \times 2 \times 2$  K-mesh were used for structure relaxation. The convergence standard was set to  $10^{-4}$  eV in electronic relaxation, and  $0.02$  eV/Å in Hellmann-Feynman on each atom. The ab initio molecular dynamics (AIMD) simulations under 300K for 6ps with a time step of 2fs were carried out to evaluate the stability of Li inserted supercell  $\text{Si}_{64-x}\text{P}_x\text{Li}_4$ . [94, 95] The substituted energy ( $E_{sub}$ ) of the doped system can be defined as:

$$E_{sub} = E(doped) - E(pristine) + x\mu_N - x\mu_P \quad (4.1)$$

where  $E(\text{doped})$  and  $E(\text{pristine})$  are the total energies of doped and pristine Si.  $\mu_N$  and  $\mu_P$  are the energy of Si and P in its reference phase, respectively. The insertion energy of Li atom can be calculated by:

$$E_{insert} = E(\text{Li} - \text{PdopedSi}) - E(\text{PdopedSi}) - E(\text{Li}) \quad (4.2)$$

where  $E(\text{Li-P doped Si})$ ,  $E(\text{P doped Si})$  and  $E(\text{Li})$  represent total energy of Li inserted P doped Si, P doped Si and Li atom.

#### **4.6.2 Fitting of EIS data and DRT analysis**

EIS fitting was performed in Python using the `impedance.py` package.[96] DRT analysis was performed in Python using the methods described by Liu and Ciucci (2020).[69]

#### **4.6.3 Fitting of GCD data**

Functions for the equations used for fitting were written in Python. Fitting was performed using least-squares minimization in the `lmfit` package developed by Newville *et. al.*[97]



## Chapter 5

# Delithiation rates of silicon-phosphorus based alloys

This chapter details the results of the physical and electrochemical characterization SiNPs containing three different concentrations of P. The focus of this portion of the work was to explore the effect of adding small quantities of P to Si on the electrochemistry, with a specific interest in increasing the rate performance of the materials. This chapter also contains a discussion of the results, as well as some thoughts on the possible mechanisms involved.

### 5.1 Materials characterisation of SiP<sub>x</sub> and Si NPs

Si-based materials obtained through the silane pyrolysis route typically give rise to amorphous nanoparticles (NPs) with relatively narrow size distribution.[37] This process conveniently allows for the preparation of nanoparticles with the target size and morphology through controlled nucleation and growth. The introduction of PH<sub>3</sub> gas into SiH<sub>4</sub> pyrolysis process resulted in the formation of SiP<sub>x</sub> NPs, where the ratio of Si:P is manipulated through control of the ratio of silane to phosphine gases supplied into the reactor during pyrolysis. This technique has been previously applied not only to produce Si nanoparticles,[37] but also to produce more complex SiN<sub>x</sub> (nano)particles with precise ratios of Si:N and

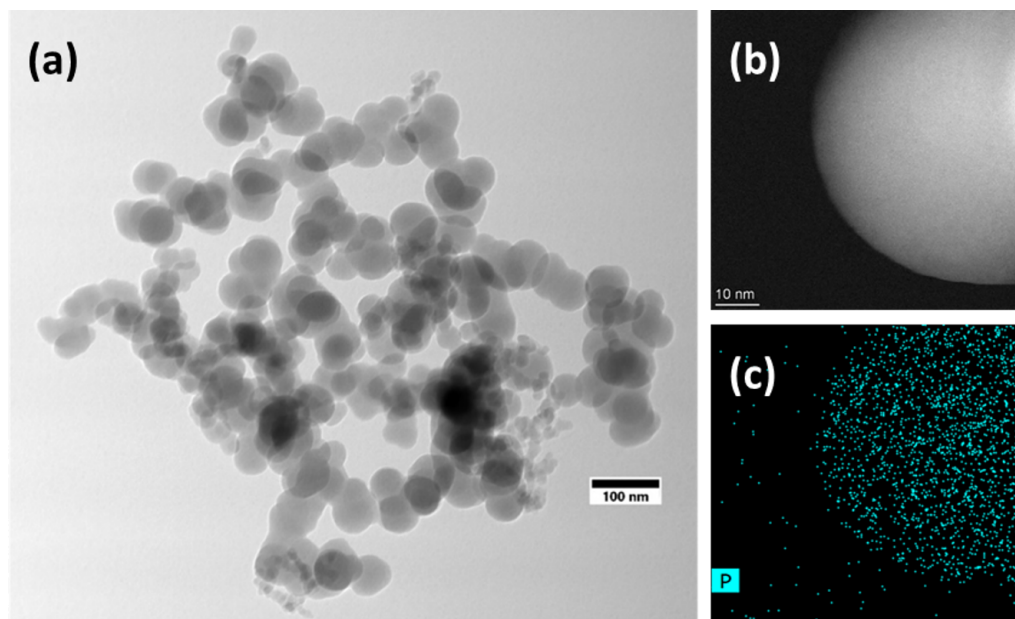


Figure 5.1: (a) TEM image showing a micron-sized aggregate of P5.2; (b) HAADF image of a single particle of the P5.2 material; (c) HAADF-EDS mapping of P in a particle of P5.2 material.

controlled morphology and particle size.[31] The obtained materials were characterized using microscopy-based methods, as the amorphous nature of the  $\text{SiP}_x$  particles as well as the formation of a solid solution of P in Si limits the selection of characterization techniques. Transmission electron microscopy (TEM) images of the nanoparticles shows a distribution of partially aggregated particles, as illustrated in Fig. 5.1a for P5.2. The microscopy characterization for materials P0, P1.5, and P3.2 is shown in Fig. A.1 on page 80 in the Appendix. These aggregates consist of primary particles with a radius below 50 nm, fused together in a branching pattern. These nanostructures are typical of Si nanomaterials prepared by  $\text{SiH}_4$  pyrolysis, and are much smaller than the critical size of 150 nm.[37, 98, 99, 12] The distributions of primary particle sizes shown in histograms in Fig. A.2 on page 81 in the Appendix illustrate a small decrease in primary particle radius with increasing P%. This difference is the most pronounced for pure Si, which shows an average particle radius 10 nm greater than the material with highest P content. The three  $\text{SiP}_x$  materials, however, show only a small variation in particle size distribution. The size of NPs is known to change the electrochemical

Table 5.1: Chemical and initial electrochemical parameters for the four Si-based materials prepared for the present study.

<b>Material name</b>	<b>P concentration (atomic %)</b>	<b>Capacity of 1<sup>st</sup> lithiation (mAhg<sup>-1</sup>)</b>	<b>ICE (%) [a]</b>
P0	0	3533	87.1 ± 0.6
P1.5	1.5	3066	88 ± 2
P3.2	3.2	2905	85 ± 1
P5.2	5.2	2830	87.7 ± 0.3

[a] Errors were calculated from the average of three cells.

properties, with larger particles showing an increase in overpotential.[89, 100] However, we do not expect these small, highly overlapped differences to cause a significant difference in electrochemistry. Fig. 5.1b and 5.1c show HAADF and HAADS-EDS images of the P5.2 material, respectively. The lack of a bright “edge” around the particle in Fig. 5.1c indicates that the P is not concentrated at the surface of the particle, but rather distributed evenly throughout. EDS spectra can be found in the Appendix in Fig. A.3 on page 81 and show very low concentrations of oxygen on the particles. For an accurate determination of the stoichiometry, the atomic percentages of P were determined by ICP-OES and are shown in Table 5.1. Furthermore, X-ray diffraction (XRD) analysis (Appendix Fig. A.4 on page 82) of the four materials confirmed their amorphous structure, with no peaks observed to indicate the presence of crystalline Si or measurable quantities of SiP/SiP<sub>2</sub> phases.[28]

## 5.2 Stability and rate capability of SiP<sub>x</sub> NPs

Galvanostatic charge-discharge (GCD) testing was performed in half-cells using Li foil as a counter electrode. The currents chosen for formation and subsequent tests were based on the capacity of the materials in order to minimise differences in stresses experienced by differing materials. This is also why current densities are reported in C-rates (with units of h<sup>-1</sup>), instead of mA g<sup>-1</sup>.

The 1<sup>st</sup> cycle charge-discharge curves for the studied materials are shown on page 82 in Appendix Fig. A.5a. Table 5.1 summarizes the data from the 1<sup>st</sup> cycle, and includes the measured gravimetric capacity taken from the first lithia-

tion step for each material, as well as the ICE. Table 5.1 shows that all the  $\text{SiP}_x$  materials have lower initial capacity than pristine Si. The change of capacity is not linear: P3.2 and P5.2 exhibiting similar initial capacities, while P1.5 has a higher capacity than other  $\text{SiP}_x$  samples. The similarity of the ICEs indicates that there is no appreciable formation of lithium phosphide ( $\text{Li}_3\text{P}$ ) or other matrix materials through any conversion reaction, as existence of such would cause the ICE to decrease as a function of the amount of P in the material. The capacities of the materials exhibit a strong negative dependence on the P%, which is greater than what would be expected from the theoretical reaction of  $\text{Si}_x\text{P}_{1-x} + (3 + 0.5x)\text{Li} \longrightarrow x[\text{Li}_{3.5}\text{Si}] + (1-x)[\text{Li}_3\text{P}]$ . This is consistent with the results of other researchers, who have reported that the initial capacity of  $\text{Si}_x\text{P}_{1-x}$  is lower than expected values.[23, 20, 28, 19] As the ICEs of all materials are very close and the conversion reaction can be neglected, it is possible to suggest that the formation of SEI is similar for all studied materials. Appendix Fig. A.5b on page 82 shows the first cycle differential capacity ( $dQ/dV$ ) plots of the studied materials. The  $\text{SiP}_x$  materials exhibit sharp peaks during lithiation below 0.3 V, which is common for the first cycle of Si. The formation of  $\text{Li}_3\text{P}$  at around 0.4 V expected from the literature has not been seen for any of the  $\text{SiP}_x$  materials studied in the present work.[28, 29, 18] The absence of distinctive features signalling the formation of lithium phosphosilicates or  $\text{Li}_3\text{P}$  are likely due to the low concentration of P in  $\text{SiP}_x$ . These species should account for less than 5% of the total capacity, and would, therefore, be lost in the much larger peaks corresponding to the formation of lithium silicide ( $\text{Li}_x\text{Si}$ ) and SEI. The two broad peaks in the delithiation step are characteristic for delithiation of the amorphous  $\alpha\text{-Li}_{3.5}\text{Si}$  and  $\alpha\text{-Li}_{2.0}\text{Si}$  phases.[43,44] The peaks that are expected for the conductive additives (mainly the conductive graphite) are too small to be visible due to the high (60% by weight) loading of Si-based material, and thus the electrochemical behaviour of the cells can be considered to be predominantly due to Si or  $\text{SiP}_x$ . The electrochemical testing was performed with the voltage cut-off was set to 0.05 V to avoid the formation of  $\text{c-Li}_{15}\text{Si}_4$  phase, which typically manifests itself by the presence of sharp peaks at 0.4 V in the delithiation curves – absent for the present materials.[89] Therefore, the advantages of forming a protective matrix with high  $\text{Li}^+$  diffusivity are not available for  $\text{SiP}_x$  at the studied range of P concentrations.

In order to study the charge/discharge behaviour of Si and Si-based materials, it is important to recognize the difference in electrochemical behaviour dur-

ing lithiation and delithiation.[77] It is important to consider these processes separately when evaluating materials particularly at high charge/discharge rates. Therefore, stability tests were carried out by lithiating and delithiating at asymmetric C-rates. The delithiation behaviour was studied by setting the delithiation rate to 0.3 C, and the lithiation rate to 0.1 C. This was done to reduce the stress on the electrode during lithiation and allow any electrochemical processes to run to completion. In this way, the behaviour of a delithiation step was not limited by the preceding lithiation step. A diagnostic cycle – where both the lithiation and delithiation C-rate was set to 0.05 C – was included after every tenth cycle to explore the evolution of the overpotential. The lithiation-dependent stability was studied in the same manner, with a slow delithiation process at 0.1 C and a faster lithiation at 0.3 C. The stability during fast delithiation (Fig. 5.2) shows that the total capacity increases for SiP<sub>x</sub> materials after the initial formation (delimited by the vertical dashed line), but not for the pristine Si (Po). Gradual capacity increases are observed in other literature, but the reason is not completely understood.[31, 101] For Po, P1.5 and P3.2 the difference between the cycling and diagnostic cycles remains unchanged, indicating that the overpotential is constant. In contrast, the disparity between the cycling and diagnostic cycles in P5.2 is larger at later cycles, which implies that the overpotential increases over time. By the 40th cycle, all the materials dropped below 80% of their capacity relative to the first cycle after formation (the 1<sup>st</sup> cycle after the dashed line). An example of the capacity retention of SiP<sub>x</sub> full cells is given in Appendix Fig. A.6 on page 83, to demonstrate the behaviour in a different system.

The lithiation-dependent performance was studied in the same manner, with a slow delithiation process at 0.1 C and a faster lithiation at 0.3 C. The performance of the materials as a function of lithiation is shown in Fig. 5.2b. Here the capacity increase is also observed. The relatively large lithiation current means that the potential limit is reached before full lithiation of the active material is achieved. This explains why the number of cycles required to reach the maximum capacity is greater than that observed in Fig. 5.2a. The difference in capacity between the fast cycles and the diagnostic cycles is more or less constant for the SiP<sub>x</sub> materials, indicating that the overpotential is consistent with repeated cycling. For Po, the small decrease in this difference indicates that the overpotential is decreasing slightly.

Rate capability tests were performed in a similar manner to the stability tests,

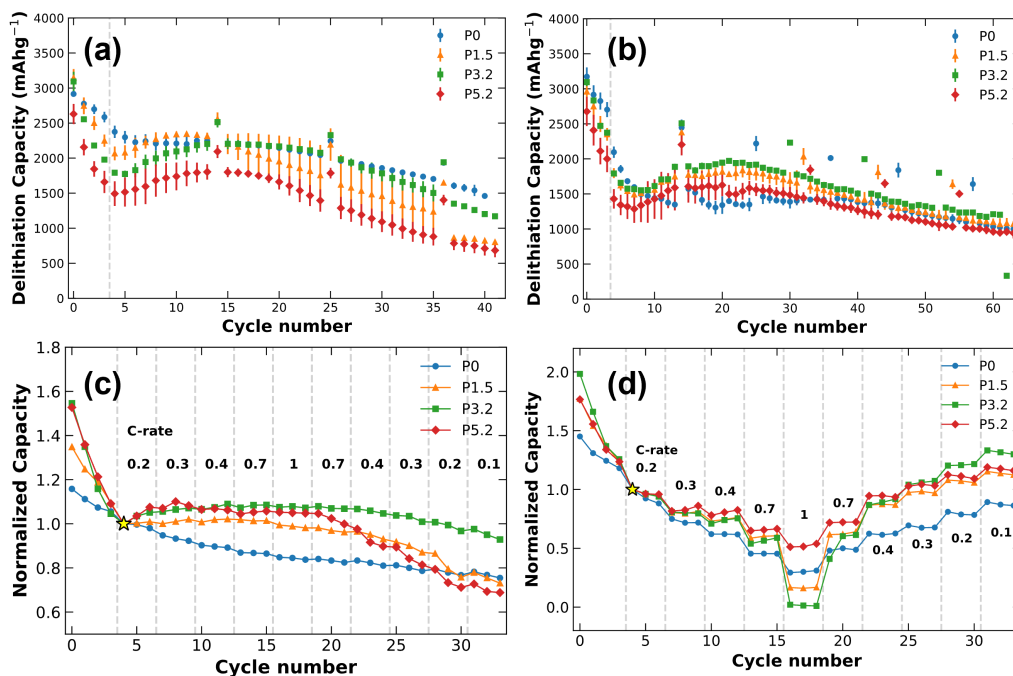


Figure 5.2: Cyclic stability and rate capability behaviour using asymmetric GCD. (a) Cyclic stability with delithiation set to 0.3 C and lithiation set to 0.1 C. (b) Cyclic stability with lithiation set to 0.3 C and delithiation set to 0.1 C. Error bars were calculated from the average of three cells. (c) Normalized delithiation rates with slow lithiation at 0.1 C. (d) Normalized lithiation rates with slow delithiation at 0.1 C. A diagnostic cycle at 0.05 C was included after every tenth cycle for the tests shown in the panels a and b. The star at cycle four in panels c and d is the normalization point, the first point after formation.

i.e. by lithiating the electrodes at 0.1 C and delithiating at increasing rates (or *vice versa*). The data is normalized to the first point after formation (marked with a star) to highlight the relative rate behaviour of the materials. Fig. 5.2c shows that the delithiation capacity is mostly independent of the applied current (within the chosen current range), and that the loss of capacity is due to ageing in the same way as the stability behaviour seen in Fig. 5.2a. Fig. 5.2d, however, shows a strong relationship between the lithiation capacity of the electrodes and the applied current. Here, the SiP<sub>x</sub> materials show slightly better capacity retention in the 0.1-0.7 C range compared to the pure Si, but at 1 C P1.5 and P3.2 perform worse than the pristine Si. The capacity is recovered once the applied current returns to C-rates below this inflection point, allowing us to conclude that this capacity loss is not due to cell failure or ageing. From this we can conclude that lithiation is the limiting factor in determining the rate capability of Si nanoparticles.

Analysis of the evolution of dQ/dV plots can provide additional insights to the differences in behaviour between the materials, explaining both the rate capabilities and the initial increase of capacities for SiP<sub>x</sub> during cycling. Fig. 5.3 and 5.4 show the changes in dQ/dV as a function of current for the delithiation and lithiation rate capability tests, respectively. From Fig. 5.3a and 5.3b, as the C-rate is increased the delithiation curve (most notably the Li<sub>3.5</sub>Si peak at 0.28 V) is shifted towards higher potentials – and when the C-rate is reduced (Fig. 5.3c and 5.3d), this trend reverses. This potential shift agrees with the expectation that the overpotential increases with the applied current, leading to a shift of the dQ/dV peaks. The reversal of this trend when decreasing the C-rate indicates that there is no significant change in impedance resulting from changing the current of the delithiation step while keeping the lithiation step fixed. Comparing the Li<sub>3.5</sub>Si peaks in Fig. 5.3a and 5.3b, it can be seen that the presence of P causes an increase in the size of Li<sub>3.5</sub>Si peak. This indicates that the capacity of this phase is increasing in the first few cycles, behaviour which is not seen for Po. The behaviour of the a-Li<sub>2.0</sub>Si peak is almost identical between Si and SiP<sub>x</sub>, and so this phase can be considered unaffected by the presence of P. The increase in capacity of the Li<sub>3.5</sub>Si peak may be due to a decrease in resistance of the cell as a result of increasing Li<sup>+</sup> diffusivity in the electrode.

Similarly to Fig. 5.3, Fig. 5.4 displays the dQ/dV curves for the lithiation-dependent rate capability. These graphs show a strong correlation between the

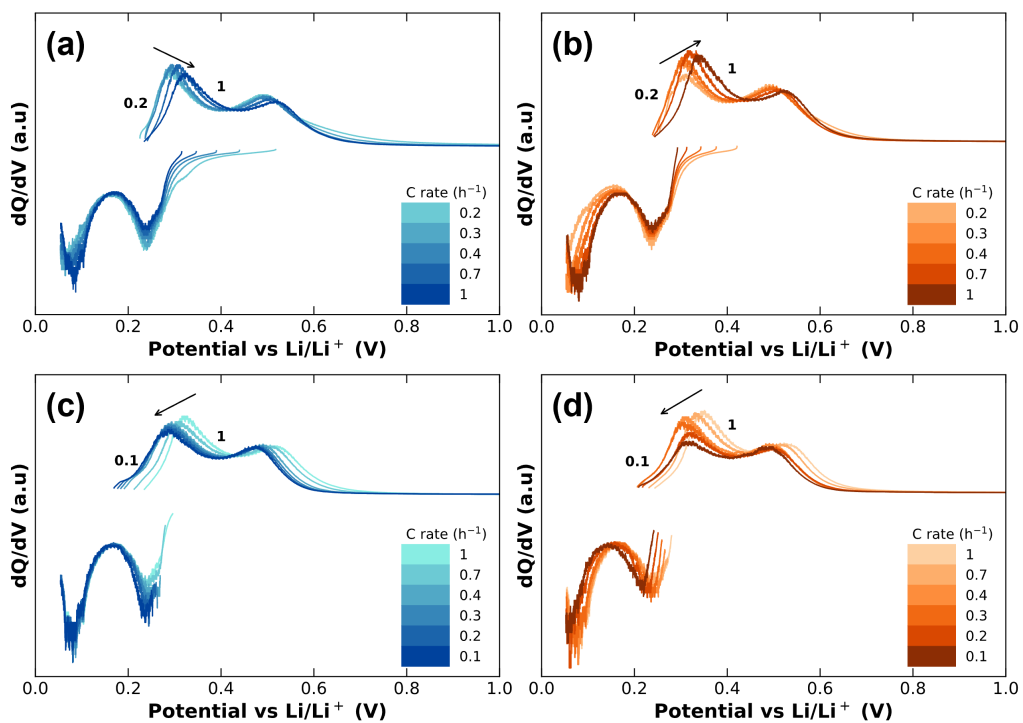


Figure 5.3:  $dQ/dV$  of rate capability experiments with lithiation rate fixed at 0.1 C and varying delithiation rates. (a, b) increasing C-rate; (c, d) decreasing C-rate. (a, c) sample Po; (b, d) sample P1.5.



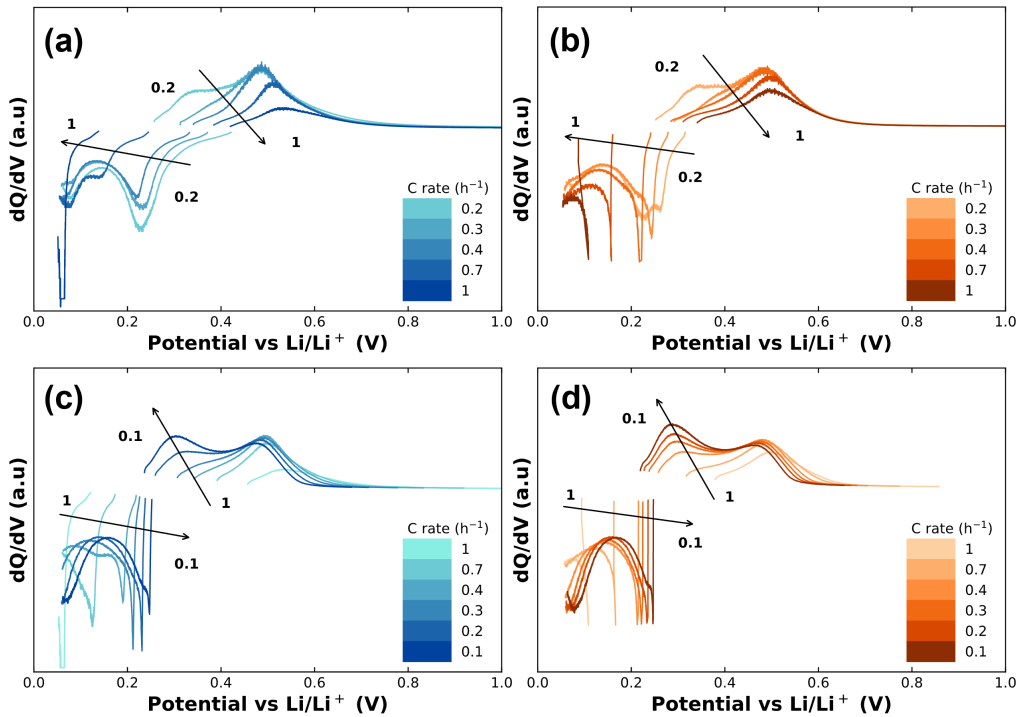


Figure 5.4:  $dQ/dV$  of rate capability experiments with delithiation rate fixed at 0.1 C and varying lithiation rates. (a, b) increasing C-rate; (c, d) decreasing C-rate. (a, c) sample PO; (b, d) sample P1.5.

$\text{Li}_{3.5}\text{Si}$  peak in the delithiation curve as a function of the lithiation rate. Unlike the behaviour shown in Fig. 5.3, Fig. 5.4a and b show that as the lithiation rate is increased, the  $\text{Li}_{3.5}\text{Si}$  peak is quickly lost, and the  $\text{Li}_{2.0}\text{Si}$  peak is strongly diminished. When decreasing the lithiation rate (Fig. 5.4c and 5.4d), the  $\text{Li}_{3.5}\text{Si}$  and  $\text{Li}_{2.0}\text{Si}$  peaks are recovered. However, the recovery of the  $\text{Li}_{3.5}\text{Si}$  peak is faster for the  $\text{SiP}_x$  materials, with a discernible peak occurring at 0.4 C for materials containing P, but not until 0.2 C for pristine Si. This means that the presence of P in the materials increases the ability for the  $\text{Li}_{3.5}\text{Si}$  to form during lithiation, and that this effect increases over time. This may be partially due to increased  $\text{Li}^+$  diffusivity of  $\text{SiP}_x$  compared to Si. However, this trend is not proportional to P%, nor does it hold at high lithiation rates. Lithiating at 1 C causes the P1.5 and P3.2 materials to have a lower capacity than PO – and in the case of P3.2, no capacity at all – which indicates that the overpotential at 1 C is very large.

Differential capacity plots are also used to explore the changes in electrochemistry over time. In the present study, they can be used to monitor the evolution of the GCD curves during and after the formation of the broad peak observed in the stability tests. Fig. A.7 and A.8 on pages 83 and 84 in the Appendices show the  $dQ/dV$  plots of P0, P1.5, P3.2, and P5.2 for cycles 6 to 14 of the delithiation and lithiation stability tests, respectively, which correspond to the cycles spanning the formation of the broad peaks in the capacity observed in Fig. 5.2a and 5.2b. The pristine Si in Appendix Fig. A.7a on page 83 shows only a slight broadening of the  $\text{Li}_{3.5}\text{Si}$  peak during delithiation, and a small decrease in overall height in the lithiation. The shift of the delithiation peaks (notably the  $\text{Li}_{3.5}\text{Si}$  peak) to lower potentials for P1.5 and P3.2 (Appendix, Fig. A.7b and A.7c on page 83, respectively) – as well as the increase in peak intensity show that lithiation of these materials is becoming easier over time. The lack of stability in P5.2 makes it difficult to discern features. This same trend can also be seen in the  $dQ/dV$  plots of the lithiation stability (Appendix Fig. A.8 on page 84). Here, the weak  $\text{Li}_{3.5}\text{Si}$  peak grows strongly between cycles 6 to 14 and the overpotential decreases, but only for materials containing P. The  $\text{Li}_{3.5}\text{Si}$  peak in pristine Si decreases and shifts to higher overpotentials over the same interval. This explains the increase in capacity seen in Fig. 5.2a and 5.2b. The behaviour seen in the cyclic stability and rate capability can be summarized thus:

1. The presence of P causes a decrease in overpotential coupled with a slow change in capacity.
2. The P-dependent effect that increases the rate capability forms slowly in the lithiation process.

During cycling we can expect reactions between P, Si and Li to occur, potentially forming small quantities of e.g.  $\text{Li}_3\text{P}$  or  $\text{Li}_2\text{SiP}_2$  (or other, more complicated phosphidosilicates). These chemical species have been shown to form in SiP and  $\text{SiP}_2$ , and similar conversions exist in  $\text{SiN}_x$ . [20, 28, 18] It has been shown that these species increase the  $\text{Li}^+$  diffusivity, and it can be hypothesised that their presence may help to explain the results observed. [32] However, the low concentration of P in the  $\text{SiP}_x$  materials studied here means that directly finding these P species via a method such as FTIR or XRD would be difficult. XPS experiments performed on P5.2 electrodes before and after formation the P2p peak confirms

that P is in the  $\text{SiP}_2$  state (Appendix Fig. A.9 on page 85).[28] Unfortunately, due to the low concentration of P it is not possible to conclude that  $\text{Li}_3\text{P}$  or phosphosilicate species are formed in  $\text{SiP}_x$ . While XPS could potentially be used to determine how P evolves upon cycling, this would require a more dedicated study. We have employed DFT/AIMD to test whether the P atoms in pristine  $\text{SiP}_x$  will affect the lithiation, and GITT and EIS to test the diffusivity and to find evidence that the P-containing materials have increased  $\text{Li}^+$  ion mobility over pure Si.

### 5.3 DFT and AIMD on $\text{SiP}_x$ and Si

To better understand the discrepancy between the different materials, it is necessary to explore the behaviour of Li atoms in close proximity to P atoms in the  $\text{SiP}_x$  system. To do this, DFT simulations were performed to calculate the Li behaviour in 64-atom Si systems containing 1, 2, or 3 P atoms. The results are summarized in Table A.1, which illustrates that as the concentration of P increases via substitution of Si, so does the energy of the system. This result indicates that inserting relatively high concentrations of P into Si is thermodynamically unfavourable, at least in the low P concentration range. Interestingly, the Li insertion energy displays a local minimum at 1.6 at% P ( $\text{Si}_{63}\text{P}$ ). An AIMD simulation was also performed to evaluate the stability of these systems (Appendix Fig. A.11 on page 86). As shown in Appendix Fig. A.10a-c on page 86, the total energy of each of the  $\text{Si}_{64}$ ,  $\text{Si}_{63}\text{P}$ , and  $\text{Si}_{62}\text{P}_2$  (0, 1.6 and 3.1 at% P, respectively) system is oscillating during the whole MD simulation, whereas the  $\text{Si}_{61}\text{P}_3$  (4.7 at% P, Appendix Fig. A.11d on page 86) system shows a remarkable change in total energy. Here one of the Li atoms shifts to neighbouring site, implying that a high P concentration will have a negative effect on lithiation and delithiation behaviour during the charge-discharge process. This “rejection” of Li in proximity to the P may explain why the broad peak in the  $\text{SiP}_x$  exists in Fig. 5.4c and 5.4d, and also why the effect is stronger for higher concentrations of P. Higher substitution energy will increase the thermodynamic instability. Lower Li insertion energy will also increase the rate capability during lithiation. The interplay between lower insertion energy and higher thermodynamic instability implies that materials with lower concentrations of P should show good rate capability as well as decent stability, both of which are supported by the experimental data.

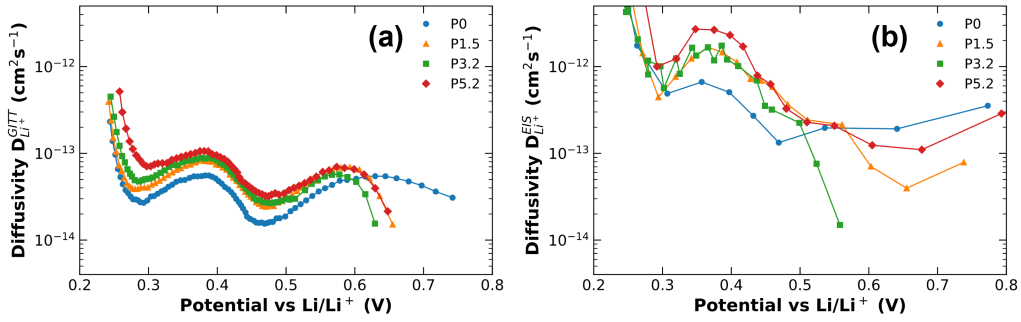


Figure 5.5: Diffusivity as a function of potential for Si and SiPx. (a) Diffusivity calculated from GITT data using Equation 5.1. (b) Diffusivity calculated from the Warburg constants from EIS data using Equation 5.2. The diffusivities are calculated at the electrode level.

## 5.4 GITT and EIS of SiPx and Si

To validate the rate behaviour of these materials, it is necessary to study the  $\text{Li}^+$  ion mobility in the materials. The diffusivity  $D_{\text{Li}^+}$  of  $\text{Li}^+$  in the electrode can be calculated from GITT data from the following equation:[4, 102, 103, 104]

$$D_{\text{Li}^+}^{\text{GITT}} = \frac{4}{\pi\tau} \left( \frac{m_B V_M}{M_B S} \right)^2 \left( \frac{\Delta E_s}{\Delta E_t} \right)^2 \quad (5.1)$$

and from EIS using:[2,45,46]

$$D_{\text{Li}^+}^{\text{EIS}} = \frac{1}{2} \left[ \left( \frac{V_M}{S F A_W} \right) (\delta E / \delta x) \right]^2 \quad (5.2)$$

Where  $\tau$  is the duration of the titration step;  $m_B$  and  $M_B$  are the molecular mass and weight of Si, respectively;  $\Delta E_s$  and  $\Delta E_t$  are the changes in equilibrium and rest potentials, respectively;  $S$  is the area of the electrode;  $F$  is Faraday's constant;  $A_W$  is the Warburg impedance; and  $\delta E / \delta x$  is the local slope of the open circuit potential (OCP) curve. The diffusivity of the lithiation process determined by GITT is given in Appendix Fig. A.12 on page 87, along with typical examples of the GITT and EIS curves, and the equivalent circuit used for fitting the EIS data.

Fig. 5.5 shows a comparison between the  $\text{Li}^+$  ion diffusivity of the materials as calculated from GITT as a function of voltage (Fig. 5.5a) and EIS (Fig. 5.5b) using equations 5.1 and 5.2, respectively. Both these figures show that the diffusivity of  $\text{Li}^+$  in  $\text{SiP}_x$  is significantly greater than for pristine Si even accounting for changes

in diffusivity as a result of particle size differences, which would lead to a roughly 2-fold increase in diffusivity of the smallest particles (P5.2) over the largest (P0). The remaining diffusivity increase is then possibly due to the presence of lithium phosphidosilicates hypothesised earlier. The difference in diffusivities calculated from GITT and EIS can be explained by the difference in equilibrium states, as the relaxation time for GITT is two hours, while that of EIS is 24 hours. This leads to an increase in the slope of  $\delta E/\delta x$ , and therefore a higher  $D_{Li^+}^{EIS}$ . The GITT technique also assumes that the diffusion is linear rather than radial, which leads to smaller values of diffusivity.[102]



## Chapter 6

# Empirical analysis of silicon GCD curves

Following the results and subsequent discussion seen in chapter 5 it became apparent that the use of  $dQ/dV$  curves was critical to the interpretation of electrochemical data, but that the data processing required to create these curves was a limiting factor to the accurate and quantitative analysis of data. This was especially apparent for relatively low-resolution datasets such as those produced on less expensive cyclers. Given the prevalence of such data in the literature, it was also apparent that the need for a general technique was of potential interest to the wider scientific community. The data used in this chapter was produced externally for two reasons: firstly to show that the approach can be applied to any data, and not just data which has been produced specifically for this purpose; and secondly to allow for the method to prove itself by comparing types of materials rarely seen together.

### 6.1 Physical considerations of the fitting function

While parameters such as  $Q$  of equation 2.8 are well defined and intrinsic to Si and the generated data, the rest are not, and likely depend on environmental factors such as material surface area and thickness, and cell resistances. That said, some educated guesses can be made as to the meaning of these parameters. The position  $c$  is theoretically equal to the equilibrium potential, but in practice over-

potentials and artefacts due to the quality of data will shift the resulting values of  $c$  away from equilibrium. Both of the scale parameters  $s$  and  $\gamma$  are inverse rate parameters and relate to how fast the process occurs. An ideal battery material at equilibrium would display no voltage change over the course of the phase change and an infinite gradient at the beginning and end of the phase. This would result in values of 0 for  $s$  and  $\gamma$ . [54] The skew parameter  $\alpha$  is a measure of the deviation from normality, and therefore represents a “lagging” effect. The size of  $\alpha$  is therefore expected to be proportional with the C-rate (with  $\alpha \rightarrow 0$  at equilibrium conditions), and is likely related to the diffusivity. Finally, the weighting parameter  $w$  defines the degree to which each of the two peaks contributes to the total capacity of the phase. This determines whether the phase is limited by the parameters in the skew-Gaussian or the Lorentzian part of the equation. To adequately fit Si data it is first necessary to set up the correct initial parameters and choose data that can be fit. Because the lithiation of Si takes place at or near the cut-off potential the tail end of the lithiation phase is too close to the cut-off potential to give good fits. We therefore apply this technique to the delithiation cycle only.

## 6.2 Parameter setup and goodness of fit

The initial parameter setup for fitting is set according to the known behaviour of Si during delithiation. The alloying phases of Si during lithiation and delithiation have been determined by NMR and PDF, and it has been shown that Si forms amorphous or crystalline phases depending on cycling conditions. [43, 42, 44] During delithiation Li is removed from amorphous  $\text{Li}_{3.5}\text{Si}$  in two distinct phases, yielding a value of  $n = 2$  for equation 2.8. The two phases are named I and II, and the parameters of the phases are distinguished using the subscripts I and II, respectively. Phase I: ( $\text{Li}_{3.5}\text{Si} \rightarrow \text{Li}_2\text{Si}$ ), is located at about 0.3 V, while phase II: ( $\text{Li}_2\text{Si} \rightarrow \text{Si}$ ) is located at about 0.48 V. From the stoichiometry of these two phases it is also possible to estimate the initial  $Q$  parameters, assuming that the material at the beginning of the GCD step consists purely of  $\text{Li}_{3.5}\text{Si}$ , and the delithiation is complete (i.e. only Si remains at the end of the cycle). This gives a theoretical stoichiometry of 1.5:2, equivalent to 43% of the capacity coming from phase I, while the remaining 57% comes from phase II.

Fig. 6.1 shows an example of the residual and fit of each phase to a GCD curve,



along with the equivalent  $dQ/dV$ . Fig. 6.1a shows how the fitting function agrees with the data, along with how the two phases contribute to the total curve. The plot of the residuals in Fig. 6.1b shows an overall excellent fit to the data, with the error not exceeding 1.5%. Analysis of the errors of the individual parameters reveals that the errors are almost all less than 10% of the parameter value, and the majority are below 5%. The exception to this is the parameter  $c$ , which due to the small values of  $c$  compared to the other parameters displayed larger errors of up to ten times the parameter value. The equivalent  $dQ/dV$  is plotted in Fig. 6.1c, with the bottom set of curves showing how the results of the fit is split into skew-Gaussian and Lorentzian curves. Phase I displays no Lorentzian behaviour, and phase II shows a sharp Lorentzian curve as well as a very broad skew-Gaussian curve. This shows that there is excellent agreement between the shape and position of the phases and the results of the fit equations, and reveals that the model is an accurate representation of the shape of the curve. Further, figure 6.1c shows that the shapes of the phases are not symmetric about the position  $c$  and that the skewness factor  $\alpha$  is crucial to accurately describe the behaviour of the delithiation curves.

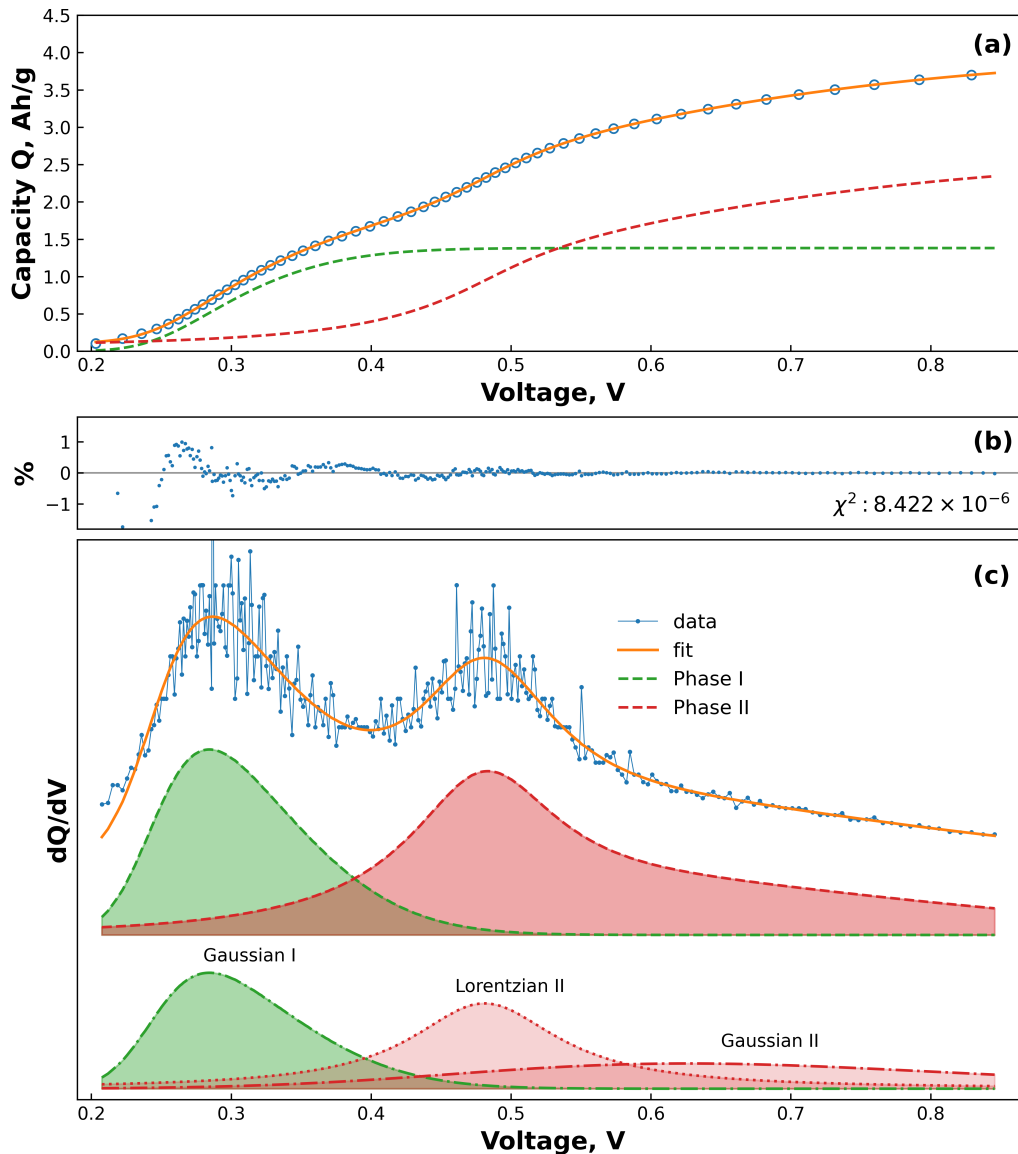


Figure 6.1: An example of the goodness of fit of cycle number 5 from a 40 nm SiTF cell. **(a)** The raw output of the fitting model, showing the input data as blue points overlaid with the best-fit determined by the program (orange line). The dotted lines are the curves of the individual phases which together make up the full fitting function. **(b)** Residuals of the fit, displayed as a percentage difference from the measured points. **(c)** The data from (a), displayed as a  $dQ/dV$  plot. The top offset shows the data as blue points overlaid with the best fit (orange line). The middle offset shows the contribution to the fit of phase I (green) and phase II (red). The bottom offset shows how the phases are composed of skew-Gaussian and Lorentzian curves.

### 6.3 Comparison of thin films and nanowires

Characterization of the NWs may be found in the original work.[89] The Coulombic efficiencies (CE) of the samples exceeded the 99.5% required for long-term cycling after about 20 cycles. An in-depth discussion of the NW CE is given in the original work.[89] Fig. 6.2 shows how the curves change with repeated cycling for an example of 40 nm TFs (Fig. 6.2a) and 9 nm NWs (Fig. 6.2b). This shows that the individual phases of the two samples behave quite differently, and also shows how important it is to consider the many experimental variables that contribute to cell behaviour. If we were to only look at the complete  $dQ/dV$  (grey curves), we might be convinced that both TFs and NWs behave quite similarly. For example, the position of phase I appears to be at about 0.32 V for both samples. However, by looking at the behaviour of only phase I (green curves), it can be seen that this phase is more skew (higher  $\alpha$ ) for the TF sample than the NW sample. Simultaneously, the position of phase I ( $c_I$ , shown as coloured circles on the curves at 0.3 V) is decreasing for the TF sample, but increasing for the NW sample. Note that the position of a phase is not necessarily the point at which the  $dQ/dV$  displays a maximum. Similarly, comparing phase II using only the total  $dQ/dV$  behaviour would limit us to discussing only the small shift in peak position experienced by the NWs. Instead, by looking at the behaviour of phase II alone (red curves), it can be seen that the Lorentzian portion of the curve is consistently narrower for TFs than for NWs and that the skew-Gaussian portion of phase II is fading slower for TFs than for NWs. This shows that the fitting function provides a powerful tool for analysing the behaviour of Si phases according to their component curves.

As seen in Fig. 6.2 the behaviour of a parameter is affected by all other parameters and it is therefore difficult to separate their behaviour and ascribe meaning to them. Nevertheless, in order to show the changes in the datasets over time, the plots of the individual parameters  $\alpha$ ,  $c$ ,  $s$ ,  $\gamma$ , and  $w$  are shown in Figs. A.13 to A.17 in the Appendix on pages 88 to 89.

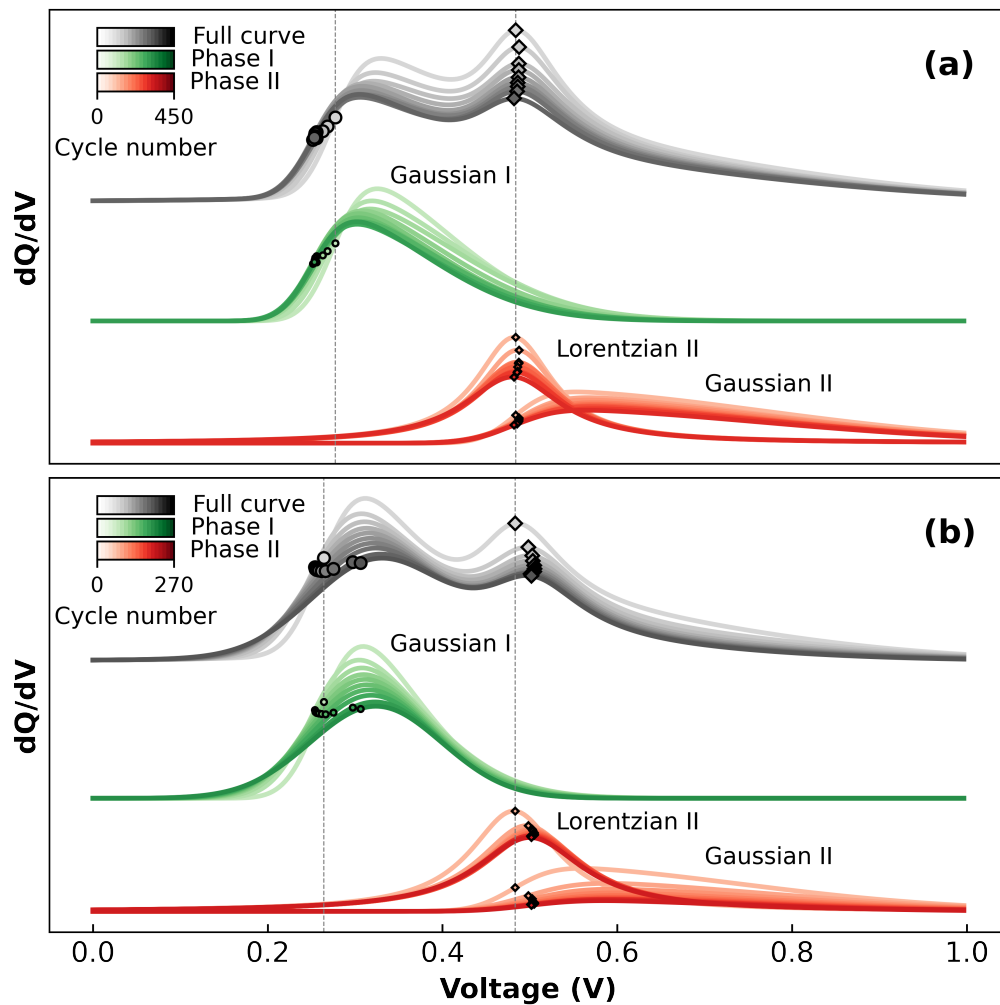


Figure 6.2: Output of fitting equation 2.8 to the data, displayed as  $dQ/dV$  and showing the evolution of the curves with cycling for **(a)** 40 nm TFs, and **(b)** 9 nm NWs. Each curve is an average of  $x$  cycles, where  $x$  is  $1/10^{th}$  of the total number of cycles. The locations of the dots and diamonds correspond to  $c_I$  and  $c_{II}$ , respectively. The dotted vertical lines denote  $c$  for the first cycles.

The differences in behaviour of the TFs and NWs shown in Fig. 6.2 give insights into the behaviour of the materials, and can give information about how equation 2.8 relates to physical phenomena occurring in the cells. For instance, the increased skewness seen in the phase I peak for TFs (Fig. 6.2a) indicates that

there is a relatively large “lagging” effect as the potential increases faster than the diffusion can equilibrate. This is consistent with the expectation that the delithiation is hindered by the long diffusion distance of Li to the surface of the Si. The less skew phase I NW peak (Appendices, Fig. 6.2b and Fig. A.13a on page 88) supports this hypothesis, as the thin NWs have lower diffusion lengths, and can diffuse Li in radial directions. The decrease in skewness factor  $\alpha_I$  seen when cycling the TFs at lower C-rates (Appendix Fig. A.13b on page 88) further corroborates this, as cycling at rates closer to equilibrium would decrease the diffusion overpotentials. Similarly, the differences in phase position  $c_I$  of phase I give information about two datasets. For thin films, the positions of phase I shift from around 270 to 250 mV over the course of cycling, while NWs show the opposite trend with the position increasing from 250 to 300 mV. In both cases however, the positions of  $c_I$  (Appendix Fig. A.14 on page 88) are very close to the equilibrium potentials determined by previous literature.[42, 43, 105] This might indicate that the overpotentials are increasing with cycling in the case of NWs but not TFs, but given that the overpotentials in TFs would also be expected to increase, this explanation alone provides an incomplete picture of the behaviour of  $c_I$ . Rather, the exact position of  $c_I$  is likely decided by the combination of diffusion effects described by  $\alpha_I$ , and the growing iR drop encroaching on the phase. Since  $\alpha_I$  is relatively stable for TFs, pushing the “start” of the data to higher voltages forces the fitting function to compensate by shifting  $c_I$  to lower values. Conversely, the decreasing  $\alpha_I$  seen for NWs causes  $c_I$  to shift to the right. It is therefore clear that  $c_I$  is not a simple function of the equilibrium potential, but is affected by the behaviour of the cell at the very start of the cycle. It would therefore be more correct to deem  $c$  an “apparent” equilibrium potential.[27, 42, 44, 77]

Finally, the scale parameter  $s_I$  gives information about how fast the delithiation is occurring in phase I.[54] While the total dQ/dV (grey curves, Fig. 6.2a and 6.2b) seem to show that the width of the phase may be slightly narrower for TFs than NWs (Fig. 6.2a and 6.2b, respectively), the output of the fitting shows that the opposite is true (Appendix Fig. A.15 on page 88). Further, the slower TF cycles in Appendix Fig. A.15b show lower values of  $s_I$ , indicating that the resistance to delithiation described by the skew-Gaussian component is dependent on the C-rate. This behaviour matches the expectation that as the applied current is reduced, the overpotentials will also be reduced.[106] This result matches the expectation that the thinner NWs should delithiate faster (relative to the applied

current) than the thicker TFs due both to the decreased diffusion distance as well as the slower C-rates.

As with phase I, analysis of phase II gives important information about the behaviour of Si. Notably,  $c_{II}$  is independent of TF thickness, and only slightly decreased at slower C-rates (Appendix Fig. A.14b on page 88), varying from 460 to 480 mV. Meanwhile,  $c_{II}$  (shown as diamonds on the curves in Fig. 6.2) for the NWs shows a small shift from 460 to 500 mV at the start of cycling before reaching a steady state. This initial increase could be due to an increase in overpotentials due to SEI formation in early cycles. The shift to lower potentials seen in phase I not reflected in phase II because the position of phase II is relatively close to the middle of the dataset. Hence, there are enough datapoints at low voltages to adequately describe the curve. While phase I is described only by the skew-Gaussian component ( $w = 1$ ), phase II is described by a combination of both the skew-Gaussian and Lorentzian components. Due to  $\alpha_{II}$  the contribution to capacity of the Lorentzian occurs earlier in the delithiation, and the contribution of the skew-Gaussian component is only significant after the maximum of the Lorentzian has been reached. The resulting behaviour indicates a relatively fast “burst” of delithiation described by the Lorentzian, followed by a slower “tail” described by the skew-Gaussian. As with the scale parameter  $s$  of the skew-Gaussian, the scale parameter  $\gamma$  of the Lorentzian also gives information about how quickly the reaction is occurring. However, unlike the behaviour seen for  $s_I$ ,  $\gamma_{II}$  is larger for NWs than for TFs (Appendices, Fig. A.16a and A.16b on page 89, respectively). This would indicate an increase in resistance to delithiation of the NWs compared to the TFs. As cycling progresses, the position of the phase is shifted to higher voltages due to increasing overpotentials, but the onset of delithiation (visible at around 0.25 V in Fig. 6.2) remains constant. The result is that  $\gamma_{II}$  increases to cover the larger potential range over which the phase occurs.

The skew-Gaussian component of phase II describes the end behaviour of the delithiation. As with  $\alpha_I$ ,  $\alpha_{II}$  is smaller for NWs than TFs (Appendices, Fig. A.13a and A.13b on page 88, respectively). This again matches the expectation that the diffusion of Li in the TFs takes longer due to the dimensionality and thickness of the materials. Similarly,  $s_{II}$  shows the same trend as  $s_I$ , and we can conclude that delithiation of phase II is hindered by the slow diffusion in the same way as for phase I.

When considering the behaviour of phase II it is important to bear in mind

the relative contribution to the phase of each component. The weighting parameter  $w$  determines whether the phase is “skew-Gaussian-limited” ( $w \rightarrow 1$ ) or “Lorentzian-limited” ( $w \rightarrow 0$ ). For the Si morphologies studied here  $w_I$  was always found to be 1. This indicates that the capacity of this phase is skew-Gaussian-limited, at least within the C-rates studied. Appendix Fig. A.17 on page 89 shows the behaviour of parameter  $w_{II}$  for phase II TFs and NWs. From this plot it can be seen that  $w$  for TFs remains stable at around 0.5 during normal cycling, while for the NWs  $w$  begins at 0.45 and trends towards 0. This means that the resistances in the TFs are not dominated by either the skew-Gaussian nor the Lorentzian parameters, but the NWs are increasingly limited by the Lorentzian. This difference could be explained by the shrinking of the NWs during delithiation coupled with the growth of SEI in the electrode during cycling. This results in a loss of electrical contact between NWs and leads to a progressive increase in electronic resistance greater than that experienced by the TFs. This hypothesis is supported by the fact that  $w_I$  was found to be equal to 1 for all samples and morphologies tested because the highly lithiated  $\text{Li}_{3.5}\text{Si}$  phase is about 3.5 times more electrically conductive than the  $\text{Li}_2\text{Si}$  phase, which is sufficient to overcome the SEI-related resistances.[107] This implies that the Lorentzian may be related to electronic resistances, while the skew-Gaussian is related to ionic resistances. Since the highly lithiated phase I has low electronic resistance the Lorentzian is very small, and therefore  $w_I = 1$ . Conversely, as the NWs lose electrical contact with progressive cycling the electrical resistances increase, and this is measured by an increase in the size of the Lorentzian. It should be noted that “related to” does not mean that all electrical resistances are explainable by the Lorentzian. Any electrochemical reaction in a battery requires both electrons and ions, and so the components of equation 2.8 are convoluted.

### 6.3.1 Phases of Si delithiation

To further highlight the ability of this method to show differences between the datasets in ways that are not obvious by  $dQ/dV$ , the capacities of the two phases normalized to the total capacity determined by the fitting are shown in Fig. 6.3. The horizontal dotted lines denote the initial guesses for the fitting of the phases as discussed in section 6.2. While this shows that the assumption made initially, *i.e.* that the datasets consist of 100%  $\text{Li}_{3.5}\text{Si}$  at the start of delithiation and 100%

Si at the end of delithiation, was not completely accurate, the fitting reveals interesting differences between the TF and NW samples. For both TFs and NWs, the first 10 to 20 cycles show an increase in the contribution to the total capacity from phase I. However, while phase I for the TFs contributes less capacity than expected throughout cycling, the capacity contribution from phase I for the NWs continues to increase and eventually exceeds the amount of capacity expected from the initial assumption made in section 6.2. The initial increase in contribution from phase I can be explained by the progressive lithiation of Si at the start of repeated cycling proposed in the literature.[31, 52, 101] In this case the resistance to lithiation of fresh Si electrodes results in the incomplete conversion of  $\text{Li}_2\text{Si} \rightarrow \text{Li}_{3.5}\text{Si}$  during lithiation. This means that at the start of the delithiation step the Si consists of a mixture of  $\text{Li}_{3.5}\text{Si}$  and  $\text{Li}_2\text{Si}$ , and results in less capacity contribution from phase I during delithiation, and more from phase II.

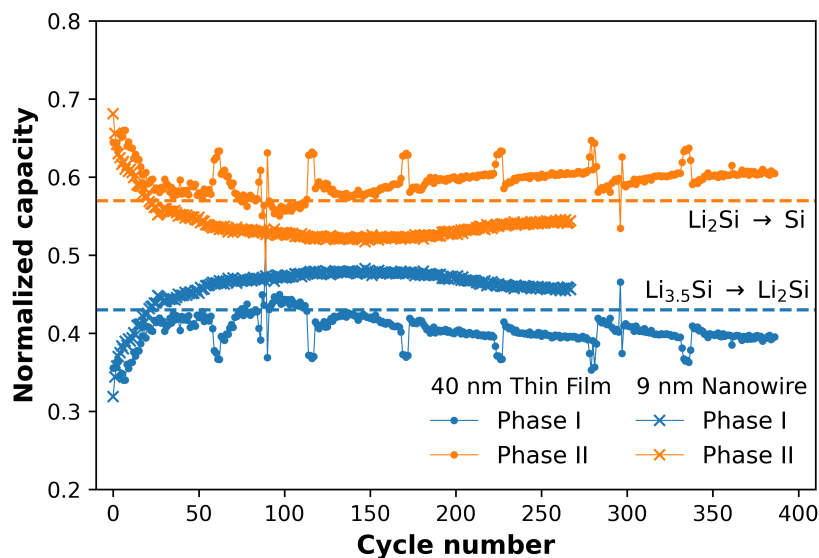


Figure 6.3: Comparison of the capacities of phases I (blue) and II (orange), for an example of thin films (dots) and nanowires (crosses). The data is normalized to the total capacity of each point as determined by the fitting. The horizontal dotted lines denote the initial guess of full conversion between the two phases.

The differences between the TFs and NWs at later cycles can be explained by differences in morphology and C-rate. With repeated cycling, the NWs experience



more pronounced SEI growth than the TFs, and therefore increased electrode resistance. This causes the voltage cutoff of the delithiation step to be reached sooner, leading to incomplete delithiation of phase II to form Si, and a disproportionately large contribution to capacity from phase I. This agrees with the observation in Fig. 6.2b that  $c_I$  is shifting to higher potentials. For TFs, the SEI growth occurs relatively slowly (compared to the NWs) and so the electrode resistance plays a less important role. Instead, the larger Li ion diffusion length experienced by the relatively thick TFs, combined with the faster C-rate used for cycling leads to incomplete formation of  $\text{Li}_{3.5}\text{Si}$  during lithiation. This means that, as with the first 10-20 cycles, the electrode consists of a mixture of  $\text{Li}_{3.5}\text{Si}$  and  $\text{Li}_2\text{Si}$  rather than just  $\text{Li}_{3.5}\text{Si}$ , and the amount of capacity extracted from phase II is increased.

## 6.4 Voltage slippage and excess Li effects

To demonstrate how well the fitting function describes the data with repeated cycling, an example of the capacities of the each of the two phases, along with the experimentally measured capacity and the total capacity output by the model are given in Fig. 6.4a as a function of the cycle number. It can be seen that the model consistently overestimates the total capacity of the cell. This is because as the slope of the voltage-capacity curve is not 0 at the cut-off potential, indicating that the cell is not fully delithiated at the end of the cycle. This extra capacity has previously been described as a “reservoir effect”, made up of unreleased Li and voltage slippage effects.[108] The size of this reservoir can be estimated from the results of the fit by the simple relation:

$$Q_{reservoir} = Q_{model} - Q_{measured} \quad (6.1)$$

where

$$Q_{model} = Q_I + Q_{II} \quad (6.2)$$

Using these formulae, it is therefore possible to calculate the size of the reservoir effect in the electrode and follow its behaviour with time. Fig. 6.4b shows schematically how the reservoir starts to grow after the voltage cut-off (black line) until it reaches a steady value when  $Q_{reservoir}$  stops increasing. Fig. 6.4c shows the results of applying equation 6.1 to the results from the two datasets, plotted

as a percentage of the measured capacity ( $Q_{reservoir}/Q_{measured}$ ). From this plot it can be seen that the size of the reservoir is strongly dependent on the morphology, with the NWs averaging about 2%, while the TFs maintain a relatively stable reservoir of about 7% of the measured capacity. However, it should be emphasised that the C-rates used to generate data for the two morphologies were not the same, with the TFs cycling at a C-rate 2.5x greater than the NWs. This will likely also contribute to the difference as the TFs have less time to delithiate fully, resulting in a larger reservoir. Nevertheless, the ability of the fitting function to discern these differences and estimate the size of the reservoir is quite valuable.

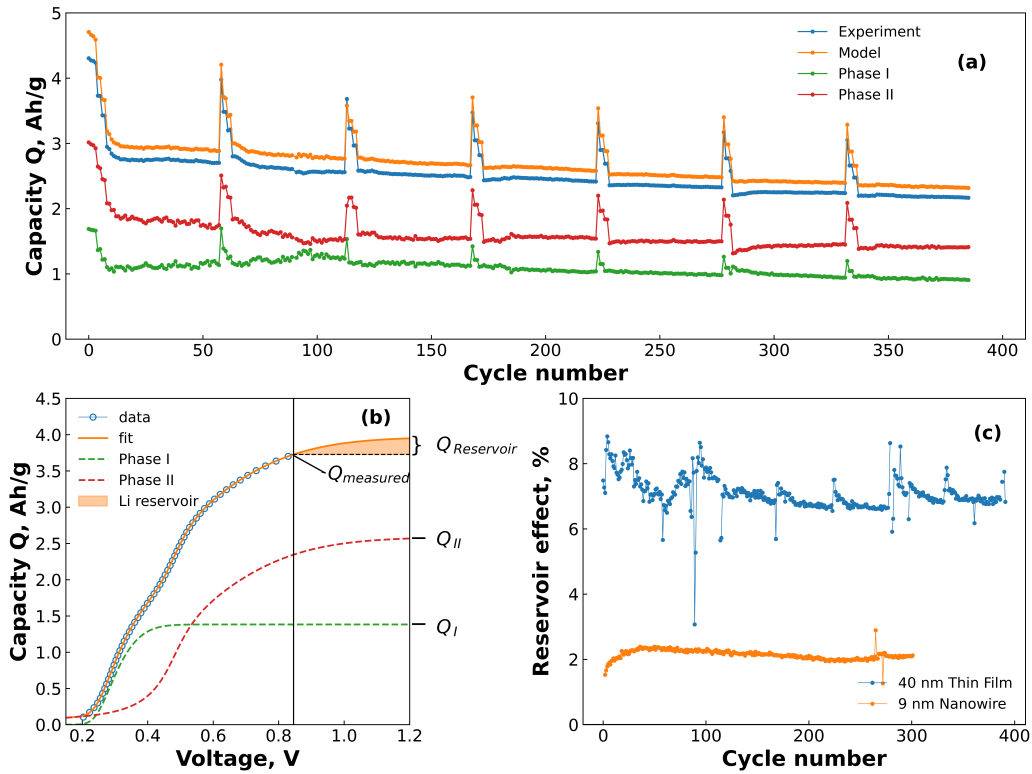


Figure 6.4: **(a)** An example of the capacity vs cycle life of a thin film sample (blue points), including the capacity contributions of each phase (green and red points) to the total capacity from the model (orange points). **(b)** Plot showing the capacity of the cell as the voltage is extended beyond the cutoff potential. The blue dots denote the raw data, while the orange line denotes the best fit. The black vertical line at  $\sim 0.85$  V denotes the end of the measured data (i.e. the cut-off potential). The orange shaded area is the reservoir. **(c)** The reservoir of the different materials as calculated from equation 6.1. The data is displayed as a percentage of the  $Q_{measured}$  for each material.



## Chapter 7

# Electrochemical impedance spectroscopy of silicon half cells

Having shown that the fitting procedure can be used to accurately fit existing data, and that it can further be used to compare datasets from different sources, the next challenge would be to identify relationships between physical processes and the empirical fit parameters. However, given that the data used for fitting was from half cells, and given that the Li electrode can have an outsize effect on the electrochemistry. It was therefore necessary to first deconvolute the interaction between the Si electrode and the CE. EIS was chosen as the main technique for this work as it could be used to give information about the nature of the data both in half cell and symmetric cell configuration. A commercially available Si material was chosen in order to allow others to replicate these results. Since the focus of this work is to find the influence of the Li electrode on the half cell as a function of potential, only a surface-level treatment of parameter values is included.

### 7.1 EIS of half and symmetric cells

Inspection of the formation cycles are shown in Fig. A.19 on page 92 in the Appendix. These reveal an initial Coulombic efficiency (ICE) of 86%. The subsequent cycles at 1/10 C had CEs of 98.6% and 99.7% indicating a relatively stable

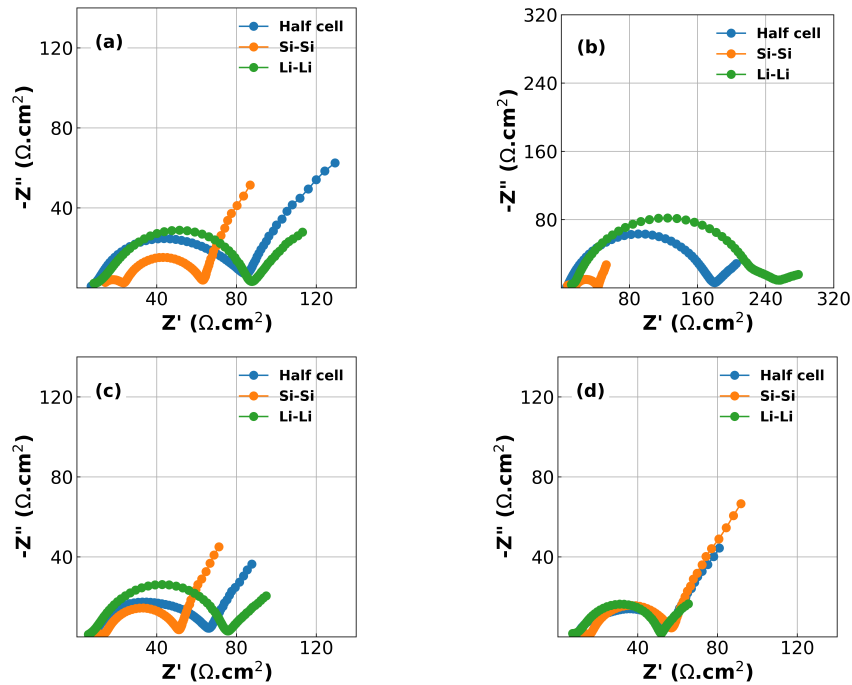


Figure 7.1: EIS spectra collected for comparison between half cells and symmetric cells at **(a)** 0.2 V in the lithiation step; **(b)** 0.07 V in the lithiation step; **(c)** 0.3 V in the delithiation step; **(d)** 0.48 V in the delithiation step.

electrode suitable for short experiments. However, it should be noted that there was a significant capacity drop between each delithiation cycle and the subsequent lithiation (87.3% and 90.1% between cycles 1 to 2 and 2 to 3, respectively), indicating that a large polarization process exists during lithiation.

Results of the EIS spectra for half-cells, Si/Si symmetric cells and Li/Li symmetric cells at each of the 4 stop potentials are given in Fig. 7.1. In all cases the Kronig-Kramers relations showed that the data was acceptable quality, with the residuals of the Kronig-Kramers and data not exceeding 1%. [70, 109] As expected, the spectra show that there is a large difference in EIS response both as a function of potential, and also between half cells and symmetric cells. [50] While one might expect that the EIS spectra of the half cells should be equal to half the sum of the Si/Si and Li/Li symmetric cells there is a non-linear relationship between the components of the cell and the EIS spectrum, especially as a function of voltage. [110] This is shown in Fig. A.20 in the Appendix on page 93.

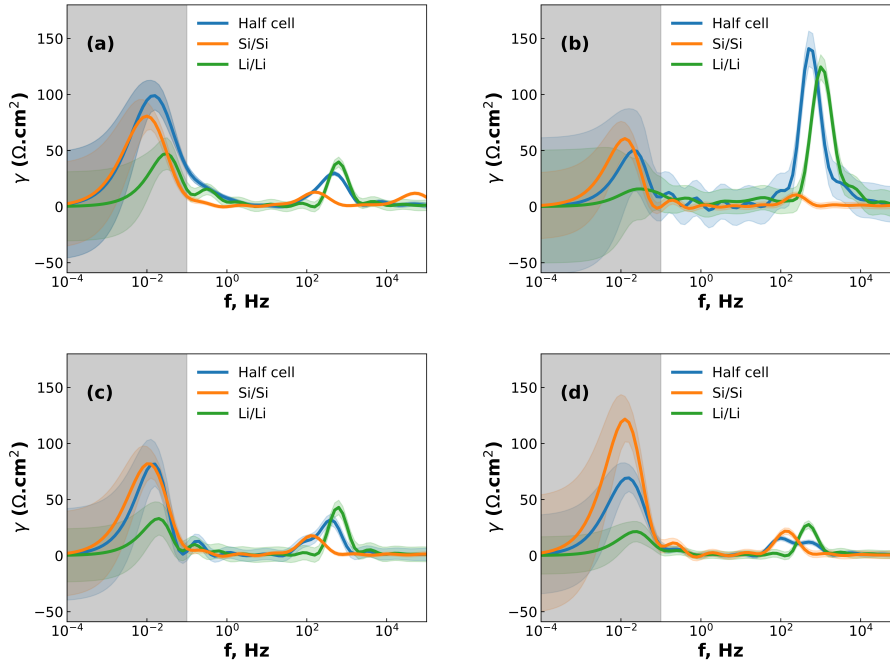


Figure 7.2: DRT spectra generated for comparison between half cells and symmetric cells at **(a)** 0.2 V in the lithiation step; **(b)** 0.07 V in the lithiation step; **(c)** 0.3 V in the delithiation step; **(d)** 0.48 V in the delithiation step. The coloured regions above and below the curves denote the confidence interval of the analysis, while the greyed out area denotes the extrapolated curves beyond the edges of the available data.

The plots in Fig. 7.1 reveal two challenges: The first is that large changes are happening at the Li CE (green lines) as a function of voltage, an electrode which is often considered to behave in a constant manner. The second is that deconvolution of the half cell impedance from that of the individual electrodes is not straightforward.

## 7.2 DRT of half and symmetric cells

While DRT can give information about the polarization processes that appear in the impedance spectrum, the analysis is limited by the necessity that the data is complete (*i.e.* that the impedance is real as  $f = 2\pi\omega \rightarrow 0$ ).<sup>[70]</sup> For LIBs this presents a difficulty since low-frequency diffusion means that the EIS data rarely

converges and the timescales required means that experiments are often limited to  $10^{-2}$  to  $10^{-3}$  Hz in the low-frequency region. One possible workaround is to “pre-process” the EIS data by removing the diffusive tail.[50, 70] This is done by modelling the diffusive region using an EC and then simply subtracting it from the data in a manner similar to applying a baseline in *e.g.* X-ray diffraction. However - and similarly to the application of a baseline in other techniques - the choice of baseline has an influence on the rest of the data, especially for features close to where the baseline is large. A different method can be used, whereby the data is assumed to converge to the real axis even if the spectrum is incomplete.[69] The DRT spectrum can then be calculated without the need to choose a baseline. It is important to note that the DRT peak characteristics (size, shape and position) which appears in the low-frequency region as a result of this assumption is not an accurate description of the polarization process. The GP method employed here uses this assumption of convergence to the real axis, and while we present the full DRT spectrum (including the peak in the diffusive region) we do not use the DRT spectrum to extrapolate information about the low-frequency polarization processes.[69] The results of DRT deconvolution for half cell and symmetric cells at each of the four stop potentials can be seen in Fig. 7.2. The large peak in the low-frequency diffusion region is an artefact due to the method extrapolating beyond the data as well as data not converging to the real axis and should therefore not be included when discussing the DRT analysis. For clarity, this region has been greyed out. In each plot in Fig. 7.2 the Si/Si and Li/Li symmetric cells consist of one peak at about  $10^2$  and  $10^3$  Hz, respectively. These correspond to the  $\text{Li}^+$  diffusion through the solid electrode and the SEI, respectively.[50, 70, 72] The half cells consist of either a broad, shouldered peak (as in the case of 7.2a to 7.2c), or two distinct but overlapping peaks (Fig. 7.2d). This indicates that the half cell behaviour is comprised of both Li and Si contributions, but due to their close proximity these may not be resolvable by fitting separate loops in the EC. Interestingly, at 0.07V (Fig. 7.2b) the Li/Li symmetric cells and the half cells show a very large polarization, indicating that the impedance at this potential is strongly dominated by the Li CE behaviour. A final small peak exists in the low frequency range at about  $10^{-1}$  Hz which may be due to diffusion of  $\text{Li}^+$  in the electrolyte. The breadth of these peaks indicates that they are likely best described by using constant phase elements (Q) rather than capacitive elements (C). Q is given by:



$$Q = \frac{1}{(j\omega)^\alpha C} \quad (7.1)$$

where  $0 < \alpha \leq 1$ .

From the analysis of the DRT plots it is possible to conclude that the cells consists of three loops: the first describes the double-layer constant phase element  $Q_{SEI}$  and layer resistance  $R_{SEI}$  along with a Warburg diffusion  $W$  describing the electrolyte-SEI interface; the second loop describes the solid electrode behaviour, with  $Q_{dl}$  and  $R_{ct}$  describing the double-layer pseudo-capacitance and charge transfer polarization of the electrode/SEI interface, respectively;[111] and the final loop describes the polarization process of the cell.[50] For large cells with low impedance and contact resistances (between electrode material and current collector) induction effects also come into play, but for coin cells these can mostly be ignored. The cell resistance is the total resistance at  $f \rightarrow \infty$ , analogous to the  $iR$ -drop seen in the first few seconds of a galvanostatic charge-discharge (GCD) curve.[50] This is commonly referred to as the solution resistance  $R_{sol}$ , and because it is a series resistance it is not included in the DRT plots.

The DRT analysis results in two ECs to describe the behaviour of the Si/Si, Li/Li and half cell spectra, one incorporating a finite space Warburg  $W_o$  which describes the  $Li^+$  solid state diffusion, and the other incorporating a finite length Warburg  $W_s$  which describes the diffusion of  $Li^+$  through the SEI. The EC is shown in Fig. 7.3, with  $W_{o/s}$  representing either the finite space or the finite length Warburg. The EC with the lowest  $\chi^2$  was chosen to represent the half cell data. It should be noted that the  $\chi^2$  for both circuits was often very small ( $\sim 10^{-6}$ ), and the difference between  $\chi^2$  values varied by less than an order of magnitude. An example of this is given in the Appendix (A.21 on page 94) for an EIS spectrum taken on a half-cell at 0.2 V and fit to both ECs. Here, both ECs show quite a good fit, but the EC containing a finite space Warburg is slightly better, which can be seen in the high-frequency region of the plot.

At intermediate potentials (0.2 and 0.3 V) the solid-state diffusion behaviour is dominant over the thin-film behaviour, while at low and high potentials (0.07 and 0.48 V) the opposite is true. This could be because the highly lithiated and highly delithiated states have limited space for solid-state diffusion, and so the thin-film behaviour becomes dominating, either as a result of the SEI on the Si WE, or on the Li CE, or both. This matches the expectation from previous

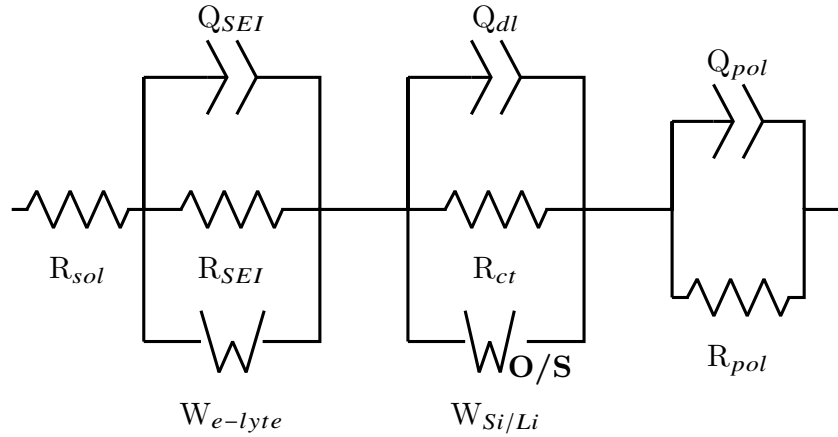


Figure 7.3: ECs of symmetric and half-cells determined by fitting to EIS data

research, which showed that the SEI cracks both during lithiation and delithiation.[50]

In cases where the exponent  $\alpha$  of the constant phase element  $Q$  is equal to 1, equation 7.1 becomes equivalent to that of a capacitor. This will in turn decrease the number of parameters needed for fitting of the data and give more easily interpreted results.

Analysis of the fitted results of the Si/Si EC and half cells within the relevant stop potentials (0.2 and 0.3 V) reveals that the  $Q_{SEI}$  parameter for the symmetric cells can be replaced with capacitors, but the same parameter for the half cells cannot. This is likely due to interference of the signal from the Li side of the half cell. The same result is seen in the high and low potentials (0.07 and 0.48 V) for the  $W_s$  EC, with the Li/Li  $Q_{SEI}$  behaving as a pure capacitor, and the half-cell showing mixed behaviour. This result is notable because it reduces the number of parameters needed to describe the symmetric cells, while simultaneously showing that the  $Q_{SEI}$  parameter of the half cells is made of a mixture of the two SEI layers.

Comparing exact values across these datasets is difficult, as the results vary not just with potential, but also with EC and cell type (symmetric and half cell). Further, the electrodes used are complex, containing different components which may have an influence on the extracted values. However, it is possible to check that some of the parameters of the fits match expected values for these types of

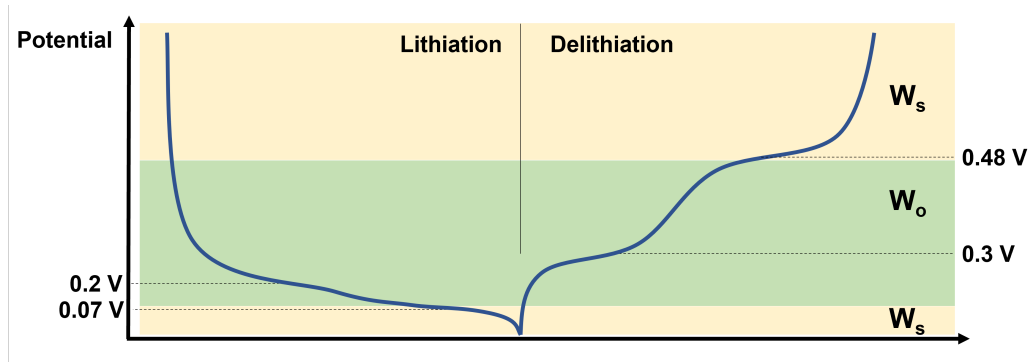


Figure 7.4: Schematic describing the behaviour of Si half cells at different points in the charge-discharge curve. The dominant diffusion behaviour is denoted on the right hand side.

cells. For example,  $R_{sol}$  was generally in the range of 2-6  $\Omega$  for both symmetric and half cells, and did not depend on the EC used. This range is in good agreement with values found in the literature.[50] Similarly, the Warburg describing the SEI-electrolyte interface is in the range 8-38  $\Omega$  for datasets containing Si electrodes, and 2.5-4  $\Omega$  for symmetric Li cells. This difference is likely due to the smaller surface area of the Li electrodes.

From the results of the fitting it is possible to draw some conclusions as to the behaviour of Si during lithiation and delithiation, and how this affects the impedance response. This is shown schematically in Fig. 7.4. Starting from the fully delithiated state and lithiating: at 0.2 V - which corresponds to the equilibrium position of the  $\text{Si} \rightarrow \text{Li}_2\text{Si}$  phase - there is both enough space and sufficient  $\text{Li}^+$  ions in the Si for the ions to move freely and be measurable by EIS on the coin cell level even in the half cell format. At 0.07 V where most of the electrode consists of  $\text{Li}_{3.5}\text{Si}$ , the high concentration of  $\text{Li}^+$  in the electrode reduces the number of mobile ions, and therefore the diffusion of  $\text{Li}^+$  through thin films such as SEI become dominating in the EIS spectrum. Further, the long timescales of the CCCV experiment mean that a thick SEI layer is able to grow on the Li CE, which then generates a strong impedance response. During delithiation the situation is very similar, with the end of the  $\text{Li}_{3.5}\text{Si} \rightarrow \text{Li}_2\text{Si}$  phase (at 0.3 V) showing a strong impedance signal from  $\text{Li}^+$  mobility in the Si, and the highly delithiated  $\text{Li}_2\text{Si} \rightarrow \text{Si}$  phase at 0.48 V showing very little signal from the  $\text{Li}^+$  in the Si, allowing the surface diffusion effects to dominate once again. This is similar to the ion mobility

effects seen in LEDs.[112] The decreased impedance of the Li CE is likely due to the decreased overpotential during deposition (*i.e.* during delithiation of the Si electrode) *vs* stripping (*i.e.* during lithiation of the Si electrode).[113]

The results obtained in this work show that it is necessary to exercise caution when studying the behaviour of high loading Si half cells. At or near the fully lithiated and delithiated states the Li CE contributes significantly to the impedance of the cell, and so SEI impedances from the Li CE can easily be misidentified as belonging to the Si WE. Should an EIS spectrum be desired e.g. at the end-of-life, it is therefore recommended to either use symmetric cells (by using at least two cycled cells), or to perform EIS at one or more potentials in the cycle, with emphasis on the intermediate potentials where the Li CE contribution is limited.

## Chapter 8

# Empirical GCD analysis of commercial silicon materials

Having determined that the Li counter electrode influences the behaviour of EIS data as a function of potential, it is now possible to make further assessments on the behaviour of Si delithiation in half cell format. In this work the techniques and methods used in chapters 6 and 7. The fitting function presented in equation 2.8 on page 14 is applied to electrodes made using a commercially available Si material, and the results are compared to data from half cell EIS experiments. The commercial material presented in this chapter differs from those of previous chapters, partly because the fitting function should be shown to be independent from the chosen material, and partly for the practical reason that this material showed superior performance in terms of cycle life to other Si materials under consideration.

### 8.1 GCD fitting of commercial Si

Inspection of the GCD curves during the three formation cycles of the commercial Si revealed a number of phases consistent with graphite, indicating that the material contains a relatively large amount of carbon (C).[114] This change is shown in the appendices in Fig. A.22 on page 95. However, these phases quickly disappeared as cycling progressed and only the Si phases and a capacitive component were detectable in the GCD curves after formation. This capacitive component

was subtracted prior to GCD fitting by applying a linear baseline to the data. The reversible capacity of the first cycle was  $520 \pm 10$  mAh/g and the initial Coulombic efficiency (ICE) was  $74 \pm 0.4\%$ , indicating that the material likely contains some oxides such as  $\text{SiO}_x$ . Both of these values are slightly lower than those supplied by the manufacturer (655 mAh/g and 83.7%, respectively), but this is likely due to the somewhat higher cut-off potential used for lithiation in these experiments than those recommended by the manufacturer. This also means that the majority of the ICE loss can be ascribed to Si-related side reactions occurring above 0.05 V, with the missing capacity belonging to the graphite below 0.05 V. The results presented here should therefore not be used to judge the quality of the chosen Si material, but rather be treated as a general study into the behaviour of any given Si material.

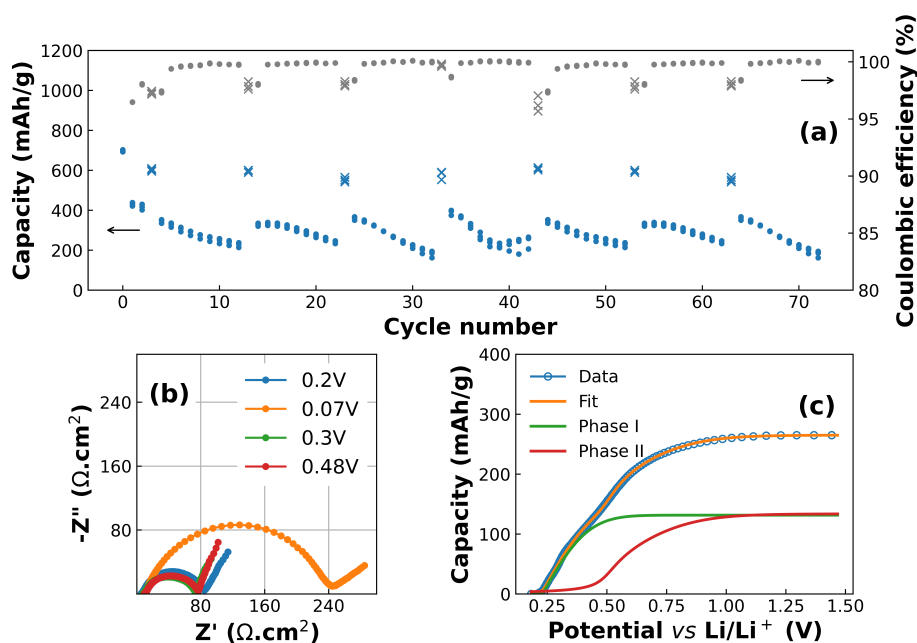


Figure 8.1: **(a)** Capacity (blue) and Coulombic efficiency (grey) as a function of cycle life. The crosses denote the slow cycles used for generating EIS spectra, while the points denote the faster cycles used for GCD fitting. **(b)** EIS spectra generated at 4 potentials in the GCD curve. **(c)** An example of the fitting function applied to the GCD curves along with the shapes of the individual phases.

Fig. 8.1 shows the results of the electrochemical experiments. Fig. 8.1a is a

plot of the capacity and CE as a function of cycle number. The crosses denote the total capacity of the slow CV charging and discharging step used for the EIS experiment (shown in Fig. 8.1b), while the points denote the much faster C/3 cycles. The reversible capacity is relatively low compared to pure Si (3579 mAh/g),<sup>[115]</sup> indicating that the material consists of a significant proportion of graphite. The cycles at C/3 show that the capacity of the electrodes fades quite quickly over the course of each group of 10 cycles, but that this capacity recovers almost completely after a slow cycle. This indicates that the cell capacity loss is not completely irreversible, at least in the short term. The CE of the slow CV cycle is quite consistently 2-2.5 % lower than the much faster C/3 cycles (97.5 % *vs* >99.5 %) indicating incomplete delithiation of the Si electrode. The exception to this rule is the fast cycle immediately after each slow cycle, which has a CE similar to that of the preceding slow cycle. An example of the EIS spectra collected during the slow cycle (denoted by crosses in Fig. 8.1a) is given in Fig. 8.1b. This shows how the EIS changes depending on the potential, with the spectrum at 0.07 V in particular showing a very large impedance loop due to the Li (CE).<sup>[50, 113, 116]</sup> Fig. 8.1c shows an example of one of the C/3 cycles in Fig. 8.1a after baseline subtraction against the potential (*vs* Li/Li<sup>+</sup>). The orange line denotes the fit of equation 2.8 to the data and the offset red and green lines correspond to phases I (equation 2.1) and II (equation 2.2), respectively. As was the case in chapter 6, the number of phases  $n = 2$  and the weighting parameter was found to be  $w_I = 1$  so that phase I was entirely skew-Gaussian limited. The raw GCD curve, together with the fit and residual can be found in Fig. A.23 on page 96 in the appendices. The residual shows an excellent fit to the data, with the difference between the fit and the data consistently below 1 %.

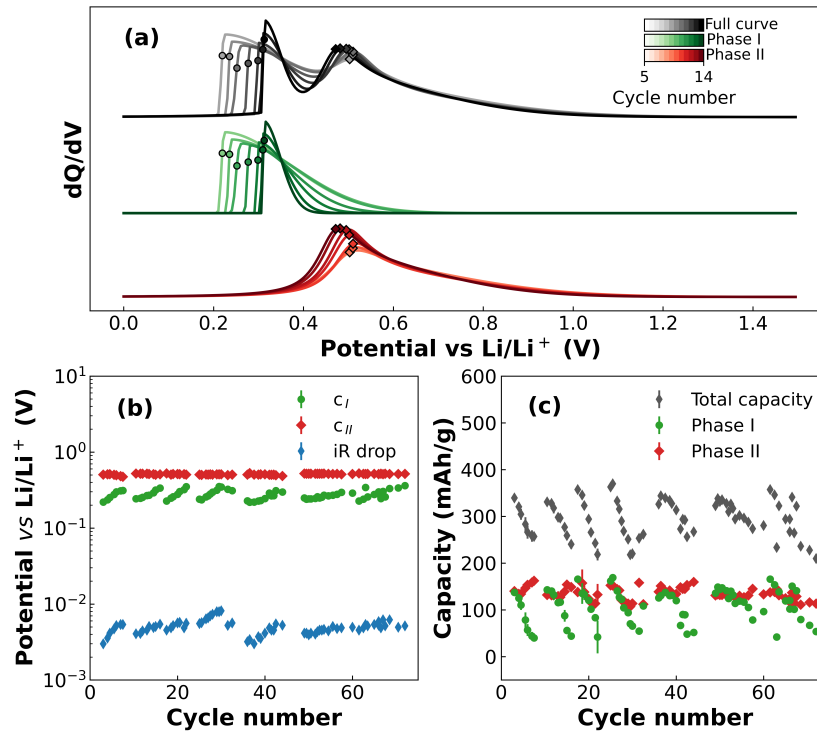


Figure 8.2: Results of fitting equation 2.8 to the GCD data. **(a)** Total  $dQ/dV$  of the first ten cycles at  $C/3$  (grey lines) and the component phases (green and red for phases I and II, respectively). Darker lines correspond to later cycles. The points and diamonds denote the location of the apparent equilibrium potentials  $c_I$  and  $c_{II}$ , respectively. **(b)** Comparison between the  $iR$  drop immediately after the start of delithiation and the apparent equilibrium potentials  $c_I$  and  $c_{II}$ , as a function of the cycle number. **(c)** Total capacity of the cells along with the capacities of the individual phases, as a function of cycle number.

Results of fitting equation 2.8 to the fast GCD curves (shown in the appendix in Fig. A.24 on page 97) is given in Fig. 8.2. Fig. 8.2a shows the  $dQ/dV$  curves of the first group of 10 cycles at  $C/3$ . The full spectrum is shown as grey curve, while the phases are offset for clarity. The points and diamonds correspond to the apparent equilibrium potentials  $c_I$  and  $c_{II}$ , respectively. This shows large changes in phase I as cycling progresses with  $c_I$  being pushed to higher potentials, causing narrowing of the phase and a decrease in the capacity (*i.e.* the area under the curve). Conversely, phase II is stable with a relatively small decrease in  $c_{II}$  and



an associated increase in capacity as a function of cycling, as shown in Fig. 8.2b and 8.2c, respectively. Fig. 8.2b shows the equilibrium potentials  $c_I$  and  $c_{II}$ , along with the iR drop (calculated by taking the difference in potential between the 0<sup>th</sup> and 2<sup>nd</sup> datapoints), while Fig. 8.2c shows the total capacity along with the capacities of the phases. From Fig. 8.2b it can be seen that the apparent equilibrium potential of phase I,  $c_I$ , is proportional to the iR drop  $V_{iR}$ . Indeed:

$$\frac{c_I}{V_{iR}} \approx 60 \quad (8.1)$$

which results in a reduced  $\chi^2$  of about 0.02. However, this relationship fails at later cycles, indicating that other factors are affecting the relationship between  $c_I$  and  $V_{iR}$ . Nevertheless it is clear that  $V_{iR}$  has a large effect on the behaviour of phase I. By comparison, the apparent equilibrium potential of phase II ( $c_{ii}$ ) is almost constant with repeated cycling, indicating that  $V_{iR}$  is not acting upon it in the same manner. The increase in  $c_I$  is correlated with the decrease in total capacity of phase I as shown in Fig. 8.2c. This shows that the capacity decrease of each batch of 10 cycles mostly stems from the drop in capacity of phase I, with the capacity of phase II remaining almost constant. The small increase in capacity of phase II seen at the end of each of the batches may be due to the model attempting to compensate for the large loss of capacity of phase I.

The results of the fitting equation show that the total capacity of the Si material is strongly affected by the position of phase I, and that this can be correlated to the iR drop  $V_{iR}$ . The fact that this effect is somewhat reversible by applying a slow cycle means that  $V_{iR}$  is not only due to irreversible resistance growth such as SEI on the Si electrode and the overpotential of the Li CE, but also due to reversible resistance growth in the potential region of phase I. The ability of the fitting function to discern and measure these dynamic changes in the cell is therefore a valuable addition to the toolset available for studying Si electrochemistry.

## 8.2 EIS and DRT of commercial Si

Determining the origin of this reversible resistance growth is very important to interpreting the data and understanding the behaviour of Si half cells such as these. By performing EIS at the maxima of the  $dQ/dV$ , it may be possible to glean some insight into the behaviour of the cells at these potentials. The long (20 h) CV

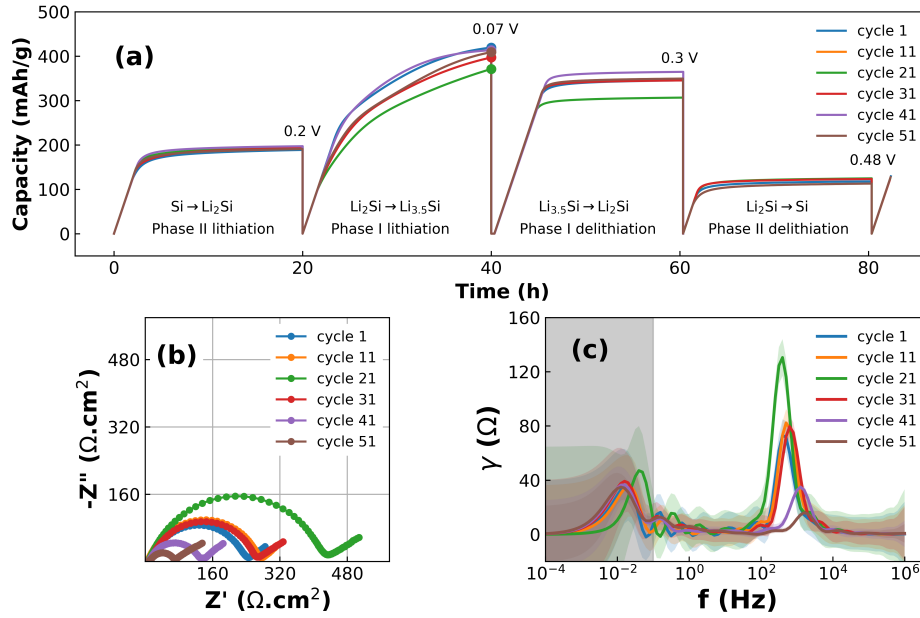
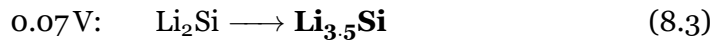


Figure 8.3: Results of performing EIS on Si half cells. **(a)** The capacity as a function of time for the slow cycle used for EIS. The circles at 40 h denote the point in time at which the EIS spectra displayed in **(b)** were collected. **(b)** EIS spectra taken at the end of the 0.07 V step. **(c)** DRT of the EIS spectra shown in **(b)**. The shape of the curves in the greyed out area are artefacts of the analysis.

step used in the experimental setup of the EIS cycle is intended to ensure that the composition of the Si electrode is at equilibrium and that the Si in the electrode is almost completely made up of the product of the target phase (shown in bold):



This can be verified by looking at the capacity of the cycle as a function of time, as shown in Fig. 8.3a. This shows that while most of the reactions have reached equilibrium at the end of the 20 h CV step (as evidenced by the slope tending towards 0), the reaction shown in equation 8.3 is not only far from equilibrated

even after 20 h, but also varies significantly as cycling progresses. This behaviour is reflected in the EIS, which shows an increase in the impedance at the same cycle (cycle 21) as the drop in capacity, as well as subsequent decrease in impedance as the capacity recovers at later cycles. The EIS spectra generated at equation 8.3 are shown in Fig. 8.3b, which show a large increase in impedance during the first 30 cycles, followed by a sharp decrease in subsequent cycles. This confirms that the capacity decrease seen in Fig. 8.2 is due to the impedance of phase I during lithiation. Having shown that a reversible resistance growth contributes to the drop in capacity of Si half cells, the question of the origin of this resistance remains. This can be elucidated by analysing the distribution of relaxation times (DRT).[50, 69, 116] DRT analysis is a method for de-convoluting the time constants  $\tau$  of an EIS spectrum. This technique relies upon the assumption that the response of an electrochemical system to a perturbation (such as an oscillating potential) decays exponentially at a particular distribution of timescales.[69] This means that an EIS spectrum can be transformed into a set of peaks corresponding to frequencies at which physical processes occur. For near-ideal processes such as corrosion on a flat surface which can be described by a resistor (R) and a capacitor ( $Z_C$ ) in parallel, the peak height and the frequency  $f = 1/(2\pi\tau)$  can be used to calculate R and  $Z_C$ , respectively. However in most cases the relaxation time of a process is a distribution rather than a single value, and so the width of the peak is increased. It should also be noted that DRT analysis requires the EIS spectrum to converge to the real impedance at  $f = 0$ . Since low-frequency diffusion effects are often present in LIBs this is rarely the case for real systems. Hence, the low-frequency region needs to be removed from consideration, either through subtraction from the data using a model equivalent circuit, or by requiring the analysis to converge to the real impedance.[50, 69] Here we employ the second method and use a Gaussian Process developed earlier to perform DRT analysis on our data.[69] The results of the DRT analysis at 0.07 V are shown in Fig. 8.3c, and these show large changes in the peak at  $10^3$  Hz associated with the Li CE.[50, 116] Over the course of the first 21 cycles this peak grows and shifts to slightly lower frequencies, but after this point the trend reverses and the peak shrinks and shifts to higher frequencies. This may be explained by crack formation in the SEI leading to reduced  $\text{Li}^+$  diffusion resistance.[117] This also explains the shift in frequency of the peak, as decreased inhomogeneity also increases the frequency at which  $\text{Li}^+$  transport processes occur.[50] This, combined with a lack

of a strong Si peak normally found at about  $10^2$  Hz means that the majority of the impedance behaviour of the half cells at a potential of 0.07 V can be ascribed to the impedances of the Li CE. However, given that the impedance decreases after the 21<sup>st</sup> cycle, the Li electrode cannot account for the reversible resistance increase seen from the GCD data which suggests that the reversible resistance stems from the Si electrode.

One possible source of this reversible resistance growth may be due to the progressive loss of  $\text{Li}^+$  ions from the Si electrode.[47, 107] The discrepancy between the capacity fade and the high CE of the fast cycles shown in Fig. 8.1a, together with the reversible nature of the fade indicate that the cause is due to the lithiation step rather than the delithiation. Also, the fade is not due to excess SEI formation, as this would be reflected in a lowered CE. The results of the fitting shown in Fig. 8.2c indicate that the capacity loss is due to phase I, which means that the lithiation of this phase is hindered at fast cycles. During fast lithiation the irreversible resistances of the cell (i.e. the SEI + Li CE overpotential + other resistances) result in a polarization of the cell which causes phase I (equation 8.3) to not become fully lithiated. This therefore also causes a decrease in capacity of phase I during delithiation (equation 8.4), which is measured by equation 2.8. Since the resistance of the Si electrode is inversely proportional to the Li concentration in Si, the subsequent cycle experiences an increased resistance, and therefore decreased lithiation. This leads to a negative feedback loop wherein the amount of  $\text{Li}^+$  inserted into phase I continuously decreases. Applying a slow cycle such as the one employed for studying the EIS increases the  $\text{Li}^+$  content in the electrode and decreases  $V_{iR}$ , which “resets” the Si electrode and therefore allows the capacity to recover.

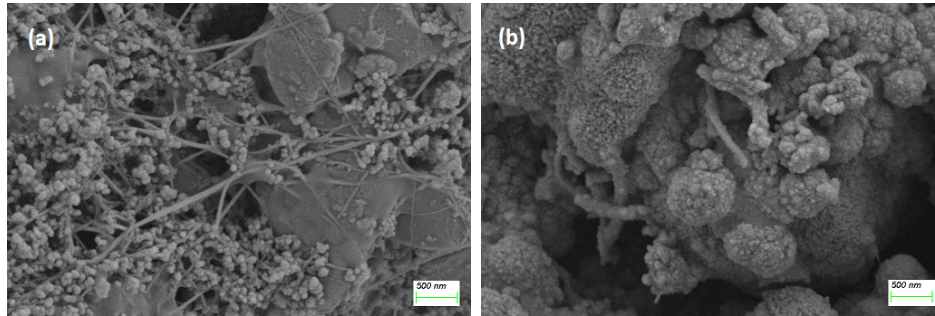


Figure 8.4: SEM images of Si electrodes **(a)** before and **(b)** after cycling.

This indicates that reducing the cell resistances may substantially improve the performance of Si materials independently of the material itself, and that the capacity fade is a result of both reversible and irreversible resistances. As seen from the EIS results at low potentials *vs*  $\text{Li}/\text{Li}^+$ , the Li CE accounts for a large portion of this resistance. Thus, high-capacity materials, and especially those with high electrode loading will be artificially hindered by the Li CE due to the large current densities required to cycle at appreciable rates.[51] Further, constructing cells with higher areas will also likely increase the performance of Si cells purely through the decrease in area resistance.

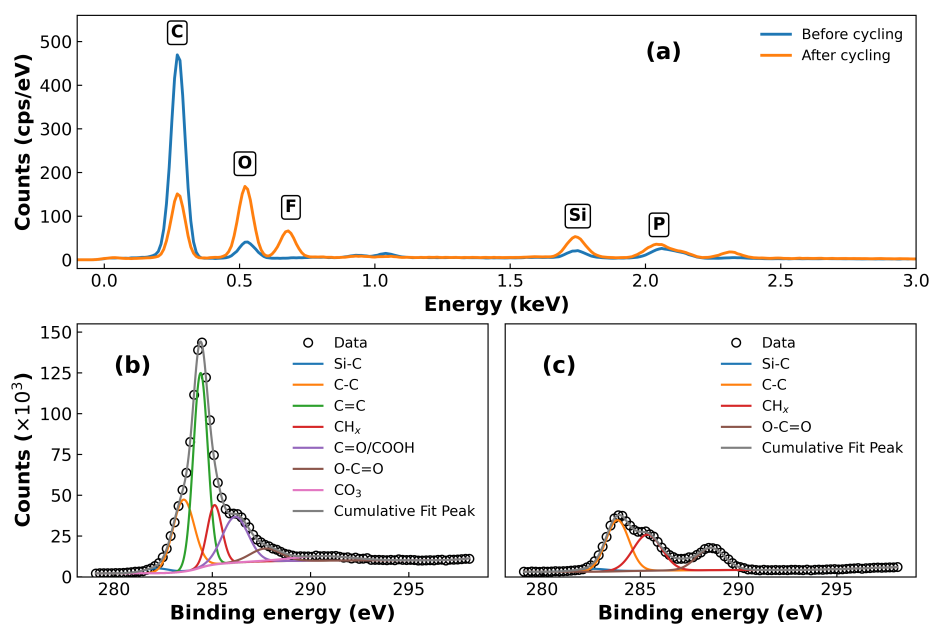


Figure 8.5: **(a)** Spot EDX of Si anodes before and after cycling. **(b)** XPS C1s spectrum of the Si anode before cycling. **(c)** XPS C1s spectrum of the Si anode after cycling.

Unfortunately, the dynamic nature of this resistance growth means that it is very difficult to measure it directly. The steady-state nature of experiments such as EIS and *ex-situ* experiments such as SEM/EDX and XPS means that they are only able to measure the irreversible resistances. Nevertheless, they are a valuable tool to gain a deeper understanding of the behaviour of the system. To show that the irreversible SEI resistance is growing on the Si electrode with time, SEM/EDX and XPS analysis was carried out on fresh, uncycled electrodes as well as electrodes disassembled at the end of cycling. The results of the SEM analysis can be found in Fig. 8.4. The uncycled electrode (Fig. 8.4a) shows how the Si electrode is made up of large micron-sized graphite/carbon particles, mixed with agglomerations of small spherical Si particles. The long fibres covering the surface are the CNTs added to the electrode to improve the conductivity. The cycled electrode in Fig. 8.4b is coated in a layer of SEI, indicating that the anode is at least partially responsible for the irreversible resistance increase seen in the GCD data. Spot EDX analysis (Fig. 8.5a) from SEM on cycled and uncycled electrodes shows a reduction of the C peak and an increase in the oxygen (O), fluorine (F) and phosphorus (P) peaks. This implies that the surface of the electrode is covered by inorganic O, F and P-rich species. These may consist of materials such as LiF, phosphates and lithium alkyl carbonates. This is consistent with the results of the XPS C1s spectra shown in Fig. 8.5b and c for the uncycled and cycled electrodes, respectively. Fig. 8.5b shows a large C=C graphite peak at 284.8 eV, as well as oxygen species such as carboxylic acids and ketones present on the surface of the graphite and other carbonaceous materials that make up the anode. The lack of a detectable C=C peak in the cycled electrode, shown in Fig. 8.5c, indicates that the graphite is obscured by the presence of a passivating SEI layer. This presence of  $\text{CH}_x$  and O-C=O groups correspond to the characteristic signature of lithium alkyl carbonates, primary components of SEI.[118, 119, 120]

The increased polarization observed in both the GCD fitting and the EIS experiments can therefore be explained in part by the excessive SEI growth often seen on Si electrodes.

The relationship between the irreversible and reversible resistances are shown schematically in Fig. 8.6. This shows how the irreversible resistances contribute to the polarization of the cell, which leads to reduced lithiation of phase I. The reduced  $\text{Li}^+$  concentration in phase I increases the resistance of the electrode, which leads to further decreases in lithiation.

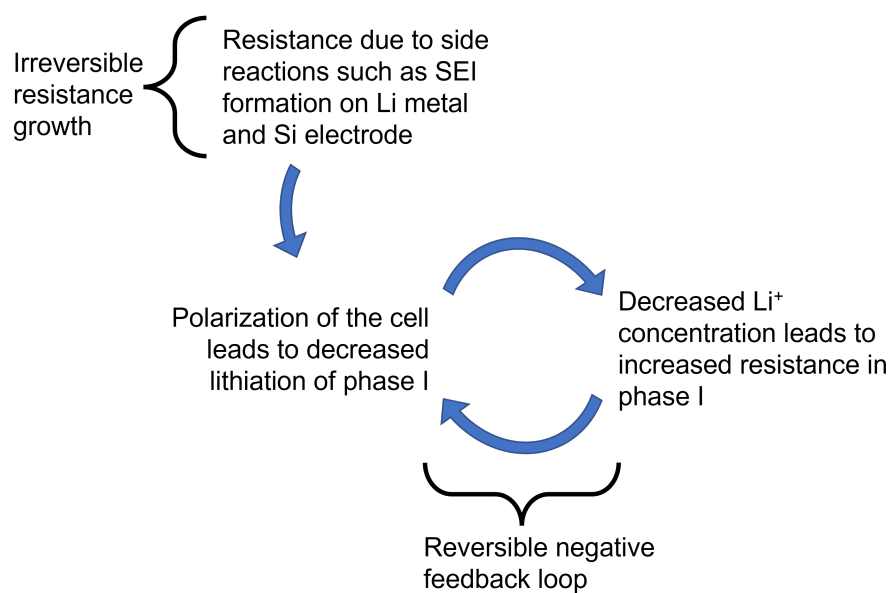


Figure 8.6: Schematic showing the process of irreversible and reversible resistance growth, and its relationship to the fast capacity fade seen in Si half cells.



## Chapter 9

# Concluding remarks

This study focussed on the behaviours of Silicon during cycling and the data analysis methods used to perform these studies. First, three silicon nanoparticle materials containing concentrations of P of 1.5, 3.2, and 5.2 at% were synthesised to compare the electrochemical behaviour of  $\text{SiP}_x$  to pure Si NPs. To decouple lithiation and delithiation behaviour the charge and discharge steps were performed at asymmetric C-rates. Delithiation was found to be enhanced for  $\text{SiP}_x$  at high C-rates compared to pure Si, while the lithiation rate capability was only better for low C-rates. GITT and EIS were used to validate the rate behaviour and showed that the diffusivity of  $\text{Li}^+$  in  $\text{SiP}_x$  is significantly greater than for pristine Si. A hypothesis is proposed whereby  $\text{Li}_3\text{P}$ ,  $\text{Li}_2\text{SiP}_2$  or other phosphidosilicates species formed during cycling could be responsible for the increased diffusivity and enhanced delithiation rate in  $\text{SiP}_x$ . However, the evidence for this is found to be inconclusive.

The reliance on  $dQ/dV$  for studying Si behaviour revealed a need for better data analysis tools. Therefore, Two datasets of externally produced data consisting of delithiation cycling data from a thin film and a nanowire study performed by different groups, were analysed using an empirical cumulative distribution function consisting of a skew pseudo-Voigt. Both datasets featured Si half cells cycled in the amorphous region of Si and the skew pseudo-Voigt was applied to each of the two electrochemical phases  $\text{Li}_{3.5}\text{Si}$  (phase I) and  $\text{Li}_2\text{Si}$  (phase II). The fitting function was found to give excellent fits to both datasets at C-rates far above equilibrium conditions, and was able to determine differences and similarities between the two morphologies studied. Phase I of the NW samples were found

to be less skew than the TFs, indicating faster delithiation. However, loss of contact between NWs and excess SEI growth also lead to increased resistances of the electrodes, in particular for the less electronically conductive phase II. Analysis of the results showed that the fitting function could determine the contribution to capacity of each of the two phases involved in the delithiation of amorphous Si and showed that this is strongly dependent on morphology and cycling rates, with NW electrodes exhibiting lower contribution to capacity than expected from phase II due to greater electrode resistance, despite larger surface area available for delithiation. Further, the results were shown to be useful in determining the extent of the reservoir effect of the cells, and showed that the thin films exhibited greater reservoir at the end of the delithiation step compared to the nanowires. This was presumed to be due in part to the greater delithiation path length, and partly to the higher C-rate used in cycling.

However, the use of Li as a counter electrode is known to impact the results of electrochemical tests. To disambiguate the Li counter electrode from the Si working electrode, a set of Si electrodes with commercial level loadings were analysed by means of EIS, both as half cells and their Si/Si and Li/Li symmetric cell equivalents. The cells were tested at four different potentials corresponding to the equilibrium potentials of the lithiation and delithiation phases. Analysis of the resulting EIS spectra by DRT showed that the half cells are described by a combination of the Si/Si and Li/Li symmetric cells, and that these are in turn best described by different ECs. The Si/Si symmetric cells are shown to fit a finite-length Warburg describing the solid-state diffusion of  $\text{Li}^+$  in Si, while the Li/Li cells are best described by a finite-space Warburg corresponding to the diffusion of  $\text{Li}^+$  through the SEI. The half cells are described either by the Si/Si or the Li/Li EC depending on the stop potential, with the high and low potentials showing Li/Li character, and the intermediate potentials showing Si/Si behaviour. Further analysis showed that both the Si/Si and Li/Li symmetric cell ECs could be simplified by replacing the two-parameter constant phase element  $Q_{SEI}$  with a single-parameter capacitive element  $C_{SEI}$ , but that the mixing of signals meant this could not be extended to the half cells. This work shows the importance of EIS as a technique for studying Si electrodes with high loading, as well the importance of carefully considering the behaviour of both electrodes in half cell EIS.

Finally, The empirical equations developed on model Si systems were applied to commercial materials. Commercial Si electrodes with high loading of

3.27 mAh/g were constructed in half-cell format and tested using GCD and EIS. A fitting function was applied to the delithiation steps, revealing that phase I, describing the reaction  $\text{Li}_2\text{Si} \rightleftharpoons \text{Li}_{3.5}\text{Si}$  is responsible for the fast but reversible capacity fade experienced by these cells. Further analysis of the data showed a relatively linear relationship between the position of phase I and the iR drop experienced by the cell at the start of delithiation, leading to the conclusion that the capacity fade is due to polarization of the cell. EIS and DRT performed near the positions of the phases showed that the reversible resistance growth came from the Si electrode. This was explained by the concept of a “negative feedback loop” whereby the large irreversible polarizations from the Si and Li electrodes decrease the  $\text{Li}^+$  concentration in phase I of the Si electrode. This leads to an increase in resistance of the Si electrode, which contributes to the polarization on the subsequent cycle. The irreversible resistance growth on the Si electrode was measured by performing SEM/EDX and XPS on uncycled and cycled electrodes. This work showcases the fitting function as a valuable technique for studying dynamic changes in commercial Si materials during cycling.



**Appendix A**

**Appendix**

Table A.1: Results from DFT simulation of  $\text{SiP}_x$

System	P concentration (atomic weight %)	P Substitution Energy $E_{sub}$ ( $\text{kJmol}^{-1}$ )	Li Insertion Energy $E_{insert}$ ( $\text{kJmol}^{-1}$ )
$\text{Si}_{64}$	0	–	66.58
$\text{Si}_{63}\text{P}$	1.6	1.93	42.45
$\text{Si}_{62}\text{P}_2$	3.1	2.90	61.65
$\text{Si}_{61}\text{P}_3$	4.7	6.75	91.66

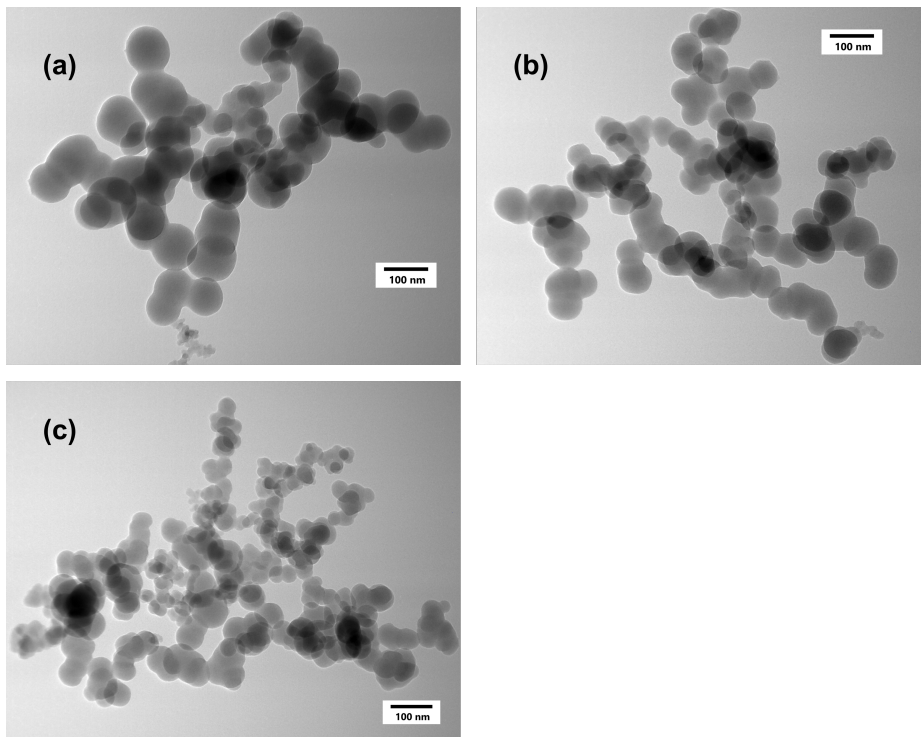


Figure A.1: TEM images of the four silicon samples, showing the micron-sized aggregates of SiNPs typical of silane decomposition. The four images are for a) P0, b) P1.5, c) P3.2. P5.2 is shown in Figure 1 in the main text

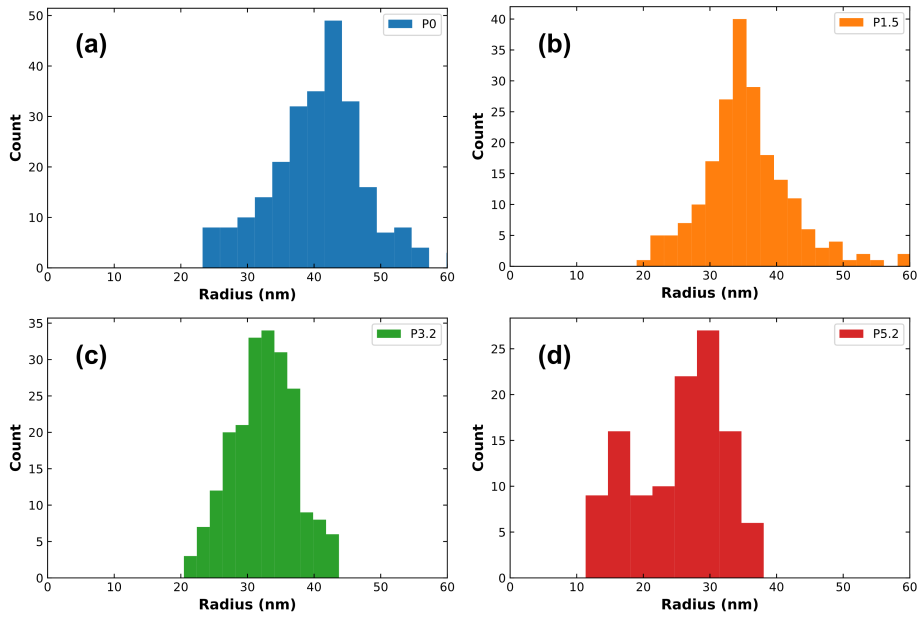


Figure A.2: Particle size distributions (counts) for SiP<sub>x</sub> NPs from TEM. a) P<sub>0</sub>, b) P<sub>1.5</sub>, c) P<sub>3.2</sub>, and d) P<sub>5.2</sub>.

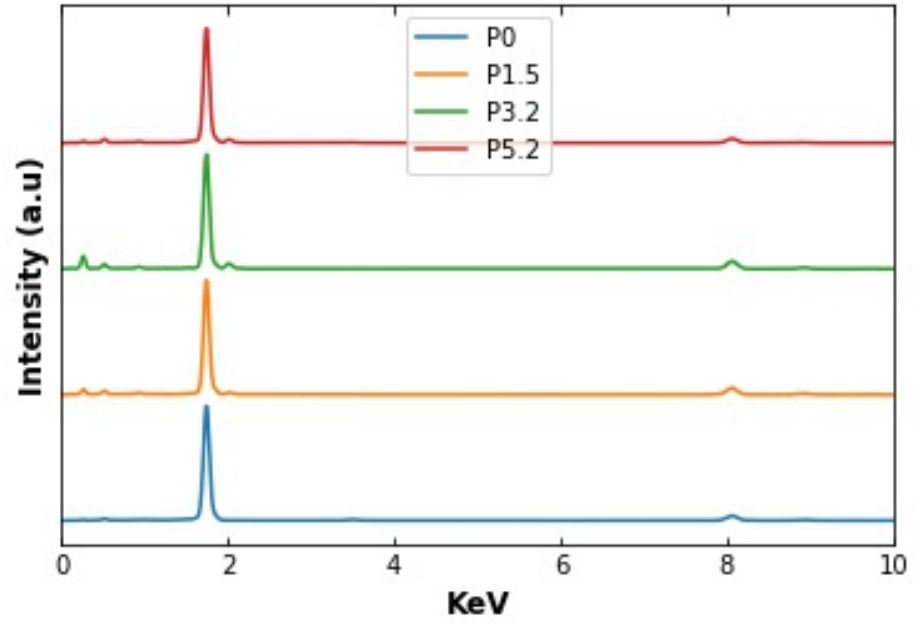


Figure A.3: EDS spectra for the 4 samples as determined from TEM. a) P<sub>0</sub>, b) P<sub>1.5</sub>, c) P<sub>3.2</sub>, and d) P<sub>5.2</sub>.

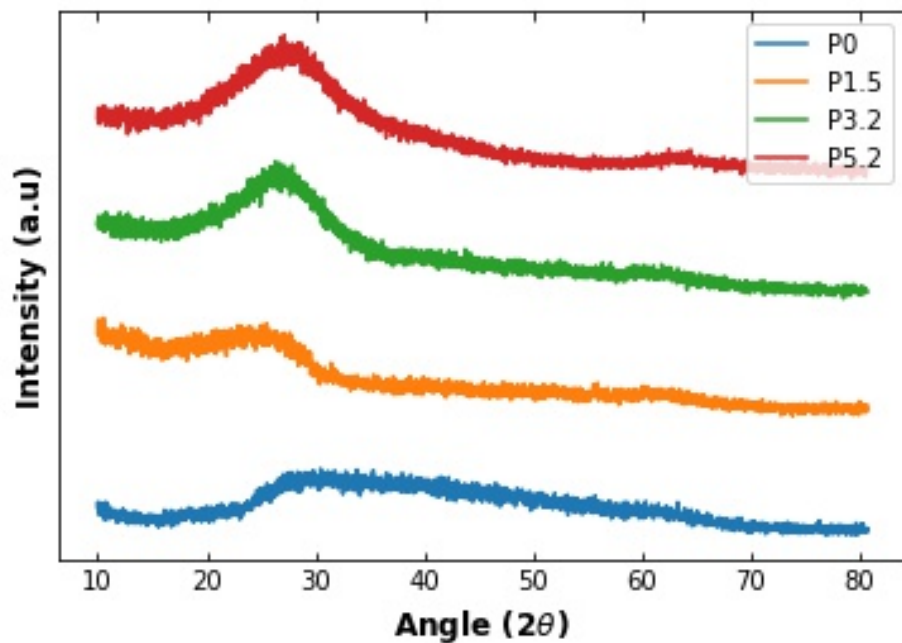


Figure A.4: XRD spectra for the 4 samples

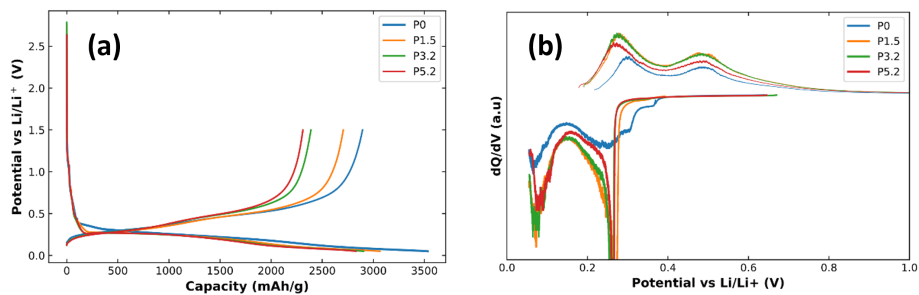


Figure A.5: Galvanostatic cycling of  $\text{SiP}_x$  alloy. (a) Voltage profiles of the 1<sup>st</sup> cycle; (b)  $dQ/dV$  profiles for the 1<sup>st</sup> cycle.



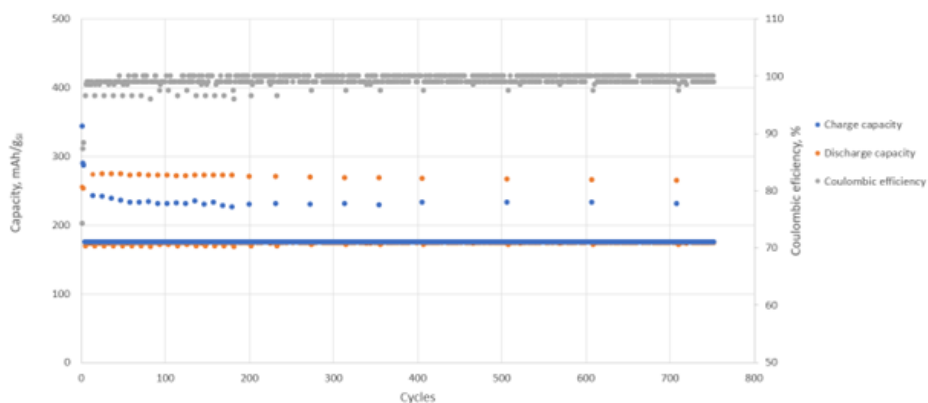


Figure A.6: An example of  $\text{SiP}_x$  / Active Carbon full cell. The  $\text{SiP}_x$  material used consists of 5 atomic % P in Si, equivalent to P5.2 in the text. The anode consists of 60%  $\text{SiP}_x$ , with the remaining 40% being made up of carbon black, conductive graphite, and sodium carboxymethylcellulose.

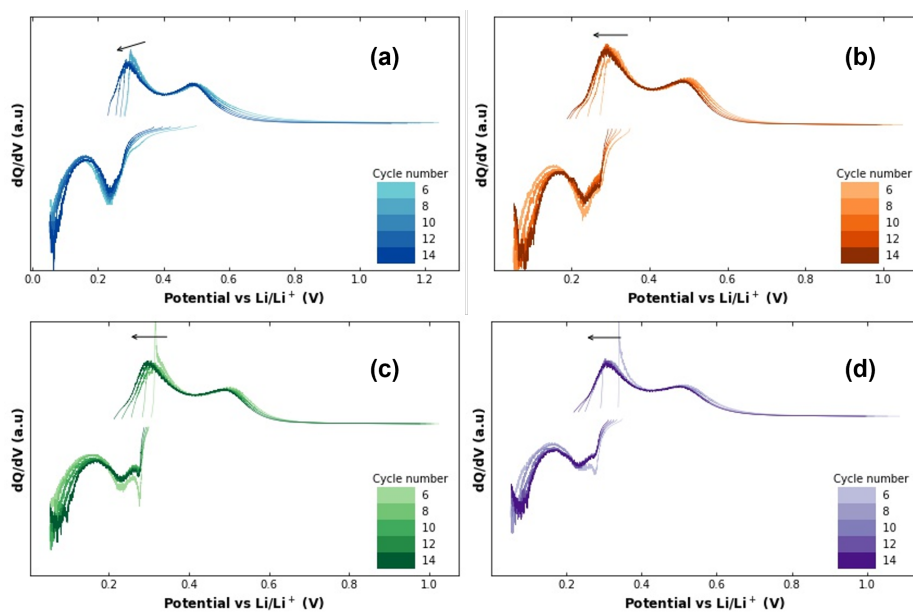


Figure A.7:  $dQ/dV$  for cycles 6-14 of the cyclic stability data presented in Fig. 5.1c. The arrows show the behaviour of the  $\text{Li}_{3.5}\text{Si}$  peak. (a) P0, (b) P1.5, (c) P3.2, (d) P5.2.

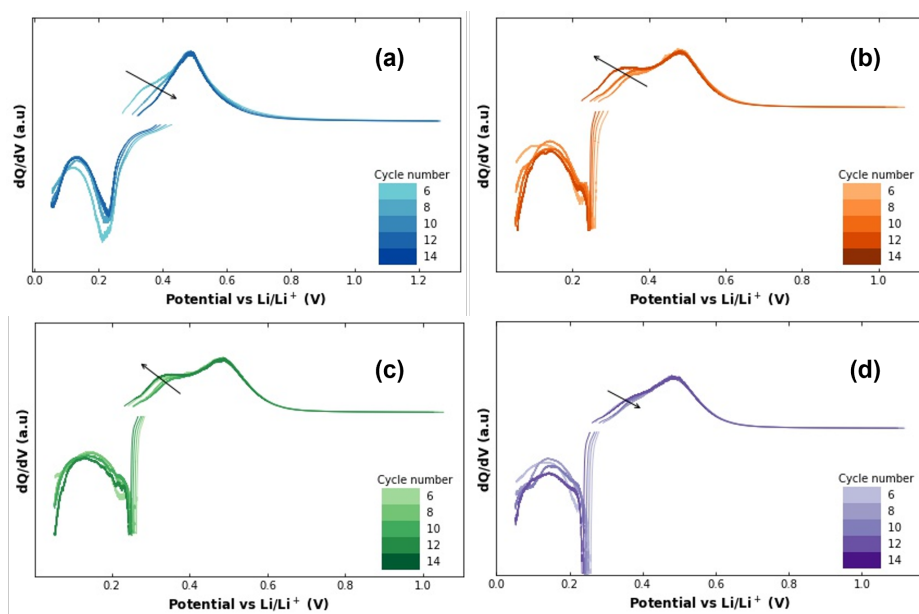


Figure A.8:  $dQ/dV$  for cycles 6-14 of the cyclic stability data presented in Fig. 5.1d. The arrows show the behaviour of the  $\text{Li}_{3.5}\text{Si}$  peak. (a) P0, (b) P1.5, (c) P3.2, (d) P5.2.

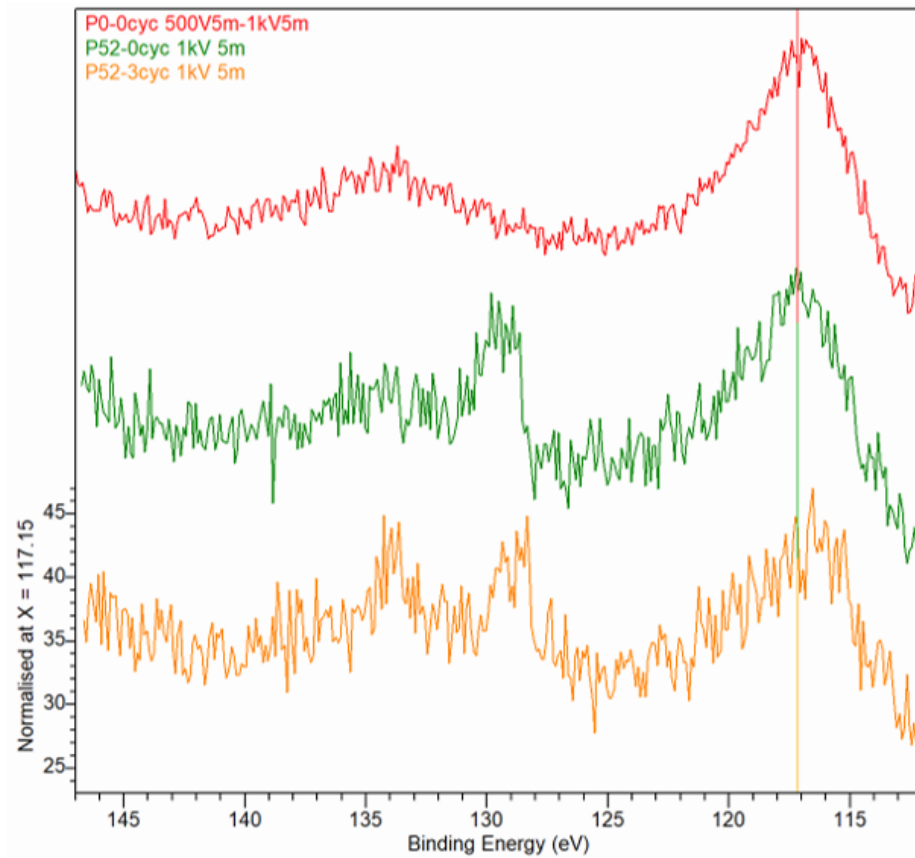


Figure A.9: XPS spectra for Electrodes before and after cycling, showing the P2p peak at 130eV. The middle (green) and bottom (red) spectra correspond to the P5.2 material before and after formation cycles, respectively. The top red line is the spectrum for the uncycled pure Si electrodes.

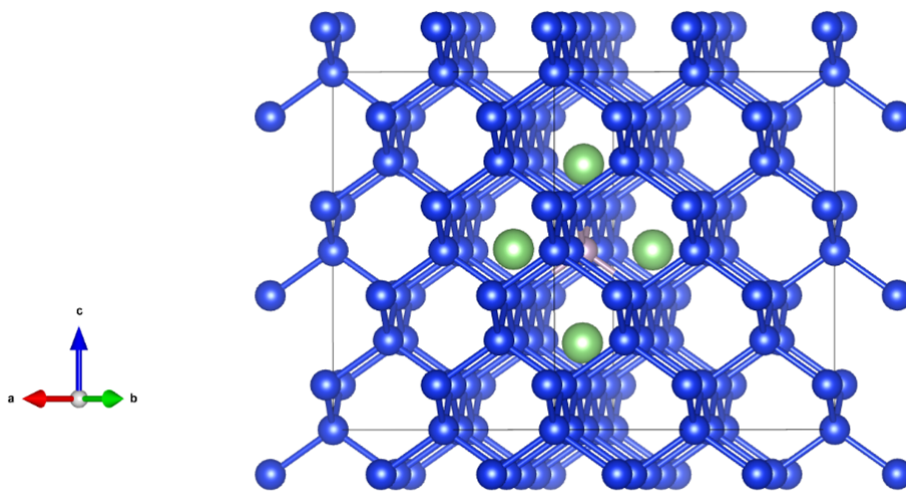


Figure A.10: Configuration of  $\text{Si}_{63}\text{PLi}_4$  (1.6% P concentration), where medium-blue, limegreen and mistyrose denote the Si, Li and P atoms, respectively

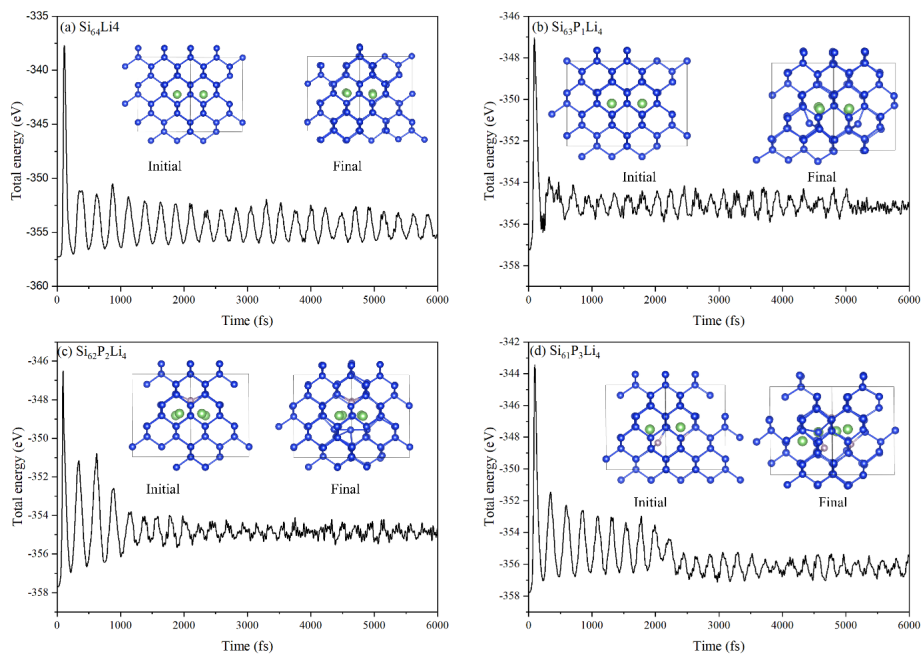


Figure A.11: Total energy variations of  $\text{Si}_{64}\text{Li}$ ,  $\text{Si}_{63}\text{P}_1\text{Li}_4$ ,  $\text{Si}_{62}\text{P}_2\text{Li}_4$  and  $\text{Si}_{61}\text{P}_3\text{Li}_4$  as a function of time for the AIMD simulation. The respective initial and final structures are shown as insets

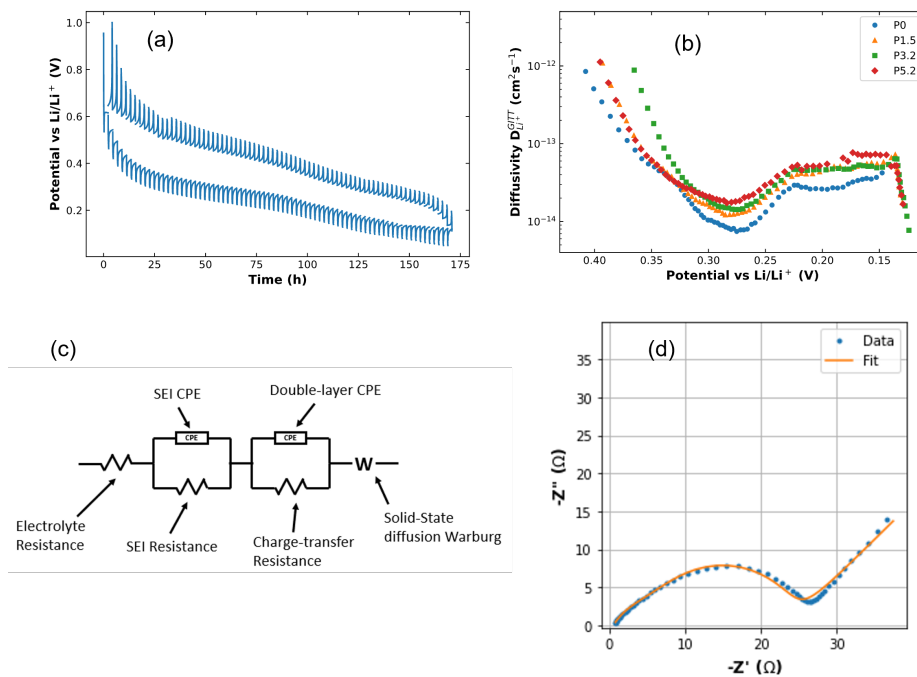


Figure A.12: (a) Typical GITT curve, in this case for P3.2. (b) Diffusivity of lithiation process for the four samples. (c) Equivalent circuit used for EIS fitting. (d) Example of EIS curve with fit. The EIS spectra were fitted to the equivalent circuit shown in (d) using modulus weighting, which gave low error values (1-5%) for the Si-related charge transfer loop and the Warburg diffusion

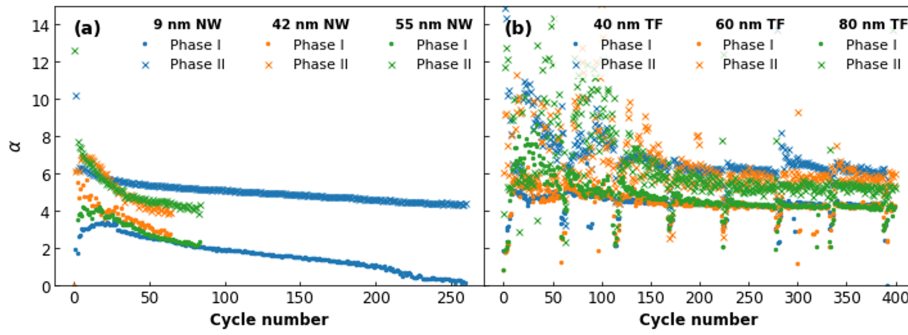


Figure A.13: The skew parameter  $\alpha$  for phases I and II for (a) NWs and (b) TFs, as a function of the cycle life.

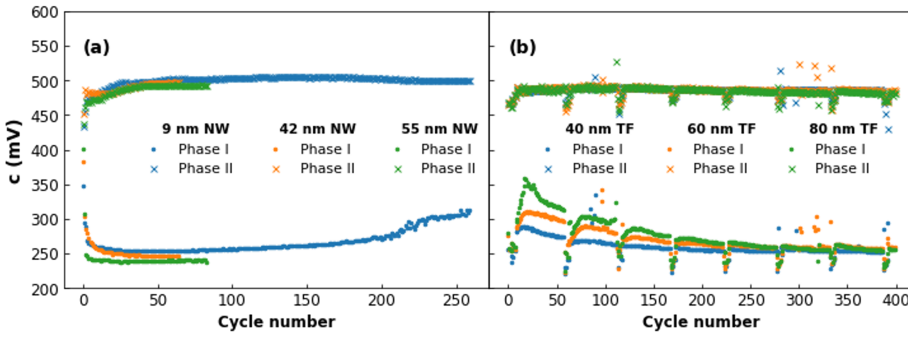


Figure A.14: The equilibrium potential  $c$  for phases I and II for (a) NWs and (b) TFs, plotted as a function of the cycle life.

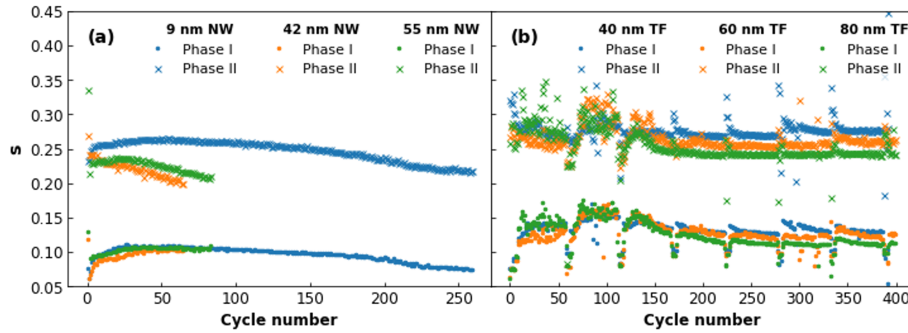


Figure A.15: The scale parameter  $s$  of the Gaussian component for phases I and II for (a) NWs and (b) TFs, plotted as a function of the cycle life.

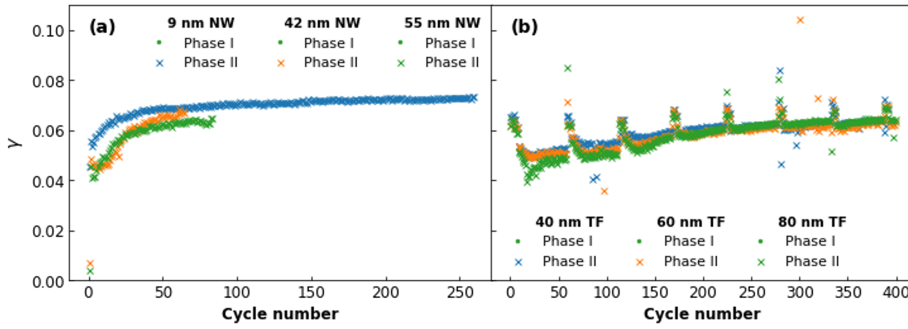


Figure A.16: The scale parameter  $\gamma$  of the Lorentzian component for phase I for (a) NWs and (b) TFs, plotted as a function of the cycle life.

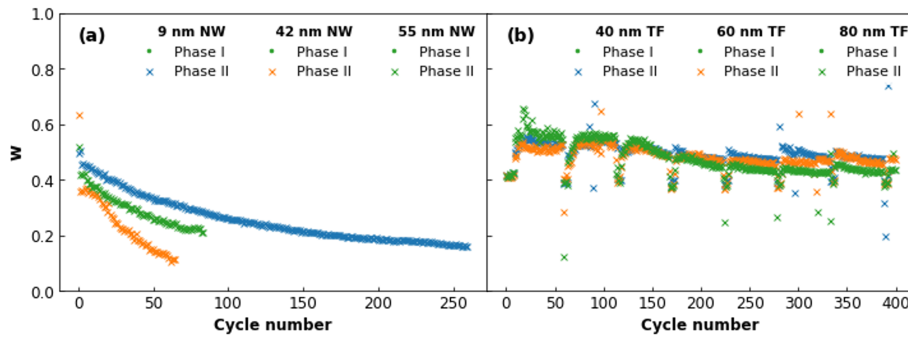


Figure A.17: The weighting parameter  $w$  for phases I and II for (a) NWs and (b) TFs, as a function of the cycle life.

Electrolyte uptake and porosity was calculated using the formulae:

$$\text{Electrolyte uptake (\%): } \frac{W_{elec} - W_{dry}}{W_{dry}} \times 100 \quad (\text{A.1})$$

$$\text{Porosity (\%): } \frac{W_{PC} - W_{dry}}{\rho_{PC} V_{dry}} \times 100 \quad (\text{A.2})$$

where  $W_{dry}$  is the mass of the dry electrode.  $W_{elec}$  and  $W_{PC}$  are the masses of the electrodes after soaking for 24 h in electrolyte and propylene carbonate (PC, Tinci), respectively.  $\rho_{PC}$  is the density of PC (1.205g/cm<sup>3</sup>) and  $V_{dry}$  is the volume of the dry electrode. The masses of the soaked electrodes were measured after removing from the solution and dabbing them with paper tissue to remove excess liquid. All experiments took place in an Argon-filled glovebox.



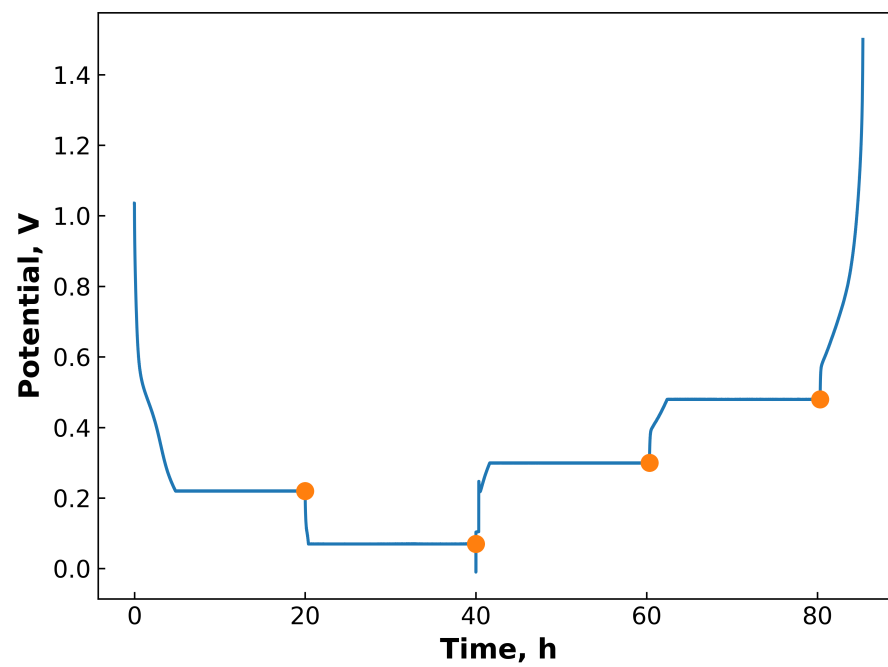


Figure A.18: An example of the cycle used for preparing the electrode for EIS, showing how the CCCV procedure is set to each “stop” potential. EIS was taken at the end of each CCCV step, as shown by the orange circles.

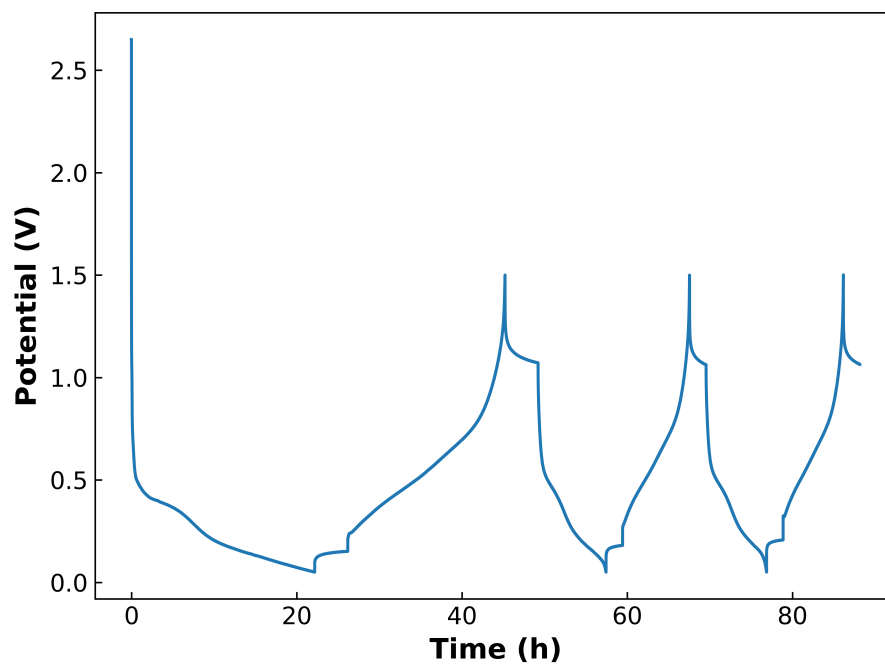


Figure A.19: An example of the formation cycles performed on Si half-cells used in this study. The first cycle was performed at  $1/20$  C, while the second and third cycles were performed at  $1/10$  C

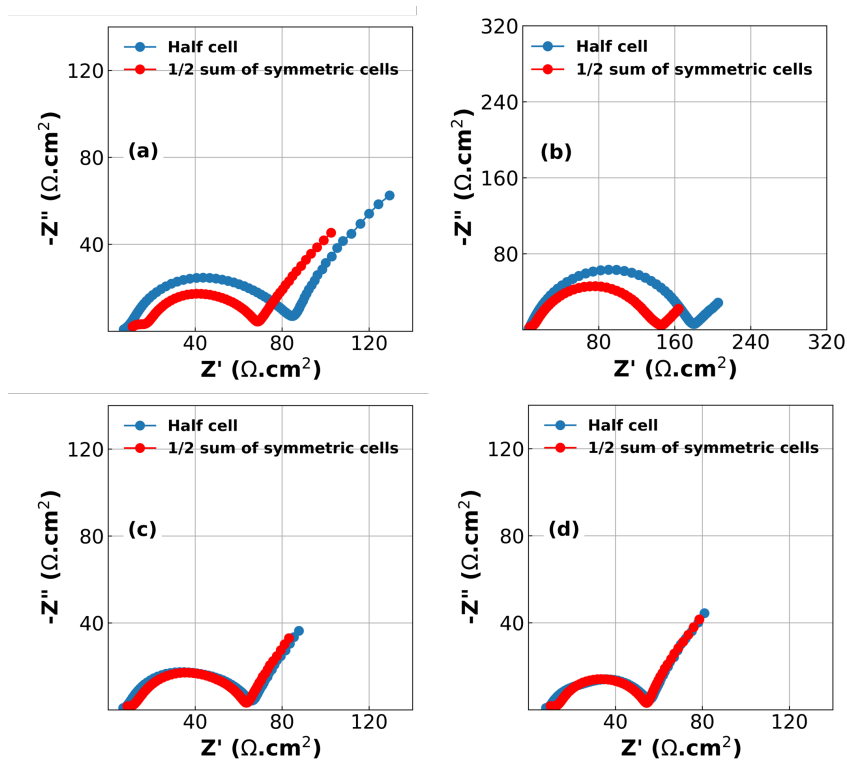


Figure A.20: EIS spectra of half cell (blue points) and the half-sum of the equivalent symmetric cells (red points) (a) 0.2 V in the lithiation step; (b) 0.07 V in the lithiation step; (c) 0.3 V in the delithiation step; (d) 0.48 V in the delithiation step.

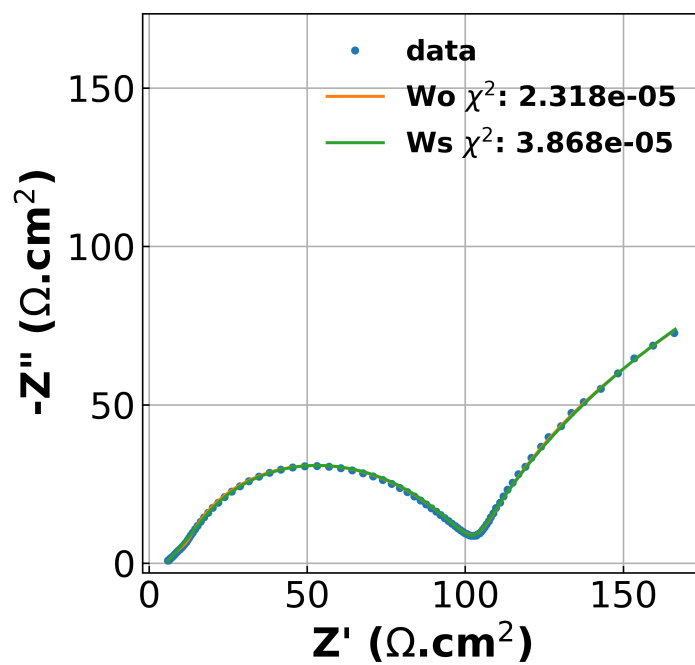


Figure A.21: Example EIS spectrum of a half-cell taken at 0.2 V, showing how the ECs given in 7.3 fit the data. The reduced  $\chi^2$  is given in the legend for each EC, with “ $W_o$ ” corresponding to the EC containing a finite space Warburg, and “ $W_s$ ” corresponding to the EC containing a finite length Warburg.

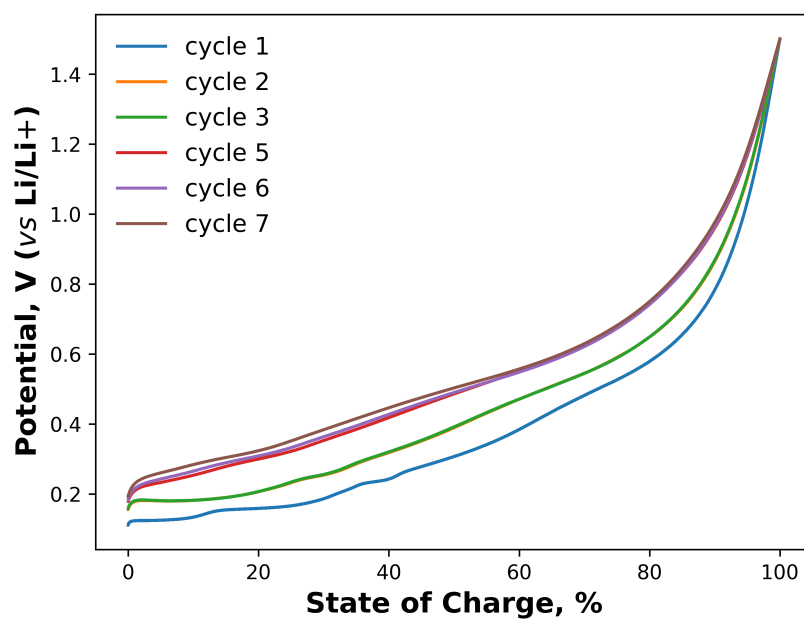


Figure A.22: Galvanostatic charge curves of the commercial Si material used in this work, and showing the progressive loss of graphitic character of the electrodes with repeated cycling. Cycle 4 is made up of two constant-current-constant-voltage steps and has therefore been omitted.

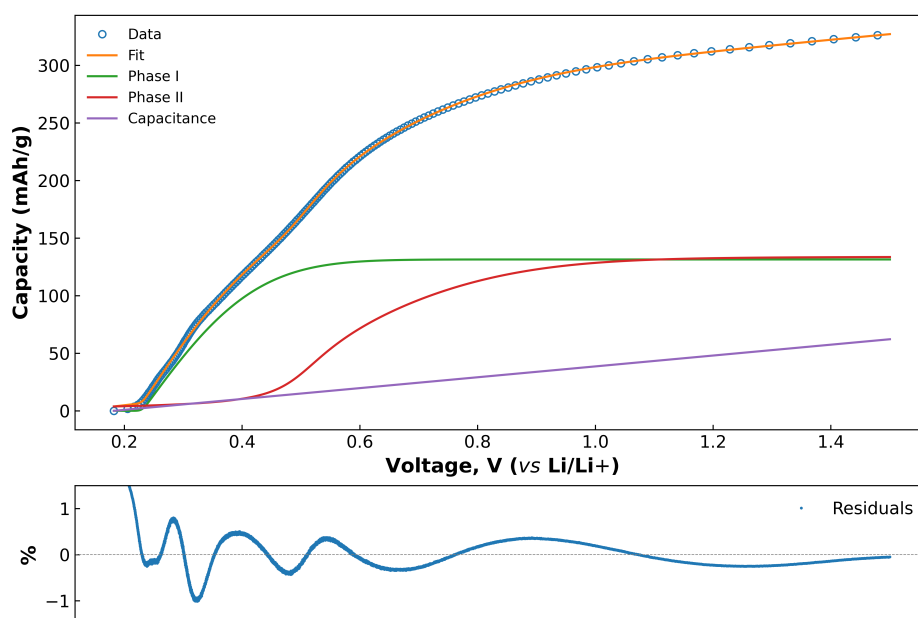


Figure A.23: Fit and residual of applying equation 2.8 to the delithiation step of Si. The purple line is the capacitance, which was used as a baseline for the fitting procedure.

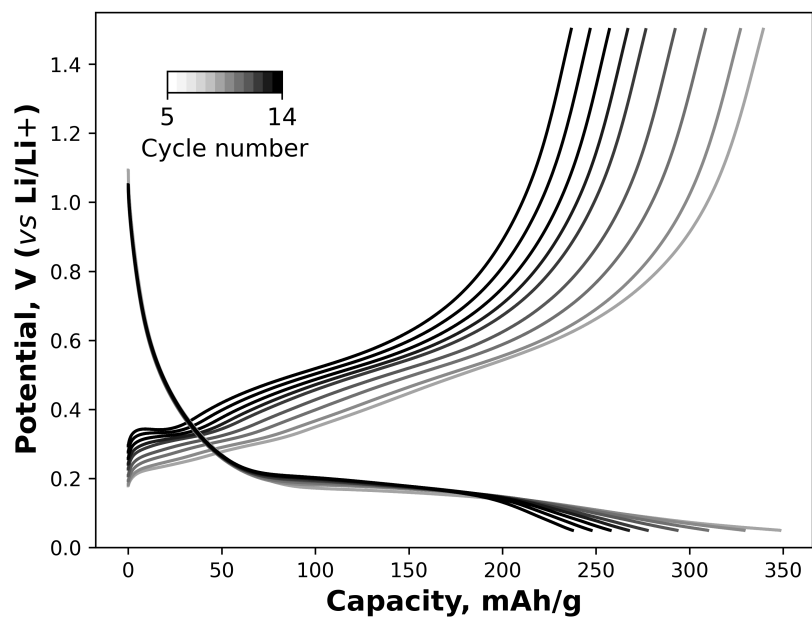


Figure A.24: An example of the GCD curves of the first batch of 10 cycles after formation and the EIS cycle. The  $dQ/dV$  curves shown in Fig. 8.2 are derived by fitting equation 2.8 to the delithiation (charge) curves shown here.





# **Appendix B**

# **Papers**

# Enabling Increased Delithiation Rates in Silicon-Based Anodes through Alloying with Phosphorus

Frederik T. Huld,<sup>\*[a, c]</sup> Samson Y. Lai,<sup>[b]</sup> Wakshum M. Tucho,<sup>[d]</sup> Rasim Batmaz,<sup>[a]</sup> Ingvild T. Jensen,<sup>[e, f]</sup> Song Lu,<sup>[c]</sup> Obinna E. Eleri,<sup>[a, c]</sup> Alexey Y. Kopusov,<sup>\*[b, e]</sup> Zhixin Yu,<sup>\*[c]</sup> and Fengliu Lou<sup>\*[a]</sup>

The capability of battery materials to deliver not only high lithium storage capacity, but also the ability to operate at high charge/discharge rates is an essential property for development of new batteries. In the present work, the influence on the charge/discharge rate behaviour of substoichiometric concentrations of phosphorus (P) in silicon (Si) nanoparticles was studied. The results revealed an increase in rate capability as a function of the P concentration between 0 and 5.2 at%, particularly during delithiation. The stoichiometry of the nano-

particles was found to strongly affect the formation of the  $\text{Li}_{3.5}\text{Si}$  phase during lithiation. Cyclic stability experiments demonstrated an initial increase in capacity for the  $\text{SiP}_x$  materials. Galvanostatic intermittent titration technique and electrochemical impedance spectroscopy demonstrated the increased lithium diffusivity with inclusion of P. Density functional theory and *ab initio* molecular dynamics were deployed to provide a rationale for the electrochemical behaviour of  $\text{SiP}_x$ .

## Introduction

Li-ion batteries (LIBs) are one of the most used energy storage devices due to their relatively high energy storage capacity, an ability to operate under high charge/discharge rates, and possibility for small size and portability.<sup>[1]</sup> As requirements for LIBs continue to grow, design and research into new active

materials for LIBs have become necessary to enable the delivery of high power and improvement of energy storage capacity. Much of the recent work has been focussed on optimizing the properties of silicon (Si) as an anode material, due to its ten-fold greater Li-ion storage capacity compared to conventionally used graphite.<sup>[2–4]</sup> However, the volume change of Si during lithiation/delithiation is also much greater than for graphite (300% vs 10%), which leads to fracturing of Si particles, delamination of the active materials from the current collector, and unstable solid electrolyte interphase (SEI) formation. All of these factors lead to rapid degradation of Si-based electrodes during electrochemical cycling.<sup>[5–7]</sup> In addition, the diffusivity of  $\text{Li}^+$  ions in Si is also lower than that in graphite ( $10^{-10}$  vs  $10^{-7}$   $\text{cm}^2/\text{s}$ ).<sup>[8,9]</sup> Low diffusivity of  $\text{Li}^+$  inside Si, as well as high charge-transfer resistance at the surface contribute to the low rate capability, which impedes the use of Si in high power applications.<sup>[2–4]</sup>

More than a decade of work has been dedicated to mitigating the effects of the volume change in Si and other materials operating through alloying mechanism. This has been approached through the use of coatings, materials engineering, and/or by nanostructuring of Si.<sup>[10–13]</sup> Alternatively, Si-based alloys and substoichiometric compounds have been proposed to change the cycling behaviour of Si,<sup>[14–17]</sup> thereby improving the intrinsic properties in combination with extrinsic methods such as nanostructuring and/or coatings. In the search for improvement of the Si-based materials and synergetic affect between Si and heteroatoms, alternative strategies have been deployed including physical mixing of Si nanoparticles and layered black phosphorus.<sup>[18]</sup>

Recently, materials such as  $\text{SiO}_x$ ,  $\text{SiN}_x$  or  $\text{SiP}_x$  have shown great promise due to their incredible cycling stability originating from conversion/alloying mechanisms.<sup>[19–24]</sup> For  $\text{SiO}_x$ ,  $\text{SiN}_x$  and  $\text{SiP}_x$  with  $x < 1$ , it has been shown that the added element participates in the formation of an inactive matrix during initial

[a] F. T. Huld, Dr. R. Batmaz, O. E. Eleri, Dr. F. Lou  
Beyonder  
Stokkamyrveien 30, N-4313 Sandnes, Norway  
E-mail: frederik@beyonder.no  
fengliu@beyonder.no

[b] Dr. S. Y. Lai, Prof. A. Y. Kopusov  
Battery Technology Department  
Institutt for Energiteknikk  
2007 Kjeller, Norway

[c] F. T. Huld, S. Lu, O. E. Eleri, Prof. Z. Yu  
University of Stavanger  
4036, Stavanger, Norway  
E-mail: zhixin.yu@uis.no

[d] Dr. W. M. Tucho  
Department of Mechanical and Structural Engineering and Materials  
University of Stavanger  
4036, Stavanger, Norway

[e] Dr. I. T. Jensen, Prof. A. Y. Kopusov  
Center for Materials Science and Nanotechnology  
Department of Chemistry  
P.O. Box 1033, Blindern, 0371 Oslo, Norway  
E-mail: Alexey.kopusov@kjemi.uio.no

[f] Dr. I. T. Jensen  
Sustainable Energy Technology  
Sintef  
Forskingsveien 1NO- 0373 Oslo, Norway

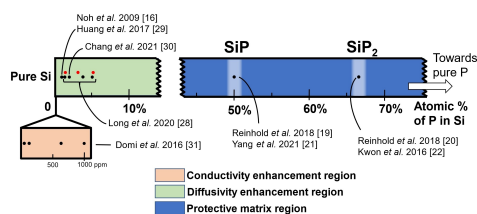
Supporting information for this article is available on the WWW under <https://doi.org/10.1002/slct.202202857>

© 2022 The Authors. ChemistrySelect published by Wiley-VCH GmbH. This is an open access article under the terms of the Creative Commons Attribution License, which permits use, distribution and reproduction in any medium, provided the original work is properly cited.

lithiation, leaving domains of pure Si as the main source of reversible capacity.<sup>[2,19,25]</sup> The advantage of these materials is the high  $\text{Li}^+$  diffusivity through the inactive matrix and the substantial decrease in swelling compared to Si, which leads to an increase in both rate capability and stability during cycling. For instance, lithium phosphidosilicates (possible products of  $\text{SiP}_x$  conversion), which consist of Li, Si and P in various ratios, have been shown to have high  $\text{Li}^+$  ion mobility, which can increase the  $\text{Li}^+$  diffusivity of Si-based anodes.<sup>[26,27]</sup> However, the major disadvantage of relatively high concentrations of added element (*i.e.*, high  $x$ ) is a decreased initial Coulombic efficiency (ICE) due to the irreversible *in situ* conversion reaction.<sup>[2,19]</sup> In addition, the electrochemistry of Si-based alloys is not straightforward, as some of the elements used for alloying can react with  $\text{Li}^+$  to form Li–Si-containing compounds, complicating the data analysis and further improvement of these otherwise promising materials.<sup>[19,28]</sup> At the present moment the results for  $\text{SiNPs}$ ,<sup>[29,30]</sup>  $\text{SiO}_x$ ,<sup>[31–33]</sup>  $\text{SiP}_x$ ,<sup>[16,20,22,23,34–36]</sup> and  $\text{SiN}_x$ <sup>[25]</sup> materials systems are still quite scattered in terms of methods of preparation, chemical compositions, particle morphologies and sizes (these are differences only at the material level) due to relative novelty of the approach. All of those discrepancies makes a direct comparison of these promising materials extremely difficult and more studies yet to be performed to develop a full understanding of these Si-based compounds.

Alternatively, the intrinsic properties of Si battery active materials can also be modified by doping. The aim of such doping is to provide a stabilization effect similar to the conversion/alloying mechanism observed at high  $x$ , but without decreasing ICE.<sup>[16,19,34–36]</sup> For instance, boron-doped Si nanoparticles were reported, but this doping was found not to improve the rate capability of the Si because boron (B) is a p-type dopant.<sup>[17]</sup> Conversely, n-type dopants, such as phosphorus (P) and arsenic (As) showed promising results for improvement of anode materials.<sup>[15,31,35–37]</sup> Furthermore, P-doped Si/graphite composites demonstrated good rate capabilities due to lower charge transfer resistance and improved  $\text{Li}^+$  transport in the material compared to pure Si.<sup>[35]</sup> P is a promising choice as an n-type dopant due to its lower toxicity compared to other candidates such as As. Depending on P concentration in Si (at doping or sub-stoichiometric levels),  $\text{SiP}_x$  is expected to maintain some of the advantages of doped Si—namely the increased conductivity relative to pure Si, but also possibly the advantages of conversion materials such as increased  $\text{Li}^+$  diffusivity and high cycling stability.

Previous work on substoichiometric  $\text{SiP}_x$  materials has shown the increase in both the conductivity and  $\text{Li}^+$  diffusivity of  $\text{SiP}_x$  at low P%.<sup>[34]</sup> However, the mechanism by which the addition of P affects the electrochemical behaviour is difficult to determine, as effects due to surface oxides and material nanostructuring play a significant role in the electrochemical behaviour. Figure 1 shows some  $\text{SiP}_x$  materials recently reported in the literature. This survey is displayed on a scale of the atomic % of P in the Si material used, which is divided into regions depending on the major mechanism attributed to



**Figure 1.** Schematic illustration showing present work on  $\text{SiP}_x$  anode materials displayed as a function of the atomic% of P in Si, as well as the main effect attributed to the P in the given concentration range. Our contribution is shown as off-set red circles.

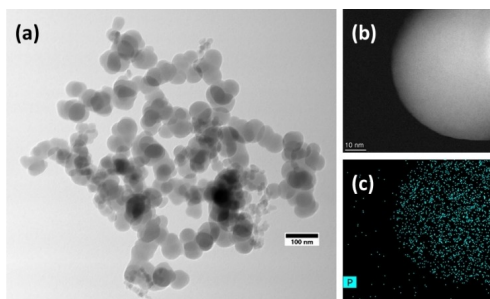
material enhancements at that P%. The contribution of the current work is shown as offset red circles.

A silane pyrolysis process was used to disambiguate the effect of low concentrations of P in Si nanoparticles by synthesizing particles of very similar morphology and with low surface oxide levels.<sup>[25,31]</sup> In the present article, we describe the synthesis of amorphous  $\text{SiP}_x$  nanoparticles with the atomic % of phosphorus in the particles ranging from 1.5 to 5.2 at% and compare their electrochemical performance to pristine Si nanoparticles of the same size.

## Results and Discussion

### Materials characterisation of $\text{SiP}_x$ and Si NPs

Si-based materials obtained through the silane pyrolysis route typically give rise to amorphous nanoparticles (NPs) with relatively narrow size distribution.<sup>[31]</sup> This process conveniently allows for the preparation of nanoparticles with the target size and morphology through controlled nucleation and growth. The introduction of  $\text{PH}_3$  gas into  $\text{SiH}_4$  pyrolysis process resulted in the formation of  $\text{SiP}_x$  NPs, where the ratio of Si:P is manipulated through control of the ratio of silane to phosphine gases supplied into the reactor during pyrolysis. This technique has been previously applied not only to produce Si nanoparticles,<sup>[31]</sup> but also to produce more complex  $\text{SiN}_x$  (nano)particles with precise ratios of Si:N and controlled morphology and particle size.<sup>[25]</sup> The obtained materials were characterized using microscopy-based methods, as the amorphous nature of the  $\text{SiP}_x$  particles as well as the formation of a solid solution of P in Si limits the selection of characterization techniques. Transmission electron microscopy (TEM) images of the nanoparticles shows a distribution of partially aggregated particles, as illustrated in Figure 2a for P5.2. The microscopy characterization for materials P0, P1.5, and P3.2 is shown in Figure S1. These aggregates consist of primary particles with a radius below 50 nm, fused together in a branching pattern. These nanostructures are typical of Si nanomaterials prepared by  $\text{SiH}_4$  pyrolysis, and are much smaller than the critical size of 150 nm.<sup>[31,38–40]</sup> The distributions of primary particle sizes shown in histograms in Figure S2 illustrate a small decrease in primary particle radius with increasing P%. This difference is the most



**Figure 2.** (a) TEM image showing a micron-sized aggregate of P5.2; (b) HAADF image of a single particle of the P5.2 material; (c) HAADF-EDS mapping of P in a particle of P5.2 material.

pronounced for pure Si, which shows an average particle radius  $\sim 10$  nm greater than the material with highest P content. The three SiP<sub>x</sub> materials, however, show only a small variation in particle size distribution. The size of NPs is known to change the electrochemical properties, with larger particles showing an increase in overpotential.<sup>[41,42]</sup> However, we do not expect these small, highly overlapped differences to cause a significant difference in electrochemistry.

Figure 2b and 2c show HAADF and HAADF-EDS images of the P5.2 material, respectively. The lack of a bright “edge” around the particle in Figure 2c indicates that the P is not concentrated at the surface of the particle, but rather distributed evenly throughout. EDS spectra can be found in Figure S3 and show very low concentrations of oxygen on the particles. For an accurate determination of the stoichiometry, the atomic percentages of P were determined by ICP-OES and are shown in Table 1. Furthermore, X-ray diffraction (XRD) analysis (Figure S4) of the four materials confirmed their amorphous structure, with no peaks observed to indicate the presence of crystalline Si or measurable quantities of SiP/SiP<sub>2</sub> phases.<sup>[21]</sup>

### Stability and rate capability of SiP<sub>x</sub> NPs

Galvanostatic charge-discharge (GCD) testing was performed in half-cells using Li foil as a counter electrode. The currents chosen for formation and subsequent tests were based on the capacity of the materials in order to minimise differences in stresses experienced by differing materials. This is also why

Material name	P concentration (atomic %)	Capacity of 1 <sup>st</sup> lithiation (mAhg <sup>-1</sup> )	ICE (%) <sup>[a]</sup>
P0	0	3,533	87.1 ± 0.6
P1.5	1.5	3,066	88 ± 2
P3.2	3.2	2,905	85 ± 1
P5.2	5.2	2,830	87.7 ± 0.3

[a] Errors were calculated from the average of three cells.

current densities are reported in C-rates (with units of h<sup>-1</sup>), instead of mA g<sup>-1</sup>.

The 1<sup>st</sup> cycle charge-discharge curves for the studied materials are shown in Figure S5a. Table 1 summarizes the data from the 1<sup>st</sup> cycle, and includes the measured gravimetric capacity taken from the first lithiation step for each material, as well as the ICE. Table 1 shows that all the SiP<sub>x</sub> materials have lower initial capacity than pristine Si. The change of capacity is not linear: P3.2 and P5.2 exhibiting similar initial capacities, while P1.5 has a higher capacity than other SiP<sub>x</sub> samples. The similarity of the ICEs indicates that there is no appreciable formation of lithium phosphide (Li<sub>3</sub>P) or other matrix materials through any conversion reaction, as existence of such would cause the ICE to decrease as a function of the amount of P in the material. The capacities of the materials exhibit a strong negative dependence on the P%, which is greater than what would be expected from the theoretical reaction of Si<sub>x</sub>P<sub>1-x</sub> + (3 + 0.5x)Li → x[Li<sub>3.5</sub>Si] + (1-x)[Li<sub>3</sub>P]. This is consistent with the results of other researchers, who have reported that the initial capacity of Si<sub>x</sub>P<sub>1-x</sub> is lower than expected values.<sup>[15,20,21,35]</sup> As the ICEs of all materials are very close and the conversion reaction can be neglected, it is possible to suggest that the formation of SEI is similar for all studied materials.

Figure S5b shows the first cycle differential capacity (dQ/dV) plots of the studied materials. The SiP<sub>x</sub> materials exhibit sharp peaks during lithiation below 0.3 V, which is common for the first cycle of Si. The formation of Li<sub>3</sub>P at around 0.4 V expected from the literature has not been seen for any of the SiP<sub>x</sub> materials studied in the present work.<sup>[21–23]</sup> The absence of distinctive features signalling the formation of lithium phosphosilicates or Li<sub>3</sub>P are likely due to the low concentration of P in SiP<sub>x</sub>. These species should account for less than 5% of the total capacity, and would, therefore, be lost in the much larger peaks corresponding to the formation of lithium silicide (Li<sub>x</sub>Si) and SEI. The two broad peaks in the delithiation step are characteristic for delithiation of the amorphous α-Li<sub>3.5</sub>Si and α-Li<sub>2.0</sub>Si phases.<sup>[43,44]</sup> The peaks that are expected for the conductive additives (mainly the conductive graphite) are too small to be visible due to the high (60% by weight) loading of Si-based material, and thus the electrochemical behaviour of the cells can be considered to be predominantly due to Si or SiP<sub>x</sub>. The electrochemical testing was performed with the voltage cut-off was set to 0.05 V to avoid the formation of c-Li<sub>15</sub>Si<sub>4</sub> phase, which typically manifests itself by the presence of sharp peaks at 0.4 V in the delithiation curves – absent for the present materials.<sup>[42]</sup> Therefore, the advantages of forming a protective matrix with high Li<sup>+</sup> diffusivity are not available for SiP<sub>x</sub> at the studied range of P concentrations.

In order to study the charge/discharge behaviour of Si and Si-based materials, it is important to recognize the difference in electrochemical behaviour during lithiation and delithiation.<sup>[45]</sup> It is important to consider these processes separately when evaluating materials particularly at high charge/discharge rates.

Therefore, stability tests were carried out by lithiating and delithiating at asymmetric C-rates. The delithiation behaviour was studied by setting the delithiation rate to 0.3 C, and the lithiation rate to 0.1 C. This was done to reduce the stress on

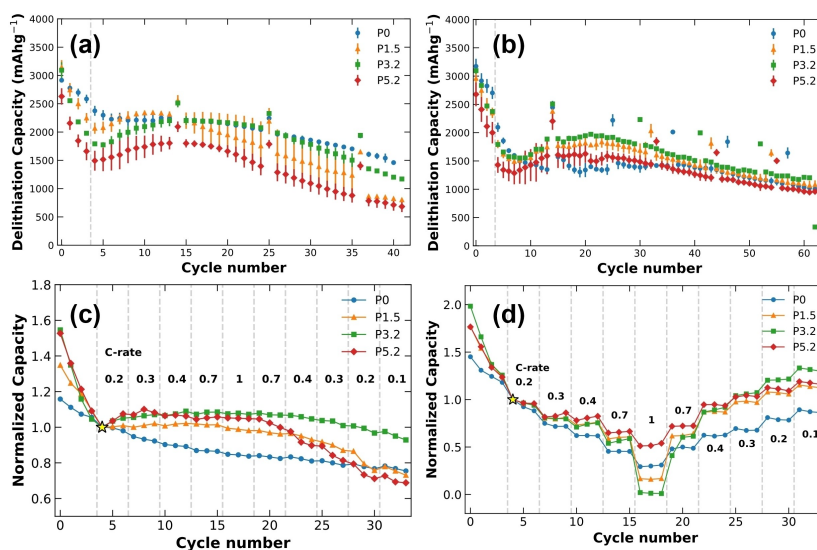
the electrode during lithiation and allow any electrochemical processes to run to completion. In this way, the behaviour of a delithiation step was not limited by the preceding lithiation step. A diagnostic cycle – where both the lithiation and delithiation C-rate was set to 0.05 C – was included after every tenth cycle to explore the evolution of the overpotential. The lithiation-dependent stability was studied in the same manner, with a slow delithiation process at 0.1 C and a faster lithiation at 0.3 C. The stability during fast delithiation (Figure 3a) shows that the total capacity increases for SiP<sub>x</sub> materials after the initial formation (delimited by the vertical dashed line), but not for the pristine Si (P0). Gradual capacity increases are observed in other literature, but the reason is not completely understood.<sup>[25,46]</sup> For P0, P1.5 and P3.2 the difference between the cycling and diagnostic cycles remains unchanged, indicating that the overpotential is constant. In contrast, the disparity between the cycling and diagnostic cycles in P5.2 is larger at later cycles, which implies that the overpotential increases over time. By the 40<sup>th</sup> cycle, all the materials dropped below 80% of their capacity relative to the first cycle after formation (the 1<sup>st</sup> cycle after the dashed line). An example of the capacity retention of SiP<sub>x</sub> full cells is given in figure S6, to demonstrate the behaviour in a different system.

The lithiation-dependent performance was studied in the same manner, with a slow delithiation process at 0.1 C and a faster lithiation at 0.3 C. The performance of the materials as a function of lithiation is shown in Figure 3b. Here the capacity increase is also observed. The relatively large lithiation current means that the potential limit is reached before full lithiation of the active material is achieved. This explains why the number

of cycles required to reach the maximum capacity is greater than that observed in Figure 3a. The difference in capacity between the fast cycles and the diagnostic cycles is more or less constant for the SiP<sub>x</sub> materials, indicating that the overpotential is consistent with repeated cycling. For P0, the small decrease in this difference indicates that the overpotential is decreasing slightly.

Rate capability tests were performed in a similar manner to the stability tests, i.e. by lithiating the electrodes at 0.1 C and delithiating at increasing rates (or *vice versa*). The data is normalized to the first point after formation (marked with a star) to highlight the relative rate behaviour of the materials. Figure 3c shows that the delithiation capacity is mostly independent of the applied current (within the chosen current range), and that the loss of capacity is due to aging in the same way as the stability behaviour seen in Figure 3a. Figure 3d, however, shows a strong relationship between the lithiation capacity of the electrodes and the applied current. Here, the SiP<sub>x</sub> materials show slightly better capacity retention in the 0.1–0.7 C range compared to the pure Si, but at 1 C P1.5 and P3.2 perform worse than the pristine Si. The capacity is recovered once the applied current returns to C-rates below this inflection point, allowing us to conclude that this capacity loss is not due to cell failure or aging. From this we can conclude that lithiation is the limiting factor in determining the rate capability of Si nanoparticles.

Analysis of the evolution of dQ/dV plots can provide additional insights to the differences in behaviour between the materials, explaining both the rate capabilities and the initial increase of capacities for SiP<sub>x</sub> during cycling. Figures 4 and 5



**Figure 3.** Cyclic stability and rate capability behaviour using asymmetric GCD. (a) Cyclic stability with delithiation set to 0.3 C and lithiation set to 0.1 C. (b) Cyclic stability with lithiation set to 0.3 C and delithiation set to 0.1 C. Error bars were calculated from the average of three cells. (c) Normalized delithiation rates with slow lithiation at 0.1 C. (d) Normalized lithiation rates with slow delithiation at 0.1 C. A diagnostic cycle at 0.05 C was included after every tenth cycle for the tests shown in the panels a and b. The star at cycle four in panels c and d is the normalization point, the first point after formation.

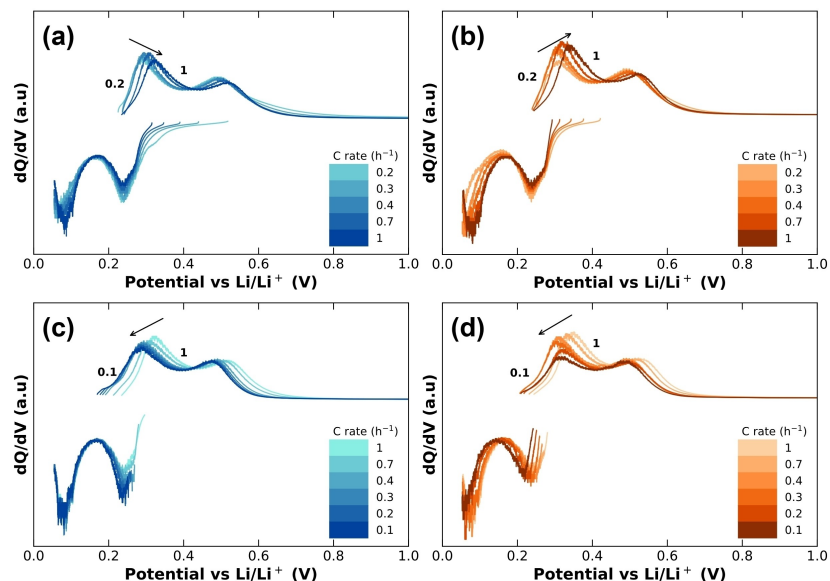


Figure 4. dQ/dV of rate capability experiments with lithiation rate fixed at 0.1 C and varying delithiation rates. (a, b) increasing C-rate; (c, d) decreasing C-rate. (a, c) sample P0; (b, d) sample P1.5.

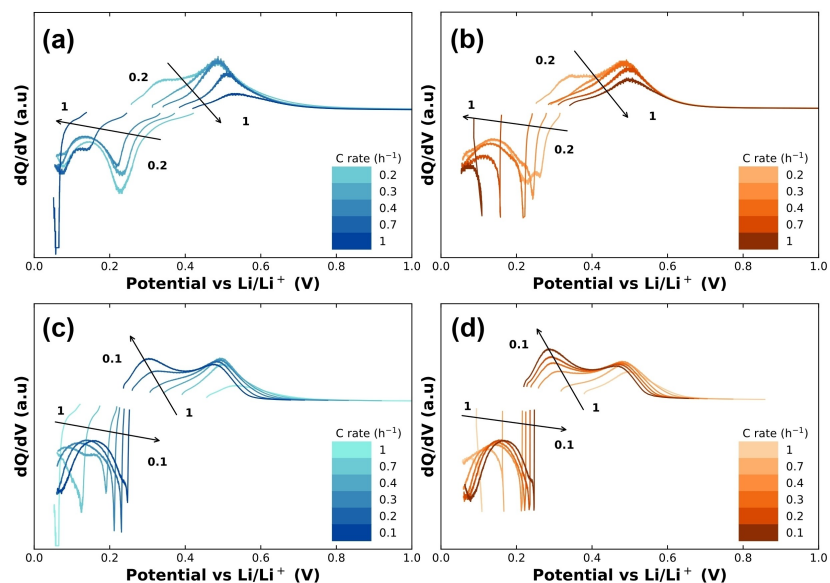


Figure 5. dQ/dV of rate capability experiments with delithiation rate fixed at 0.1 C and varying lithiation rates. (a, b) increasing C-rate; (c, d) decreasing C-rate. (a, c) sample P0; (b, d) sample P1.5.

show the changes in dQ/dV as a function of current for the delithiation and lithiation rate capability tests, respectively.

From Figures 4a and 4b, as the C-rate is increased the delithiation curve (most notably the Li<sub>3.5</sub>Si peak at ~0.28 V) is shifted towards higher potentials – and when the C-rate is

reduced (Figures 4c and 4d), this trend reverses. This potential shift agrees with the expectation that the overpotential increases with the applied current, leading to a shift of the dQ/dV peaks. The reversal of this trend when decreasing the C-rate indicates that there is no significant change in impedance resulting from changing the current of the delithiation step while keeping the lithiation step fixed. Comparing the  $\text{Li}_{3.5}\text{Si}$  peaks in Figures 4a and 4b, it can be seen that the presence of P causes an increase in the size of  $\text{Li}_{3.5}\text{Si}$  peak. This indicates that the capacity of this phase is increasing in the first few cycles, behaviour which is not seen for P0. The behaviour of the  $\alpha\text{-Li}_{2.0}\text{Si}$  peak is almost identical between Si and  $\text{SiP}_x$ , and so this phase can be considered unaffected by the presence of P. The increase in capacity of the  $\text{Li}_{3.5}\text{Si}$  peak may be due to a decrease in resistance of the cell as a result of increasing  $\text{Li}^+$  diffusivity in the electrode.

Similarly to Figure 4, Figure 5 displays the dQ/dV curves for the lithiation-dependent rate capability. These graphs show a strong correlation between the  $\text{Li}_{3.5}\text{Si}$  peak in the delithiation curve as a function of the lithiation rate. Unlike the behaviour shown in Figure 4, Figures 5a and b show that as the lithiation rate is increased, the  $\text{Li}_{3.5}\text{Si}$  peak is quickly lost, and the  $\text{Li}_{2.0}\text{Si}$  peak is strongly diminished. When decreasing the lithiation rate (Figures 5c and 5d), the  $\text{Li}_{3.5}\text{Si}$  and  $\text{Li}_{2.0}\text{Si}$  peaks are recovered. However, the recovery of the  $\text{Li}_{3.5}\text{Si}$  peak is faster for the  $\text{SiP}_x$  materials, with a discernible peak occurring at 0.4 C for materials containing P, but not until 0.2 C for pristine Si. This means that the presence of P in the materials increases the ability for the  $\text{Li}_{3.5}\text{Si}$  to form during lithiation, and that this effect increases over time. This may be partially due to increased  $\text{Li}^+$  diffusivity of  $\text{SiP}_x$  compared to Si. However, this trend is not proportional to P%, nor does it hold at high lithiation rates. Lithiating at 1 C causes the P1.5 and P3.2 materials to have a lower capacity than P0 – and in the case of P3.2, no capacity at all – which indicates that the overpotential at 1 C is very large.

Differential capacity plots are also used to explore the changes in electrochemistry over time. In the present study, they can be used to monitor the evolution of the GCD curves during and after the formation of the broad peak observed in the stability tests. Figures S7 and S8 show the dQ/dV plots of P0, P1.5, P3.2, and P5.2 for cycles 6 to 14 of the delithiation and lithiation stability tests, respectively, which correspond to the cycles spanning the formation of the broad peaks in the capacity observed in Figures 2a and 2b. The pristine Si in Figure S7a shows only a slight broadening of the  $\text{Li}_{3.5}\text{Si}$  peak during delithiation, and a small decrease in overall height in the lithiation. The shift of the delithiation peaks (notably the  $\text{Li}_{3.5}\text{Si}$  peak) to lower potentials for P1.5 and P3.2 (Figures S7b and S7c, respectively) – as well as the increase in peak intensity show that lithiation of these materials is becoming easier over time. The lack of stability in P5.2 makes it difficult to discern features. This same trend can also be seen in the dQ/dV plots of the lithiation stability (Figure S8). Here, the weak  $\text{Li}_{3.5}\text{Si}$  peak grows strongly between cycles 6 to 14 and the overpotential decreases, but only for materials containing P. The  $\text{Li}_{3.5}\text{Si}$  peak in pristine Si decreases and shifts to higher overpotentials over

the same interval. This explains the increase in capacity seen in Figures 3a and 3b.

The behaviour seen in the cyclic stability and rate capability can be summarized thus:

1. The presence of P causes a decrease in overpotential coupled with a slow change in capacity.
2. The P-dependent effect that increases the rate capability forms slowly in the lithiation process.

During cycling we can expect reactions between P, Si and Li to occur, potentially forming small quantities of e.g.  $\text{Li}_3\text{P}$  or  $\text{Li}_2\text{SiP}_2$  (or other, more complicated phosphidosilicates). These chemical species have been shown to form in  $\text{SiP}$  and  $\text{SiP}_2$ , and similar conversions exist in  $\text{SiN}_x$ .<sup>[20,21,23]</sup> It has been shown that these species increase the  $\text{Li}^+$  diffusivity, and it can be hypothesised that their presence may help to explain the results observed.<sup>[26]</sup>

However, the low concentration of P in the  $\text{SiP}_x$  materials studied here means that directly finding these P species via a method such as FTIR or XRD would be difficult. XPS experiments performed on P5.2 electrodes before and after formation the P 2p peak confirms that P is in the  $\text{SiP}_2$  state (Figure S9).<sup>[21]</sup> Unfortunately, due to the low concentration of P it is not possible to conclude that  $\text{Li}_3\text{P}$  or phosphidosilicate species are formed in  $\text{SiP}_x$ . While XPS could potentially be used to determine how P evolves upon cycling, this would require a more dedicated study.

We have employed DFT/AIMD to test whether the P atoms in pristine  $\text{SiP}_x$  will affect the lithiation, and GITT and EIS to test the diffusivity and to find evidence that the P-containing materials have increased  $\text{Li}^+$  ion mobility over pure Si.

#### DFT and AIMD on $\text{SiP}_x$ and Si

To better understand the discrepancy between the different materials, it is necessary to explore the behaviour of Li atoms in close proximity to P atoms in the  $\text{SiP}_x$  system. To do this, DFT simulations were performed to calculate the Li behaviour in 64-atom Si systems containing 1, 2, or 3 P atoms. The results are summarized in Table S1, which illustrates that as the concentration of P increases via substitution of Si, so does the energy of the system. This result indicates that inserting relatively high concentrations of P into Si is thermodynamically unfavourable, at least in the low P concentration range. Interestingly, the Li insertion energy displays a local minimum at 1.6 at% P ( $\text{Si}_{63}\text{P}$ ). An AIMD simulation was also performed to evaluate the stability of these systems (shown in Figure S11). As shown in Figure S10a-c, the total energy of each of the  $\text{Si}_{64}$ ,  $\text{Si}_{63}\text{P}$ , and  $\text{Si}_{62}\text{P}_2$  (0, 1.6 and 3.1 at% P, respectively) system is oscillating during the whole MD simulation, whereas the  $\text{Si}_{61}\text{P}_3$  (4.7 at% P, Figure S11d) system shows a remarkable change in total energy. Here one of the Li atoms shifts to neighbouring site, implying that a high P concentration will have a negative effect on lithiation and delithiation behaviour during the charge-discharge process. This “rejection” of Li in proximity to the P may explain why the broad peak in the  $\text{SiP}_x$  exists in Figures 2c and 2d, and also why the effect is stronger for higher concentrations of P.

Higher substitution energy will increase the thermodynamic instability. Lower Li insertion energy will also increase the rate capability during lithiation. The interplay between lower insertion energy and higher thermodynamic instability implies that materials with lower concentrations of P should show good rate capability as well as decent stability, both of which are supported by the experimental data.

### GITT and EIS of SiP<sub>x</sub> and Si

To validate the rate behaviour of these materials, it is necessary to study the Li<sup>+</sup> ion mobility in the materials. The diffusivity  $D_{Li^+}$  of Li<sup>+</sup> in the electrode can be calculated from GITT data from the following equation:<sup>[2,47–49]</sup>

$$D_{Li^+}^{GITT} = \frac{4}{\pi\tau} \left( \frac{m_B V_M}{M_B S} \right)^2 \left( \frac{\Delta E_s}{\Delta E_t} \right)^2 \quad (1)$$

and from EIS using:<sup>[2,45,46]</sup>

$$D_{Li^+}^{EIS} = 1/2 \left[ \left( \frac{V_M}{SFA_w} \right) \left( \frac{\delta E}{\delta x} \right) \right]^2 \quad (2)$$

Where  $\tau$  is the duration of the titration step;  $m_B$  and  $M_B$  are the molecular mass and weight of Si, respectively;  $\Delta E_s$  and  $\Delta E_t$  are the changes in equilibrium and rest potentials, respectively;  $S$  is the area of the electrode;  $F$  is Faraday's constant;  $A_w$  is the Warburg impedance; and  $\delta E/\delta x$  is the local slope of the open circuit potential (OCP) curve. The diffusivity of the lithiation process determined by GITT is given in Figure S12, along with typical examples of the GITT and EIS curves, and the equivalent circuit used for fitting the EIS data.

Figure 6 shows a comparison between the Li<sup>+</sup> ion diffusivity of the materials as calculated from GITT as a function of voltage (Figure 6a) and EIS (Figure 6b) using equations 1 and 2, respectively. Both these figures show that the diffusivity of Li<sup>+</sup> in SiP<sub>x</sub> is significantly greater than for pristine Si even accounting for changes in diffusivity as a result of particle size differences, which would lead to a roughly 2-fold increase in diffusivity of the smallest particles (P5.2) over the largest (P0). The remaining diffusivity increase is then possibly due to the presence of lithium phosphidosilicates hypothesised earlier.

The difference in diffusivities calculated from GITT and EIS can be explained by the difference in equilibrium states, as the relaxation time for GITT is two hours, while that of EIS is 24 hours. This leads to an increase in the slope of  $\delta E/\delta x$ , and therefore a higher  $D_{Li^+}^{EIS}$ . The GITT technique also assumes that the diffusion is linear rather than radial, which leads to smaller values of diffusivity.<sup>[47]</sup>

### Conclusion

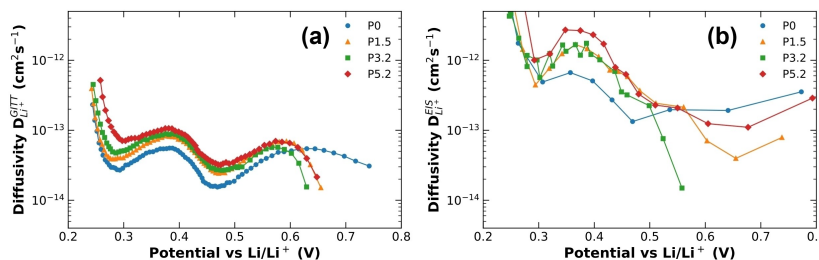
Three silicon nanoparticle materials containing concentrations of P of 1.5, 3.2, and 5.2 at% were synthesised to compare the electrochemical behaviour of SiP<sub>x</sub> to pure Si NPs. To decouple lithiation and delithiation behaviour the charge and discharge steps were performed at asymmetric C-rates. Delithiation was found to be enhanced for SiP<sub>x</sub> at high C-rates compared to pure Si, while the lithiation rate capability was only better for low C-rates. GITT and EIS were used to validate the rate behaviour and showed that the diffusivity of Li<sup>+</sup> in SiP<sub>x</sub> is significantly greater than for pristine Si. A hypothesis is proposed whereby Li<sub>3</sub>P, Li<sub>2</sub>SiP<sub>2</sub> or other phosphidosilicates species formed during cycling could be responsible for the increased diffusivity and enhanced delithiation rate in SiP<sub>x</sub>. However, the evidence for this is found to be inconclusive.

### Supporting Information Summary

The supporting information contains the experimental section, as well as TEM images and analysis, XRD, EDS, and charge-discharge plots related to the results and discussion of this article. Further details regarding the computational methods can also be found in the supporting information.

### Acknowledgements

The authors would like to thank the Norwegian Research Council and Beyond AS for the financial support of this project under project No. 304644. Funding support for the manufacturing of particles was provided by the Regional Research Fund of Vestland, Norway under Project No. 299410.



**Figure 6.** Diffusivity as a function of potential for Si and SiP<sub>x</sub>. (a) Diffusivity calculated from GITT data using Equation 1. (b) Diffusivity calculated from the Warburg constants from EIS data using Equation 2. The diffusivities are calculated at the electrode level.



### Conflict of Interest

F. T. Huld, O. E. Eleri, R. Batmaz and F. Lou are employees of Beyonder, a Norwegian battery manufacturing company. F. T. Huld and F. Lou also own stock in Beyonder. The remaining authors declare no conflict of interest.

### Data Availability Statement

Research data are made available on request.

**Keywords:** Li-ion batteries · Silicon phosphorus alloy · nanoparticles · rate capability · Density functional theory

- [1] Y. Liu, R. Zhang, J. Wang, Y. Wang, *iScience* **2021**, *24*, 102332.
- [2] K. Pan, F. Zou, M. Canova, Y. Zhu, J.-H. Kim, *J. Power Sources* **2019**, *413*, 20–28.
- [3] C. K. Chan, R. Ruffo, S. S. Hong, Y. Cui, *J. Power Sources* **2009**, *189*, 1132–1140.
- [4] P. Li, G. Zhao, X. Zheng, X. Xu, C. Yao, W. Sun, S. X. Dou, *Energy Storage Mater.* **2018**, *15*, 422–446.
- [5] M. N. Obrovac, *Curr. Opin. Electrochem.* **2018**, *9*, 8–17.
- [6] J. P. Pender, G. Jha, D. H. Youn, J. M. Ziegler, I. Andoni, E. J. Choi, A. Heller, B. S. Dunn, P. S. Weiss, R. M. Penner, C. B. Mullins, *ACS Nano* **2020**, *14*, 1243–1295.
- [7] V. Vanpeene, J. Villanova, A. King, B. Lestriez, E. Maire, L. Roué, *Adv. Energy Mater.* **2019**, *9*, 1803947.
- [8] A. Funabiki, M. Inaba, Z. Ogumi, S. Yuasa, J. Otsuji, A. Tasaka, *J. Electrochem. Soc.* **1998**, *145*, 172–178.
- [9] K. Persson, V. A. Sethuraman, L. J. Hardwick, Y. Hinuma, Y. S. Meng, A. van der Ven, V. Srinivasan, R. Kostecki, G. Ceder, *J. Phys. Chem. Lett.* **2010**, *1*, 1176–1180.
- [10] X. Shen, Z. Tian, R. Fan, L. Shao, D. Zhang, G. Cao, L. Kou, Y. Bai, *J. Energy Chem.* **2018**, *27*, 1067–1090.
- [11] R. Teki, M. K. Datta, R. Krishnan, T. C. Parker, T.-M. Lu, P. N. Kumta, N. Koratkar, *Small* **2009**, *5*, 2236–2242.
- [12] Z. Jiao, Y. Gao, S. Liu, S. Huang, Y. Jiang, Z. Chen, B. Zhao, *Electrochim. Acta* **2018**, *283*, 1702–1711.
- [13] R. Batmaz, F. M. Hassan, D. Higgins, Z. P. Cano, X. Xiao, Z. Chen, *J. Power Sources* **2018**, *407*, 84–91.
- [14] M. Ge, J. Rong, X. Fang, C. Zhou, *Nano Lett.* **2012**, *12*, 2318–2323.
- [15] O. Salihoglu, Y. E. Kahlout, *Mat. Res.* **2019**, *22*, e20180303.
- [16] J.-H. Noh, K.-Y. Lee, J.-K. Lee, *Trans. Nonferrous Met. Soc. China* **2009**, *19*, 1018–1022.
- [17] M. Ge, J. Rong, X. Fang, A. Zhang, Y. Lu, C. Zhou, *Nano Res.* **2013**, *6*, 174–181.
- [18] K. Roy, M. Wahid, D. Puthusseri, A. Patrike, S. Muduli, R. Vaidyanathan, S. Ogale, *Sustain. Energy Fuels* **2019**, *3*, 245–250.
- [19] A. Ulvestad, H. F. Andersen, I. J. T. Jensen, T. T. Mongstad, J. P. Mæhlen, Ø. Prytz, M. Kirkengen, *Sci. Rep.* **2018**, *8*, 8634.
- [20] R. Reinhold, D. Mikhailova, T. Gemming, A. B. Missyul, C. Nowka, S. Kaskel, L. Giebeler, *J. Mater. Chem. A* **2018**, *6*, 19974–19978.
- [21] R. Reinhold, U. Stoeck, H.-J. Grafe, D. Mikhailova, T. Jaumann, S. Oswald, S. Kaskel, L. Giebeler, *ACS Appl. Mater. Interfaces* **2018**, *10*, 7096–7106.
- [22] H. Yang, B. Yu, S. Gu, H. Huang, Y. Zhang, D. Liu, X. Zhang, Y. Kang, J. Wang, P. K. Chu, X.-F. Yu, *Nanoscale* **2021**, *13*, 51–58.
- [23] H.-T. Kwon, C. K. Lee, K.-J. Jeon, C.-M. Park, *ACS Nano* **2016**, *10*, 5701–5709.
- [24] T. Chen, J. Wu, Q. Zhang, X. Su, *J. Power Sources* **2017**, *363*, 126–144.
- [25] A. Ulvestad, M. O. Skare, C. E. Foss, H. Krogsæter, J. F. Reichstein, T. J. Preston, J. P. Mæhlen, H. F. Andersen, A. Y. Kopusov, *ACS Nano* **2021**, *15*, 16777–16787.
- [26] S. Strangmüller, H. Eickhoff, D. Müller, W. Klein, G. Raudaschl-Sieber, H. Kirchhain, C. Sedlmeier, V. Baran, A. Senyshyn, V. L. Deringer, L. van Wüllen, H. A. Gasteiger, T. F. Fässler, *J. Am. Chem. Soc.* **2019**, *141*, 14200–14209.
- [27] A. Haffner, T. Bräuniger, D. Johrendt, *Angew. Chem. Int. Ed.* **2016**, *55*, 13585–13588; *Angew. Chem.* **2016**, *128*, 13783–13786.
- [28] M. Miyachi, H. Yamamoto, H. Kawai, T. Ohta, M. Shirakata, *J. Electrochem. Soc.* **2005**, *152*, A2089.
- [29] J. K. Lee, K. B. Smith, C. M. Hayner, H. H. Kung, *Chem. Commun.* **2010**, *46*, 2025.
- [30] S. Chen, L. Shen, P. A. van Aken, J. Maier, Y. Yu, *Adv. Mater.* **2017**, *29*, 1605650.
- [31] S. Y. Lai, J. P. Mæhlen, T. J. Preston, M. O. Skare, M. U. Nagell, A. Ulvestad, D. Lemordant, A. Y. Kopusov, *Nanoscale Adv.* **2020**, *2*, 5335–5342.
- [32] Q. Pan, P. Zuo, T. Mu, C. Du, X. Cheng, Y. Ma, Y. Gao, G. Yin, *J. Power Sources* **2017**, *347*, 170–177.
- [33] G. Li, J.-Y. Li, F.-S. Yue, Q. Xu, T.-T. Zuo, Y.-X. Yin, Y.-G. Guo, *Nano Energy* **2019**, *60*, 485–492.
- [34] B. Long, Y. Zou, Z. Li, Z. Ma, W. Jiang, H. Zou, H. Chen, *ACS Appl. Energy Mater.* **2020**, *3*, 5572–5580.
- [35] S. Huang, L.-Z. Cheong, D. Wang, C. Shen, *ACS Appl. Mater. Interfaces* **2017**, *9*, 23672–23678.
- [36] C.-B. Chang, C.-Y. Tsai, K.-T. Chen, H.-Y. Tuan, *ACS Appl. Energy Mater.* **2021**, *4*, 3160–3168.
- [37] Y. Domi, H. Usui, M. Shimizu, Y. Kakimoto, H. Sakaguchi, *ACS Appl. Mater. Interfaces* **2016**, *8*, 7125–7132.
- [38] H. F. Andersen, W. Filtvedt, J. P. Mæhlen, T. T. Mongstad, M. Kirkengen, A. Holt, *ECS Trans.* **2014**, *62*, 97–105.
- [39] R. Körner, M. P. M. Jank, H. Ryssel, H.-J. Schmid, W. Peukert, *J. Aerosol Sci.* **2010**, *41*, 998–1007.
- [40] X. H. Liu, L. Zhong, S. Huang, S. X. Mao, T. Zhu, J. Y. Huang, *ACS Nano* **2012**, *6*, 1522–1531.
- [41] S. Martinet, in *Nanomaterials for Sustainable Energy* (Ed.: Q. Li), Springer Cham, **2016**, p. 471–512.
- [42] C. Keller, A. Desruets, S. Karuppiah, E. Martin, J. Alper, F. Boismain, C. Villeveille, N. Herlin-Boime, C. Haon, P. Chenevier, *Nanomaterials* **2021**, *11*, 307.
- [43] K. Ogata, E. Salager, C. J. Kerr, A. E. Fraser, C. Ducati, A. J. Morris, S. Hofmann, C. P. Grey, *Nat. Commun.* **2014**, *5*, 3217.
- [44] M. N. Obrovac, L. Christensen, *Electrochem. Solid-State Lett.* **2004**, *7*, A93.
- [45] V. A. Sethuraman, V. Srinivasan, J. Newman, *J. Electrochem. Soc.* **2013**, *160*, A394–A403.
- [46] C. E. L. Foss, S. Müssig, A. M. Svensson, P. J. S. Vie, A. Ulvestad, J. P. Mæhlen, A. Y. Kopusov, *Sci. Rep.* **2020**, *10*, 13193.
- [47] E. Deiss, *Electrochim. Acta* **2005**, *50*, 2927–2932.
- [48] W. Weppner, R. A. Huggins, *Annu. Rev. Mater. Sci.* **1978**, *8*, 269–311.
- [49] C. Ho, I. D. Raistrick, R. A. Huggins, *J. Electrochem. Soc.* **1980**, *127*, 343–350.
- [50] M. Murbach, B. Gerwe, N. Dawson-Elli, L. Tsui, *JOSS* **2020**, *5*, 2349.

Submitted: August 2, 2022

Accepted: October 19, 2022

# ChemistrySelect

Supporting Information

## **Enabling Increased Delithiation Rates in Silicon-Based Anodes through Alloying with Phosphorus**

Frederik T. Huld,\* Samson Y. Lai, Wakshum M. Tucho, Rasim Batmaz, Ingvild T. Jensen, Song Lu, Obinna E. Eleri, Alexey Y. Kopusov,\* Zhixin Yu,\* and Fengliu Lou\*

## **Supporting Information**

### **Table of Contents**

1. Experimental Section
  - 1.1. Si NP synthesis and characterization
  - 1.2. Electrode fabrication and testing
  - 1.3. Computational methods
2. Physical Characterisation
  - 2.1. TEM images
  - 2.2. TEM particle size analysis
  - 2.3. EDS
  - 2.4. XRD
3. Electrochemistry and further characterization
  - 3.1. GCD
  - 3.2. Full Cell Example
  - 3.3. Delithiation Stability
  - 3.4. Lithiation Stability
  - 3.5. XPS
4. Computational Methods
  - 4.1. Configuration
  - 4.2. Computational Results
  - 4.3. Total energy variations
5. Diffusivity, GITT and EIS

## 1 Experimental Section

### 1.1 Si NP synthesis and characterization

Amorphous nanoparticles (NPs) of Si and SiP<sub>x</sub> were synthesized through monosilane (SiH<sub>4</sub>) pyrolysis as described in our previous reports.<sup>[31]</sup> For the synthesis of SiP<sub>x</sub> NPs, alloying was performed *in situ* by introducing phosphine gas (PH<sub>3</sub>) into the free space reactor (FSR) along with SiH<sub>4</sub>. Proper safety protocols are required: SiH<sub>4</sub> and PH<sub>3</sub> gases are both hazardous gases due to being pyrophoric, while PH<sub>3</sub> gas is toxic at concentrations as low as 50 ppm. The resultant Si and SiP<sub>x</sub> NPs were isolated through filtration of the gas stream. Si and SiP<sub>x</sub> NP alloys were synthesized with P levels of 0, 1.5, 3.2, and 5.2 at% are referred to as P0, P1.5, P3.2, and P5.2 respectively throughout the study.

Energy-dispersive X-ray spectroscopy (EDS) equipped on transmission electron microscope (TEM, JEOL JEM-2100) was used to determine the presence of P in the particles, and P concentrations were determined using inductively coupled plasma-optical emission spectroscopy (ICP-OES). X-ray diffraction (XRD, Bruker, D8 Advance) was performed on powder samples that had been dispersed in ethanol and dropped onto a silicon low background sample holder. Samples for TEM/EDS analysis were prepared by sonicating ~1 mg of NPs in ~10 mL of ethanol for 30 minutes, before dropping onto the grid (holey carbon films on 200 mesh Cu grids, Micro to Nano) and allowing them to dry at room temperature. High-angle annular dark-field (HAADF) and HAADF-EDS were performed on an FEI Titan G2 60-300 scanning transmission electron microscope (STEM).

### 1.2 Electrode fabrication and testing

An aqueous anode slurry (20 wt% solids content) was prepared using KOH/citric acid buffer (pH 3, <5 wt%) with the solid fraction, carboxymethylcellulose (CMC, 15 wt%, 10000 Mw, Walcoco), SiP<sub>x</sub> (60 wt%), conductive graphite (10 wt%, SFG-6L, Imerys), and carbon black (15 wt%, C65, Imerys). The slurry was mixed in a planetary ball mill (MSK-SFM-1, MTI Corp.) at 400 rpm. To avoid contamination of the materials, an agate cup and zirconia balls were used for ball milling. The balls weighed 10 g each, and

a ball:slurry mass ratio of 10:1 was used. The mixing procedure was as follows: water and buffer solution were mixed in the agate cup before addition of CMC, which was then dissolved by mixing for 15 minutes. The graphite, carbon black, and SiP<sub>x</sub> NPs were added sequentially, mixing for 15 minutes between addition of each ingredient. After the addition of SiP<sub>x</sub> NPs, the mixing continued for 2 hours to produce a smooth dark brown slurry. The slurry was then deposited on 19 μm thick dendritic copper foil (SE-Cu58, Schlenk) by doctor blade height set to 80 μm. After drying at room temperature, the electrodes were calendered (MSK-HRP-4, MTI) at 120 °C and cut into 15 mm diameter discs. The final mass of active material per electrode was 1.8 ± 0.2 mg cm<sup>-2</sup>. The calendaring reduced the electrode thickness to 7 ± 1 μm (together with Cu current collector - from 29 ± 2 μm to 26 ± 1 μm).

Half cells were assembled in an argon-filled glove box using CR2032 coin cell parts (MTI), a paper separator (19 mm diameter, Tf4030, NKK), 50 μL electrolyte (TC-E8593, TINCI). Li foil (diameter 15 mm, thickness 0.45 mm, Sigma Aldrich) was used as the counter electrode. Three-electrode cells were assembled using PAT-cells (EL-Cell) with Li as the reference and counter electrodes.

GCD tests were performed in triplicate, and all cells were subjected to formation cycling prior to testing (BTS4000, Neware). Due to equipment limitations, EIS and CV were limited to one cell per test. The formation cycles consisted of one cycle at 0.05 C, followed by three cycles at 0.1 C. The formation current was initially calculated assuming an active material capacity of 3,579 mAh g<sup>-1</sup>, but later adjusted to reflect the experimentally determined initial (1<sup>st</sup> lithiation) capacities of the materials. A 4-hour rest was used to equilibrate the cells between each step. The lower and upper potential limits for all the experiments was set to 0.05 and 1.5 V, respectively. Asymmetric rate testing was performed by lithiating at a fixed 0.1 C and varying the delithiation rate, and *vice versa*. Due to the short cycle life of Si electrodes with high Si content only three cycles were performed at each C-rate. Asymmetric stability tests were performed by lithiating at a

fixed 0.1 C and delithiating at 0.3 C. GITT was performed by titrating at 0.04 C for 900 s followed by a 2 h rest. This yielded roughly 100 points per curve.

Uncycled electrodes for XPS were used as-is. Cycled electrodes for X-ray photoelectron spectroscopy (XPS) were disassembled, rinsed in DMC to remove excess electrolyte, and dried. Ablation was performed by Ar<sup>+</sup> sputtering prior to measurement. XPS was performed on a Thetaprobe (Thermo Scientific).

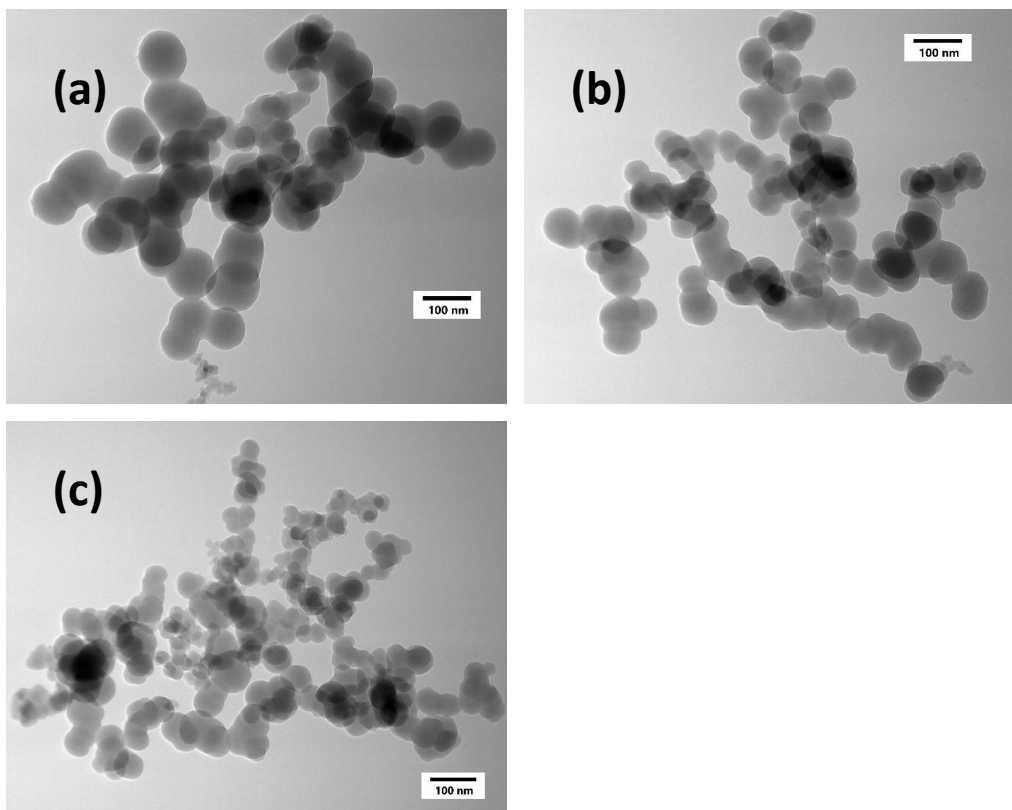
EIS was performed on a Metrohm Autolab and Nova 2.1 software. EIS experiments were prepared by titrating at 0.05 C for 1 h, followed by a 24 h rest. The EIS was performed between 10<sup>5</sup> and 0.01 Hz, with an amplitude  $V_{\text{RMS}}$  of 5 mV. EIS fitting was performed in Python using the impedance.py package.<sup>[50]</sup>

### **1.3 Computational methods**

The details of the methods used for computations can be found in the supporting information file. In short, a 2x2x2 Si supercell consisting of 64 Si atoms was used as the base, and P was used to substitute either 1, 2 or 3 Si atoms, giving values of 0, 1.6, 3.1, and 4.7 atomic% P, approximately equal to the synthesised NPs. The Li concentration in the supercell was set to 4 atoms, equivalent to 12.5%. The Li insertion energy ( $E_{\text{insert}}$ ) was calculated, along with the substitution energies ( $E_{\text{sub}}$ ).

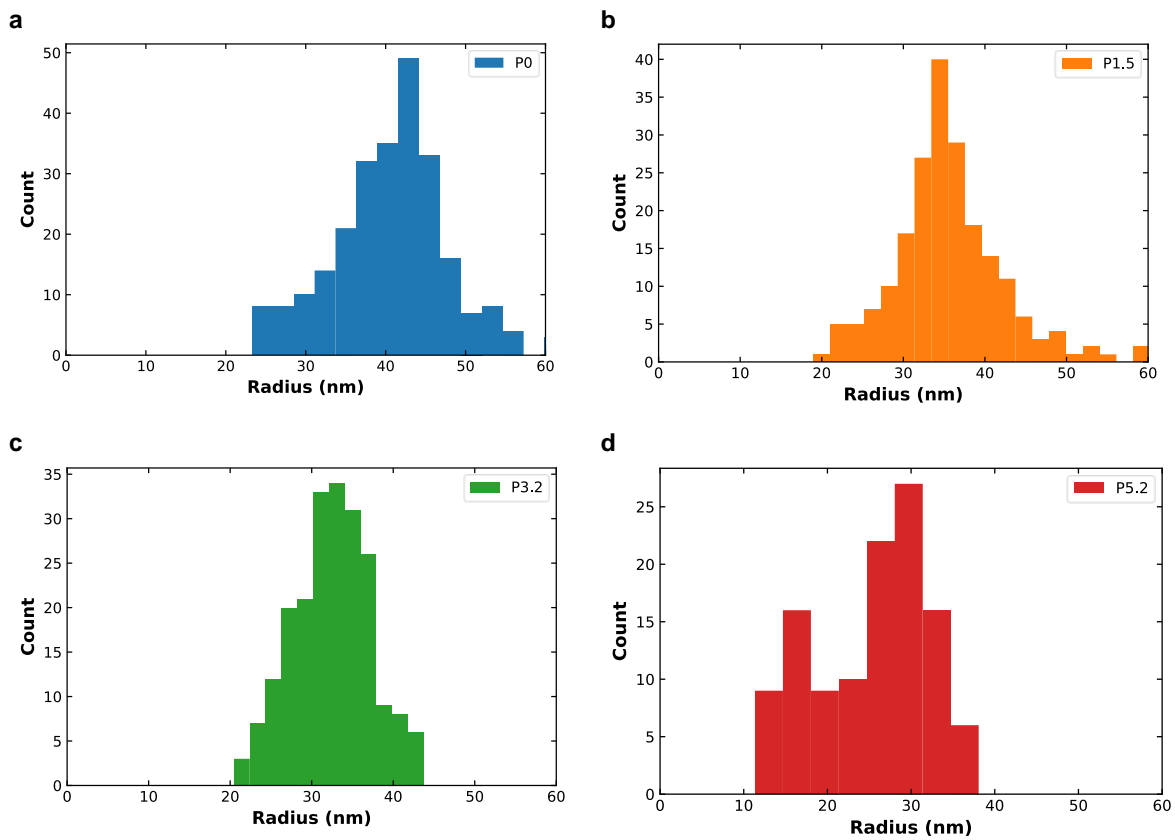
## 2 Physical Characterisation

### 2.1 TEM – images



**Figure S1:** TEM images of the four silicon samples, showing the micron-sized aggregates of SiNPs typical of silane decomposition. The four images are for a) P0, b) P1.5, c) P3.2. P5.2 is shown in Figure 1 in the main text

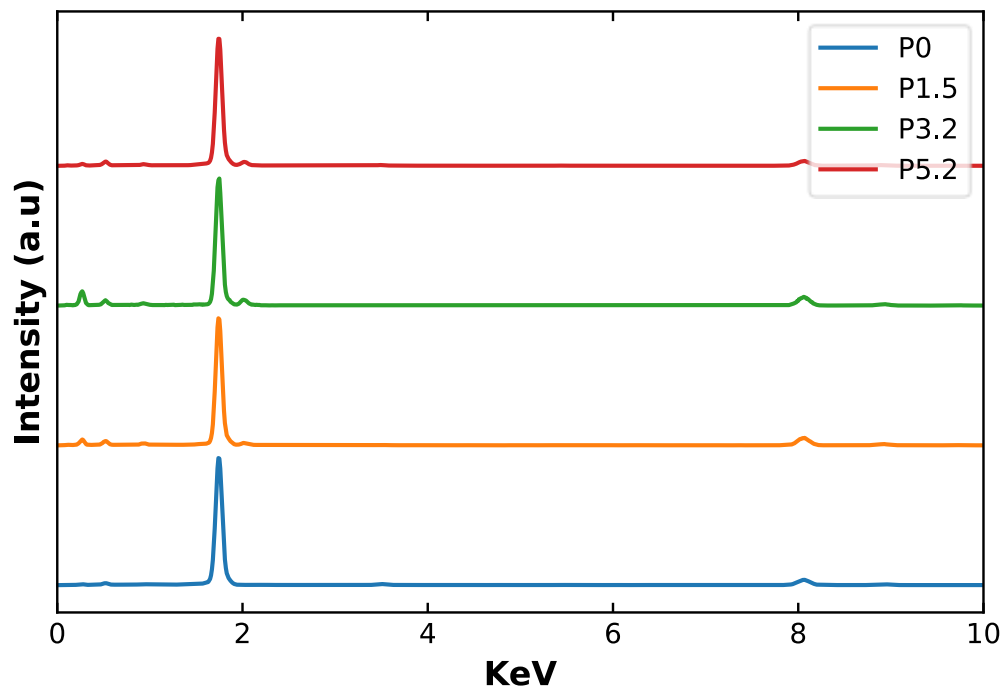
## 2.2 TEM – Particle size analysis



**Figure S2** – Particle size distributions (counts) for SiP<sub>x</sub> NPs from TEM. a) P0, b) P1.5, c) P3.2, and d) P5.2.



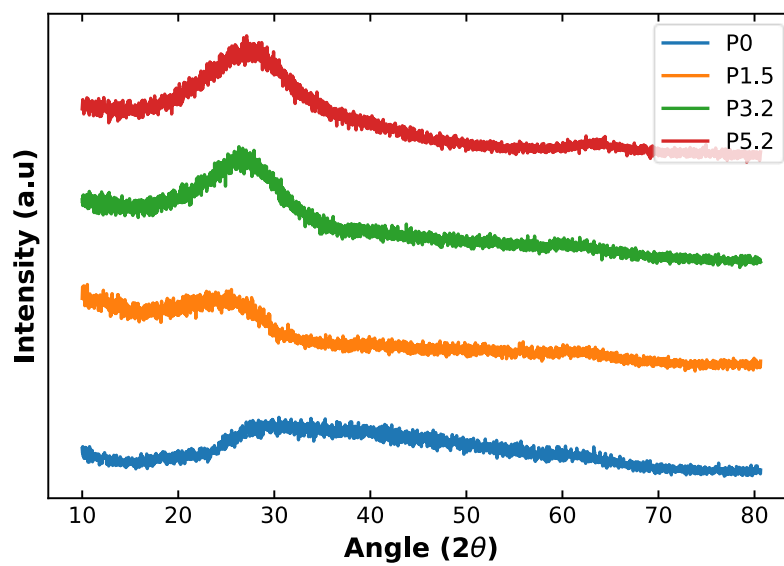
### 2.3 EDS



**Figure S3** – EDS spectra for the 4 samples as determined from TEM. a) P0, b) P1.5, c) P3.2, and d) P5.2.

Small amounts of Cu and C are ascribed to the copper grid. The oxygen peaks present in the EDS spectra are likely due to formation of native oxide on the samples prior to analysis.

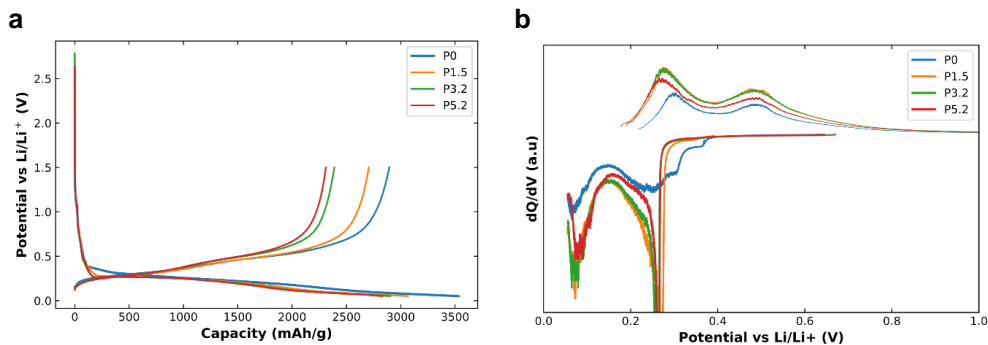
## 2.4 XRD



**Figure S4** – EDS spectra for the 4 samples. a) P0, b) P1.5, c) P3.2, and d) P5.2.

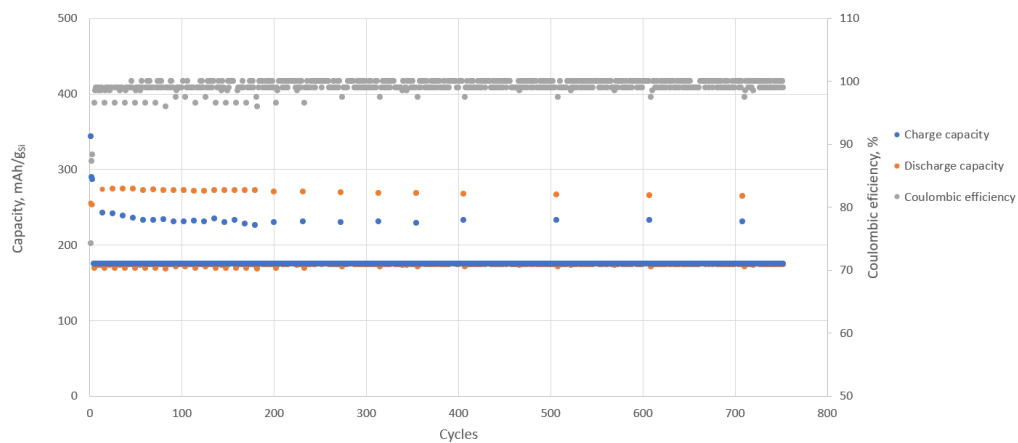
### 3. Electrochemistry

#### 3.1 GCD



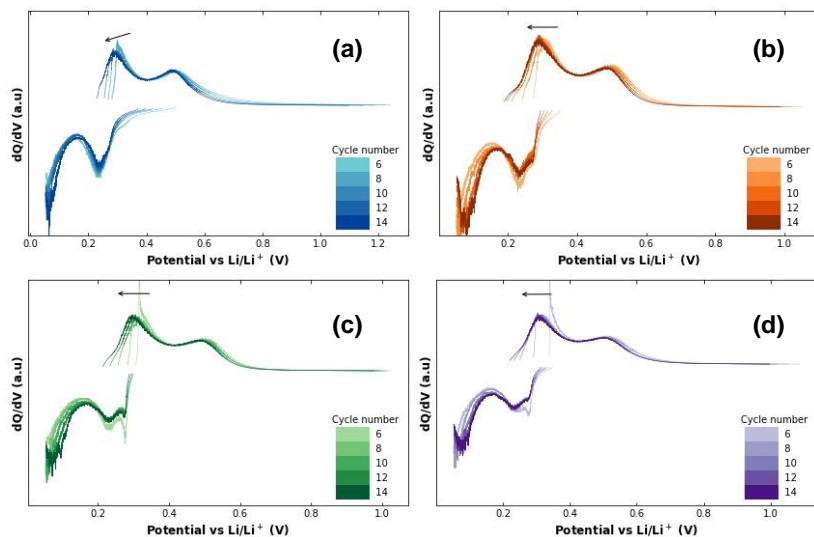
**Figure S5**—Galvanostatic cycling of SiP<sub>x</sub> alloy. (a) Voltage profiles of the 1<sup>st</sup> cycle; (b) dQ/dV profiles for the 1<sup>st</sup> cycle.

#### 3.2 Full cell example



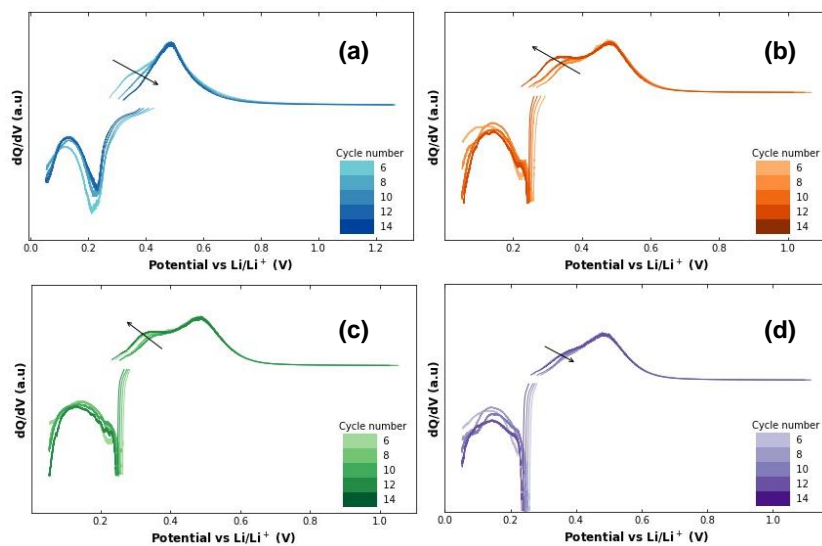
**Figure S6** – An example of SiP<sub>x</sub> / Active Carbon full cell. The SiP<sub>x</sub> material used consists of 5 atomic % P in Si, equivalent to P5.2 in the text. The anode consists of 60% SiP<sub>x</sub>, with the remaining 40% being made up of carbon black, conductive graphite, and sodium carboxymethylcellulose.

### 3.3 Delithiation Stability



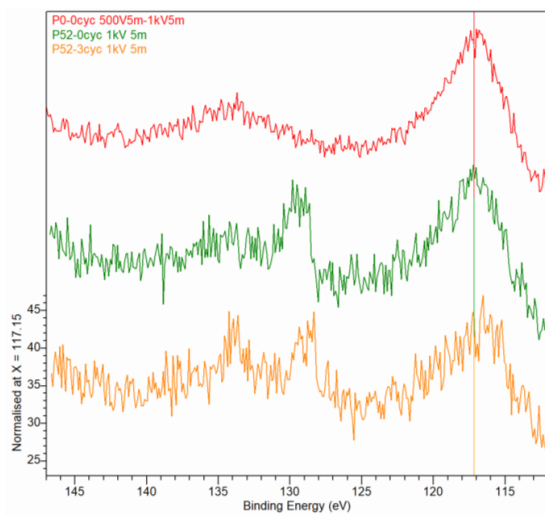
**Figure S7** –  $dQ/dV$  for cycles 6-14 of the cyclic stability data presented in Figures 2c. The arrows show the behaviour of the Li<sub>3.5</sub>Si peak. (a) P0, (b) P1.5, (c) P3.2, (d) P5.2.

### 3.4 Lithiation Stability



**Figure S8** –  $dQ/dV$  for cycles 6-14 of the cyclic stability data presented in Figures 2d. The arrows show the behaviour of the Li<sub>3.5</sub>Si peak. (a) P0, (b) P1.5, (c) P3.2, (d) P5.2.

### 3.5 XPS



**Figure S9** XPS spectra for Electrodes before and after cycling, showing the P 2p peak at ~130eV. The middle (green) and bottom (red) spectra correspond to the P5.2 material before and after formation cycles, respectively. The top red line is the spectrum for the uncycled pure Si electrodes.

## 4 Computational methods

A 2×2×2 Si supercell with different number of Li and P atoms ( $\text{Si}_{64-x}\text{P}_x\text{Li}_4$ ) (see Fig. S1,) was used for the calculation of insertion energy at diverse situations. In our calculation, the concentration of Li atom was fixed to 12.5%, which is consistent with previous studies <sup>1</sup>. The first principle calculation was performed in the Vienna ab initio simulation package (VASP) <sup>2</sup>. The ion-electron interactions were described by projector augmented wave (PAW) method <sup>3</sup>, and the generalized gradient approximation (GGA) of Perdew-Burke-Ernzerhof (PBE-sol) <sup>4</sup> was chosen to describe electron exchange and correlation energy. A kinetic cutoff energy was set to 500 eV. The Brillouin zone was sampled by a  $\Gamma$ -centered Monkhorst-Pack. A 2×2×2 K-mesh were used for structure relaxation. The convergence standard was set to  $10^{-4}$  eV in electronic relaxation, and  $0.02\text{eV}/\text{\AA}$  in Hellmann-Feynman on each atom. The *ab initio* molecular dynamics (AIMD) <sup>5,6</sup> simulations under 300K for 6ps with a time step of 2fs were carried out to evaluate the stability of Li inserted supercell  $\text{Si}_{64-x}\text{P}_x\text{Li}_4$ . The substituted energy ( $E_{\text{sub}}$ ) of the doped system can be defined as following formulate:

$$E_{\text{sub}} = E(\text{doped}) - E(\text{pristine}) + x\mu_{\text{N}} - x\mu_{\text{P}}$$

where  $E(\text{doped})$  and  $E(\text{pristine})$  are the total energies of doped and pristine Si.  $\mu_{\text{N}}$  and  $\mu_{\text{P}}$  is the energy of Si and P in its reference phase.

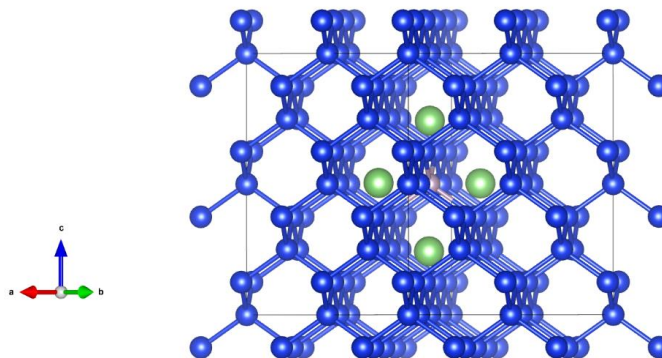
The insertion energy of Li atom can be calculated by equation below:

$$E_{\text{inset}} = E(\text{Li-P doped Si}) - E(\text{P doped Si}) - E(\text{Li})$$

where  $E(\text{Li-P doped Si})$ ,  $E(\text{P doped Si})$  and  $E(\text{Li})$  represent total energy of Li inserted P doped Si, P doped Si and Li atom.

1. DOI: 10.1021/acsami.6b00386
2. G. Kresse and J. Furthmuller, *Comput. Mater. Sci.*, 1996, 6,15-50.
3. P. E. Blochl, *Phys. Rev. B.*, 1994, 50, 17953.
4. J. P. Perdew, K. Burke and M. Ernzerhof, *Phys. Rev. Lett.*,1996, 77, 3865.
5. G. Kresse and J. Hafner, *Phys. Rev. B*, **1993**, 47, 558.
6. C. Su, H. Jiang and J. Feng, *Phys. Rev. B*, 2013, **87**, 075453.

## 4.1 Configuration



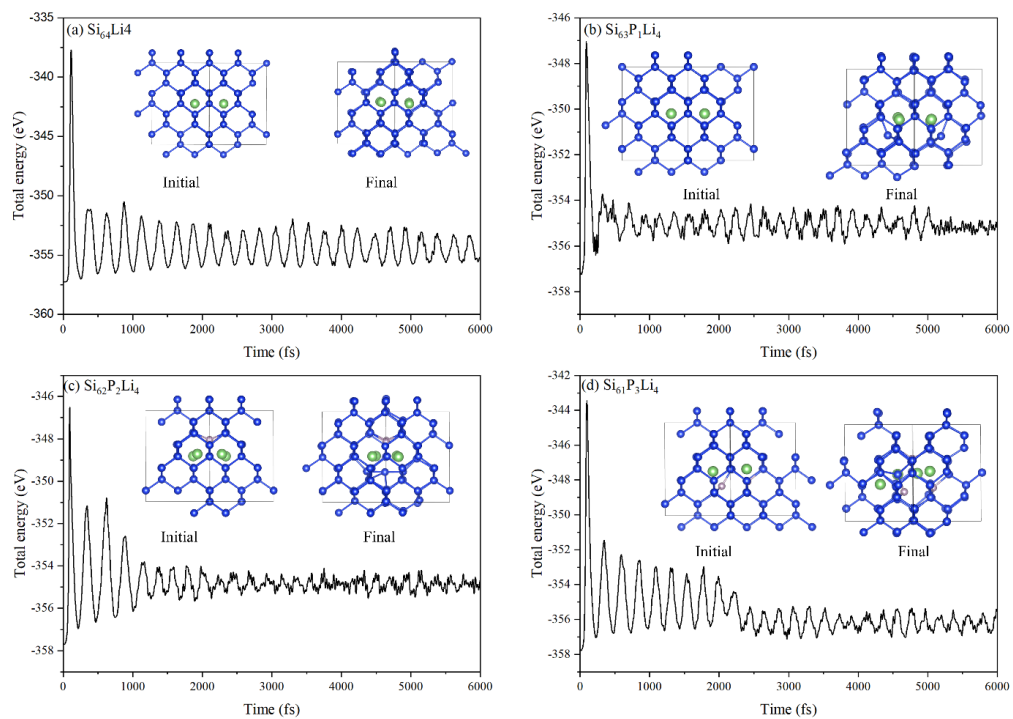
**Figure S10** – Configuration of  $\text{Si}_{63}\text{PLi}_4$  (1.6% P concentration), where mediumblue, limegreen and mistyrose denote the Si, Li and P atoms, respectively

## 4.2 Computational results

System	P concentration	P Substitution Energy	Li Insertion Energy	$E_{\text{insert}}$
	(atomic weight %)	$E_{\text{sub}} (\text{kJmol}^{-1})$	$(\text{kJmol}^{-1})$	
$\text{Si}_{64}$	0	-		66.58
$\text{Si}_{63}\text{P}$	1.6	1.93		42.45
$\text{Si}_{62}\text{P}_2$	3.1	2.90		61.65
$\text{Si}_{61}\text{P}_3$	4.7	6.75		91.66

**Table S1** Results from DFT simulation of  $\text{SiP}_x$

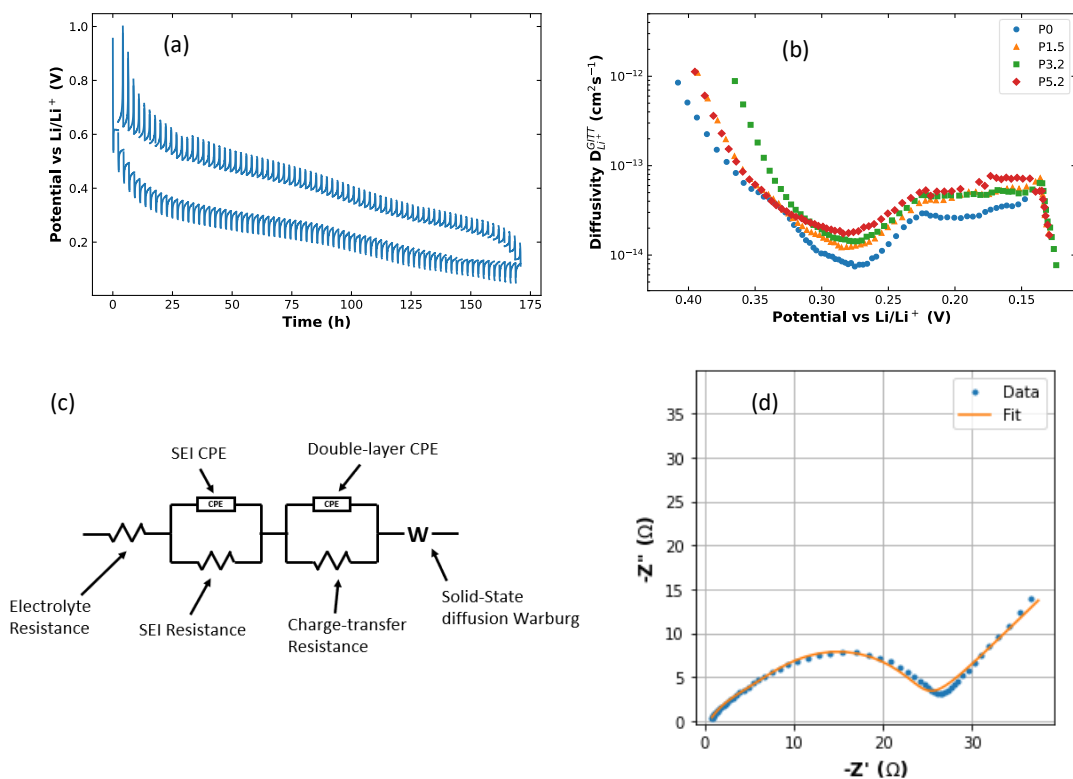
### 4.3 Total energy variations



**Figure S11** Total energy variations of  $\text{Si}_{64}\text{Li}$ ,  $\text{Si}_{63}\text{P}_1\text{Li}_4$ ,  $\text{Si}_{62}\text{P}_2\text{Li}_4$  and  $\text{Si}_{61}\text{P}_3\text{Li}_4$  as a function of time for the AIMD simulation. The respective initial and final structures are shown as insets



## 5 Diffusivity, GITT and EIS


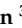






**Figure S12** – (a) Typical GITT curve, in this case for P3.2. (b) Diffusivity of lithiation process for the four samples. (c) Equivalent circuit used for EIS fitting. (d) Example of EIS curve with fit.

The EIS spectra were fitted to the equivalent circuit shown in Figure S11d using modulus weighting, which gave low error values (1-5%) for the Si-related charge transfer loop and the Warburg diffusion

Article

# Revealing Silicon's Delithiation Behaviour through Empirical Analysis of Galvanostatic Charge–Discharge Curves

Frederik T. Huld <sup>1,2,\*</sup> , Jan Petter Mæhlen <sup>3</sup> , Caroline Keller <sup>4,5</sup> , Samson Y. Lai <sup>2,3</sup> , Obinna E. Eleri <sup>1,2</sup>, Alexey Y. Kopusov <sup>3,6,\*</sup> , Zhixin Yu <sup>2,\*</sup>  and Fengliu Lou <sup>1,\*</sup>

- <sup>1</sup> Beyonder, Stokkamyrveien 30, 4313 Sandnes, Norway  
<sup>2</sup> Department of Energy and Petroleum Engineering, University of Stavanger, Kjølv Egeland's hus, Kristine Bonnevis vei, 4021 Stavanger, Norway  
<sup>3</sup> Department of Battery Technology, Institute for Energy Technology (IFE), Instituttveien 18, 2007 Kjeller, Norway  
<sup>4</sup> CEA, CNRS, IRIG, SYMMES, University Grenoble Alpes, 38000 Grenoble, France  
<sup>5</sup> CEA, LITEN, DEHT, University Grenoble Alpes, 38000 Grenoble, France  
<sup>6</sup> Center for Materials Science and Nanotechnology, Department of Chemistry, P.O. Box 1033, Blindern, 0371 Oslo, Norway  
\* Correspondence: frederik@beyonder.no (F.T.H.); alexey.kopusov@kjemi.uio.no (A.Y.K.); zhixin.yu@uis.no (Z.Y.); fengliu@beyonder.no (F.L.)

**Abstract:** The galvanostatic charge–discharge (GCD) behaviour of silicon (Si) is known to depend strongly on morphology, cycling conditions and electrochemical environment. One common method for analysing GCD curves is through differential capacity, but the data processing required necessarily degrades the results. Here we present a method of extracting empirical information from the delithiation step in GCD data for Si at C-rates above equilibrium conditions. We find that the function is able to quickly and accurately determine the best fit to historical half-cell data on amorphous Si nanowires and thin films, and analysis of the results reveals that the function is capable of distinguishing the capacity contributions from the  $\text{Li}_{3.5}\text{Si}$  and  $\text{Li}_2\text{Si}$  phases to the total capacity. The method can also pick up small differences in the phase behaviour of the different samples, making it a powerful technique for further analysis of Si data from the literature. The method was also used for predicting the size of the reservoir effect (the apparent amount of Li remaining in the electrode), making it a useful technique for quickly determining voltage slippage and related phenomena. This work is presented as a starting point for more in-depth empirical analysis of Si GCD data.

**Keywords:** silicon anodes; differential capacity; data analysis; thin films; nanowires; incremental capacity analysis



**Citation:** Huld, F.T.; Mæhlen, J.P.; Keller, C.; Lai, S.Y.; Eleri, O.E.; Kopusov, A.Y.; Yu, Z.; Lou, F. Revealing Silicon's Delithiation Behaviour through Empirical Analysis of Galvanostatic Charge–Discharge Curves. *Batteries* **2023**, *9*, 251. <https://doi.org/10.3390/batteries9050251>

Academic Editor: Matthieu Dubarry

Received: 26 February 2023

Revised: 16 April 2023

Accepted: 25 April 2023

Published: 27 April 2023



**Copyright:** © 2023 by the authors. Licensee MDPI, Basel, Switzerland. This article is an open access article distributed under the terms and conditions of the Creative Commons Attribution (CC BY) license (<https://creativecommons.org/licenses/by/4.0/>).

## 1. Introduction

Ever-growing demand for efficient energy storage has highlighted the need for new materials that can increase the power, charge rate, and storage capacity of lithium-ion batteries (LIBs). One such material is silicon (Si), which exhibits an almost 10-fold increase in gravimetric capacity compared to graphite (3579 vs. 372 mAh/g) [1–3]. Si has therefore been studied as an anode material by many groups, who have made excellent progress in furthering our understanding of Si electrochemistry, as well as developing the viability of the material for use in batteries [1,3–8]. Chief among the findings is that Si can alloy lithium (Li) up to  $\text{Li}_{3.75}\text{Si}$ , accompanied by extreme (roughly 300%) swelling of the material [9–11]. This causes fracturing of the Si material and excess solid electrolyte interphase (SEI) formation, which leads to cell failure in just a few cycles. Further, research has shown that the Li ion diffusivity in Si is quite low compared to graphite [12–14]. To address these issues, researchers have developed and studied nanostructures, coatings, the inclusion of dopants and heteroatoms, as well as electrode binders and fabrication methods [15–22]. Despite the improvements provided by this work, Si remains a difficult material to use in LIBs.

The study of Si electrochemistry has often proceeded by comparing physical and chemical analysis as measured by, e.g., nuclear magnetic resonance (NMR), energy dispersive spectrometers (EDS) or X-ray photo-electron spectroscopy (XPS), and imaging such as transmission electron microscopy (TEM) and scanning electron microscopy (SEM). Together with galvanostatic charge–discharge (GCD) behaviour, this has been used to determine the relationship between the electrochemistry of Si and its physical changes [6,9,19,23,24]. However, since it is often difficult to see features in GCD curves, this relationship has often been displayed using the differential capacity ( $dQ/dV$ ) plotted versus the voltage. The  $dQ/dV$  produces peaks at the voltages where the faradaic reactions occur most strongly, and is therefore a simple way to visualise the changes in the electrochemical behaviour of a cell during charging or discharging [25]. The position, size, and shape of a given peak gives information about the electrochemical processes and changes in the cell [26–29]. Unfortunately, the often heavy data processing required to generate  $dQ/dV$  curves from raw GCD data complicates the extraction of quantitative information. Digital data output from cell cyclers is discontinuous and the resolution is limited. This means generating  $dQ/dV$  curves requires smoothing, interpolation, and/or binning in order to produce feasible fits [30–32]. The choice of method and the degree of smoothing performed affects the final shape of the  $dQ/dV$  curve, which in turn can affect the interpretation. A highly smoothed  $dQ/dV$  curve may produce a more visually appealing plot than a less smoothed one, but the amount of information displayed is also decreased, as sharp peaks are de-emphasised or removed completely. As a result,  $dQ/dV$  plots are used for qualitative rather than quantitative assessment. Nevertheless, the understanding that more quantitative information is available in  $dQ/dV$  plots has led some researchers to propose data analysis techniques such as fitting of normal distributions to analyse  $dQ/dV$  plots [33,34]. Good quality  $dQ/dV$  plots with minimal smoothing can give a good fit to the data, but GCD data produced by less precise cyclers or data generated without the express purpose of applying fitting functions do not contain the necessary resolution to allow for this type of analysis.

Conversely, GCD curves can also be interpreted as integrals (i.e., cumulative distribution functions) of  $dQ/dV$  peaks [32,35,36]. Fitting functions used in previous research include Lorentzian, Gaussian, and pseudo-Voigt distributions, where the number of components corresponds to the number of phases in the GCD curve. This solves the issues that arise from data smoothing when fitting  $dQ/dV$  curves and allows for fitting of lower-resolution data, but the main focus has been on estimating the state-of-health (SOH) of full cells. These methods have been shown to give excellent fit to cells containing lithium iron phosphate (LFP), nickel manganese cobalt oxide (NMC), and graphite, especially at low charge–discharge rates [32,35–38]. For half-cells where Li foil is used as a counter electrode, this approach can be used to extract information about material behaviour from cycling data without the need for relying on  $dQ/dV$  curves.

Before setting up empirical fitting experiments, it is necessary to consider the advantages and limitations of the techniques and methods in use. The main advantage is to apply relatively simple equations that describe the data as it is, rather than how it ought to be, without the express need for specialized experiments. This allows for the use of data which was not initially designed for this purpose. The obvious disadvantage of empirical fitting is that the meaning of the variables is not clear; they are “black boxes” whose meaning is dependent on as-yet unknown physical phenomena. Nevertheless, applying an empirical fitting function to data and extracting empirical parameters can give important groundwork for later analyses, and can elucidate trends in data that may prove to be important even if the interpretation of the results is not straightforward.

In the context of Si, empirical fitting could be used to determine changes in the electrochemical behaviour of various Si-based materials or under different cycling conditions. To achieve this, the chosen fitting function must account for the behaviour of Si during cycling. For example, diffusivity is lower for Si than for the graphite/NMC or graphite/LFP cells used in previous research [14,32,35,36,39]. The shape of the  $dQ/dV$  curves is affected by these factors, with curves being skewed away from normal as conditions deviate from

equilibrium [26]. Further to this, fitting these empirical equations is usually performed using data generated at or near equilibrium conditions, C-rates which are too low for long cycle life experiments, and which are therefore not often reported in the literature beyond use as either formation or diagnostic cycles. Our aim is to use GCD data from the literature, data which is cycled at rates far above equilibrium. As a result, the assumption of normality which is shown to be a good approximation for other systems may not be true for Si. Hence, the Gaussian portion of the pseudo-Voigt function used in the previous literature has been replaced with a skew-normal distribution function to describe the Si phases [32].

This work presents the results of fitting an empirical fitting function to Si half-cell data and analyses the resulting fit parameters. We correlate the fit parameters to the expected physical behaviour of the cell, and ascribe general physical behaviour to the components of each phase. In order to showcase the analytical method presented here, Si GCD data were obtained with the permission of the authors from previous work involving Si. The datasets were chosen based on the simple, well-defined morphologies of the Si without addition of coatings or dopants. Two datasets consisting of GCD data from nanowires (NWs) and thin films (TFs) were chosen. This gave two avenues for exploration, namely, a morphology with controlled 2D diffusion radius and large surface area (the NWs), and a morphology with controlled 1D diffusion length and small surface area (the TFs). The suitability of the fitting method is validated and the meaning of the parameters is discussed to reveal the differences and similarities in the behaviour of Si in different morphologies. As a result, this methodology facilitates the analysis of the electrochemical data in greater details and the exploration of the contributions of multiple electrochemical processes.

## 2. Materials and Methods

### 2.1. Description of Materials

A summary of the Si materials along with the source is given in Table 1.

**Table 1.** Physical properties of the Si materials used in this work.

Si Morphology	Thickness/ Diame- ter (nm)	Surface Area (m <sup>2</sup> /g)	Electrode Density (g/cm <sup>3</sup> )	Current Density at 1C (mA/g)	Reference
Nanowire	9	194	0.42	0.52	[16]
	42	108	0.33	0.73	
	55	85	0.29	0.85	
Thin Film	40	10.7		0.033	This work
	60	7.15	2.329	0.045	
	80	5.36		0.067	

The amorphous TF electrodes were produced by sputtering Si directly onto the copper current collector as described elsewhere [40]. The NW electrodes consisted of 50 wt.% Si, 25 wt.% carboxymethylcellulose (CMC) and 25 wt.% carbon black by weight, and loading ranged from 0.25 to 0.41 mg/cm<sup>2</sup>. CR2032 half-cells were constructed using Celgard separator and the electrolyte consisted of 1/1 v/v ethylene carbonate/diethylene carbonate (EC/DEC), with 1M LiPF<sub>6</sub>, 10 wt.% fluoroethylene carbonate (FEC), and 2 wt.% vinylene carbonate (VC). Further details can be found in the original manuscript [16].

The thin film electrodes were prepared by plasma-enhanced chemical vapor deposition (PECVD, Oxford Instruments Plasmalab System133) using silane (SiH<sub>4</sub>) as a precursor. The films were deposited on flat copper substrates, which were washed with ethanol prior to deposition. The thickness of the film was controlled by the deposition time [41].

### 2.2. Cell Cycling and Data Analysis

Given the differences in purpose of the original work, the data generated from the materials in Table 1 were not produced under identical conditions. After formation at 0.05 C (22.5 to 36 μA/cm<sup>2</sup> depending on the electrode loading), the SiNWs were cycled at 0.2 C (90 to 144 μA/cm<sup>2</sup>) in the range of 0.01–1 V with a constant voltage hold at the end

of each lithiation step. The capacity of the carbon black (20 mAh/g) contributed less than 0.3% to the total capacity of the cells, and was therefore ignored. Cycling was performed on an Biologic VMP3 multichannel potentiostat (Biologic, Seyssinet-Pariset, France) [16].

After a formation stage consisting of three cycles at 0.05 C (1.7 to 3.4  $\mu\text{A}/\text{cm}^2$  depending on the film thickness), the SiTFs were cycled using a constant current of 0.5 C (16.8 to 33.5  $\mu\text{A}/\text{cm}^2$ ) in the range of 0.05–1 V with regular diagnostic cycles after every 50 cycles. The diagnostic cycles consisted of one cycle at 0.05 C, two cycles at 0.2 (6.7 to 13.4  $\mu\text{A}/\text{cm}^2$ ), C, and two cycles at 0.5 C. Cycling experiments were conducted at 25 °C in temperature-controlled cabinets (VWR INCU-Line) using an Arbin LBT battery tester.

Fitting was performed in Python using the lmfit package.

### 3. Results and Discussion

The fitting function describing the capacity  $Q$  as a function of the potential  $E$  is described by Equation (1):

$$f(E) = \sum_{k=1}^n Q_k \left[ w_k \left( \frac{1}{2} \left( 1 + \Phi_k \left( \frac{E - c_k}{\sqrt{2}s_k} \right) \right) - 2T_k \left( \frac{E - c_k}{\sqrt{2}s_k}, \alpha_k \right) \right) + (1 - w_k) \left( \frac{1}{\pi} \arctan \left( \frac{E - c_k}{\gamma} \right) + \frac{1}{2} \right) \right] \quad (1)$$

where  $c$  is the position of the phase,  $s$  is the scale of the skew-Gaussian part, and  $\alpha$  is the skewness factor which describes the deviation of the phase from normality.  $\Phi$  and  $T$  are the error function and Owen's T functions, respectively.  $\gamma$  is the scale parameter of the Lorentzian part, also known as the half-width-at-half-maximum (HWHM). The weighting parameter  $w$  is used to separate the contribution to  $Q$  of the peaks.  $k$  is the index of the electrochemical phases in the GCD curve, and  $n$  is the number of phases. The two scale parameters  $s$  and  $\gamma$  are not necessarily related, and have therefore been allowed to vary independently.

While parameters such as  $Q$  of Equation (1) are well defined and intrinsic to Si and the generated data, the rest are not, and likely depend on environmental factors such as material surface area and thickness, and cell resistances. That said, some educated guesses can be made as to the meaning of these parameters. The position  $c$  is theoretically equal to the equilibrium potential, but in practice, overpotentials and artefacts due to the quality of data will shift the resulting values of  $c$  away from equilibrium. Both of the scale parameters  $s$  and  $\gamma$  are inverse rate parameters and relate to how fast the process occurs. An ideal battery material at equilibrium would display no voltage change over the course of the phase change and an infinite gradient at the beginning and end of the phase. This would result in values of 0 for  $s$  and  $\gamma$  [25]. The skew parameter  $\alpha$  is a measure of the deviation from normality, and therefore represents a "lagging" effect. The size of  $\alpha$  is therefore expected to be proportional with the C-rate (with  $\alpha \rightarrow 0$  at equilibrium conditions), and is likely related to the diffusivity. Finally, the weighting parameter  $w$  defines the degree to which each of the two peaks contributes to the total capacity of the phase. This determines whether the phase is limited by the parameters in the skew-Gaussian or the Lorentzian part of the equation. To adequately fit Si data, it is first necessary to set up the correct initial parameters and choose data that can be fit. Because the lithiation of Si takes place at or near the cut-off potential, the tail end of the lithiation phase is too close to the cut-off potential to give good fits. We therefore apply this technique to the delithiation cycle only.

#### 3.1. Parameter Setup and Goodness of Fit

The initial parameter setup for fitting is set according to the known behaviour of Si during delithiation. The alloying phases of Si during lithiation and delithiation have been determined by NMR and PDF, and it has been shown that Si forms amorphous or crystalline phases depending on cycling conditions [6,23,42]. During delithiation, Li is removed from amorphous  $\text{Li}_{3.5}\text{Si}$  in two distinct phases, yielding a value of  $n = 2$  for Equation (1). The two phases are named I and II, and the parameters of the phases are distinguished using the subscripts I and II, respectively. Phase I ( $\text{Li}_{3.5}\text{Si} \rightarrow \text{Li}_2\text{Si}$ ) is located at about 0.3 V, while phase II ( $\text{Li}_2\text{Si} \rightarrow \text{Si}$ ) is located at about 0.48 V. From the stoichiometry

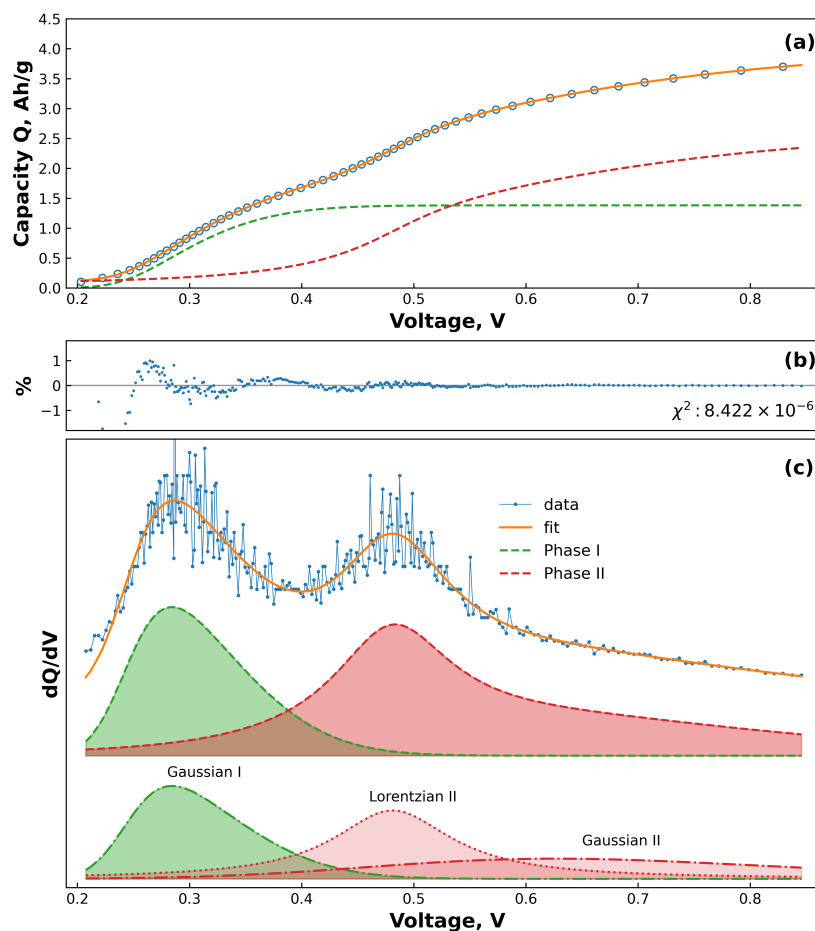
of these two phases it is also possible to estimate the initial  $Q$  parameters, assuming that the material at the beginning of the GCD step consists purely of  $\text{Li}_{3.5}\text{Si}$ , and the delithiation is complete (i.e., only Si remains at the end of the cycle). This gives a theoretical stoichiometry of 1.5:2, equivalent to 43% of the capacity coming from phase I, while the remaining 57% comes from phase II.

Figure 1 shows an example of the residual and fit of each phase to a GCD curve, along with the equivalent  $dQ/dV$ . Figure 1a shows how the fitting function agrees with the data, along with how the two phases contribute to the total curve. The plot of the residuals in Figure 1b shows an overall excellent fit to the data, with the error not exceeding 1.5%. Analysis of the errors of the individual parameters reveals that the errors are almost all less than 10% of the parameter value, and the majority are below 5%. The exception to this is the parameter  $c$ , which due to the small values of  $c$  compared to the other parameters, displayed larger errors of up to ten times the parameter value. The equivalent  $dQ/dV$  is plotted in Figure 1c, with the bottom set of curves showing how the results of the fit is split into skew-Gaussian and Lorentzian curves. Phase I displays no Lorentzian behaviour, and phase II shows a sharp Lorentzian curve as well as a very broad skew-Gaussian curve. This shows that there is excellent agreement between the shape and position of the phases and the results of the fit equations, and reveals that the model is an accurate representation of the shape of the curve. Further, Figure 1c shows that the shapes of the phases are not symmetric about the position  $c$  and that the skewness factor  $\alpha$  is crucial to accurately describe the behaviour of the delithiation curves.

### 3.2. Comparison of Thin Films and Nanowires

Characterization of the NWs may be found in the original work [16]. The Coulombic efficiencies (CE) of the samples exceeded the 99.5% required for long-term cycling after about 20 cycles. An in-depth discussion of the NW CE is given in the original work [16]. Figure 2 shows how the curves change with repeated cycling for an example of 40 nm TFs (Figure 2a) and 9 nm NWs (Figure 2b). This shows that the individual phases of the two samples behave quite differently, and also shows how important it is to consider the many experimental variables that contribute to cell behaviour. If we were to only look at the complete  $dQ/dV$  (grey curves), we might be convinced that both TFs and NWs behave quite similarly. For example, the position of phase I appears to be at about 0.32 V for both samples. However, by looking at the behaviour of only phase I (green curves), it can be seen that this phase is more skewed (higher  $\alpha$ ) for the TF sample than the NW sample. Simultaneously, the position of phase I ( $c_I$ , shown as coloured circles on the curves at 0.3 V) is decreasing for the TF sample, but increasing for the NW sample. Note that the position of a phase is not necessarily the point at which the  $dQ/dV$  displays a maximum. Similarly, comparing phase II using only the total  $dQ/dV$  behaviour would limit us to discussing only the small shift in peak position experienced by the NWs. Instead, by looking at the behaviour of phase II alone (red curves), it can be seen that the Lorentzian portion of the curve is consistently narrower for TFs than for NWs and that the skew-Gaussian portion of phase II is fading slower for TFs than for NWs. This shows that the fitting function provides a powerful tool for analysing the behaviour of Si phases according to their component curves.

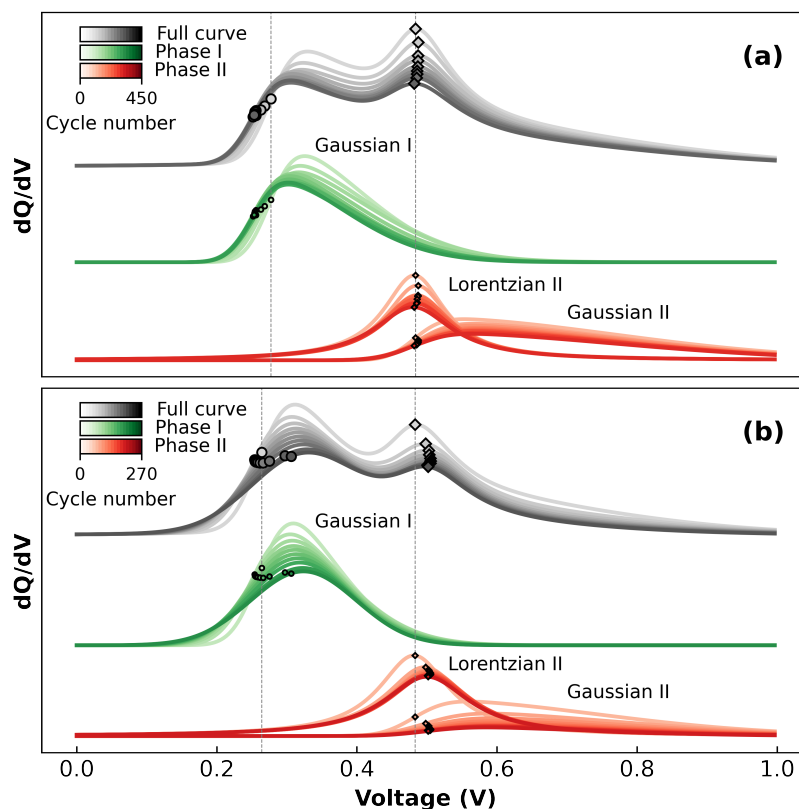
As seen in Figure 2, the behaviour of a parameter is affected by all other parameters and it is therefore difficult to separate their behaviour and ascribe meaning to them. Nevertheless, in order to show the changes in the datasets over time, the plots of the individual parameters  $\alpha$ ,  $c$ ,  $s$ ,  $\gamma$ , and  $w$  are shown in the SI.



**Figure 1.** An example of the goodness of fit of cycle number 5 from a 40 nm SiTF cell. (a) The raw output of the fitting model, showing the input data as blue points overlaid with the best-fit determined by the program (orange line). The dotted lines are the curves of the individual phases which together make up the full fitting function. (b) Residuals of the fit, displayed as a percentage difference from the measured points. (c) The data from (a), displayed as a  $dQ/dV$  plot. The top offset shows the data as blue points overlaid with the best fit (orange line). The middle offset shows the contribution to the fit of phase I (green) and phase II (red). The bottom offset shows how the phases are composed of skew-Gaussian and Lorentzian curves.

The differences in behaviour of the TFs and NWs shown in Figure 2 give insights into the behaviour of the materials, and can give information about how Equation (1) relates to physical phenomena occurring in the cells. For instance, the increased skewness seen in the phase I peak for TFs (Figure 2a) indicates that there is a relatively large “lagging” effect as the potential increases faster than the diffusion can equilibrate. This is consistent with the expectation that the delithiation is hindered by the long diffusion distance of Li to the surface of the Si. The less skewed phase I NW peak (Figures 2b and S1a) supports this hypothesis, as the thin NWs have lower diffusion lengths, and can diffuse Li in radial directions. The decrease in skewness factor  $\alpha_I$  seen when cycling the TFs at lower C-rates (Figure S1b) further corroborates this, as cycling at rates closer to equilibrium would decrease the diffusion overpotentials. Similarly, the differences in phase position  $c_I$  of phase I give information about two datasets. For thin films, the positions of phase I shift

from around 270 to 250 mV over the course of cycling, while NWs show the opposite trend, with the position increasing from 250 to 300 mV. In both cases, however, the positions of  $c_I$  (Figure S2) are very close to the equilibrium potentials determined by the previous literature [6,42,43]. This might indicate that the overpotentials are increasing with cycling in the case of NWs but not TFs, but given that the overpotentials in TFs would also be expected to increase, this explanation alone provides an incomplete picture of the behaviour of  $c_I$ . Rather, the exact position of  $c_I$  is likely decided by the combination of diffusion effects described by  $\alpha_I$ , and the growing iR drop encroaching on the phase. Since  $\alpha_I$  is relatively stable for TFs, pushing the “start” of the data to higher voltages forces the fitting function to compensate by shifting  $c_I$  to lower values. Conversely, the decreasing  $\alpha_I$  seen for NWs causes  $c_I$  to shift to the right. It is therefore clear that  $c_I$  is not a simple function of the equilibrium potential, but is affected by the behaviour of the cell at the very start of the cycle. It would therefore be more correct to deem  $c$  an “apparent” equilibrium potential [6,14,23,44].



**Figure 2.** Output of fitting Equation (1) to the data, displayed as  $dQ/dV$  and showing the evolution of the curves with cycling for (a) 40 nm TFs, and (b) 9 nm NWs. Each curve is an average of  $x$  cycles, where  $x$  is 1/10th of the total number of cycles. The locations of the dots and diamonds correspond to  $c_I$  and  $c_{II}$ , respectively. The dotted vertical lines denote  $c$  for the first cycles.

Finally, the scale parameter  $s_I$  gives information about how fast the delithiation is occurring in phase I [25]. While the total  $dQ/dV$  (grey curves, Figure 2a,b) seem to show that the width of the phase may be slightly narrower for TFs than NWs (Figure 2a and 2b, respectively), the output of the fitting shows that the opposite is true (Figure S3). Further, the slower TF cycles in Figure S3b show lower values of  $s_I$ , indicating that the resistance to



delithiation described by the skew-Gaussian component is dependent on the C-rate. This behaviour matches the expectation that as the applied current is reduced, the overpotentials will also be reduced [45]. This result matches the expectation that the thinner NWs should delithiate faster (relative to the applied current) than the thicker TFs due both to the decreased diffusion distance as well as the slower C-rates.

As with phase I, analysis of phase II gives important information about the behaviour of Si. Notably,  $c_{II}$  is independent of TF thickness, and only slightly decreased at slower C-rates (Figure S2b), varying from 460 to 480 mV. Meanwhile,  $c_{II}$  (shown as diamonds on the curves in Figure 2) for the NWs shows a small shift from 460 to 500 mV at the start of cycling before reaching a steady state. This initial increase could be due to an increase in overpotentials due to SEI formation in early cycles. The shift to lower potentials seen in phase I is not reflected in phase II because the position of phase II is relatively close to the middle of the dataset. Hence, there are enough datapoints at low voltages to adequately describe the curve. While phase I is described only by the skew-Gaussian component ( $w = 1$ ), phase II is described by a combination of both the skew-Gaussian and Lorentzian components. Due to  $\alpha_{II}$ , the contribution to capacity of the Lorentzian occurs earlier in the delithiation, and the contribution of the skew-Gaussian component is only significant after the maximum of the Lorentzian has been reached. The resulting behaviour indicates a relatively fast “burst” of delithiation described by the Lorentzian, followed by a slower “tail” described by the skew-Gaussian. As with the scale parameter  $s$  of the skew-Gaussian, the scale parameter  $\gamma$  of the Lorentzian also gives information about how quickly the reaction is occurring. However, unlike the behaviour seen for  $s_I$ ,  $\gamma_{II}$  is larger for NWs than for TFs (Figure S4a and S4b, respectively). This would indicate an increase in resistance to delithiation of the NWs compared to the TFs. As cycling progresses, the position of the phase is shifted to higher voltages due to increasing overpotentials, but the onset of delithiation (visible at around 0.25 V in Figure 2) remains constant. The result is that  $\gamma_{II}$  increases to cover the larger potential range over which the phase occurs.

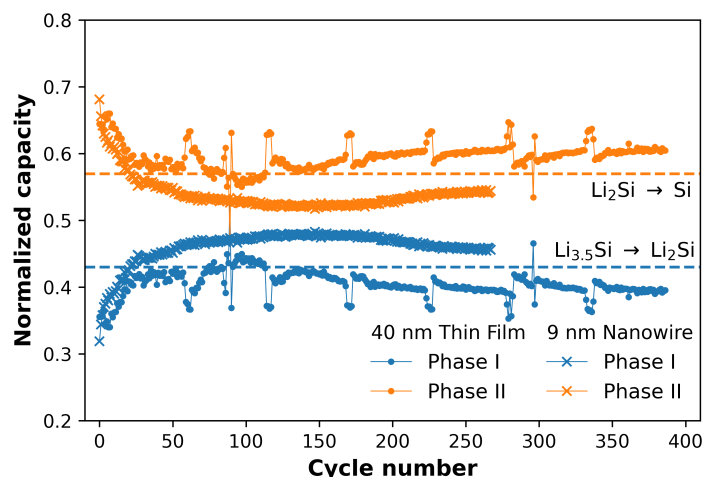
The skew-Gaussian component of phase II describes the end behaviour of the delithiation. As with  $\alpha_I$ ,  $\alpha_{II}$  is smaller for NWs than TFs (Figure S1a and S1b, respectively). This again matches the expectation that the diffusion of Li in the TFs takes longer due to the dimensionality and thickness of the materials. Similarly,  $s_{II}$  shows the same trend as  $s_I$ , and we can conclude that delithiation of phase II is hindered by the slow diffusion in the same way as for phase I.

When considering the behaviour of phase II, it is important to bear in mind the relative contribution to the phase of each component. The weighting parameter  $w$  determines whether the phase is “skew-Gaussian-limited” ( $w \rightarrow 1$ ) or “Lorentzian-limited” ( $w \rightarrow 0$ ). For the Si morphologies studied here,  $w_I$  was always found to be 1. This indicates that the capacity of this phase is skew-Gaussian-limited, at least within the C-rates studied. Figure S5 shows the behaviour of parameter  $w_{II}$  for phase II TFs and NWs. From this plot, it can be seen that  $w$  for TFs remains stable at around 0.5 during normal cycling, while for the NWs  $w$  begins at 0.45 and trends towards 0. This means that the resistances in the TFs are not dominated by either the skew-Gaussian nor the Lorentzian parameters, but the NWs are increasingly limited by the Lorentzian. This difference could be explained by the shrinking of the NWs during delithiation coupled with the growth of SEI in the electrode during cycling. This results in a loss of electrical contact between NWs and leads to a progressive increase in resistance greater than that experienced by the TFs. This hypothesis is supported by the fact that  $w_I = 1$  for all samples and morphologies tested because the highly lithiated  $\text{Li}_{3.5}\text{Si}$  phase is about 3.5 times more conductive than the  $\text{Li}_2\text{Si}$  phase, which is sufficient to overcome the SEI-related resistances [46].

### 3.3. Phases of Si Delithiation

To further highlight the ability of this method to show differences between the datasets in ways that are not obvious by  $dQ/dV$ , the capacities of the two phases normalized to the total capacity determined by the fitting are shown in Figure 3. The horizontal dotted

lines denote the initial guesses for the fitting of the phases as discussed in Section 3.1. While this shows that the assumption made initially, i.e., that the datasets consist of 100%  $\text{Li}_{3.5}\text{Si}$  at the start of delithiation and 100% Si at the end of delithiation, was not completely accurate, the fitting reveals interesting differences between the TF and NW samples. For both TFs and NWs, the first 10 to 20 cycles show an increase in the contribution to the total capacity from phase I. However, while phase I for the TFs contributes less capacity than expected throughout cycling, the capacity contribution from phase I for the NWs continues to increase and eventually exceeds the amount of capacity expected from the initial assumption made in Section 3.1. The initial increase in contribution from phase I can be explained by the progressive lithiation of Si at the start of repeated cycling proposed in the literature [19,20,47]. In this case, the resistance to lithiation of fresh Si electrodes results in the incomplete conversion of  $\text{Li}_2\text{Si} \rightarrow \text{Li}_{3.5}\text{Si}$  during lithiation. This means that at the start of the delithiation step the Si consists of a mixture of  $\text{Li}_{3.5}\text{Si}$  and  $\text{Li}_2\text{Si}$ , and results in less capacity contribution from phase I during delithiation, and more from phase II.



**Figure 3.** Comparison of the capacities of phases I (blue) and II (orange), for an example of thin films (dots) and nanowires (crosses). The data is normalized to the total capacity of each point as determined by the fitting. The horizontal dotted lines denote the initial guess of full conversion between the two phases.

The differences between the TFs and NWs at later cycles can be explained by differences in morphology and C-rate. With repeated cycling, the NWs experience more pronounced SEI growth than the TFs, and therefore increased electrode resistance. This causes the voltage cut-off of the delithiation step to be reached sooner, leading to incomplete delithiation of phase II to form Si, and a disproportionately large contribution to capacity from phase I. This agrees with the observation in Figure 2b that  $c_1$  is shifting to higher potentials. For TFs, the SEI growth occurs relatively slowly (compared to the NWs) and so the electrode resistance plays a less important role. Instead, the larger Li ion diffusion length experienced by the relatively thick TFs, combined with the faster C-rate used for cycling, leads to incomplete formation of  $\text{Li}_{3.5}\text{Si}$  during lithiation. This means that, as with the first 10–20 cycles, the electrode consists of a mixture of  $\text{Li}_{3.5}\text{Si}$  and  $\text{Li}_2\text{Si}$  rather than just  $\text{Li}_{3.5}\text{Si}$ , and the amount of capacity extracted from phase II is increased.

#### 3.4. Voltage Slippage and Excess Li Effects

To demonstrate how well the fitting function describes the data with repeated cycling, an example of the capacities of the each of the two phases, along with the experimentally measured capacity and the total capacity output by the model are given in Figure 4a as a

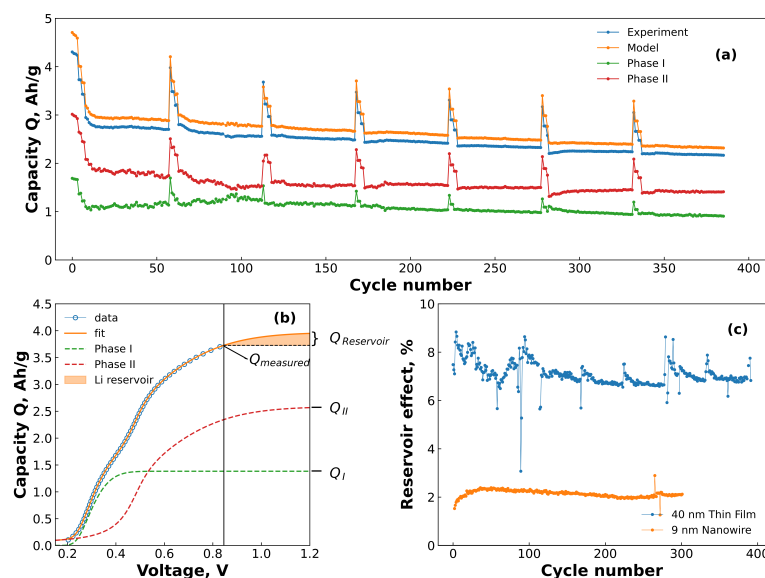
function of the cycle number. It can be seen that the model consistently overestimates the total capacity of the cell. This is because as the slope of the voltage–capacity curve is not 0 at the cut-off potential, indicating that the cell is not fully delithiated at the end of the cycle. This extra capacity has previously been described as a “reservoir effect”, made up of unreleased Li and voltage slippage effects [48]. The size of this reservoir can be estimated from the results of the fit by the simple relation:

$$Q_{\text{reservoir}} = Q_{\text{model}} - Q_{\text{measured}} \quad (2)$$

where

$$Q_{\text{model}} = Q_I + Q_{II} \quad (3)$$

Using these formulae, it is therefore possible to calculate the size of the reservoir effect in the electrode and follow its behaviour with time. Figure 4b shows schematically how the reservoir starts to grow after the voltage cut-off (black line) until it reaches a steady value when  $Q_{\text{reservoir}}$  stops increasing. Figure 4c shows the results of applying Equation (2) to the results from the two datasets, plotted as a percentage of the measured capacity ( $Q_{\text{reservoir}} / Q_{\text{measured}}$ ). From this plot it can be seen that the size of the reservoir is strongly dependent on the morphology, with the NWs averaging about 2%, while the TFs maintain a relatively stable reservoir of about 7% of the measured capacity. However, it should be emphasised that the C-rates used to generate data for the two morphologies were not the same, with the TFs cycling at a C-rate 2.5x greater than the NWs. This will likely also contribute to the difference as the TFs have less time to delithiate fully, resulting in a larger reservoir. Nevertheless, the ability of the fitting function to discern these differences and estimate the size of the reservoir is quite valuable.



**Figure 4.** (a) An example of the capacity vs cycle life of a thin film sample (blue points), including the capacity contributions of each phase (green and red points) to the total capacity from the model (orange points). (b) Plot showing the capacity of the cell as the voltage is extended beyond the cut-off potential. The blue dots denote the raw data, while the orange line denotes the best fit. The black vertical line at  $\sim 0.85$  V denotes the end of the measured data (i.e., the cut-off potential). The orange shaded area is the reservoir. (c) The reservoir of the different materials as calculated from Equation (2). The data is displayed as a percentage of the  $Q_{\text{measured}}$  for each material.

#### 4. Conclusions

Two datasets of previously published data consisting of delithiation cycling data from a thin film and a nanowire study performed by different groups, were analysed using an empirical cumulative distribution function consisting of a skewed pseudo-Voigt. Both datasets featured Si half-cells cycled in the amorphous region of Si and the skewed pseudo-Voigt was applied to each of the two electrochemical phases  $\text{Li}_{3.5}\text{Si}$  (phase I) and  $\text{Li}_2\text{Si}$  (phase II). The fitting function was found to give excellent fits to both datasets at C-rates far above equilibrium conditions, and was able to determine differences and similarities between the two morphologies studied. Phase I of the NW samples were found to be less skewed than the TFs, indicating faster delithiation. However, loss of contact between NWs and excess SEI growth also lead to increased resistances of the electrodes, in particular for the less electronically conductive phase II. Analysis of the results showed that the fitting function could determine the contribution to capacity of each of the two phases involved in the delithiation of amorphous Si and showed that this is strongly dependent on morphology and cycling rates, with NW electrodes exhibiting lower contribution to capacity than expected from phase II due to greater electrode resistance, despite the larger surface area available for delithiation. Further, the results were shown to be useful in determining the extent of the reservoir effect of the cells, and showed that the thin films exhibited a greater reservoir at the end of the delithiation step compared to the nanowires. This was presumed to be due in part to the greater delithiation path length, and partly to the higher C-rate used in cycling. In conclusion, the fitting function shows promise as a tool to extract more information from Si cycling data even if that data is not generated with the express goal of fitting, and we invite other researchers to apply this method to their past and future data.

**Supplementary Materials:** The following supporting information can be downloaded at: <https://www.mdpi.com/article/10.3390/batteries9050251/s1>. Figure S1: The skew parameter  $\alpha$  for phases I and II for (a) NWs and (b) TFs, as a function of the cycle life; Figure S2: The equilibrium potential  $c$  for phases I and II for (a) NWs and (b) TFs, plotted as a function of the cycle life; Figure S3: The scale parameter  $s$  of the Gaussian component for phases I and II for (a) NWs and (b) TFs, plotted as a function of the cycle life; Figure S4: The scale parameter  $\lambda$  of the Lorentzian component for phase I for (a) NWs and (b) TFs, plotted as a function of the cycle life; Figure S5: The weighting parameter  $w$  for phases I and II for (a) NWs and (b) TFs, as a function of the cycle life.

**Author Contributions:** Conceptualization, F.T.H.; Methodology, F.T.H. and J.P.M.; Software, F.T.H.; Validation, F.T.H., C.K., J.P.M. and O.E.E.; Formal Analysis, F.T.H.; Investigation, F.T.H.; Data Curation, F.T.H., C.K., S.Y.L., A.Y.K. and J.P.M.; Writing—Original Draft Preparation, F.T.H.; Writing—Review and Editing, F.T.H., C.K., J.P.M., O.E.E., S.Y.L., A.Y.K. and Z.Y.; Visualization, F.T.H.; Supervision, F.L. and Z.Y.; Project Administration, F.L.; Funding Acquisition, F.L. All authors have read and agreed to the published version of the manuscript.

**Funding:** This research was funded by the Research Council of Norway grant number 304644.

**Institutional Review Board Statement:** Not applicable.

**Informed Consent Statement:** Not applicable.

**Data Availability Statement:** Data is available upon reasonable request.

**Acknowledgments:** The authors acknowledge Rasim Batmaz and Jørn Døvling of Beyonder for their advice and many useful discussions. The thin film electrochemical experiments were funded by the Research Council of Norway through the ENERGIX Project No. 280985, and performed within MoZEES, a Norwegian Centre for Environment-friendly Energy Research (FME), co-sponsored by the Research Council of Norway (project number 257653) and 40 partners from research, industry, and the public sector. The authors would also like to thank Pascale Chenevier for her advice on SiNWs.

**Conflicts of Interest:** F.T.H., O.E.E. and F.L. declare that they are employees of Beyonder AS, a Norwegian battery manufacturer. F.T.H. and F.L. further declare that they own stock in Beyonder AS. The remaining authors do not declare a conflict of interest.

## References

1. Yin, Y.; Wan, L.; Guo, Y. Silicon-Based Nanomaterials for Lithium-Ion Batteries. *Chin. Sci. Bull.* **2012**, *57*, 4104–4110. [[CrossRef](#)]
2. McDowell, M.T.; Lee, S.W.; Nix, W.D.; Cui, Y. 25th Anniversary Article: Understanding the Lithiation of Silicon and Other Alloying Anodes for Lithium-Ion Batteries. *Adv. Mater.* **2013**, *25*, 4966–4985. [[CrossRef](#)] [[PubMed](#)]
3. Li, P.; Zhao, G.; Zheng, X.; Xu, X.; Yao, C.; Sun, W.; Dou, S.X. Recent Progress on Silicon-Based Anode Materials for Practical Lithium-Ion Battery Applications. *Energy Storage Mater.* **2018**, *15*, 422–446. [[CrossRef](#)]
4. Bloom, I.; Jansen, A.N.; Abraham, D.P.; Knuth, J.; Jones, S.A.; Battaglia, V.S.; Henriksen, G.L. Differential Voltage Analyses of High-Power, Lithium-Ion Cells 1. *J. Power Sources* **2005**, *139*, 295–303. [[CrossRef](#)]
5. Chevrier, V.L.; Zwanziger, J.W.; Dahn, J.R. First Principles Studies of Silicon as a Negative Electrode Material for Lithium-Ion Batteries. *Can. J. Phys.* **2009**, *87*, 625–632. [[CrossRef](#)]
6. Ogata, K.; Salager, E.; Kerr, C.; Fraser, A.; Ducati, C.; Morris, A.; Hofmann, S.; Grey, C. Revealing Lithium–Silicide Phase Transformations in Nano-Structured Silicon-Based Lithium Ion Batteries via in Situ NMR Spectroscopy. *Nat. Commun.* **2014**, *5*, 3217. [[CrossRef](#)]
7. Chevrier, V.L.; Liu, L.; Wohl, R.; Chandrasoma, A.; Vega, J.A.; Eberman, K.W.; Stegmaier, P.; Figgemeier, E. Design and Testing of Prelithiated Full Cells with High Silicon Content. *J. Electrochem. Soc.* **2018**, *165*, A1129–A1136. [[CrossRef](#)]
8. Kitada, K.; Pecher, O.; Magusin, P.C.M.M.; Groh, M.F.; Weatherup, R.S.; Grey, C.P. Unraveling the Reaction Mechanisms of SiO Anodes for Li-Ion Batteries by Combining *In Situ*  $^7\text{Li}$  and *Ex Situ*  $^7\text{Li}/^{29}\text{Si}$  Solid-State NMR Spectroscopy. *J. Am. Chem. Soc.* **2019**, *141*, 7014–7027. [[CrossRef](#)]
9. Beaulieu, L.Y.; Hatchard, T.D.; Bonakdarpour, A.; Fleischauer, M.D.; Dahn, J.R. Reaction of Li with Alloy Thin Films Studied by In Situ AFM. *J. Electrochem. Soc.* **2003**, *150*, A1457. [[CrossRef](#)]
10. Limthongkul, P.; Jang, Y.I.; Dudney, N.J.; Chiang, Y.M. Electrochemically-Driven Solid-State Amorphization in Lithium-Silicon Alloys and Implications for Lithium Storage. *Acta Mater.* **2003**, *51*, 1103–1113. [[CrossRef](#)]
11. Obrovac, M.N.; Krause, L.J. Reversible Cycling of Crystalline Silicon Powder. *J. Electrochem. Soc.* **2007**, *154*, A103. [[CrossRef](#)]
12. Wang, M.; Xiao, X.; Huang, X. Study of Lithium Diffusivity in Amorphous Silicon via Finite Element Analysis. *J. Power Sources* **2016**, *307*, 77–85. [[CrossRef](#)]
13. Swamy, T.; Chiang, Y.M. Electrochemical Charge Transfer Reaction Kinetics at the Silicon-Liquid Electrolyte Interface. *J. Electrochem. Soc.* **2015**, *162*, A7129–A7134. [[CrossRef](#)]
14. Sethuraman, V.A.; Srinivasan, V.; Newman, J. Analysis of Electrochemical Lithiation and Delithiation Kinetics in Silicon. *J. Electrochem. Soc.* **2013**, *160*, A394–A403. [[CrossRef](#)]
15. Lai, S.Y.; Mæhlen, J.P.; Preston, T.J.; Skare, M.O.; Nagell, M.U.; Ulvestad, A.; Lemordant, D.; Kopolov, A.Y. Morphology Engineering of Silicon Nanoparticles for Better Performance in Li-ion Battery Anodes. *Nanoscale Adv.* **2020**, *2*, 5335–5342. [[CrossRef](#)]
16. Keller, C.; Desrués, A.; Karuppiah, S.; Martin, E.; Alper, J.; Boismain, F.; Villevieille, C.; Herlin-Boime, N.; Haon, C.; Chenevier, P. Effect of Size and Shape on Electrochemical Performance of Nano-Silicon-Based Lithium Battery. *Nanomaterials* **2021**, *11*, 307. [[CrossRef](#)] [[PubMed](#)]
17. Alvarez Barragan, A.; Nava, G.; Wagner, N.J.; Mangolini, L. Silicon-Carbon Composites for Lithium-Ion Batteries: A Comparative Study of Different Carbon Deposition Approaches. *J. Vac. Sci. Technol. Nanotechnol. Microelectron. Mater. Process. Meas. Phenom.* **2018**, *36*, 011402. [[CrossRef](#)]
18. Bernard, P.; Alper, J.P.; Haon, C.; Herlin-Boime, N.; Chandresis, M. Electrochemical Analysis of Silicon Nanoparticle Lithiation — Effect of Crystallinity and Carbon Coating Quantity. *J. Power Sources* **2019**, *435*, 226769. [[CrossRef](#)]
19. Huld, F.T.; Lai, S.Y.; Tucho, W.M.; Batmaz, R.; Jensen, I.T.; Lu, S.; Eleri, O.E.; Kopolov, A.Y.; Yu, Z.; Lou, F. Enabling Increased Delithiation Rates in Silicon-Based Anodes through Alloying with Phosphorus. *ChemistrySelect* **2022**, *7*, e202202857. [[CrossRef](#)]
20. Ulvestad, A.; Skare, M.O.; Foss, C.E.; Krogsæter, H.; Reichstein, J.F.; Preston, T.J.; Mæhlen, J.P.; Andersen, H.F.; Kopolov, A.Y. Stoichiometry-Controlled Reversible Lithiation Capacity in Nanostructured Silicon Nitrides Enabled by in Situ Conversion Reaction. *ACS Nano* **2021**, *15*, 16777–16787. [[CrossRef](#)]
21. Chen, L.; Xie, X.; Xie, J.; Wang, K.; Yang, J. Binder Effect on Cycling Performance of Silicon/Carbon Composite Anodes for Lithium Ion Batteries. *J. Appl. Electrochem.* **2006**, *36*, 1099–1104. [[CrossRef](#)]
22. Huang, L.H.; Li, C.C. Effects of Interactions between Binders and Different-Sized Silicons on Dispersion Homogeneity of Anodes and Electrochemistry of Lithium-Silicon Batteries. *J. Power Sources* **2019**, *409*, 38–47. [[CrossRef](#)]
23. Li, J.; Dahn, J.R. An In Situ X-Ray Diffraction Study of the Reaction of Li with Crystalline Si. *J. Electrochem. Soc.* **2007**, *154*, A156. [[CrossRef](#)]
24. McDowell, M.T.; Ryu, I.; Lee, S.W.; Wang, C.; Nix, W.D.; Cui, Y. Studying the Kinetics of Crystalline Silicon Nanoparticle Lithiation with In Situ Transmission Electron Microscopy. *Adv. Mater.* **2012**, *24*, 6034–6041. [[CrossRef](#)] [[PubMed](#)]
25. Olson, J.Z.; López, C.M.; Dickinson, E.J.F. Differential Analysis of Galvanostatic Cycle Data from Li-Ion Batteries: Interpretative Insights and Graphical Heuristics. *Chem. Mater.* **2023**, *35*, 1487–1513. [[CrossRef](#)]
26. Palagonia, M.S.; Erinmwingbovo, C.; Brogioli, D.; La Mantia, F. Comparison between Cyclic Voltammetry and Differential Charge Plots from Galvanostatic Cycling. *J. Electroanal. Chem.* **2019**, *847*, 113170. [[CrossRef](#)]
27. Dubarry, M.; Truchot, C.; Liaw, B.Y. Cell Degradation in Commercial LiFePO<sub>4</sub> Cells with High-Power and High-Energy Designs. *J. Power Sources* **2014**, *258*, 408–419. [[CrossRef](#)]

28. Dubarry, M.; Liaw, B.Y. Identify Capacity Fading Mechanism in a Commercial LiFePO<sub>4</sub> Cell. *J. Power Sources* **2009**, *194*, 541–549. [[CrossRef](#)]
29. Dubarry, M.; Liaw, B.Y.; Chen, M.S.; Chyan, S.S.; Han, K.C.; Sie, W.T.; Wu, S.H. Identifying Battery Aging Mechanisms in Large Format Li Ion Cells. *J. Power Sources* **2011**, *196*, 3420–3425. [[CrossRef](#)]
30. Li, Y.; Abdel-Monem, M.; Gopalakrishnan, R.; Berecibar, M.; Nanini-Maury, E.; Omar, N.; van den Bossche, P.; Van Mierlo, J. A Quick On-Line State of Health Estimation Method for Li-ion Battery with Incremental Capacity Curves Processed by Gaussian Filter. *J. Power Sources* **2018**, *373*, 40–53. [[CrossRef](#)]
31. Li, X.; Wang, Z.; Yan, J. Prognostic Health Condition for Lithium Battery Using the Partial Incremental Capacity and Gaussian Process Regression. *J. Power Sources* **2019**, *421*, 56–67. [[CrossRef](#)]
32. He, J.; Bian, X.; Liu, L.; Wei, Z.; Yan, F. Comparative Study of Curve Determination Methods for Incremental Capacity Analysis and State of Health Estimation of Lithium-Ion Battery. *J. Energy Storage* **2020**, *29*, 101400. [[CrossRef](#)]
33. Yoon, T.; Nguyen, C.C.; Seo, D.M.; Lucht, B.L. Capacity Fading Mechanisms of Silicon Nanoparticle Negative Electrodes for Lithium Ion Batteries. *J. Electrochem. Soc.* **2015**, *162*, A2325–A2330. [[CrossRef](#)]
34. Thompson, N.; Cohen, T.; Alamdari, S.; Hsu, C.W.; Williamson, G.; Beck, D.; Holmberg, V. DiffCapAnalyzer: A Python Package for Quantitative Analysis of Total Differential Capacity Data. *J. Open Source Softw.* **2020**, *5*, 2624. [[CrossRef](#)]
35. Li, X.; Jiang, J.; Wang, L.Y.; Chen, D.; Zhang, Y.; Zhang, C. A Capacity Model Based on Charging Process for State of Health Estimation of Lithium Ion Batteries. *Appl. Energy* **2016**, *177*, 537–543. [[CrossRef](#)]
36. Bian, X.; Liu, L.; Yan, J. A Model for State-of-Health Estimation of Lithium Ion Batteries Based on Charging Profiles. *Energy* **2019**, *177*, 57–65. [[CrossRef](#)]
37. Pang, H.; Guo, L.; Wu, L.; Jin, J.; Zhang, F.; Liu, K. A Novel Extended Kalman Filter-Based Battery Internal and Surface Temperature Estimation Based on an Improved Electro-Thermal Model. *J. Energy Storage* **2021**, *41*, 102854. [[CrossRef](#)]
38. Pang, H.; Wu, L.; Liu, J.; Liu, X.; Liu, K. Physics-Informed Neural Network Approach for Heat Generation Rate Estimation of Lithium-Ion Battery under Various Driving Conditions. *J. Energy Chem.* **2023**, *78*, 1–12. [[CrossRef](#)]
39. Sivonxay, E.; Aykol, M.; Persson, K.A. The Lithiation Process and Li Diffusion in Amorphous SiO<sub>2</sub> and Si from First-Principles. *Electrochim. Acta* **2020**, *331*, 135344. [[CrossRef](#)]
40. Hasa, I.; Haregewoin, A.M.; Zhang, L.; Tsai, W.Y.; Guo, J.; Veith, G.M.; Ross, P.N.; Kostecki, R. Electrochemical Reactivity and Passivation of Silicon Thin-Film Electrodes in Organic Carbonate Electrolytes. *ACS Appl. Mater. Interfaces* **2020**, *12*, 40879–40890. [[CrossRef](#)]
41. Ulvestad, A.; Mæhlen, J.P.; Kirkengen, M. Silicon Nitride as Anode Material for Li-ion Batteries: Understanding the SiN<sub>x</sub> Conversion Reaction. *J. Power Sources* **2018**, *399*, 414–421. [[CrossRef](#)]
42. Key, B.; Morcrette, M.; Tarascon, J.M.; Grey, C.P. Pair Distribution Function Analysis and Solid State NMR Studies of Silicon Electrodes for Lithium Ion Batteries: Understanding the (De)Lithiation Mechanisms. *J. Am. Chem. Soc.* **2011**, *133*, 503–512. [[CrossRef](#)] [[PubMed](#)]
43. Tritsaris, G.A.; Zhao, K.; Okeke, O.U.; Kaxiras, E. Diffusion of Lithium in Bulk Amorphous Silicon: A Theoretical Study. *J. Phys. Chem. C* **2012**, *116*, 22212–22216. [[CrossRef](#)]
44. Ulvestad, A.; Andersen, H.F.; Jensen, I.J.T.; Mongstad, T.T.; Mæhlen, J.P.; Prytz, Ø.; Kirkengen, M. Substoichiometric Silicon Nitride—An Anode Material for Li-ion Batteries Promising High Stability and High Capacity. *Sci. Rep.* **2018**, *8*, 8634. [[CrossRef](#)]
45. Fly, A.; Chen, R. Rate Dependency of Incremental Capacity Analysis (dQ/dV) as a Diagnostic Tool for Lithium-Ion Batteries. *J. Energy Storage* **2020**, *29*, 101329. [[CrossRef](#)]
46. Pollak, E.; Salitra, G.; Baranchugov, V.; Aurbach, D. In Situ Conductivity, Impedance Spectroscopy, and Ex Situ Raman Spectra of Amorphous Silicon during the Insertion/Extraction of Lithium. *J. Phys. Chem. C* **2007**, *111*, 11437–11444. [[CrossRef](#)]
47. Foss, C.E.L.; Müssig, S.; Svensson, A.M.; Vie, P.J.S.; Ulvestad, A.; Mæhlen, J.P.; Kozosov, A.Y. Anodes for Li-ion Batteries Prepared from Microcrystalline Silicon and Enabled by Binder's Chemistry and Pseudo-Self-Healing. *Sci. Rep.* **2020**, *10*, 13193. [[CrossRef](#)]
48. Rodrigues, M.T.F. Capacity and Coulombic Efficiency Measurements Underestimate the Rate of SEI Growth in Silicon Anodes. *J. Electrochem. Soc.* **2022**, *169*, 080524. [[CrossRef](#)]

**Disclaimer/Publisher's Note:** The statements, opinions and data contained in all publications are solely those of the individual author(s) and contributor(s) and not of MDPI and/or the editor(s). MDPI and/or the editor(s) disclaim responsibility for any injury to people or property resulting from any ideas, methods, instructions or products referred to in the content.

## Supporting Information

### Revealing silicon's delithiation behaviour through empirical analysis of galvanostatic charge-discharge curves

Frederik T Huld<sup>1,2,†,\*</sup>, Jan Petter Mæhlen<sup>3</sup>, Caroline Keller<sup>4,5</sup>, Samson Y Lai<sup>2,3</sup>, Obinna E Eleri<sup>1,2,†</sup>, Alexey Y Koposov<sup>3,6\*</sup>, Zhixin Yu<sup>2\*</sup>, and Fengliu Lou<sup>1,\*</sup>

- 1 Beyonder, Stokkamyrveien 30, N-4313, Sandnes (Norway)
- 2 Department of Energy and Petroleum Engineering, University of Stavanger, Kjølvs Egelands hus, Kristine Bonnevis vei, 4021, Stavanger (Norway)
- 3 Department of Battery Technology, Institute for Energy Technology (IFE) Instituttveien 18, 2007, Kjeller (Norway)
- 4 Univ. Grenoble Alpes, CEA, CNRS, IRIG, SYMMES, 38000, Grenoble (France)
- 5 Univ. Grenoble Alpes, CEA, LITEN, DEHT, 38000, Grenoble (France)
- 6 Center for Materials Science and Nanotechnology, Department of Chemistry, P.O. Box 1033, Blindern, 0371, Oslo (Norway)

Correspondence:

frederik@beyonder.no (F.T.H.)

alexey.koposov@kjemi.uio.no (A.Y.K.)

zhixin.yu@uis.no (Z.Y.)

fengliu@beyonder.no (F.L.)

† Current address: Affiliation 2.

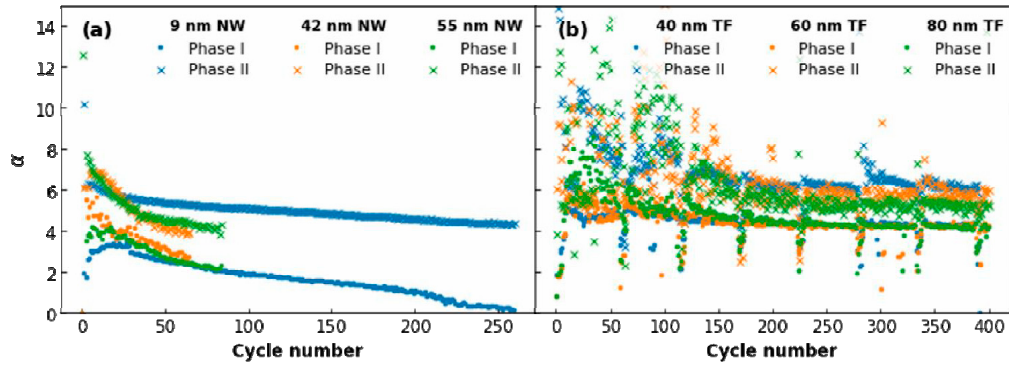


Figure S1 – The skew parameter  $\alpha$  for phases I and II for (a) NWs and (b) TFs, as a function of the cycle life.

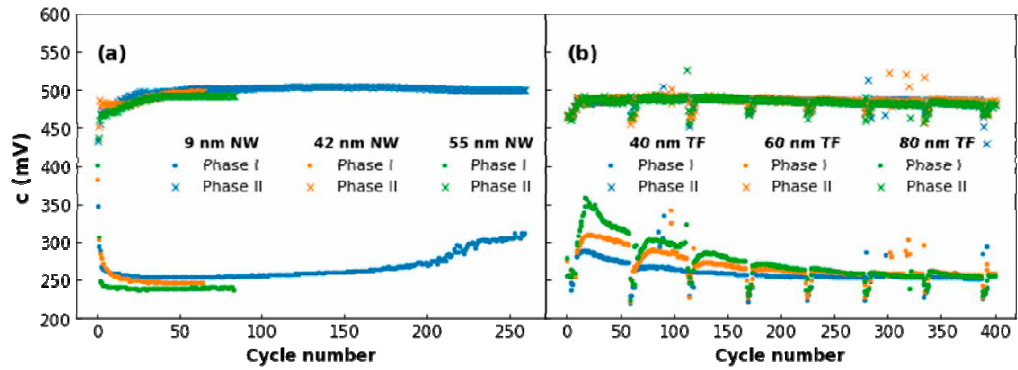


Figure S2 – The equilibrium potential  $c$  for phases I and II for (a) NWs and (b) TFs, plotted as a function of the cycle life.

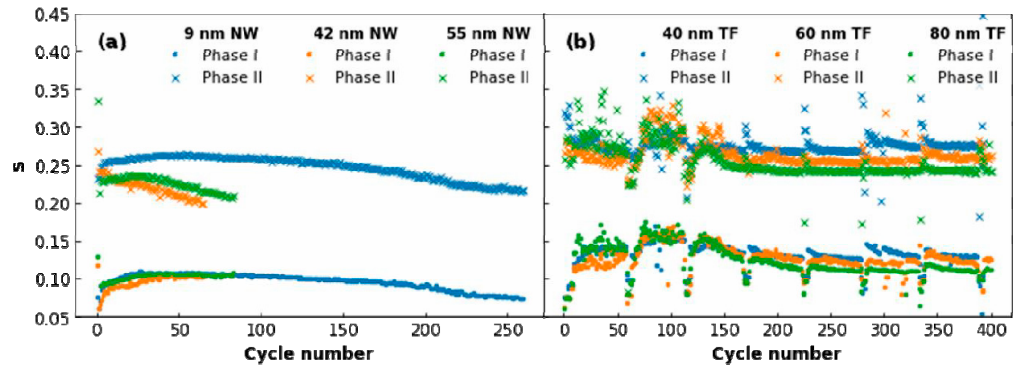


Figure S3 – The scale parameter  $s$  of the Gaussian component for phases I and II for (a) NWs and (b) TFs, plotted as a function of the cycle life



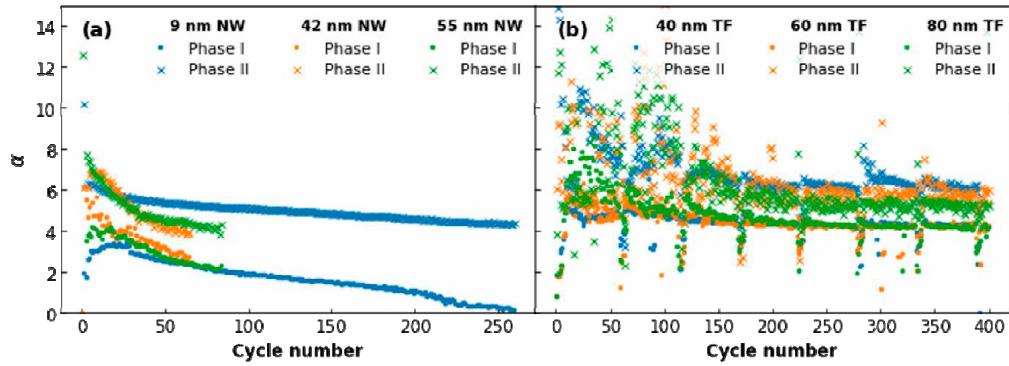


Figure S4 – The scale parameter  $\gamma$  of the Lorentzian component for phase I for (a) NWs and (b) TFs, plotted as a function of the cycle life

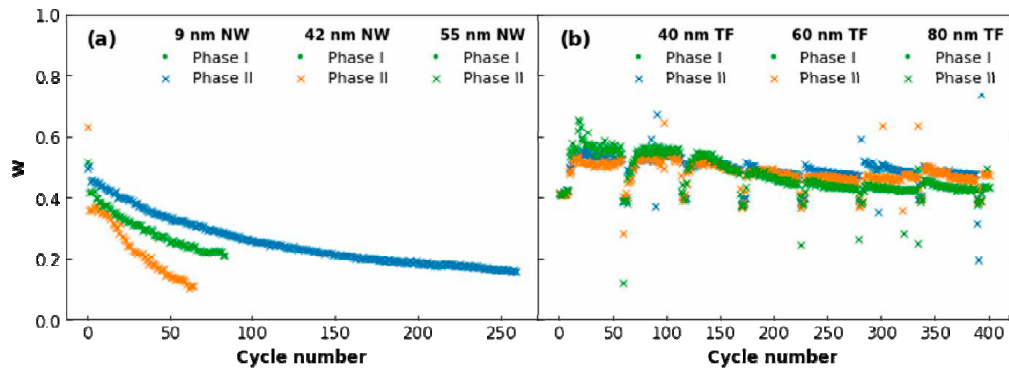


Figure S5 – The weighting parameter  $w$  for phases I and II for (a) NWs and (b) TFs, as a function of the cycle life



Cite this: DOI: 10.1039/d3ya00181d

# Unravelling the electrochemical impedance spectroscopy of silicon half cells with commercial loading†

Frederik T. Huld, \*<sup>ab</sup> Zhixin Yu \*<sup>a</sup> and Fengliu Lou\*<sup>b</sup>

Silicon (Si) is an important anode material for lithium ion batteries (LIBs), and increasing the loading of Si electrodes is an important step towards commercialization. However, half cells commonly used for Si studies are limited by polarization of the lithium (Li) counter electrode, especially at high Si loading. To study the interplay between Si and Li electrodes, a set of electrochemical impedance spectroscopy (EIS) spectra are generated using cycled Si half cells at four different potentials in the charge–discharge profile, and then repeated using symmetric Si/Si and Li/Li cells assembled from half cells cycled to equivalent stages in the cycle. Distribution of relaxation times (DRT) analysis is used to design equivalent circuits (ECs) for both Si/Si and Li/Li symmetric cells incorporating both electrolyte and electrode-related diffusion, and these are applied to the half cells. The results demonstrate that the behaviour of half cells is dominated by the solid electrolyte interphase (SEI) impedances at the Li counter electrode at the low and high potentials where the Li<sup>+</sup> mobility signal in Si is limited, while the Si electrode is dominant at intermediate potentials where the signal from mobile Li<sup>+</sup> is strong. EIS studies of Si half cells should therefore be performed at intermediate potentials, or as symmetric cells.

Received 25th April 2023,  
Accepted 22nd June 2023

DOI: 10.1039/d3ya00181d

rsc.li/energy-advances

## 1 Introduction

Silicon (Si) is widely touted as the future of lithium (Li) ion storage materials due to its large theoretical capacity of 3579 mA h g<sup>-1</sup>.<sup>1</sup> However, issues of stability have limited its use in commercial lithium-ion batteries (LIBs).<sup>2,3</sup> These issues arise in large part due to the extreme swelling (300%) experienced by the material during charging which causes rapid solid electrolyte interphase (SEI) growth.<sup>4</sup> This in turn quickly uses up cyclable lithium and electrolyte, leading to cell failure after only a few cycles.<sup>2,3,5,6</sup> Understanding and mitigating these failure mechanisms has resulted in a large amount of research in recent years, with published strategies ranging from coatings on nanomaterials, to nanostructuring, to use of dopants and heteroatoms.<sup>5,7–11</sup> However, in order to achieve good performance Si electrodes in the literature often contain very low loading.<sup>12</sup> This makes it difficult to assess the suitability of these materials for commercial applications where the loading requirements are much higher. Higher loading of Si in the

electrode exacerbate the issues of swelling and poor conductivity. As a result testing of these materials at high loading is a relatively unexplored area of research.<sup>12–14</sup> A further issue affecting high loading Si electrodes is the almost ubiquitous use of Li counter electrodes (CE). Li is highly polarizable and forms dendrites above 1 mA cm<sup>-2</sup>, which makes it difficult to produce reliable data.<sup>15,16</sup> Despite these disadvantages the use of Si/Li half cells in the literature is unlikely to cease, and it is therefore important to understand the interplay of the electrodes in these systems.

An established and sensitive method for studying the electrochemistry of Si is electrochemical impedance spectroscopy (EIS).<sup>17</sup> Unfortunately, this sensitivity means that distinguishing between features and noise is very difficult, and the design of the cell and the experiment surroundings is very important. For instance, performing EIS directly on half cells will result in the generated spectrum containing information from both the working and counter electrodes (WE and CE, respectively), as well as the electrolyte and separator located in between them. This can be avoided by introducing a reference electrode (RE) into the cell in proximity with the WE, but this increases the construction complexity and cost, and requires consideration of the RE electrode chemistry.<sup>15</sup> The use of symmetric cells (where both the WE and CE are identical) is also an option, but these cells cannot be cycled, and can therefore not easily be used for cycling studies. Therefore, in much of the high loading Si literature EIS is used as a complementary technique

<sup>a</sup> Department of Energy and Petroleum Engineering, University of Stavanger, Kjølvs Egelands hus, Kristine Bonnevis vei, 4021, Stavanger, Norway.  
E-mail: frederik.huld@uis.no, zhixin.yu@uis.no

<sup>b</sup> Beyond, Stokkamyrveien 30, N-4313, Sandnes, Norway.  
E-mail: frederik@beyond.no, fengliu@beyond.no

† Electronic supplementary information (ESI) available. See DOI: <https://doi.org/10.1039/d3ya00181d>



in full-cell or half-cell (*vs.* Li/Li<sup>+</sup>) setup to show *e.g.* the increase in resistance of a cell before and after cycling.<sup>13,14</sup> Equivalent circuits (ECs) have been designed to describe the behaviour of Si electrodes at low loading.<sup>18–20</sup> These ECs vary considerably in the literature, but more recent work has shown that the inclusion of a finite-length Warburg diffusion element ( $W_o$ ) is useful for describing the diffusion behaviour of Li<sup>+</sup> ions within the Si material.<sup>18,21</sup> A similar diffusion element, the finite-space Warburg ( $W_s$ ) has also been shown to be useful for describing Li<sup>+</sup> diffusion through thin films such as SEI layers formed on the Li CE.<sup>21</sup> Recently, the use of distribution of relaxation times (DRT) analysis has also been employed to deconvolve the data generated by impedance experiments.<sup>18,22,23</sup> This technique gives information on the number of processes occurring in the data, and is a useful technique for designing ECs. A peak in the DRT spectrum corresponds to a polarization process and the position (in Hz), size (in  $\Omega$  cm<sup>2</sup>), and shape gives information on the electrochemistry of the process.<sup>18,22–24</sup>

Si has very different behaviour during charging and discharging, and EIS offers the possibility of helping to understand these differences.<sup>18</sup> Amorphous Si cycled in the region 0.05 to 1.5 V *vs.* Li/Li<sup>+</sup> displays two electrochemical phases. During lithiation, Li reacts with Si to form Li<sub>2</sub>Si at around 0.25 V. As the potential is decreased to about 0.07 V Li<sub>2</sub>Si reacts to form Li<sub>3.5</sub>Si. Delithiation reverses this reaction, with Li<sub>3.5</sub>Si forming Li<sub>2</sub>Si at about 0.28 V, and the resulting Li<sub>2</sub>Si forming pure Si at about 0.48 V and higher.<sup>25–27</sup> The ECs of Si half cells at these potentials are not necessarily all the same, especially when considering the effect of the Li CE.

In this work, we will construct and test a commercially available Si material in electrodes with high loading in both half-cell and symmetric configuration to investigate the changes to the EIS spectrum at different potentials. This comparison will be used to differentiate between effects occurring due to the Si WE and those due to the Li CE in half cells. The EIS spectra will be collected at the potentials at which each phase is at equilibrium using a constant-current constant-voltage (CCCV) step to ensure that the phase is allowed to run to completion and the electrode consists mainly of the product of the desired phase. The symmetric cells will be assembled from half cells which have been cycled to each of these points in the cycle. DRT analysis will be used to inform the design of the ECs used in this work, and these will be used to elucidate the behaviour of the high loading Si electrodes in half cells.

## 2 Experimental

### 2.1 Electrode preparation

Si electrode slurries were prepared in an overhead stirrer (Dispermat LC30). The slurry consisted of 5% carboxymethylcellulose (CMC, Walcoel 10000), 2% KOH/citric acid buffer (pH 3), 0.5% carbon nanotubes (CNT, Lanxi Zhide), 9.5% carbon black (C65, Imerys), 80% Si powder (SCC55, Group 14), and 3% SBR (BM-451B, Zeon). The slurry was made by sequential addition of powders and stirring in a ball mill at 2500 rpm for

15 minutes, followed by a stirring step of 2 h at 2500 rpm. The final addition consisted of SBR, which was mixed slowly at 700 rpm for 15 minutes. Electrodes containing higher concentrations of Si material were found to be too brittle after cycling to be disassembled and reassembled. Carbon black was found to increase the stability of the electrode while having a negligible effect on the electrochemistry.

The slurry was coated onto 10  $\mu$ m copper foil using a doctor blade with a blade height of 130  $\mu$ m and dried at room temperature overnight. This resulted in an electrode loading of 3.38 mg cm<sup>-2</sup> and a thickness of 59.6  $\mu$ m. The electrolyte uptake and porosity were 89% and 35.6%, respectively. Details of these experiments may be found in the ESI.<sup>†</sup><sup>28</sup> The reversible gravimetric capacity of the Si material in the 0.05–1 V range was 1290 mA h g<sup>-1</sup> at a current density of 0.179 mA cm<sup>-2</sup>, yielding an area capacity of 3.49 mA h cm<sup>-2</sup> for these electrodes. 15 mm diameter electrodes were cut from the electrode sheet for coin cell assembly.

### 2.2 Coin cell assembly, disassembly, and reassembly

All assembly, disassembly and reassembly was performed in an Argon-filled glove box. CR2032 coin cells (stainless steel, MTI) were assembled by placing the Si electrode (15 mm dia.) in the cap (the o-ring and the cap are glued together in MTI's coin cell parts), followed by electrolyte (25  $\mu$ l, TC-E8593, TINCI) to wet the electrode surface. This was then covered with two layers of paper separator (19 mm dia., Tf4030), followed by a further 25  $\mu$ l of electrolyte. Next, the Li electrode (16 mm dia, 750  $\mu$ m thick, Sigma Aldrich) was placed on top of the separator followed by the spacer (0.5 mm), the spring, and finally the base.

Disassembly was performed using a decrimping machine (Hohsen), taking care not to short-circuit or damage the electrodes.

Reassembly was performed in almost the same manner as for half-cells, using fresh coin cell parts, separator, and electrolyte. For Si/Si symmetric cells the 0.5 mm spacer was replaced with a 1 mm spacer to account for the thickness of the Si electrodes.

### 2.3 Cycling and EIS procedures

Once assembled, coin cells were placed on the cycling machine (BTS 4000, Neware) and discharged to 1.5 V before being resting for 12 h. Following this rest the cells were cycled once at 1/20C (0.179 mA cm<sup>-2</sup>) and twice at 1/10C (0.358 mA cm<sup>-2</sup>) for a total of three cycles. The voltage limits were 0.05–1.5 V.

The EIS cycling procedure was started immediately at the end of the formation, and is given in Table 1. The C-rate for each step in Table 1 was 1/10C. EIS experiments were performed at the end of each CCCV step. A plot of this procedure can be seen in Fig. S1 in the ESI.<sup>†</sup>

EIS spectra were collected on an Autolab potentiostat (Metrohm) connected using two-electrode setup to a coin cell holder from Neware. Spectra were collected using Nova 2.13 software at the open circuit voltage (OCV) using an amplitude of 5 mV in the frequency ( $f$ ) range of 10<sup>-2</sup> to 10<sup>5</sup> Hz, at 15 points per decade. EIS spectra for symmetric cells were collected after resting for 24 h.



**Table 1** The procedure used for charging and discharging the cells to the desired potential for EIS experiments

Step type	Stop potential (V)	Step time (h)
CCCV	0.2	20
CCCV	0.07	20
CC	0.05	—
Rest	—	0.3
CCCV	0.3	20
CCCV	0.48	20
CC	1.5	—

DRT analysis was performed in Python using the Gaussian Process (GP) GP-DRT method described by Liu and Ciucci (2019).<sup>22</sup> This models the DRT based on the assumption that the peaks in the DRT spectrum are normal distributions. Fitting was performed using the `impedance.py` package in Python.<sup>29</sup>

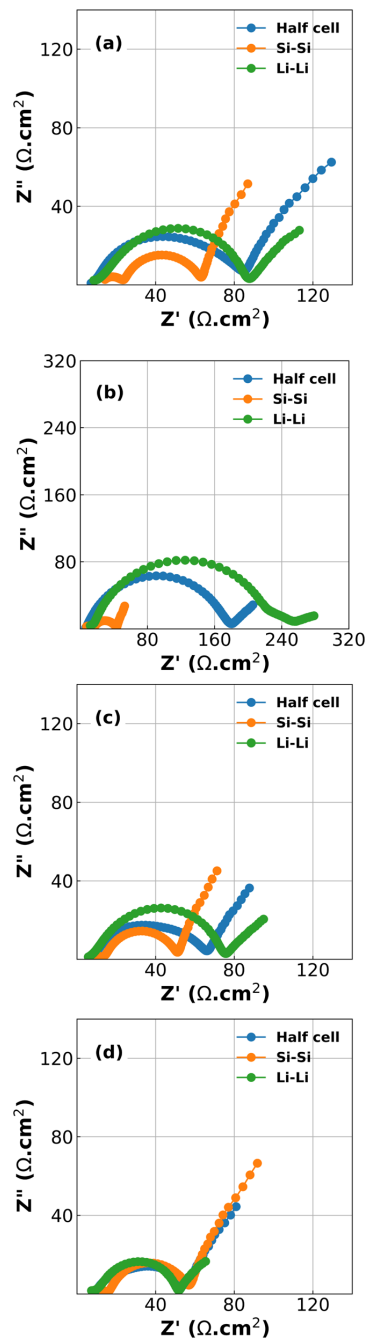
### 3 Results and discussion

Inspection of the formation cycles are shown in Fig. S2 in the ESI.† These reveal an initial Coulombic efficiency (ICE) of 86%. The subsequent cycles at 1/10C had CEs of 98.6% and 99.7% indicating a relatively stable electrode suitable for short experiments. However, it should be noted that there was a significant capacity drop between each delithiation cycle and the subsequent lithiation (87.3% and 90.1% between cycles 1 to 2 and 2 to 3, respectively), indicating that a large polarization process exists during lithiation.

Results of the EIS spectra for half-cells, Si/Si symmetric cells and Li/Li symmetric cells at each of the 4 stop potentials are given in Fig. 1. In all cases the Kramers–Kronig relations showed that the data was acceptable quality, with the residuals of the Kramers–Kronig and data not exceeding 1%.<sup>23,30</sup> As expected, the spectra show that there is a large difference in EIS response both as a function of potential, and also between half cells and symmetric cells.<sup>18</sup> While one might expect that the EIS spectra of the half cells should be equal to half the sum of the Si/Si and Li/Li symmetric cells there is a non-linear relationship between the components of the cell and the EIS spectrum, especially as a function of voltage.<sup>31</sup> This is shown in Fig. S3 in the ESI.†

The plots in Fig. 1 reveal two challenges: the first is that large changes are happening at the Li CE (green lines) as a function of voltage, an electrode which is often considered to behave in a constant manner. The second is that deconvolution of the half cell impedance from that of the individual electrodes is not straightforward.

While DRT can give information about the polarization processes that appear in the impedance spectrum, the analysis is limited by the necessity that the data is complete (*i.e.* that the impedance is real as  $f = 2\pi\omega \rightarrow 0$ ).<sup>23</sup> For LIBs this presents a difficulty since low-frequency diffusion means that the EIS data rarely converges and the timescales required means that experiments are often limited to  $10^{-2}$  to  $10^{-3}$  Hz in the low-frequency region. One possible workaround is to “pre-process” the EIS data by removing the diffusive tail.<sup>18,23</sup> This is done by modelling the



**Fig. 1** EIS spectra collected for comparison between half cells and symmetric cells at (a) 0.2 V in the lithiation step; (b) 0.07 V in the lithiation step; (c) 0.3 V in the delithiation step; (d) 0.48 V in the delithiation step.

diffusive region using an EC and then simply subtracting it from the data in a manner similar to applying a baseline in *e.g.* X-ray



diffraction. However – and similarly to the application of a baseline in other techniques – the choice of baseline has an influence on the rest of the data, especially for features close to where the baseline is large. A different method can be used, whereby the data is assumed to converge to the real axis even if the spectrum is incomplete.<sup>22</sup> The DRT spectrum can then be calculated without the need to choose a baseline. It is important to note that the DRT peak characteristics (size, shape and position) which appears in the low-frequency region as a result of this assumption is not an accurate description of the polarization process. The GP method employed here uses this assumption of convergence to the real axis, and while we present the full DRT spectrum (including the peak in the diffusive region) we do not use the DRT spectrum to extrapolate information about the low-frequency polarization processes.<sup>22</sup> The results of DRT deconvolution for half cell and symmetric cells at each of the four stop potentials can be seen in Fig. 2. The large peak in the low-frequency diffusion region is an artefact due to the method extrapolating beyond the data as well as data not converging to the real axis and should therefore not be included when discussing the DRT analysis. For clarity, this region has been greyed out. In each plot in Fig. 2 the Si/Si and Li/Li symmetric cells consist of one peak at about  $10^2$  and  $10^3$  Hz, respectively. These correspond to the  $\text{Li}^+$  diffusion through the solid electrode and the SEI, respectively.<sup>18,23,24</sup> The half cells consist of either a broad, shouldered peak (as in the case of 2a to 2c), or two distinct but

overlapping peaks (Fig. 2d). This indicates that the half cell behaviour is comprised of both Li and Si contributions, but due to their close proximity these may not be resolvable by fitting separate loops in the EC. Interestingly, at 0.07 V (Fig. 2b) the Li/Li symmetric cells and the half cells show a very large polarization, indicating that the impedance at this potential is strongly dominated by the Li CE behaviour. A final small peak exists in the low frequency range at about  $10^{-1}$  Hz which may be due to diffusion of  $\text{Li}^+$  in the electrolyte. The breadth of these peaks indicates that they are likely best described by using constant phase elements ( $Q$ ) rather than capacitive elements ( $C$ ).  $Q$  is given by:

$$Q = \frac{1}{(j\omega)^\alpha C} \quad (1)$$

where  $0 < \alpha \leq 1$ .

From the analysis of the DRT plots it is possible to conclude that the cells consists of three loops: the first describes the double-layer constant phase element  $Q_{\text{SEI}}$  and layer resistance  $R_{\text{SEI}}$  along with a Warburg diffusion  $W$  describing the electrolyte–SEI interface; the second loop describes the solid electrode behaviour, with  $Q_{\text{dl}}$  and  $R_{\text{ct}}$  describing the double-layer pseudo-capacitance and charge transfer polarization of the electrode/SEI interface, respectively;<sup>32</sup> and the final loop describes the polarization process of the cell.<sup>18</sup> For large cells with low impedance and contact resistances (between electrode material and current collector) induction effects also come into play, but

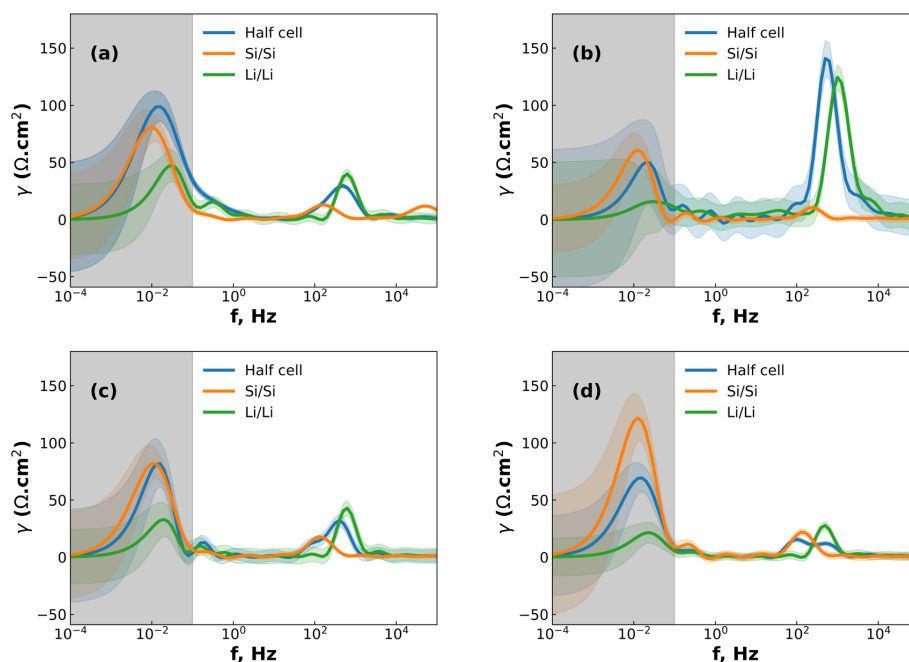


Fig. 2 DRT spectra generated for comparison between half cells and symmetric cells at (a) 0.2 V in the lithiation step; (b) 0.07 V in the lithiation step; (c) 0.3 V in the delithiation step; (d) 0.48 V in the delithiation step. The coloured regions above and below the curves denote the confidence interval of the analysis, while the greyed out area denotes the extrapolated curves beyond the edges of the available data.



for coin cells these can mostly be ignored. The cell resistance is the total resistance at  $f \rightarrow \infty$ , analogous to the  $iR$ -drop seen in the first few seconds of a galvanostatic charge–discharge (GCD) curve.<sup>18</sup> This is commonly referred to as the solution resistance  $R_{sol}$ , and because it is a series resistance it is not included in the DRT plots.

The DRT analysis results in two ECs to describe the behaviour of the Si/Si, Li/Li and half cell spectra, one incorporating a finite space Warburg  $W_o$  which describes the  $Li^+$  solid state diffusion, and the other incorporating a finite length Warburg  $W_s$  which describes the diffusion of  $Li^+$  through the SEI. The EC is shown in Fig. 3, with  $W_{o/s}$  representing either the finite space or the finite length Warburg. The EC with the lowest  $\chi^2$  was chosen to represent the half cell data. It should be noted that the  $\chi^2$  for both circuits was often very small ( $\sim 10^{-6}$ ), and the difference between  $\chi^2$  values varied by less than an order of magnitude.

At intermediate potentials (0.2 and 0.3 V) the solid-state diffusion behaviour is dominant over the thin-film behaviour, while at low and high potentials (0.07 and 0.48 V) the opposite is true. This could be because the highly lithiated and highly delithiated states have limited space for solid-state diffusion, and so the thin-film behaviour becomes dominating, either as a result of the SEI on the Si WE, or on the Li CE, or both. This matches the expectation from previous research, which showed that the SEI cracks both during lithiation and delithiation.<sup>18</sup>

In cases where the exponent  $\alpha$  of the constant phase element Q is equal to 1, eqn (1) becomes equivalent to that of a capacitor. This will in turn decrease the number of parameters needed for fitting of the data and give more easily interpreted results.

Analysis of the fitted results of the Si/Si EC and half cells within the relevant stop potentials (0.2 and 0.3 V) reveals that the  $Q_{SEI}$  parameter for the symmetric cells can be replaced with capacitors, but the same parameter for the half cells cannot. This is likely due to interference of the signal from the Li side of the half cell. The same result is seen in the high and low potentials (0.07 and 0.48 V) for the  $W_s$  EC, with the Li/Li  $Q_{SEI}$  behaving as a pure capacitor, and the half-cell showing mixed behaviour. This result is notable because it reduces the number of parameters needed to describe the symmetric cells, while simultaneously showing that the  $Q_{SEI}$  parameter of the half cells is made of a mixture of the two SEI layers.

From the results of the fitting it is possible to draw some conclusions as to the behaviour of Si during lithiation and

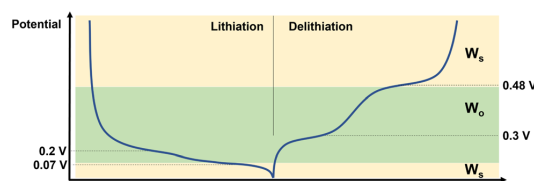


Fig. 4 Schematic describing the behaviour of Si half cells at different points in the charge–discharge curve. The dominant diffusion behaviour is denoted on the right hand side.

delithiation, and how this affects the impedance response. This is shown schematically in Fig. 4. Starting from the fully delithiated state and lithiating: at 0.2 V – which corresponds to the equilibrium position of the  $Si \rightarrow Li_2Si$  phase – there is both enough space and sufficient  $Li^+$  ions in the Si for the ions to move freely and be measurable by EIS on the coin cell level even in the half cell format. At 0.07 V where most of the electrode consists of  $Li_{3.5}Si$ , the high concentration of  $Li^+$  in the electrode reduces the number of mobile ions, and therefore the diffusion of  $Li^+$  through thin films such as SEI become dominating in the EIS spectrum. Further, the long timescales of the CCCV experiment mean that a thick SEI layer is able to grow on the Li CE, which then generates a strong impedance response. During delithiation the situation is very similar, with the end of the  $Li_{3.5}Si \rightarrow Li_2Si$  phase (at 0.3 V) showing a strong impedance signal from  $Li^+$  mobility in the Si, and the highly delithiated  $Li_2Si \rightarrow Si$  phase at 0.48 V showing very little signal from the  $Li^+$  in the Si, allowing the surface diffusion effects to dominate once again. This is similar to the ion mobility effects seen in LEDs.<sup>33</sup> The decreased impedance of the Li CE is likely due to the decreased overpotential during deposition (*i.e.* during delithiation of the Si electrode) vs. stripping (*i.e.* during lithiation of the Si electrode).<sup>34</sup>

The results obtained in this work show that it is necessary to exercise caution when studying the behaviour of high loading Si half cells. At or near the fully lithiated and delithiated states the Li CE contributes significantly to the impedance of the cell, and so SEI impedances from the Li CE can easily be misidentified as belonging to the Si WE. Should an EIS spectrum be desired *e.g.* at the end-of life, it is therefore recommended to either use symmetric cells (by using at least two cycled cells), or to perform EIS at one or more potentials in the cycle, with emphasis on the intermediate potentials where the Li CE contribution is limited.

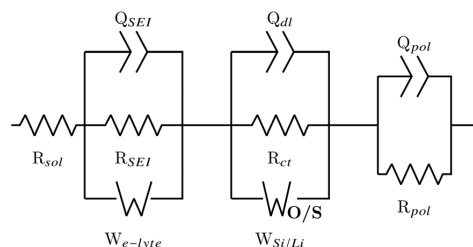


Fig. 3 ECs of symmetric and half-cells determined by fitting to EIS data.

## 4 Conclusion

A set of Si electrodes with commercial level loadings were analysed by means of EIS, both as half cells and their Si/Si and Li/Li symmetric cell equivalents. The cells were tested at four different potentials corresponding to the equilibrium potentials of the lithiation and delithiation phases. Analysis of the resulting EIS spectra by DRT showed that the half cells are described by a combination of the Si/Si and Li/Li symmetric cells, and that these are in turn best described by different ECs.



The Si/Si symmetric cells are shown to fit a finite-length Warburg describing the solid-state diffusion of  $\text{Li}^+$  in Si, while the Li/Li cells are best described by a finite-space Warburg corresponding to the diffusion of  $\text{Li}^+$  through the SEI. The half cells are described either by the Si/Si or the Li/Li EC depending on the stop potential, with the high and low potentials showing Li/Li character, and the intermediate potentials showing Si/Si behaviour. Further analysis showed that both the Si/Si and Li/Li symmetric cell ECs could be simplified by replacing the two-parameter constant phase element  $Q_{\text{SEI}}$  with a single-parameter capacitive element  $C_{\text{SEI}}$ , but that the mixing of signals meant this could not be extended to the half cells. This work shows the importance of EIS as a technique for studying Si electrodes with high loading, as well the importance of carefully considering the behaviour of both electrodes in half cell EIS.

## Author contributions

F. T. Huld: conceptualization; data curation; software; formal analysis; investigation; visualization; methodology; writing – original draft; writing – review and editing. Z. Yu: supervision; project administration; writing – review and editing. F. Lou: resources; supervision; funding acquisition; project administration; writing – review and editing.

## Conflicts of interest

F. T. Huld and F. Lou declare that they are employees and stockholders of Beyonder AS, a Norwegian battery company. The remaining authors do not declare a conflict of interest.

## References

- M. T. McDowell, S. W. Lee, W. D. Nix and Y. Cui, *Adv. Mater.*, 2013, **25**, 4966–4985.
- M. Obrovac, *Curr. Opin. Electrochem.*, 2018, **9**, 8–17.
- V. Vanpeene, J. Villanova, A. King, B. Lestriez, E. Maire and L. Roué, *Adv. Energy Mater.*, 2019, **9**, 1803947.
- M. N. Obrovac and L. J. Krause, *J. Electrochem. Soc.*, 2007, **154**, A103.
- F. T. Huld, S. Y. Lai, W. M. Tucho, R. Batmaz, I. T. Jensen, S. Lu, O. E. Eleri, A. Y. Kopusov, Z. Yu and F. Lou, *ChemistrySelect*, 2022, **7**, e202202857.
- J. P. Pender, G. Jha, D. H. Youn, J. M. Ziegler, I. Andoni, E. J. Choi, A. Heller, B. S. Dunn, P. S. Weiss, R. M. Penner and C. B. Mullins, *ACS Nano*, 2020, **14**, 1243–1295.
- X. Shen, Z. Tian, R. Fan, L. Shao, D. Zhang, G. Cao, L. Kou and Y. Bai, *J. Energy Chem.*, 2018, **27**, 1067–1090.
- R. Teki, M. K. Datta, R. Krishnan, T. C. Parker, T.-M. Lu, P. N. Kumta and N. Koratkar, *Small*, 2009, **5**, 2236–2242.
- R. Batmaz, F. M. Hassan, D. Higgins, Z. P. Cano, X. Xiao and Z. Chen, *J. Power Sources*, 2018, **407**, 84–91.
- A. Ulvestad, M. O. Skare, C. E. Foss, H. Krogsæter, J. F. Reichstein, T. J. Preston, J. P. Mæhlen, H. F. Andersen and A. Y. Kopusov, *ACS Nano*, 2021, **15**, 16777–16787.
- L. Luo, H. Yang, P. Yan, J. J. Travis, Y. Lee, N. Liu, D. Molina Piper, S.-H. Lee, P. Zhao, S. M. George, J.-G. Zhang, Y. Cui, S. Zhang, C. Ban and C.-M. Wang, *ACS Nano*, 2015, **9**, 5559–5566.
- Z. Chen, C. Wang, J. Lopez, Z. Lu, Y. Cui and Z. Bao, *Adv. Energy Mater.*, 2015, **5**, 1401826.
- Y. Wang, H. Xu, X. Chen, H. Jin and J. Wang, *Energy Storage Mater.*, 2021, **38**, 121–129.
- J. Lu, J. Liu, X. Gong, S. Pang, C. Zhou, H. Li, G. Qian and Z. Wang, *Energy Storage Mater.*, 2022, **46**, 594–604.
- F. La Mantia, C. Wessells, H. Deshazer and Y. Cui, *Electrochem. Commun.*, 2013, **31**, 141–144.
- M. Ender, J. Illig and E. Ivers-Tiffée, *J. Electrochem. Soc.*, 2017, **164**, A71–A79.
- A. J. Bard and L. R. Faulkner, *Electrochemical Methods: Fundamentals and Applications*, Wiley, New York, 2nd edn, 2001.
- K. Pan, F. Zou, M. Canova, Y. Zhu and J.-H. Kim, *J. Power Sources*, 2020, **479**, 229083.
- D. A. Lozhkina, A. M. Rumyantsev and E. V. Astrova, *Semiconductors*, 2020, **54**, 383–391.
- F. Paloukis, C. Elmasides, F. Farmakis, P. Selinis, S. G. Neophytides and N. Georgoulas, *J. Power Sources*, 2016, **331**, 285–292.
- M. Levi, *Solid State Ionics*, 2001, **143**, 309–318.
- J. Liu and F. Ciucci, *Electrochim. Acta*, 2020, **331**, 135316.
- J. Illig, M. Ender, T. Chrobak, J. P. Schmidt, D. Klotz and E. Ivers-Tiffée, *J. Electrochem. Soc.*, 2012, **159**, A952–A960.
- J. P. Schmidt, T. Chrobak, M. Ender, J. Illig, D. Klotz and E. Ivers-Tiffée, *J. Power Sources*, 2011, **196**, 5342–5348.
- K. Ogata, E. Salager, C. Kerr, A. Fraser, C. Ducati, A. Morris, S. Hofmann and C. Grey, *Nat. Commun.*, 2014, **5**, 3217.
- B. Key, M. Morcrette, J.-M. Tarascon and C. P. Grey, *J. Am. Chem. Soc.*, 2011, **133**, 503–512.
- K. Kitada, O. Pecher, P. C. M. M. Magusin, M. F. Groh, R. S. Weatherup and C. P. Grey, *J. Am. Chem. Soc.*, 2019, **141**, 7014–7027.
- Y.-S. Wu, C.-C. Yang, S.-P. Luo, Y.-L. Chen, C.-N. Wei and S. J. Lue, *Int. J. Hydrogen Energy*, 2017, **42**, 6862–6875.
- M. Murbach, B. Gerwe, N. Dawson-Elli and L.-K. Tsui, *J. Open Source Software*, 2020, **5**, 2349.
- M. Schönleber and E. Ivers-Tiffée, *Electrochem. Commun.*, 2015, **61**, 45–48.
- C. H. Chen, J. Liu and K. Amine, *J. Power Sources*, 2001, **96**, 321–328.
- Z. C. Huertas, D. Settipani, C. Flox, J. R. Morante, T. Kallio and J. J. Biendicho, *Sci. Rep.*, 2022, **12**, 137.
- J. C. deMello, N. Tessler, S. C. Graham and R. H. Friend, *Phys. Rev. B: Condens. Matter Mater. Phys.*, 1998, **57**, 12951–12963.
- J. Seok, C. N. Gannett, S.-H. Yu and H. D. Abruña, *Anal. Chem.*, 2021, **93**, 15459–15467.



## Supporting Information (SI)

### Unravelling the electrochemical impedance spectroscopy of silicon half cells with commercial loading

Frederik T Huld,<sup>a,b</sup> Zhixin Yu,<sup>a</sup> and Fengliu Lou<sup>b</sup>

**a** – Department of Energy and Petroleum Engineering, University of Stavanger, Kjølvs Egelands hus, Kristine Bonnevis vei, 4021, Stavanger, Norway. E-mail: [frederik.huld@uis.no](mailto:frederik.huld@uis.no); [zhixin.yu@uis.no](mailto:zhixin.yu@uis.no)

**b** – Beyonder, Stokkamyrveien 30, N-4313, Sandnes, Norway. E-mail: [frederik@beyonder.no](mailto:frederik@beyonder.no); [fengliu@beyonder.no](mailto:fengliu@beyonder.no)

#### Electrolyte uptake and porosity measurements

<b>Electrolyte uptake (%)</b> : $\frac{W_{elec} - W_{dry}}{W_{dry}} \times 100$
<b>Porosity (%)</b> : $\frac{W_{PC} - W_{dry}}{\rho_{PC} V_{dry}} \times 100$

where  $W_{dry}$  is the mass of the dry electrode.  $W_{elec}$  and  $W_{PC}$  are the masses of the electrodes after soaking for 24 h in electrolyte and propylene carbonate (PC, Tinci), respectively.  $\rho_{PC}$  is the density of PC (1.205g/cm<sup>3</sup>) and  $V_{dry}$  is the volume of the dry electrode.

The masses of the soaked electrodes were measured after removing from the solution and dabbing them with paper tissue to remove excess liquid. All experiments took place in an Argon-filled glovebox.



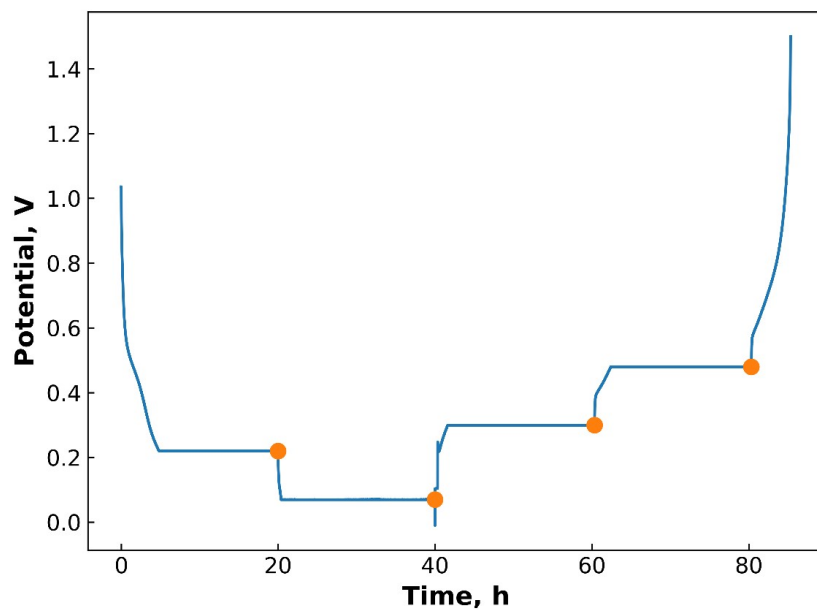


Figure S1. An example of the cycle used for preparing the electrode for EIS, showing how the CCCV procedure is set to each "stop" potential. EIS was taken at the end of each CCCV step, as shown by the orange circles.

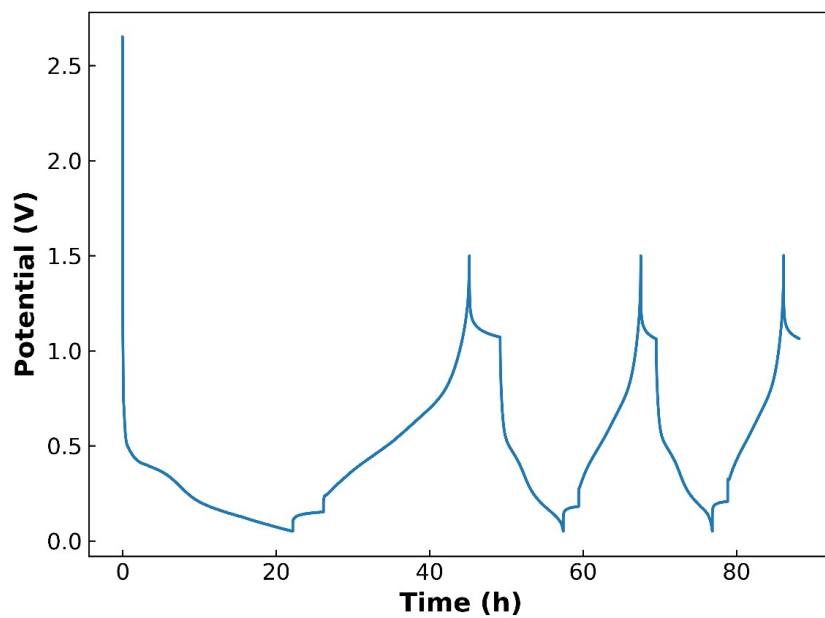


Figure S2. An example of the formation cycles performed on Si half-cells used in this study. The first cycle was performed at  $1/20$  C, while the second and third cycles were performed at  $1/10$  C

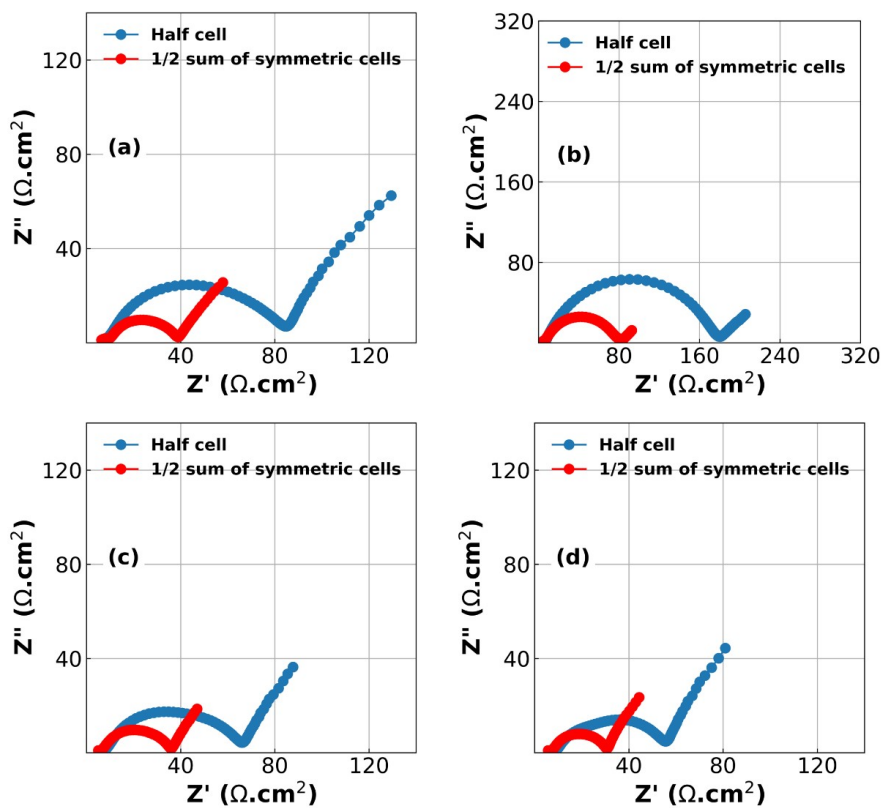


Figure S3. EIS spectra of half cell (blue points) and the half-sum of the equivalent symmetric cells (red points) (a) 0.2 V in the lithiation step; (b) 0.07 V in the lithiation step; (c) 0.3 V in the delithiation step; (d) 0.48 V in the delithiation step.

# New Insights into the Behaviour of Commercial Silicon Electrode Materials *via* Empirical Fitting of Galvanostatic Charge-Discharge Curves

Frederik T. Huld,<sup>\*[a, b]</sup> Obinna E. Eleri,<sup>[a, b]</sup> Fengliu Lou,<sup>\*[b]</sup> and Zhixin Yu<sup>\*[a]</sup>

Silicon (Si) materials for use in Lithium ion batteries (LIBs) are of continued interest to battery manufacturers. With an increasing number of commercially available Si materials, evaluating their performance becomes a challenge. Here, we use an empirical fitting function presented earlier to aid in the analysis of galvanostatic charge-discharge data of commercial Si half-cells with relatively high loading. We find that the fitting procedure is capable of detecting dynamic changes in the cell, such as

reversible capacity fade of the Si electrode. This fading is found to be due to the highly lithiated  $\text{Li}_2\text{Si} \rightleftharpoons \text{Li}_{3.5}\text{Si}$  phase and that the behaviour is strongly dependent on the potential of this phase. EIS reveals that the Si electrode is responsible for the reversible behaviour due to progressive loss of  $\text{Li}^+$  leading to increasing resistance. SEM/EDX and XPS characterization are also employed to determine the origin of the irreversible resistance growth on the Si electrodes.

## Introduction

Commercially available silicon (Si) materials for use in lithium-ion batteries (LIBs) are a convenient way for battery manufacturers to improve their own products without the need for extremely costly and time-consuming in-house material development. Several such Si materials are already available, ranging from pure Si with capacities close to theoretical values, to heavily coated, modified, or blended materials. This poses a challenge, as comparing across materials from different suppliers is not straightforward. To fairly evaluate a given Si material therefore requires taking the intrinsic behaviour into account and analysing this to determine if it is suitable for the desired system.

A number of simple electrochemical characterization techniques are available to test Si electrodes and give information on the behaviour of the material. The most common is galvanostatic charge-discharge (GCD), whereby cells are charged and discharged in a manner similar to that experienced by full cells. This is often combined with electrochemical impedance spectroscopy (EIS) to give information about the impedances in the cell.<sup>[1,2]</sup> Non-electrochemical, *ex situ* characterization techniques

such as X-ray photoelectron spectroscopy (XPS) and scanning electron microscopy (SEM) have also been employed extensively to study Si electrodes. XPS has been used to study the reaction mechanism of Si/SiO during cycling as well as studying the formation of solid electrolyte interphase (SEI) on electrodes. SEM is a common technique for determining sub-micrometre sized structural changes such as crack formation in electrodes that appear as a result of cycling.<sup>[3–5]</sup>

Despite the usefulness and pervasiveness of GCD data in the literature, surprisingly little in-depth analysis is employed to study this data. A large number of published articles only present GCD data in order to show the capacity (Q), coulombic efficiencies (CE), and differential capacity (dQ/dV) from the GCD curves. dQ/dV gives more information on the lithiation and delithiation phases present in Si but due to issues with data processing these are commonly used qualitatively, and Q and CE require just the final datapoints of the GCD curve (out of several thousand points per curve).<sup>[6–9]</sup> Gaining a better understanding of how these phases behave under different conditions will be important for designing better and more stable Si-containing LIBs.<sup>[6–10]</sup> Differential voltage (dV/dQ) is also a useful technique for studying phase transitions of materials, with the added advantage that smoothing is unnecessary.<sup>[11–13]</sup> However, the phase transitions in Si electrodes are extremely broad, making it very difficult to extract meaningful peaks from this type of analysis.

In order to extract additional information from GCD curves, empirical cumulative distribution functions (CDFs) have been developed.<sup>[6,9,14,15]</sup> These allow for the analysis of Si GCD data without the need for differentiation, thereby avoiding some of the information loss which is inevitably encountered. A CDF which has been shown to fit GCD data well even at high C-rates has been shown previously.<sup>[6]</sup> This CDF consists of a skew-Gaussian coupled with a Lorentzian to form a skew pseudo-Voigt and was shown to be able to accurately fit the delithiation phases of amorphous Si thin films as well as amorphous Si

[a] F. T. Huld, O. E. Eleri, Prof. Dr. Z. Yu  
Department of Energy and Petroleum Engineering, University of Stavanger,  
Kjølv Egeland's hus, Kristine Bonnevis vei, 4021, Stavanger, Norway  
E-mail: zhixin.yu@uis.no  
frederik.huld@uis.no

[b] F. T. Huld, O. E. Eleri, Dr. F. Lou  
Beyond, Stokkamyrvæien 30, N-4313, Sandnes, Norway  
E-mail: frederik@beyond.no  
fengliu@beyond.no

Supporting information for this article is available on the WWW under  
<https://doi.org/10.1002/celec.202300393>

© 2023 The Authors. ChemElectroChem published by Wiley-VCH GmbH. This is an open access article under the terms of the Creative Commons Attribution License, which permits use, distribution and reproduction in any medium, provided the original work is properly cited.

nanowires. The Lorentzian (or Cauchy) distribution is often used in combination with the Gaussian (or normal) distribution to describe spectroscopic peaks such as XPS where the use of single distributions is insufficient to explain the curve shape.<sup>[16,17]</sup> Applying this equation to commercial Si materials is a promising way to quickly gain increased understanding of both the method and the materials themselves. The empirical CDF for the capacity  $Q_k$  of Si as a function of the potential  $E$  with  $n$  delithiation phases is defined as:

$$f(E) = \sum_{k=1}^n Q_k [w_k G_k(E) + (1 - w_k) L_k(E)] \quad (1)$$

where  $G_k(E)$  and  $L_k(E)$  are the skew-Gaussian and Lorentzian components of phase  $k$ , respectively.  $w_k$  is a weighting factor ( $0 \leq w \leq 1$ ) which determines the contribution of the skew-Gaussian or Lorentzian portions of the pseudo-Voigt CDF to the capacity of the phase.  $G_k(E)$  and  $L_k(E)$  are given by:

$$G_k(E) = \frac{1}{2} \left( 1 + \Phi_k \left( \frac{E - c_k}{\sqrt{2s_k}} \right) \right) - 2T_k \left( \frac{E - c_k}{\sqrt{2s_k}}, \alpha_k \right) \quad (2)$$

and

$$L_k(E) = \frac{1}{\pi} \arctan \left( \frac{E - c_k}{\gamma} \right) + \frac{1}{2} \quad (3)$$

where  $c_k$  is the position (*i.e.* apparent equilibrium potential) of the phase,  $s_k$  is the width of the Skew-Gaussian, and  $\alpha_k$  is the skewness factor describing the deviation from equilibrium.<sup>[6,18]</sup> In Eq. (3),  $\gamma_k$  is the width of the Lorentzian. There are advantages to using an empirical equation such as this one over a theoretical model, and there are many examples of empirical equations, such as the Stefan–Boltzmann equation for thermal radiation of a blackbody, or rate equations used in chemical rate kinetics.<sup>[19,20]</sup> Firstly, the equations can be relatively simple, allowing for fast determination of important features. Secondly, they can be applied to a broad variety of datasets generated from experiments or cells which were not designed with this particular application in mind. For example, cumulative CDFs have been used on commercial cells, as well as on Si half cell data from published works.<sup>[6,15]</sup> However, the empirical nature of these equations means that the exact behaviour of the parameters involved must be determined experimentally.

Eq. (1) describes the shapes of the lithiation/delithiation phases of amorphous Si, which can be generalized by:<sup>[21–23]</sup>



The behaviour of these two phases ( $n=2$ ) has previously been shown to vary depending on factors such as morphology and C-rate.<sup>[6]</sup> Further, the use of lithium (Li) metal as counter electrode (CE) for studying Si has been shown to have significant effect on the results.<sup>[1,24–26]</sup> Phase I (Eq. (4)) exists at

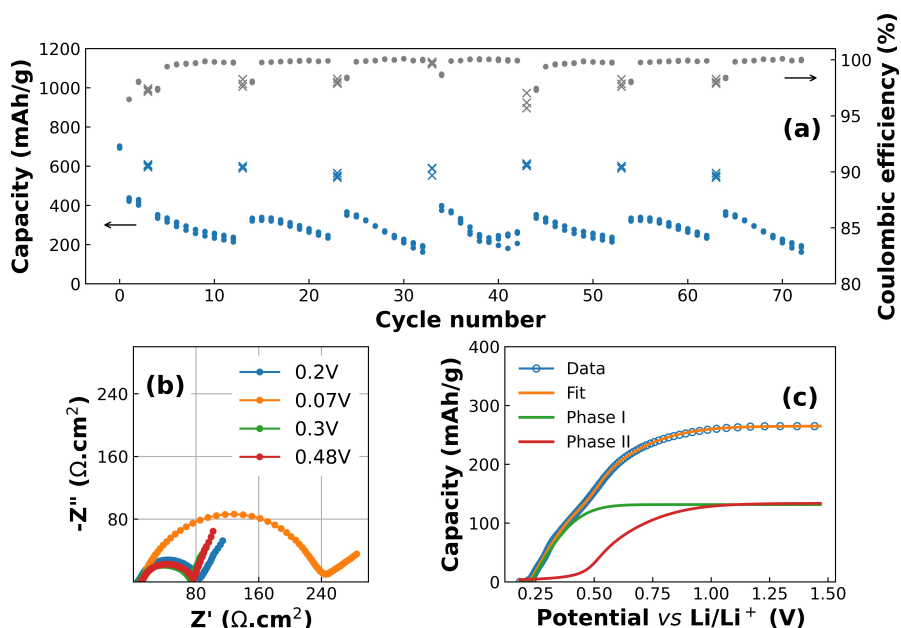
low potentials vs Li/Li<sup>+</sup>, forming Li<sub>3.5</sub>Si at 0.07 V during lithiation and Li<sub>2</sub>Si at around 0.3 V during delithiation. Phase II (Eq. (5)) exists at higher potentials (again vs Li/Li<sup>+</sup>), forming Li<sub>2</sub>Si at 0.2 V, and delithiating to Si at around 0.48 V. We note that these values are approximations, calculated from the maxima of the dQ/dV, and vary depending on the electrochemical and physical environment of the cell (intrinsic and extrinsic resistances, material morphologies, electrode setup, current density, state of health, etc.).<sup>[6,9,15]</sup> For example, the delithiation dQ/dV of Si nanowires display sharper and less skewed peaks at 0.3 V than thin films of similar thicknesses.<sup>[6]</sup> This is also why the position of the phase c is deemed an “apparent” equilibrium potential in the literature.<sup>[6]</sup> Note that due to the presence of the skewness factor  $\alpha$  in Eq. (2), the position of the phase c is not the same as the maximum point of the peak in a plot of dQ/dV vs V.

In this work we will apply Eq. (1) to the delithiation of GCD cycling data from electrodes constructed using a commercially available Si material at an electrode loading higher than what is typically observed in the literature.<sup>[6,27,28]</sup> EIS will also be performed at potentials corresponding to the maxima of the dQ/dV during both the lithiation and delithiation to give additional information on the behaviour of Si. SEM with energy-dispersive X-ray spectroscopy (EDX) and XPS will be used to validate the results of the GCD analysis.

## Results and Discussion

Inspection of the GCD curves during the three formation cycles of the commercial Si revealed a number of phases consistent with graphite, indicating that the material contains a relatively large amount of carbon (C).<sup>[29]</sup> This change is shown in the supplementary information (SI) in Figure S1. However, these phases quickly disappeared as cycling progressed and only the Si phases and a capacitive component were detectable in the GCD curves after formation. This capacitive component was subtracted prior to GCD fitting by applying a linear baseline to the data. The reversible capacity of the first cycle was  $520 \pm 10$  mAh/g and the initial Coulombic efficiency (ICE) was  $74 \pm 0.4\%$ , indicating that the material likely contains some oxides such as SiO<sub>x</sub>. Both of these values are slightly lower than those supplied by the manufacturer (655 mAh/g and 83.7%, respectively), but this is likely due to the somewhat higher cut-off potential used for lithiation in these experiments than those recommended by the manufacturer. This also means that the majority of the ICE loss can be ascribed to Si-related side reactions occurring above 0.05 V, with the missing capacity belonging to the graphite below 0.05 V. The results presented here should therefore not be used to judge the quality of the chosen Si material, but rather be treated as a general study into the behaviour of any given Si material.

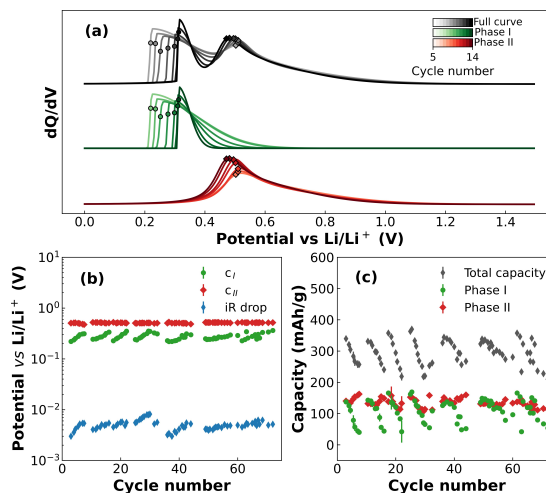
Figure 1 shows the results of the electrochemical experiments. Figure 1a is a plot of the capacity and CE as a function of cycle number. The crosses denote the total capacity of the slow CV charging and discharging step used for the EIS experiment (shown in Figure 1b), while the points denote the much faster C/3 cycles. The reversible capacity is relatively low



**Figure 1.** (a) Capacity (blue) and Coulombic efficiency (grey) as a function of cycle life. The crosses denote the slow cycles used for generating EIS spectra, while the points denote the faster cycles used for GCD fitting. (b) EIS spectra generated at 4 potentials in the GCD curve. (c) An example of the fitting function applied to the GCD curves along with the shapes of the individual phases.

compared to pure Si (3579 mAh/g),<sup>[30]</sup> indicating that the material consists of a significant proportion of graphite. The cycles at  $C/3$  show that the capacity of the electrodes fades quite quickly over the course of each group of 10 cycles, but that this capacity recovers almost completely after a slow cycle. This indicates that the cell capacity loss is not completely irreversible, at least in the short term. The CE of the slow CV cycle is quite consistently 2–2.5% lower than the much faster  $C/3$  cycles (97.5% vs >99.5%) indicating incomplete delithiation of the Si electrode. The exception to this rule is the fast cycle immediately after each slow cycle, which has a CE similar to that of the preceding slow cycle. An example of the EIS spectra collected during the slow cycle (denoted by crosses in Figure 1a) is given in Figure 1b. This shows how the EIS changes depending on the potential, with the spectrum at 0.07 V in particular showing a very large impedance loop due to the Li (CE).<sup>[1,24,31]</sup> Figure 1c shows an example of one of the  $C/3$  cycles in Figure 1a after baseline subtraction against the potential (vs  $\text{Li/Li}^+$ ). The orange line denotes the fit of Eq. (1) to the data and the offset red and green lines correspond to phases I (Eq. (4)) and II (Eq. (5)), respectively. The raw GCD curve, together with the fit and residual can be found in Figure S2 in the SI. The residual shows an excellent fit to the data, with the difference between the fit and the data consistently below 1%.

Results of fitting Eq. (1) to the fast GCD curves is given in Figure 2. Figure 2a shows the  $dQ/dV$  curves of the first ten cycles at  $C/3$ . The full spectrum is shown as grey curve, while the phases are offset for clarity. The points and diamonds



**Figure 2.** Results of fitting Eq. (1) to the GCD data. (a) Total  $dQ/dV$  of the first ten cycles at  $C/3$  (grey lines) and the component phases (green and red for phases I and II, respectively). Darker lines correspond to later cycles. The points and diamonds denote the location of the apparent equilibrium potentials  $c_i$  and  $c_{ii}$ , respectively. (b) Comparison between the iR drop immediately after the start of delithiation and the apparent equilibrium potentials  $c_i$  and  $c_{ii}$ , as a function of the cycle number. (c) Total capacity of the cells along with the capacities of the individual phases, as a function of cycle number.

correspond to the apparent equilibrium potentials  $c_i$  and  $c_{ii}$ , respectively. This shows large changes in phase I as cycling progresses with  $c_i$  being pushed to higher potentials, causing narrowing of the phase and a decrease in the capacity (i.e. the area under the curve). Conversely, phase II is stable with a relatively small decrease in  $c_{ii}$  and an associated increase in capacity as a function of cycling, as shown in Figure 2b and 2c, respectively. Figure 2b shows the equilibrium potentials  $c_i$  and  $c_{ii}$ , along with the iR drop (calculated by taking the difference in potential between the 0<sup>th</sup> and 2<sup>nd</sup> datapoints), while Figure 2c shows the total capacity along with the capacities of the phases. From Figure 2b it can be seen that the apparent equilibrium potential of phase I,  $c_i$ , is proportional to the iR drop  $V_{iR}$ . Indeed:

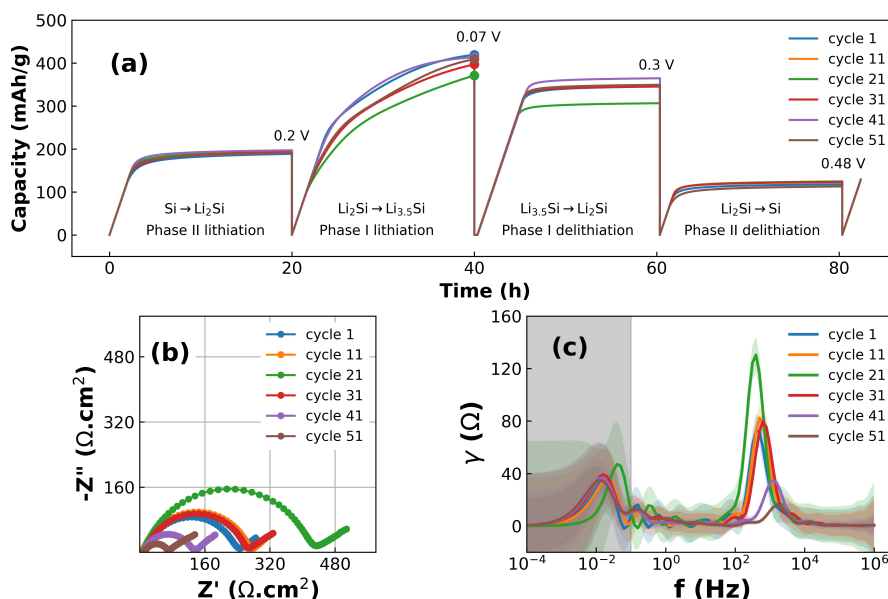
$$\frac{c_i}{V_{iR}} \approx 60 \quad (6)$$

which results in a reduced  $\chi^2$  of about 0.02. However, this relationship fails at later cycles, indicating that other factors are affecting the relationship between  $c_i$  and  $V_{iR}$ . Nevertheless it is clear that  $V_{iR}$  has a large effect on the behaviour of phase I. By comparison, the apparent equilibrium potential of phase II ( $c_{ii}$ ) is almost constant with repeated cycling, indicating that  $V_{iR}$  is not acting upon it in the same manner. The increase in  $c_i$  is correlated with the decrease in total capacity of phase I as shown in Figure 2c. This shows that the capacity decrease of each batch of 10 cycles mostly stems from the drop in capacity of phase I, with the capacity of phase II remaining almost constant. The small increase in capacity of phase II seen at the end of each of the batches may be due to the model attempting to compensate for the large loss of capacity of phase I. The results of the fitting equation show that the total capacity of the Si material is strongly affected by the position of phase I, and that this can be correlated to the iR drop  $V_{iR}$ . The fact that this effect is somewhat reversible by applying a slow cycle means that  $V_{iR}$  is not only due to irreversible resistance growth such as SEI on the Si electrode and the overpotential of the Li CE, but also due to reversible resistance growth in the potential region of phase I. The ability of the fitting function to discern and measure these dynamic changes in the cell is therefore a valuable addition to the toolset available for studying Si electrochemistry.

Determining the origin of this reversible resistance growth is very important to interpreting the data and understanding the behaviour of Si half cells such as these. By performing EIS at the maxima of the dQ/dV, it may be possible to glean some insight into the behaviour of the cells at these potentials. The long (20 h) CV step used in the experimental setup of the EIS cycle is intended to ensure that the composition of the Si electrode is at equilibrium and that the Si in the electrode is almost completely made up of the product of the target phase (shown in bold):



This can be verified by looking at the capacity of the cycle as a function of time, as shown in Figure 3a. This shows that while most of the reactions have reached equilibrium at the end of the 20 h CV step (as evidenced by the slope tending towards 0), the reaction shown in Eq. (8) is not only far from equilibrated even after 20 h, but also varies significantly as cycling progresses. This behaviour is reflected in the EIS, which shows an increase in the impedance at the same cycle (cycle 21) as the drop in capacity, as well as subsequent decrease in impedance as the capacity recovers at later cycles. The EIS spectra generated at Eq. (8) are shown in Figure 3b, which show a large increase in impedance during the first 30 cycles, followed by a sharp decrease in subsequent cycles. This confirms that the capacity decrease seen in Figure 2 is due to the impedance of phase I during lithiation. Having shown that a reversible resistance growth contributes to the drop in capacity of Si half cells, the question of the origin of this resistance remains. This can be elucidated by analysing the distribution of relaxation times (DRT).<sup>[1,24,32]</sup> DRT analysis is a method for deconvoluting the time constants  $\tau$  of an EIS spectrum. This technique relies upon the assumption that the response of an electrochemical system to a perturbation (such as an oscillating potential) decays exponentially at a particular distribution of timescales.<sup>[32]</sup> This means that an EIS spectrum can be transformed into a set of peaks corresponding to frequencies at which physical processes occur. For near-ideal processes such as corrosion on a flat surface which can be described by a resistor (R) and a capacitor ( $Z_C$ ) in parallel, the peak height and the frequency  $f = 1/(2\pi\tau)$  can be used to calculate R and  $Z_C$ , respectively. However in most cases the relaxation time of a process is a distribution rather than a single value, and so the width of the peak is increased. It should also be noted that DRT analysis requires the EIS spectrum to converge to the real impedance at  $f = 0$ . Since low-frequency diffusion effects are often present in LIBs this is rarely the case for real systems. Hence, the low-frequency region needs to be removed from consideration, either through subtraction from the data using a model equivalent circuit, or by requiring the analysis to converge to the real impedance.<sup>[1,32]</sup> Here we employ the second method and use a Gaussian Process developed earlier to perform DRT analysis on our data.<sup>[32]</sup> The results of the DRT analysis at 0.07 V are shown in Figure 3c, and these show large changes in the peak at  $10^3$  Hz associated with the Li CE.<sup>[1,24]</sup> Over the course of the first 21 cycles this peak grows and shifts to slightly lower frequencies, but after this point the trend reverses and the peak shrinks and shifts to higher frequencies. This may be explained by crack formation in the SEI leading to reduced  $\text{Li}^+$  diffusion resistance.<sup>[33]</sup> This also explains the shift in frequency of the peak, as decreased inhomogeneity also increases the frequency at which  $\text{Li}^+$  transport processes occur.<sup>[1]</sup> This, combined with a lack of a strong Si peak normally



**Figure 3.** Results of performing EIS on Si half cells. (a) The capacity as a function of time for the slow cycle used for EIS. The circles at 40 h denote the point in time at which the EIS spectra displayed in (b) were collected. (b) EIS spectra taken at the end of the 0.07 V step. (c) DRT of the EIS spectra shown in (b). The shape of the curves in the greyed out area are artefacts of the analysis.

found at about  $10^2$  Hz means that the majority of the impedance behaviour of the half cells at a potential of 0.07 V can be ascribed to the impedances of the Li CE. However, given that the impedance decreases after the 21<sup>st</sup> cycle, the Li electrode cannot account for the reversible resistance increase seen from the GCD data which suggests that the reversible resistance stems from the Si electrode.

One possible source of this reversible resistance growth may be due to the progressive loss of  $\text{Li}^+$  ions from the Si electrode.<sup>[6,34]</sup> The discrepancy between the capacity fade and the high CE of the fast cycles shown in Figure 1a, together with the reversible nature of the fade indicate that the cause is due to the lithiation step rather than the delithiation. Also, the fade is not due to excess SEI formation, as this would be reflected in a lowered CE. The results of the fitting shown in Figure 2c indicate that the capacity loss is due to phase I, which means that the lithiation of this phase is hindered at fast cycles. During fast lithiation the irreversible resistances of the cell (i.e. the SEI + Li CE overpotential + other resistances) result in a polarization of the cell which causes phase I (Eq. (8)) to not become fully lithiated. This therefore also causes a decrease in capacity of phase I during delithiation (Eq. (9)), which is measured by Eq. (1). Since the resistance of the Si electrode is inversely proportional to the Li concentration in Si, the subsequent cycle experiences an increased resistance, and therefore decreased lithiation. This leads to a negative feedback loop wherein the amount of  $\text{Li}^+$  inserted into phase I continuously decreases. Applying a slow cycle such as the one employed for studying the EIS increases the  $\text{Li}^+$  content in the electrode and decreases

$V_{IR}$ ), which “resets” the Si electrode and therefore allows the capacity to recover.

This indicates that reducing the cell resistances may substantially improve the performance of Si materials independently of the material itself, and that the capacity fade is a result of both reversible and irreversible resistances. As seen from the EIS results at low potentials vs  $\text{Li}/\text{Li}^+$ , the Li CE accounts for a large portion of this resistance. Thus, high-capacity materials, and especially those with high electrode loading will be artificially hindered by the Li CE due to the large current densities required to cycle at appreciable rates.<sup>[25]</sup> Further, constructing cells with higher areas will also likely increase the performance of Si cells purely through the decrease in area resistance.

Unfortunately, the dynamic nature of this resistance growth means that it is very difficult to measure it directly. The steady-state nature of experiments such as EIS and *ex-situ* experiments such as SEM/EDX and XPS means that they are only able to measure the irreversible resistances. Nevertheless, they are a valuable tool to gain a deeper understanding of the behaviour of the system. To show that the irreversible SEI resistance is growing on the Si electrode with time, SEM/EDX and XPS analysis was carried out on fresh, uncycled electrodes as well as electrodes disassembled at the end of cycling. The results of the SEM analysis can be found in Figure 4. The uncycled electrode (Figure 4a) shows how the Si electrode is made up of large micron-sized graphite/carbon particles, mixed with agglomerations of small spherical Si particles. The long fibres covering the surface are the CNTs added to the electrode to improve the conductivity. The cycled electrode in Figure 4b is coated in a

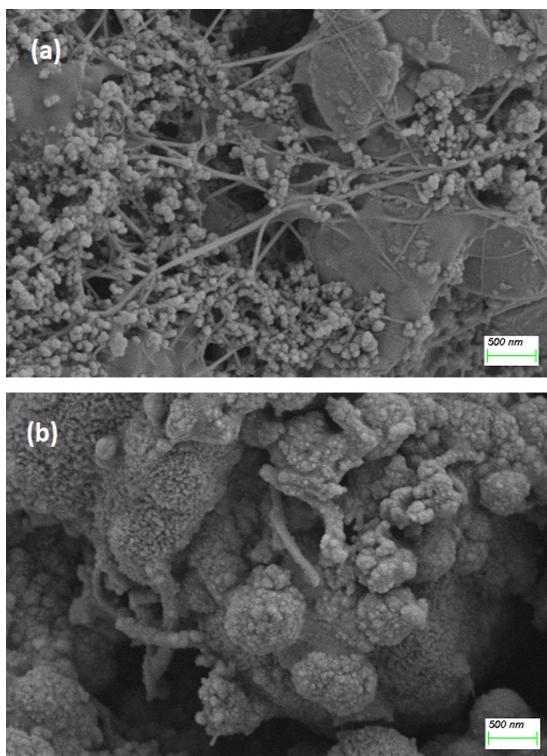


Figure 4. SEM images of Si electrodes (a) before and (b) after cycling.

layer of SEI, indicating that the anode is at least partially responsible for the irreversible resistance increase seen in the GCD data. Spot EDX analysis (Figure 5a) from SEM on cycled and uncycled electrodes shows a reduction of the C peak and an increase in the oxygen (O), fluorine (F) and phosphorus (P) peaks. This implies that the surface of the electrode is covered by inorganic O, F and P-rich species. These may consist of materials such as LiF, phosphates and lithium alkyl carbonates. This is consistent with the results of the XPS C1s spectra shown in Figure 5b and 5c for the uncycled and cycled electrodes, respectively. Figure 5b shows a large C=C graphite peak at 284.8 eV, as well as oxygen species such as carboxylic acids and ketones present on the surface of the graphite and other carbonaceous materials that make up the anode. The lack of a detectable C=C peak in the cycled electrode, shown in Figure 5c, indicates that the graphite is obscured by the presence of a passivating SEI layer. This presence of  $\text{CH}_x$  and  $\text{O}-\text{C}=\text{O}$  groups correspond to the characteristic signature of lithium alkyl carbonates, primary components of SEI.<sup>[35–37]</sup>

The increased polarization observed in both the GCD fitting and the EIS experiments can therefore be explained in part by the excessive SEI growth often seen on Si electrodes.

The relationship between the irreversible and reversible resistances are shown schematically in Figure 6. This shows how the irreversible resistances contribute to the polarization of the

cell, which leads to reduced lithiation of phase I. The reduced  $\text{Li}^+$  concentration in phase I increases the resistance of the electrode, which leads to further decreases in lithiation.

## Conclusions

Commercial Si electrodes with high loading of 3.27 mAh/g were constructed in half-cell format and tested using GCD and EIS. A fitting function was applied to the delithiation steps, revealing that phase I, describing the reaction  $\text{Li}_2\text{Si} \rightleftharpoons \text{Li}_{3.5}\text{Si}$  is responsible for the fast but reversible capacity fade experienced by these cells. Further analysis of the data showed a relatively linear relationship between the position of phase I and the  $iR$  drop experienced by the cell at the start of delithiation, leading to the conclusion that the capacity fade is due to polarization of the cell. EIS and DRT performed near the positions of the phases showed that the reversible resistance growth came from the Si electrode. This was explained by the concept of a “negative feedback loop” whereby the large irreversible polarizations from the Si and Li electrodes decrease the  $\text{Li}^+$  concentration in phase I of the Si electrode. This leads to an increase in resistance of the Si electrode, which contributes to the polarization on the subsequent cycle. The irreversible resistance growth on the Si electrode was measured by performing SEM/EDX and XPS on uncycled and cycled electrodes. This work showcases the fitting function as a valuable technique for studying dynamic changes in commercial Si materials during cycling.

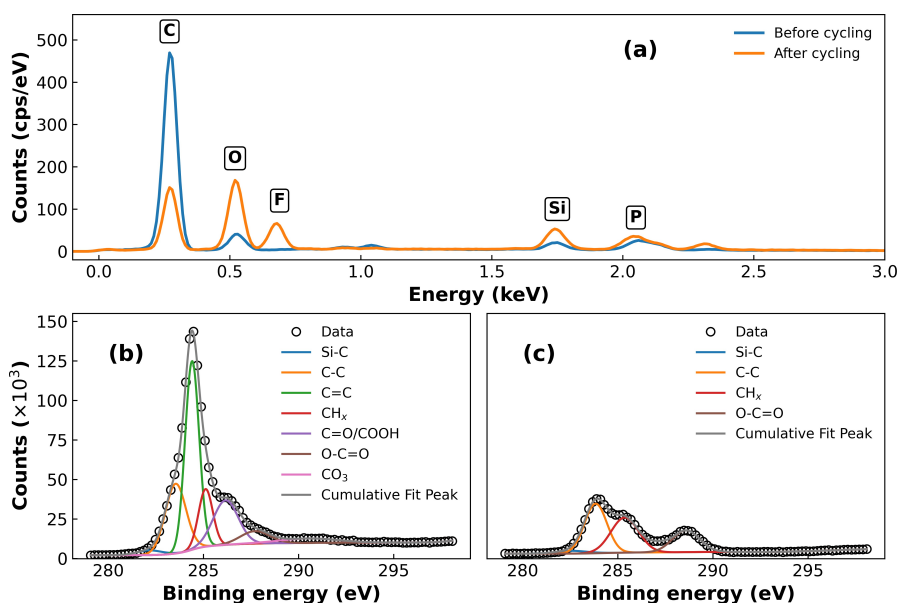
## Experimental

Electrode slurries were prepared by high-speed stirring in a manner described previously, using SL650-SOC (Iopsilon) as the active material.<sup>[24]</sup> Electrode sheets were made by coating onto 10  $\mu\text{m}$  thick copper foil using a doctor blade with a blade height of 130  $\mu\text{m}$  and dried at room temperature. This yielded electrodes with a material loading of 3.27  $\text{mg}/\text{cm}^2$  and a thickness of 48  $\mu\text{m}$ . The Si material loading was 80%; the binders consisted of 5% carboxymethylcellulose (CMC, Walcoel 10000) and 3% styrene butadiene rubber (SBR, BM-451B, Zeon) along with 2% KOH/citric acid buffer to aid the adhesion; 0.5% carbon nanotubes (CNT, Lanxi Zhid) and 9.5% carbon black (CB, Group 14) were added as conductive additives.

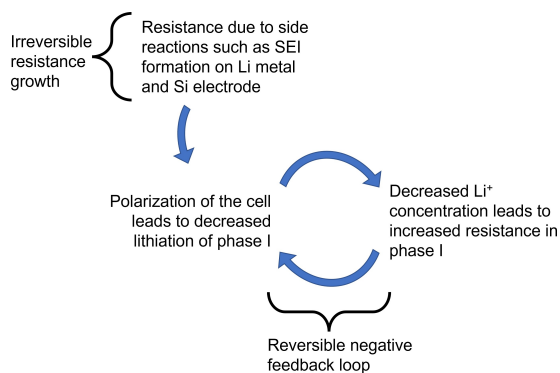
Coin half-cells were constructed in CR2032 format (MTI) in an Argon-filled glovebox in a manner described previously.<sup>[3]</sup> The electrolyte used was commercially available TC-E8593 (TINCl).

After assembly the coin cells were immediately discharged to 1.5 V, followed by a 12 h rest. Three formation cycles were performed in the range 0.05–1.5 V. These consisted of 1 cycle at C/20 (83  $\mu\text{A}/\text{cm}^2$ ) followed by 2 cycles at C/10 (0.166  $\text{mA}/\text{cm}^2$ ). The formation was followed by the slow cycle for EIS, which was performed by using a C/10, 20 h constant-current constant-voltage (CCCV) step to the desired “stop” potential. The stop potentials for lithiation were 0.2 V and 0.07 V, while for delithiation they were set to 0.3 V and 0.48 V. EIS was performed at the end of each of these stop potentials. After the slow cycle, a batch of 10 “fast” cycles at C/3 (0.55  $\text{mA}/\text{cm}^2$ ) were performed. This procedure of one slow EIS cycle and 10 fast cycles was repeated until the cells failed.





**Figure 5.** (a) Spot EDX of Si anodes before and after cycling. (b) XPS C1s spectrum of the Si anode before cycling. (c) XPS C1s spectrum of the Si anode after cycling.



**Figure 6.** Schematic showing the process of irreversible and reversible resistance growth, and its relationship to the fast capacity fade seen in Si half cells.

EIS was performed on coin half cells using a potentiostat (Autolab, Metrohm). The oscillation amplitude was set to 5 mV in the frequency range of  $10^5$  to  $10^{-2}$  Hz. Analysis of the spectra was performed using the impedance package in Python,<sup>[38]</sup> and distribution of relaxation times (DRT) analysis was performed in Python using the methods described by Liu and Ciucci (2020).<sup>[32]</sup>

GCD fitting was performed on the delithiation step of the fast cycles using the Imfit package in Python, as described previously.<sup>[6,39]</sup> Since the lithiation of Si occurs very close to the cut-off potential, it is not possible to accurately fit the lithiation step of the GCD curves. Therefore, only the delithiation step is fit.

Characterization via SEM/EDX (ZEISS/Oxford Instruments) and XPS (Thermo Fisher) was performed on both cycled and uncycled

electrodes. Cycled electrodes were prepared by disassembly of cycled cells in an Argon-filled glovebox and rinsed three times in DMC before drying to remove excess electrolyte salt.

### Conflict of Interests

F.T. Huld and F. Lou declare that they are employees and stockholders of Beyonder AS, a Norwegian battery company. The remaining authors do not declare a conflict of interest.

### Data Availability Statement

The data that support the findings of this study are available from the corresponding author upon reasonable request.

**Keywords:** capacity fade · electrochemical impedance spectroscopy · incremental capacity analysis · lithium ion batteries · silicon anodes

- [1] K. Pan, F. Zou, M. Canova, Y. Zhu, J.-H. Kim, *J. Power Sources* **2020**, *479*, 229083.
- [2] F. Paloukis, C. Elmasides, F. Farmakis, P. Selinis, S. G. Neophytides, N. Georgoulas, *J. Power Sources* **2016**, *331*, 285.
- [3] F. T. Huld, S. Y. Lai, W. M. Tucho, R. Batmaz, I. T. Jensen, S. Lu, O. E. Eleri, A. Y. Kopolov, Z. Yu, F. Lou, *ChemistrySelect* **2022**, *7*, e202202857.
- [4] H. Wu, L. Zheng, J. Zhan, N. Du, W. Liu, J. Ma, L. Su, L. Wang, *J. Power Sources* **2020**, *449*, 227513.
- [5] S. Y. Lai, J. P. Mæhlen, T. J. Preston, M. O. Skare, M. U. Nagell, A. Ulvestad, D. Lemordant, A. Y. Kopolov, *Nanoscale Adv.* **2020**, *2*, 5335.
- [6] F. T. Huld, J. P. Mæhlen, C. Keller, S. Y. Lai, O. E. Eleri, A. Y. Kopolov, Z. Yu, F. Lou, *Batteries* **2023**, *9*, 251.

- [7] Y. Li, M. Abdel-Monem, R. Gopalakrishnan, M. Berecibar, E. Nanini-Maury, N. Omar, P. van den Bossche, J. Van Mierlo, *J. Power Sources* **2018**, *373*, 40.
- [8] X. Li, Z. Wang, J. Yan, *J. Power Sources* **2019**, *421*, 56.
- [9] J. He, X. Bian, L. Liu, Z. Wei, F. Yan, *J. Energy Storage* **2020**, *29*, 101400.
- [10] A. J. Smith, J. R. Dahn, *J. Electrochem. Soc.* **2012**, *159*, A290.
- [11] I. Bloom, A. N. Jansen, D. P. Abraham, J. Knuth, S. A. Jones, V. S. Battaglia, G. L. Henriksen, *J. Power Sources* **2005**, *139*, 295.
- [12] I. Bloom, J. P. Christophersen, D. P. Abraham, K. L. Gering, *J. Power Sources* **2006**, *157*, 537.
- [13] I. Bloom, L. K. Walker, J. K. Basco, D. P. Abraham, J. P. Christophersen, C. D. Ho, *J. Power Sources* **2010**, *195*, 877.
- [14] X. Li, J. Jiang, L. Y. Wang, D. Chen, Y. Zhang, C. Zhang, *Appl. Energy* **2016**, *177*, 537.
- [15] X. Bian, L. Liu, J. Yan, *Energy* **2019**, *177*, 57.
- [16] G. K. Wertheim, M. A. Butler, K. W. West, D. N. E. Buchanan, *Rev. Sci. Instrum.* **1974**, *45*, 1369.
- [17] J. Olivero, R. Longbothum, *Journal of Quantitative Spectroscopy and Radiative Transfer* **1977**, *17*, 233.
- [18] M. S. Palagonia, C. Erinmwingbovo, D. Brogioli, F. La Mantia, *J. Electroanal. Chem.* **2019**, *847*, 113170.
- [19] M. J. Stefan, *Über die Beziehung zwischen der Wärmestrahlung und der Temperatur*, vol. 1 **1879** pages 391–428.
- [20] P. W. Atkins, J. De Paula, *Atkins' Physical Chemistry*, W. H. Freeman, New York, 8th ed edition **2006**.
- [21] K. Ogata, E. Salager, C. Kerr, A. Fraser, C. Ducati, A. Morris, S. Hofmann, C. Grey, *Nat. Commun.* **2014**, *5*, 3217.
- [22] B. Key, M. Morcrette, J.-M. Tarascon, C. P. Grey, *J. Am. Chem. Soc.* **2011**, *133*, 503.
- [23] J. Li, J. R. Dahn, *J. Electrochem. Soc.* **2007**, *154*, A156.
- [24] F. Huld, Z. Yu, F. Lou, *Energy Advances* **2023**, page 10.1039/D3YA00181D.
- [25] F. La Mantia, C. Wessells, H. Deshazer, Y. Cui, *Electrochem. Commun.* **2013**, *31*, 141.
- [26] M. Ender, J. Illig, E. Ivers-Tiffée, *J. Electrochem. Soc.* **2017**, *164*.
- [27] Z. Chen, C. Wang, J. Lopez, Z. Lu, Y. Cui, Z. Bao, *Adv. Energy Mater.* **2015**, *5*, 1401826.
- [28] Y. Wang, H. Xu, X. Chen, H. Jin, J. Wang, *Energy Storage Mater.* **2021**, *38*, 121.
- [29] F. Dinkelacker, P. Marzak, J. Yun, Y. Liang, A. S. Bandarenka, *ACS Appl. Mater. Interfaces* **2018**, *10*, 14063.
- [30] H. Tian, F. Xin, X. Wang, W. He, W. Han, *J. Mater.* **2015**, *1*, 153.
- [31] J. Seok, C. N. Gannett, S.-H. Yu, H. D. Abruña, *Anal. Chem.* **2021**, *93*, 15459.
- [32] J. Liu, F. Ciucci, *Electrochim. Acta* **2020**, *331*, 135316.
- [33] A. Ramasubramanian, V. Yurkiv, T. Foroozan, M. Ragone, R. Shahbazian-Yassar, F. Mashayek, *ACS Appl. Energy Mater.* **2020**, *3*, 10560.
- [34] E. Pollak, G. Salitra, V. Baranchugov, D. Aurbach, *J. Phys. Chem. C* **2007**, *111*, 11437.
- [35] P. Verma, P. Maire, P. Novák, *Electrochim. Acta* **2010**, *55*, 6332.
- [36] M. Smith, L. Scudiero, J. Espinal, J.-S. McEwen, M. Garcia-Perez, *Carbon* **2016**, *110*, 155.
- [37] X. Chen, X. Wang, D. Fang, *Fullerenes Nanotubes Carbon Nanostruct.* **2020**, *28*, 1048.
- [38] M. Murbach, B. Gerwe, N. Dawson-Elli, L.-K. Tsui, *Journal of Open Source Software* **2020**, *5*, 2349.
- [39] M. Newville, R. Otten, A. Nelson, T. Stensitzki, A. Ingarciola, D. Allan, A. Fox, F. Carter, Michał, R. Osborn, D. Pustakhod, Ineuhaus, S. Weigand, A. Aristov, Glenn, C. Deil, mgunyo, Mark, A. L. R. Hansen, G. Pasquevich, L. Foks, N. Zobrist, O. Frost, Stuermer, azelcer, A. Polloreno, A. Persaud, J. H. Nielsen, M. Pompili, S. Caldwell, Lmfit/Lmfit-Py: 1.2.0, Zenodo **2023**.

Manuscript received: August 7, 2023

Revised manuscript received: September 18, 2023

Version of record online: October 12, 2023

# ChemElectroChem

Supporting Information

## **New Insights into the Behaviour of Commercial Silicon Electrode Materials *via* Empirical Fitting of Galvanostatic Charge-Discharge Curves**

Frederik T. Huld,\* Obinna E. Eleri, Fengliu Lou,\* and Zhixin Yu\*

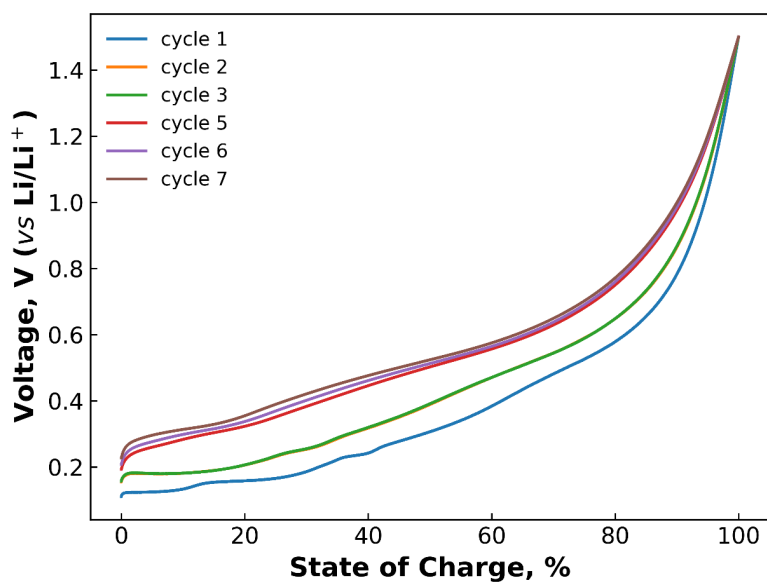


Figure S1. Galvanostatic charge curves of the commercial Si material shows the progressive loss of graphitic character of the electrodes with repeated cycling. Cycle 4 is made up of two constant-current-constant-voltage steps and has therefore been omitted.

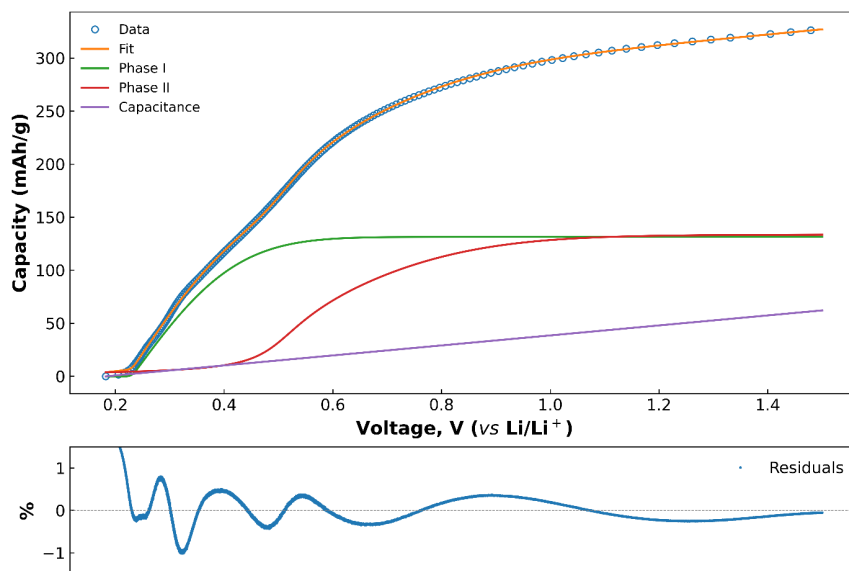


Figure S2. Fit and residual of applying equation 1 to the delithiation step of Si. The purple line is the capacitance, which was used as a baseline for the fitting procedure.

# References

- [1] Yangtao Liu et al. “Current and Future Lithium-Ion Battery Manufacturing”. In: *iScience* 24.4 (Apr. 2021), p. 102332. ISSN: 25890042. DOI: 10.1016/j.isci.2021.102332.
- [2] Matthew T. McDowell et al. “25th Anniversary Article: Understanding the Lithiation of Silicon and Other Alloying Anodes for Lithium-Ion Batteries”. In: *Advanced Materials* 25.36 (Sept. 2013), pp. 4966–4985. ISSN: 09359648. DOI: 10.1002/adma.201301795.
- [3] YaXia Yin, LiJun Wan, and YuGuo Guo. “Silicon-Based Nanomaterials for Lithium-Ion Batteries”. In: *Chinese Science Bulletin* 57.32 (Nov. 2012), pp. 4104–4110. ISSN: 1001-6538, 1861-9541. DOI: 10.1007/s11434-012-5017-2.
- [4] Ke Pan et al. “Systematic Electrochemical Characterizations of Si and SiO Anodes for High-Capacity Li-Ion Batteries”. In: *Journal of Power Sources* 413 (Feb. 2019), pp. 20–28. ISSN: 03787753. DOI: 10.1016/j.jpowsour.2018.12.010.
- [5] Candace K. Chan et al. “Surface Chemistry and Morphology of the Solid Electrolyte Interphase on Silicon Nanowire Lithium-Ion Battery Anodes”. In: *Journal of Power Sources* 189.2 (Apr. 2009), pp. 1132–1140. ISSN: 03787753. DOI: 10.1016/j.jpowsour.2009.01.007.
- [6] Peng Li et al. “Recent Progress on Silicon-Based Anode Materials for Practical Lithium-Ion Battery Applications”. In: *Energy Storage Materials* 15 (Nov. 2018), pp. 422–446. ISSN: 24058297. DOI: 10.1016/j.ensm.2018.07.014.
- [7] M.N. Obrovac. “Si-Alloy Negative Electrodes for Li-ion Batteries”. In: *Current Opinion in Electrochemistry* 9 (June 2018), pp. 8–17. ISSN: 24519103. DOI: 10.1016/j.coelec.2018.02.002.
- [8] Joshua P. Pender et al. “Electrode Degradation in Lithium-Ion Batteries”. In: *ACS Nano* 14.2 (Feb. 2020), pp. 1243–1295. ISSN: 1936-0851, 1936-086X. DOI: 10.1021/acsnano.9b04365.
- [9] Victor Vanpeene et al. “Dynamics of the Morphological Degradation of Si-Based Anodes for Li-Ion Batteries Characterized by In Situ Synchrotron X-Ray Tomography”. In: *Advanced Energy Materials* 9.18 (May 2019), p. 1803947. ISSN: 1614-6832, 1614-6840. DOI: 10.1002/aenm.201803947.
- [10] Atsushi Funabiki et al. “Impedance Study on the Electrochemical Lithium Intercalation into Natural Graphite Powder”. In: *Journal of The Electrochemical Society* 145.1 (Jan. 1998), pp. 172–178. ISSN: 0013-4651, 1945-7111. DOI: 10.1149/1.1838231.
- [11] Kristin Persson et al. “Lithium Diffusion in Graphitic Carbon”. In: *The Journal of Physical Chemistry Letters* 1.8 (Apr. 2010), pp. 1176–1180. ISSN: 1948-7185, 1948-7185. DOI: 10.1021/jz100188d.

- [12] Xiao Hua Liu et al. “Size-Dependent Fracture of Silicon Nanoparticles During Lithiation”. In: *ACS Nano* 6.2 (Feb. 2012), pp. 1522–1531. ISSN: 1936-0851, 1936-086X. DOI: 10.1021/nn204476h.
- [13] Matthew T. McDowell et al. “Studying the Kinetics of Crystalline Silicon Nanoparticle Lithiation with In Situ Transmission Electron Microscopy”. In: *Advanced Materials* 24.45 (Nov. 2012), pp. 6034–6041. ISSN: 0935-9648, 1521-4095. DOI: 10.1002/adma.201202744.
- [14] Ranganath Teki et al. “Nanostructured Silicon Anodes for Lithium Ion Rechargeable Batteries”. In: *Small* 5.20 (Oct. 2009), pp. 2236–2242. ISSN: 16136810, 16136829. DOI: 10.1002/smll.200900382.
- [15] Xiaohui Shen et al. “Research Progress on Silicon/Carbon Composite Anode Materials for Lithium-Ion Battery”. In: *Journal of Energy Chemistry* 27.4 (July 2018), pp. 1067–1090. ISSN: 20954956. DOI: 10.1016/j.jechem.2017.12.012.
- [16] Zheng Jiao et al. “Controlled Scalable Synthesis of Yolk-Shell Structured Large-Size Industrial Silicon with Interconnected Carbon Network for Lithium Storage”. In: *Electrochimica Acta* 283 (Sept. 2018), pp. 1702–1711. ISSN: 00134686. DOI: 10.1016/j.electacta.2018.07.143.
- [17] Yasuhiro Domi et al. “Effect of Phosphorus-Doping on Electrochemical Performance of Silicon Negative Electrodes in Lithium-Ion Batteries”. In: *ACS Applied Materials & Interfaces* 8.11 (Mar. 2016), pp. 7125–7132. ISSN: 1944-8244, 1944-8252. DOI: 10.1021/acsami.6b00386.
- [18] Hyuk-Tae Kwon et al. “Silicon Diphosphide: A Si-Based Three-Dimensional Crystalline Framework as a High-Performance Li-Ion Battery Anode”. In: *ACS Nano* 10.6 (June 2016), pp. 5701–5709. ISSN: 1936-0851, 1936-086X. DOI: 10.1021/acsnano.6b02727.
- [19] Shiqiang Huang et al. “Nanostructured Phosphorus Doped Silicon/Graphite Composite as Anode for High-Performance Lithium-Ion Batteries”. In: *ACS Applied Materials & Interfaces* 9.28 (July 2017), pp. 23672–23678. ISSN: 1944-8244, 1944-8252. DOI: 10.1021/acsami.7b04361.
- [20] R. Reinhold et al. “Silicon Monophosphide as a Possible Lithium Battery Anode Material”. In: *Journal of Materials Chemistry A* 6.41 (2018), pp. 19974–19978. ISSN: 2050-7488, 2050-7496. DOI: 10.1039/C8TA06983B.
- [21] Rasim Batmaz et al. “Highly Durable 3D Conductive Matrixed Silicon Anode for Lithium-Ion Batteries”. In: *Journal of Power Sources* 407 (Dec. 2018), pp. 84–91. ISSN: 03787753. DOI: 10.1016/j.jpowsour.2018.08.035.
- [22] Mingyuan Ge et al. “Porous Doped Silicon Nanowires for Lithium Ion Battery Anode with Long Cycle Life”. In: *Nano Letters* 12.5 (May 2012), pp. 2318–2323. ISSN: 1530-6984, 1530-6992. DOI: 10.1021/nl300206e.
- [23] Omer Salihoglu and Yasser El Kahlout. “Doped Silicon Nanowires for Lithium Ion Battery Anodes”. In: *Materials Research* 22.2 (2019), e20180303. ISSN: 1980-5373, 1516-1439. DOI: 10.1590/1980-5373-mr-2018-0303.
- [24] Jae-Hyun Noh, Kwan-Young Lee, and Joong-Kee Lee. “Electrochemical Characteristics of Phosphorus Doped Si-C Composite for Anode Active Material of Lithium Secondary Batteries”. In: *Transactions of Nonferrous Metals Society of China* 19.4 (Aug. 2009), pp. 1018–1022. ISSN: 10036326. DOI: 10.1016/S1003-6326(08)60399-4.

- [25] Mingyuan Ge et al. “Scalable Preparation of Porous Silicon Nanoparticles and Their Application for Lithium-Ion Battery Anodes”. In: *Nano Research* 6.3 (Mar. 2013), pp. 174–181. ISSN: 1998-0124, 1998-0000. DOI: 10.1007/s12274-013-0293-y.
- [26] Kingshuk Roy et al. “High Capacity, Power Density and Cycling Stability of Silicon Li-ion Battery Anodes with a Few Layer Black Phosphorus Additive”. In: *Sustainable Energy & Fuels* 3.1 (2019), pp. 245–250. ISSN: 2398-4902. DOI: 10.1039/C8SE00476E.
- [27] Asbjørn Ulvestad et al. “Substoichiometric Silicon Nitride – An Anode Material for Li-ion Batteries Promising High Stability and High Capacity”. In: *Scientific Reports* 8.1 (June 2018), p. 8634. ISSN: 2045-2322. DOI: 10.1038/s41598-018-26769-8.
- [28] Romy Reinhold et al. “Surface and Electrochemical Studies on Silicon Diphosphide as Easy-to-Handle Anode Material for Lithium-Based Batteries—the Phosphorus Path”. In: *ACS Applied Materials & Interfaces* 10.8 (Feb. 2018), pp. 7096–7106. ISSN: 1944-8244, 1944-8252. DOI: 10.1021/acsami.7b18697.
- [29] Huanhuan Yang et al. “Silicon Monophosphides with Controlled Size and Crystallinity for Enhanced Lithium Anodic Performance”. In: *Nanoscale* 13.1 (Jan. 2021), pp. 51–58. ISSN: 2040-3372. DOI: 10.1039/D0NR07386E.
- [30] Tao Chen et al. “Recent Advancement of SiO<sub>x</sub> Based Anodes for Lithium-Ion Batteries”. In: *Journal of Power Sources* 363 (Sept. 2017), pp. 126–144. ISSN: 03787753. DOI: 10.1016/j.jpowsour.2017.07.073.
- [31] Asbjørn Ulvestad et al. “Stoichiometry-Controlled Reversible Lithiation Capacity in Nanostructured Silicon Nitrides Enabled by *in Situ* Conversion Reaction”. In: *ACS Nano* 15.10 (Oct. 2021), pp. 16777–16787. ISSN: 1936-0851, 1936-086X. DOI: 10.1021/acsnano.1c06927.
- [32] Stefan Strangmüller et al. “Fast Ionic Conductivity in the Most Lithium-Rich Phosphidosilicate Li<sub>14</sub>SiP<sub>6</sub>”. In: *Journal of the American Chemical Society* 141.36 (Sept. 2019), pp. 14200–14209. ISSN: 0002-7863, 1520-5126. DOI: 10.1021/jacs.9b05301.
- [33] Arthur Haffner, Thomas Bräuniger, and Dirk Johrendt. “Supertetrahedral Networks and Lithium-Ion Mobility in Li<sub>2</sub>SiP<sub>2</sub> and LiSi<sub>2</sub>P<sub>3</sub>”. In: *Angewandte Chemie International Edition* 55.43 (Oct. 2016), pp. 13585–13588. ISSN: 14337851. DOI: 10.1002/anie.201607074.
- [34] Mariko Miyachi et al. “Analysis of SiO Anodes for Lithium-Ion Batteries”. In: *Journal of The Electrochemical Society* 152.10 (2005), A2089. ISSN: 00134651. DOI: 10.1149/1.2013210.
- [35] Jeong K. Lee et al. “Silicon Nanoparticles–Graphene Paper Composites for Li Ion Battery Anodes”. In: *Chemical Communications* 46.12 (2010), p. 2025. ISSN: 1359-7345, 1364-548X. DOI: 10.1039/b919738a.
- [36] Shuangqiang Chen et al. “Dual-Functionalized Double Carbon Shells Coated Silicon Nanoparticles for High Performance Lithium-Ion Batteries”. In: *Advanced Materials* 29.21 (June 2017), p. 1605650. ISSN: 09359648. DOI: 10.1002/adma.201605650.
- [37] Samson Y. Lai et al. “Morphology Engineering of Silicon Nanoparticles for Better Performance in Li-ion Battery Anodes”. In: *Nanoscale Advances* 2.11 (2020), pp. 5335–5342. ISSN: 2516-0230. DOI: 10.1039/D0NA00770F.

- [38] Qingrui Pan et al. “Improved Electrochemical Performance of Micro-Sized SiO<sub>2</sub>-based Composite Anode by Prelithiation of Stabilized Lithium Metal Powder”. In: *Journal of Power Sources* 347 (Apr. 2017), pp. 170–177. ISSN: 03787753. DOI: 10.1016/j.jpowsour.2017.02.061.
- [39] Ge Li et al. “Reducing the Volume Deformation of High Capacity SiO<sub>x</sub>/G/C Anode toward Industrial Application in High Energy Density Lithium-Ion Batteries”. In: *Nano Energy* 60 (June 2019), pp. 485–492. ISSN: 22112855. DOI: 10.1016/j.nanoen.2019.03.077.
- [40] Bo Long et al. “Effect of Phosphorus Doping on Conductivity, Diffusion, and High Rate Capability in Silicon Anode for Lithium-Ion Batteries”. In: *ACS Applied Energy Materials* 3.6 (June 2020), pp. 5572–5580. ISSN: 2574-0962, 2574-0962. DOI: 10.1021/acsaem.0c00534.
- [41] Che-Bin Chang et al. “Solution-Grown Phosphorus-Hyperdoped Silicon Nanowires/Carbon Nanotube Bilayer Fabric as a High-Performance Lithium-Ion Battery Anode”. In: *ACS Applied Energy Materials* 4.4 (Apr. 2021), pp. 3160–3168. ISSN: 2574-0962, 2574-0962. DOI: 10.1021/acsaem.0c02932.
- [42] K. Ogata et al. “Revealing Lithium–Silicide Phase Transformations in Nano-Structured Silicon-Based Lithium Ion Batteries via in Situ NMR Spectroscopy”. In: *Nature Communications* 5.1 (Feb. 2014), p. 3217. ISSN: 2041-1723. DOI: 10.1038/ncomms4217.
- [43] Baris Key et al. “Pair Distribution Function Analysis and Solid State NMR Studies of Silicon Electrodes for Lithium Ion Batteries: Understanding the (De)Lithiation Mechanisms”. In: *Journal of the American Chemical Society* 133.3 (Jan. 2011), pp. 503–512. ISSN: 0002-7863, 1520-5126. DOI: 10.1021/ja108085d.
- [44] Jing Li and J. R. Dahn. “An In Situ X-Ray Diffraction Study of the Reaction of Li with Crystalline Si”. In: *Journal of The Electrochemical Society* 154.3 (2007), A156. ISSN: 00134651. DOI: 10.1149/1.2409862.
- [45] Xiaolei Bian, Longcheng Liu, and Jinying Yan. “A Model for State-of-Health Estimation of Lithium Ion Batteries Based on Charging Profiles”. In: *Energy* 177 (June 2019), pp. 57–65. ISSN: 03605442. DOI: 10.1016/j.energy.2019.04.070.
- [46] Jiangtao He et al. “Comparative Study of Curve Determination Methods for Incremental Capacity Analysis and State of Health Estimation of Lithium-Ion Battery”. In: *Journal of Energy Storage* 29 (June 2020), p. 101400. ISSN: 2352152X. DOI: 10.1016/j.est.2020.101400.
- [47] Frederik T. Huld et al. “Revealing Silicon’s Delithiation Behaviour through Empirical Analysis of Galvanostatic Charge–Discharge Curves”. In: *Batteries* 9.5 (Apr. 2023), p. 251. ISSN: 2313-0105. DOI: 10.3390/batteries9050251.
- [48] Keitaro Kitada et al. “Unraveling the Reaction Mechanisms of SiO Anodes for Li-Ion Batteries by Combining *in Situ* <sup>7</sup>Li and *Ex Situ* <sup>7</sup>Li/ <sup>29</sup>Si Solid-State NMR Spectroscopy”. In: *Journal of the American Chemical Society* 141.17 (May 2019), pp. 7014–7027. ISSN: 0002-7863, 1520-5126. DOI: 10.1021/jacs.9b01589.
- [49] Asbjørn Ulvestad, Jan Petter Mæhlen, and Martin Kirkengen. “Silicon Nitride as Anode Material for Li-ion Batteries: Understanding the SiN<sub>x</sub> Conversion Reaction”. In: *Journal of Power Sources* 399 (Sept. 2018), pp. 414–421. ISSN: 03787753. DOI: 10.1016/j.jpowsour.2018.07.109.



- [50] Ke Pan et al. “Comprehensive Electrochemical Impedance Spectroscopy Study of Si-Based Anodes Using Distribution of Relaxation Times Analysis”. In: *Journal of Power Sources* 479 (Dec. 2020), p. 229083. ISSN: 03787753. DOI: 10.1016/j.jpowsour.2020.229083.
- [51] F. La Mantia et al. “Reliable Reference Electrodes for Lithium-Ion Batteries”. In: *Electrochemistry Communications* 31 (June 2013), pp. 141–144. ISSN: 13882481. DOI: 10.1016/j.elecom.2013.03.015.
- [52] Frederik T. Huld et al. “Enabling Increased Delithiation Rates in Silicon-Based Anodes through Alloying with Phosphorus”. In: *ChemistrySelect* 7.42 (2022), e202202857. ISSN: 2365-6549. DOI: 10.1002/slct.202202857.
- [53] L. Y. Beaulieu et al. “Reaction of Li with Alloy Thin Films Studied by In Situ AFM”. In: *Journal of The Electrochemical Society* 150.11 (2003), A1457. ISSN: 00134651. DOI: 10.1149/1.1613668.
- [54] Jarred Z. Olson, Carmen M. López, and Edmund J. F. Dickinson. “Differential Analysis of Galvanostatic Cycle Data from Li-Ion Batteries: Interpretative Insights and Graphical Heuristics”. In: *Chemistry of Materials* (Feb. 2023), acs.chemmater.2c01976. ISSN: 0897-4756, 1520-5002. DOI: 10.1021/acs.chemmater.2c01976.
- [55] Maria Sofia Palagonia et al. “Comparison between Cyclic Voltammetry and Differential Charge Plots from Galvanostatic Cycling”. In: *Journal of Electroanalytical Chemistry* 847 (Aug. 2019), p. 113170. ISSN: 15726657. DOI: 10.1016/j.jelechem.2019.05.052.
- [56] Matthieu Dubarry, Cyril Truchot, and Bor Yann Liaw. “Cell Degradation in Commercial LiFePO<sub>4</sub> Cells with High-Power and High-Energy Designs”. In: *Journal of Power Sources* 258 (July 2014), pp. 408–419. ISSN: 03787753. DOI: 10.1016/j.jpowsour.2014.02.052.
- [57] Matthieu Dubarry and Bor Yann Liaw. “Identify Capacity Fading Mechanism in a Commercial LiFePO<sub>4</sub> Cell”. In: *Journal of Power Sources* 194.1 (Oct. 2009), pp. 541–549. ISSN: 03787753. DOI: 10.1016/j.jpowsour.2009.05.036.
- [58] Matthieu Dubarry et al. “Identifying Battery Aging Mechanisms in Large Format Li Ion Cells”. In: *Journal of Power Sources* 196.7 (Apr. 2011), pp. 3420–3425. ISSN: 03787753. DOI: 10.1016/j.jpowsour.2010.07.029.
- [59] Yi Li et al. “A Quick On-Line State of Health Estimation Method for Li-ion Battery with Incremental Capacity Curves Processed by Gaussian Filter”. In: *Journal of Power Sources* 373 (Jan. 2018), pp. 40–53. ISSN: 03787753. DOI: 10.1016/j.jpowsour.2017.10.092.
- [60] Xiaoyu Li, Zhenpo Wang, and Jinying Yan. “Prognostic Health Condition for Lithium Battery Using the Partial Incremental Capacity and Gaussian Process Regression”. In: *Journal of Power Sources* 421 (May 2019), pp. 56–67. ISSN: 03787753. DOI: 10.1016/j.jpowsour.2019.03.008.
- [61] Taeho Yoon et al. “Capacity Fading Mechanisms of Silicon Nanoparticle Negative Electrodes for Lithium Ion Batteries”. In: *Journal of The Electrochemical Society* 162.12 (2015), A2325–A2330. ISSN: 0013-4651, 1945-7111. DOI: 10.1149/2.0731512jes.
- [62] Nicole Thompson et al. “DiffCapAnalyzer: A Python Package for Quantitative Analysis of Total Differential Capacity Data”. In: *Journal of Open Source Software* 5.54 (Oct. 2020), p. 2624. ISSN: 2475-9066. DOI: 10.21105/joss.02624.

- [63] Allen J. Bard and Larry R. Faulkner. *Electrochemical Methods: Fundamentals and Applications*. 2nd ed. New York: Wiley, 2001. ISBN: 978-0-471-04372-0.
- [64] Yong Wang et al. “Novel Constructive Self-Healing Binder for Silicon Anodes with High Mass Loading in Lithium-Ion Batteries”. In: *Energy Storage Materials* 38 (June 2021), pp. 121–129. ISSN: 24058297. DOI: 10.1016/j.ensm.2021.03.003.
- [65] Jijun Lu et al. “Upcycling of Photovoltaic Silicon Waste into Ultrahigh Areal-Loaded Silicon Nanowire Electrodes through Electrothermal Shock”. In: *Energy Storage Materials* 46 (Apr. 2022), pp. 594–604. ISSN: 24058297. DOI: 10.1016/j.ensm.2022.01.051.
- [66] D. A. Lozhkina, A. M. Rumyantsev, and E. V. Astrova. “Impedance Spectroscopy of Porous Silicon and Silicon-Carbon Anodes Produced by Sintering”. In: *Semiconductors* 54.3 (Mar. 2020), pp. 383–391. ISSN: 1063-7826, 1090-6479. DOI: 10.1134/S1063782620030124.
- [67] Fotis Paloukis et al. “Electrochemical Impedance Spectroscopy Study in Micro-Grain Structured Amorphous Silicon Anodes for Lithium-Ion Batteries”. In: *Journal of Power Sources* 331 (Nov. 2016), pp. 285–292. ISSN: 03787753. DOI: 10.1016/j.jpowsour.2016.09.062.
- [68] M.D Levi, Z Lu, and D. Aurbach. “Application of Finite-Diffusion Models for the Interpretation of Chronoamperometric and Electrochemical Impedance Responses of Thin Lithium Insertion V<sub>2</sub>O<sub>5</sub> Electrodes”. In: *Solid State Ionics* 143.3-4 (July 2001), pp. 309–318. ISSN: 01672738. DOI: 10.1016/S0167-2738(01)00819-0.
- [69] Jiapeng Liu and Francesco Ciucci. “The Gaussian Process Distribution of Relaxation Times: A Machine Learning Tool for the Analysis and Prediction of Electrochemical Impedance Spectroscopy Data”. In: *Electrochimica Acta* 331 (Jan. 2020), p. 135316. ISSN: 00134686. DOI: 10.1016/j.electacta.2019.135316.
- [70] J. Illig et al. “Separation of Charge Transfer and Contact Resistance in LiFePO<sub>4</sub>-Cathodes by Impedance Modeling”. In: *Journal of The Electrochemical Society* 159.7 (2012), A952–A960. ISSN: 0013-4651, 1945-7111. DOI: 10.1149/2.030207jes.
- [71] Bernard A. Boukamp. “Fourier Transform Distribution Function of Relaxation Times; Application and Limitations”. In: *Electrochimica Acta* 154 (Feb. 2015), pp. 35–46. ISSN: 00134686. DOI: 10.1016/j.electacta.2014.12.059.
- [72] Jan Philipp Schmidt et al. “Studies on LiFePO<sub>4</sub> as Cathode Material Using Impedance Spectroscopy”. In: *Journal of Power Sources* 196.12 (June 2011), pp. 5342–5348. ISSN: 03787753. DOI: 10.1016/j.jpowsour.2010.09.121.
- [73] Xue Li et al. “A Capacity Model Based on Charging Process for State of Health Estimation of Lithium Ion Batteries”. In: *Applied Energy* 177 (Sept. 2016), pp. 537–543. ISSN: 03062619. DOI: 10.1016/j.apenergy.2016.05.109.
- [74] Hui Pang et al. “A Novel Extended Kalman Filter-Based Battery Internal and Surface Temperature Estimation Based on an Improved Electro-Thermal Model”. In: *Journal of Energy Storage* 41 (Sept. 2021), p. 102854. ISSN: 2352152X. DOI: 10.1016/j.est.2021.102854.

- [75] Hui Pang et al. “Physics-Informed Neural Network Approach for Heat Generation Rate Estimation of Lithium-Ion Battery under Various Driving Conditions”. In: *Journal of Energy Chemistry* 78 (Mar. 2023), pp. 1–12. ISSN: 20954956. DOI: 10.1016/j.jechem.2022.11.036.
- [76] Eric Sivonxay, Muratahan Aykol, and Kristin A. Persson. “The Lithiation Process and Li Diffusion in Amorphous SiO<sub>2</sub> and Si from First-Principles”. In: *Electrochimica Acta* 331 (Jan. 2020), p. 135344. ISSN: 00134686. DOI: 10.1016/j.electacta.2019.135344.
- [77] Vijay A. Sethuraman, Venkat Srinivasan, and John Newman. “Analysis of Electrochemical Lithiation and Delithiation Kinetics in Silicon”. In: *Journal of The Electrochemical Society* 160.2 (2013), A394–A403. ISSN: 0013-4651, 1945-7111. DOI: 10.1149/2.008303jes.
- [78] M. J. Stefan. “Über die Beziehung zwischen der Warmestrahlung und der Temperatur”. In: vol. 1. 1879, pp. 391–428.
- [79] P. W. Atkins and Julio De Paula. *Atkins’ Physical Chemistry*. 8th ed. New York: W.H. Freeman, 2006. ISBN: 978-0-7167-8759-4.
- [80] V. L. Chevrier and J. R. Dahn. “First Principles Model of Amorphous Silicon Lithiation”. In: *Journal of The Electrochemical Society* 156.6 (2009), A454. ISSN: 00134651. DOI: 10.1149/1.3111037.
- [81] Christopher M. DeLuca, Kurt Maute, and Martin L. Dunn. “Effects of Electrode Particle Morphology on Stress Generation in Silicon during Lithium Insertion”. In: *Journal of Power Sources* 196.22 (Nov. 2011), pp. 9672–9681. ISSN: 03787753. DOI: 10.1016/j.jpowsour.2011.07.035.
- [82] Siladitya Pal et al. “Modeling the Delamination of Amorphous-Silicon Thin Film Anode for Lithium-Ion Battery”. In: *Journal of Power Sources* 246 (Jan. 2014), pp. 149–159. ISSN: 03787753. DOI: 10.1016/j.jpowsour.2013.06.089.
- [83] Yunki Gwak, Janghyuk Moon, and Maenghyo Cho. “Multi-Scale Analysis of an Electrochemical Model Including Coupled Diffusion, Stress, and Nonideal Solution in a Silicon Thin Film Anode”. In: *Journal of Power Sources* 307 (Mar. 2016), pp. 856–865. ISSN: 03787753. DOI: 10.1016/j.jpowsour.2016.01.037.
- [84] Yang Jiang et al. “Voltage Hysteresis Model for Silicon Electrodes for Lithium Ion Batteries, Including Multi-Step Phase Transformations, Crystallization and Amorphization”. In: *Journal of The Electrochemical Society* 167.13 (Oct. 2020), p. 130533. ISSN: 0013-4651, 1945-7111. DOI: 10.1149/1945-7111/abbbba.
- [85] Shweta Dhillon et al. “Modelling Capacity Fade in Silicon-Graphite Composite Electrodes for Lithium-Ion Batteries”. In: *Electrochimica Acta* 377 (May 2021), p. 138067. ISSN: 00134686. DOI: 10.1016/j.electacta.2021.138067.
- [86] Zheng Chen et al. “High-Areal-Capacity Silicon Electrodes with Low-Cost Silicon Particles Based on Spatial Control of Self-Healing Binder”. In: *Advanced Energy Materials* 5.8 (Apr. 2015), p. 1401826. ISSN: 16146832. DOI: 10.1002/aenm.201401826.
- [87] M. Ender, J. Illig, and E. Ivers-Tiffée. “Three-Electrode Setups for Lithium-Ion Batteries”. In: *Journal of The Electrochemical Society* 164.2 (2017). DOI: 10.1149/2.0231702jes.

- [88] Ivana Hasa et al. “Electrochemical Reactivity and Passivation of Silicon Thin-Film Electrodes in Organic Carbonate Electrolytes”. In: *ACS Applied Materials & Interfaces* 12.36 (Sept. 2020), pp. 40879–40890. ISSN: 1944-8244, 1944-8252. DOI: 10.1021/acsmi.0c09384.
- [89] Caroline Keller et al. “Effect of Size and Shape on Electrochemical Performance of Nano-Silicon-Based Lithium Battery”. In: *Nanomaterials* 11.2 (Jan. 2021), p. 307. ISSN: 2079-4991. DOI: 10.3390/nano11020307.
- [90] Yi-Shiuan Wu et al. “PVDF-HFP/PET/PVDF-HFP Composite Membrane for Lithium-Ion Power Batteries”. In: *International Journal of Hydrogen Energy* 42.10 (Mar. 2017), pp. 6862–6875. ISSN: 03603199. DOI: 10.1016/j.ijhydene.2016.11.201.
- [91] G. Kresse and J. Furthmüller. “Efficiency of Ab-Initio Total Energy Calculations for Metals and Semiconductors Using a Plane-Wave Basis Set”. In: *Computational Materials Science* 6.1 (July 1996), pp. 15–50. ISSN: 09270256. DOI: 10.1016/0927-0256(96)00008-0.
- [92] P. E. Blöchl. “Projector Augmented-Wave Method”. In: *Physical Review B* 50.24 (Dec. 1994), pp. 17953–17979. ISSN: 0163-1829, 1095-3795. DOI: 10.1103/PhysRevB.50.17953.
- [93] John P. Perdew, Kieron Burke, and Matthias Ernzerhof. “Generalized Gradient Approximation Made Simple”. In: *Physical Review Letters* 77.18 (Oct. 1996), pp. 3865–3868. ISSN: 0031-9007, 1079-7114. DOI: 10.1103/PhysRevLett.77.3865.
- [94] G. Kresse and J. Hafner. “Ab Initio Molecular Dynamics for Liquid Metals”. In: *Physical Review B* 47.1 (Jan. 1993), pp. 558–561. ISSN: 0163-1829, 1095-3795. DOI: 10.1103/PhysRevB.47.558.
- [95] Cong Su, Hua Jiang, and Ji Feng. “Two-Dimensional Carbon Allotrope with Strong Electronic Anisotropy”. In: *Physical Review B* 87.7 (Feb. 2013), p. 075453. ISSN: 1098-0121, 1550-235X. DOI: 10.1103/PhysRevB.87.075453.
- [96] Matthew Murbach et al. “Impedance.Py: A Python Package for Electrochemical Impedance Analysis”. In: *Journal of Open Source Software* 5.52 (Aug. 2020), p. 2349. ISSN: 2475-9066. DOI: 10.21105/joss.02349.
- [97] Matt Newville et al. *Lmfit/Lmfit-Py: 1.2.0*. Zenodo. Apr. 2023. DOI: 10.5281/zenodo.7810964.
- [98] Hanne Flåten Andersen et al. “Production of Silicon Particles for High-Capacity Anode Material Yielding Outstanding Production Capacity”. In: *ECS Transactions* 62.1 (Nov. 2014), pp. 97–105. ISSN: 1938-5862, 1938-6737. DOI: 10.1149/06201.0097ecst.
- [99] R. Körmer et al. “Aerosol Synthesis of Silicon Nanoparticles with Narrow Size Distribution—Part 1: Experimental Investigations”. In: *Journal of Aerosol Science* 41.11 (Nov. 2010), pp. 998–1007. ISSN: 00218502. DOI: 10.1016/j.jaerosci.2010.05.007.
- [100] Sebastien Martinet. “Nanomaterials for Rechargeable Lithium Batteries”. In: *Nanomaterials for Sustainable Energy*. Ed. by Quan Li. Cham: Springer International Publishing, 2016, pp. 471–512. ISBN: 978-3-319-32021-2. DOI: 10.1007/978-3-319-32023-6\_13.
- [101] Carl Erik Lie Foss et al. “Anodes for Li-ion Batteries Prepared from Microcrystalline Silicon and Enabled by Binder’s Chemistry and Pseudo-Self-Healing”. In: *Scientific Reports* 10.1 (Aug. 2020), p. 13193. ISSN: 2045-2322. DOI: 10.1038/s41598-020-70001-5.

- [102] E. Deiss. “Spurious Chemical Diffusion Coefficients of Li<sup>+</sup> in Electrode Materials Evaluated with GITT”. In: *Electrochimica Acta* 50.14 (May 2005), pp. 2927–2932. ISSN: 00134686. DOI: 10.1016/j.electacta.2004.11.042.
- [103] W Weppner and R A Huggins. “Electrochemical Methods for Determining Kinetic Properties of Solids”. In: *Annual Review of Materials Science* 8.1 (Aug. 1978), pp. 269–311. ISSN: 0084-6600. DOI: 10.1146/annurev.ms.08.080178.001413.
- [104] C. Ho, I. D. Raistrick, and R. A. Huggins. “Application of A-C Techniques to the Study of Lithium Diffusion in Tungsten Trioxide Thin Films”. In: *Journal of The Electrochemical Society* 127.2 (Feb. 1980), pp. 343–350. ISSN: 0013-4651, 1945-7111. DOI: 10.1149/1.2129668.
- [105] Georgios A. Tritsarlis et al. “Diffusion of Lithium in Bulk Amorphous Silicon: A Theoretical Study”. In: *The Journal of Physical Chemistry C* 116.42 (Oct. 2012), pp. 22212–22216. ISSN: 1932-7447, 1932-7455. DOI: 10.1021/jp307221q.
- [106] A. Fly and R. Chen. “Rate Dependency of Incremental Capacity Analysis (dQ/dV) as a Diagnostic Tool for Lithium-Ion Batteries”. In: *Journal of Energy Storage* 29 (June 2020), p. 101329. ISSN: 2352152X. DOI: 10.1016/j.est.2020.101329.
- [107] Elad Pollak et al. “In Situ Conductivity, Impedance Spectroscopy, and Ex Situ Raman Spectra of Amorphous Silicon during the Insertion/Extraction of Lithium”. In: *The Journal of Physical Chemistry C* 111.30 (Aug. 2007), pp. 11437–11444. ISSN: 1932-7447, 1932-7455. DOI: 10.1021/jp0729563.
- [108] Marco-Tulio F. Rodrigues. “Capacity and Coulombic Efficiency Measurements Underestimate the Rate of SEI Growth in Silicon Anodes”. In: *Journal of The Electrochemical Society* 169.8 (Aug. 2022), p. 080524. ISSN: 0013-4651, 1945-7111. DOI: 10.1149/1945-7111/ac8a21.
- [109] M. Schönleber and E. Ivers-Tiffée. “The Distribution Function of Differential Capacity as a New Tool for Analyzing the Capacitive Properties of Lithium-Ion Batteries”. In: *Electrochemistry Communications* 61 (Dec. 2015), pp. 45–48. ISSN: 13882481. DOI: 10.1016/j.elecom.2015.09.024.
- [110] C H Chen, J Liu, and K Amine. “Symmetric Cell Approach and Impedance Spectroscopy of High Power Lithium-Ion Batteries”. In: *Journal of Power Sources* 96.2 (June 2001), pp. 321–328. DOI: 10.1016/S0378-7753(00)00666-2.
- [111] Zahilia Cabán Huertas et al. “High Performance Silicon Electrode Enabled by Titanicone Coating”. In: *Scientific Reports* 12.1 (Jan. 2022), p. 137. ISSN: 2045-2322. DOI: 10.1038/s41598-021-04105-x.
- [112] J. C. deMello et al. “Ionic Space-Charge Effects in Polymer Light-Emitting Diodes”. In: *Physical Review B* 57.20 (May 1998), pp. 12951–12963. ISSN: 0163-1829, 1095-3795. DOI: 10.1103/PhysRevB.57.12951.
- [113] Jeeseok Seok et al. “Understanding the Impacts of Li Stripping Overpotentials at the Counter Electrode by Three-Electrode Coin Cell Measurements”. In: *Analytical Chemistry* 93.46 (Nov. 2021), pp. 15459–15467. DOI: 10.1021/acs.analchem.1c03422.

- [114] Franz Dinkelacker et al. “Multistage Mechanism of Lithium Intercalation into Graphite Anodes in the Presence of the Solid Electrolyte Interface”. In: *ACS Applied Materials & Interfaces* 10.16 (Apr. 2018), pp. 14063–14069. ISSN: 1944-8244, 1944-8252. DOI: 10.1021/acsami.7b18738.
- [115] Huajun Tian et al. “High Capacity Group-IV Elements (Si, Ge, Sn) Based Anodes for Lithium-Ion Batteries”. In: *Journal of Materiomics* 1.3 (Sept. 2015), pp. 153–169. ISSN: 23528478. DOI: 10.1016/j.jmat.2015.06.002.
- [116] Frederik Huld, Zhixin Yu, and Fengliu Lou. “Unravelling the Electrochemical Impedance Spectroscopy of Silicon Half Cells with Commercial Loading”. In: *Energy Advances* (2023), 10.1039.D3YA00181D. ISSN: 2753-1457. DOI: 10.1039/D3YA00181D.
- [117] Ajaykrishna Ramasubramanian et al. “Stability of Solid-Electrolyte Interphase (SEI) on the Lithium Metal Surface in Lithium Metal Batteries (LMBs)”. In: *ACS Applied Energy Materials* 3.11 (Nov. 2020), pp. 10560–10567. ISSN: 2574-0962, 2574-0962. DOI: 10.1021/acsaem.0c01605.
- [118] Pallavi Verma, Pascal Maire, and Petr Novák. “A Review of the Features and Analyses of the Solid Electrolyte Interphase in Li-ion Batteries”. In: *Electrochimica Acta* 55.22 (Sept. 2010), pp. 6332–6341. ISSN: 00134686. DOI: 10.1016/j.electacta.2010.05.072.
- [119] Matthew Smith et al. “Improving the Deconvolution and Interpretation of XPS Spectra from Chars by Ab Initio Calculations”. In: *Carbon* 110 (Dec. 2016), pp. 155–171. ISSN: 00086223. DOI: 10.1016/j.carbon.2016.09.012.
- [120] Xiangnan Chen, Xiaohui Wang, and De Fang. “A Review on C1s XPS-spectra for Some Kinds of Carbon Materials”. In: *Fullerenes, Nanotubes and Carbon Nanostructures* 28.12 (Dec. 2020), pp. 1048–1058. ISSN: 1536-383X, 1536-4046. DOI: 10.1080/1536383X.2020.1794851.



University  
of Stavanger

4036 Stavanger

Tel: +47 51 83 10 00

E-mail: [post@uis.no](mailto:post@uis.no)

[www.uis.no](http://www.uis.no)

© 2024 **Frederik Thorbjørn Huld**